Adsorption and Self-assembly of Cobalt(II)-Tetraphenylporphyrin on Cu(110)

UNIVERSITY OF LIVERPOOL

Thesis submitted in accordance with the requirements of the University of Liverpool for the degree of Doctor in Philosophy

by

Philip John Donovan

Department of Chemistry
University of Liverpool

October 2009

Abstract

Adsorption and self-assembly of Cobalt(II)-Tetraphenylporphyrin on Cu(110)

In a combined scanning tunneling microscopy (STM) and periodic density functional theory (DFT) study, the fundamental forces driving the adsorption and self-assembly of Co(II)-Tetraphenylporphyrin (Co-TPP) molecules on the Cu(110) surface are investigated.

Adsorption of Co-TPP on Cu(110) at room temperature leads to the creation of three distinct highly organised assemblies (Structures 1, 2 and 3). Structures 1 and 2 form long range chiral arrays that are fully commensurate with the underlying surface lattice, with equivalent but mirror domains described by the one-molecule G^{λ} = (2 4, -6 -2) and G^{δ} = (-6 2, 2 -4) unit cells for Structure 1 and the two-molecule G^{λ} = (4 7, -7 -2) and G^{δ} = (-7 2, 4 -7) unit cells for Structure 2. The existence of mirror domains is attributed to the directionality of the intermolecular π–π interactions, which, in Structure 3, alternate between positive and negative directions relative to the Cu axes, resulting in a single copper-aligned unit cell, G = (12 0, 0 8), and a racemic organisation of alternating mirror-opposite molecular orientations that, unusually, incorporates adatoms. Structures 1-3 are constructed with a total of six distinct intermolecular interactions, which also form phase boundaries and other phenomena whose appearance is related to the sublimation conditions. Three orientations of isolated molecule also exist: two chiral and one that shares its symmetry axes with those of the copper surface.

Periodic DFT calculations have been carried out on the substrate-aligned isolated molecule and the Structure 1 chiral array by Matthew Dyer of the group of Mats Persson in the University of Liverpool's Surface Science

Research Centre. Isolated molecules are shown to adopt a saddled macrocycle geometry with twisted phenyl groups as it adsorbs at the long-bridge site. In stark contrast, the Structure 1 conformer adsorbs at the short-bridge site and takes on a conformation with a mostly flat macrocycle and strongly tilted phenyls. Experimental STM images are well explained in terms of these conformational considerations as well as electronic effects.

An energetic balance is performed using the DFT results and shows that the cost of molecule and substrate deformations is substantially greater for the Structure 1 geometry at $+268.3 kJmol^{-1}$, compared to $+136 kJmol^{-1}$ for the isolated conformer. However, for both conformers, these costs are recuperated by a considerable interaction between the molecular core and the substrate that results in a net adsorption energy of around $-96 kJmol^{-1}$ for both geometries. Crucially, it is found that the severe phenyl tilting deformations in the Structure 1 conformer favours intermolecular $\pi-\pi$ interactions, whose small but pivotal energy gain of about $-25 kJmol^{-1}$ drives the formation of extended structures. The optimisation of all four intermolecular interactions per molecule and the adaptation of the phenyls to the surface corrugation also pins individual molecules in a chiral propeller-like conformation in Structure 1. This likely applies to Structure 2 also, but not necessarily Structure 3.

This work reveals that the surface not only plays a role in immobilising and organising porphyrins in two dimensions, but that a strong macrocycle-surface interaction may trigger unexpected molecular structures, thus extending the range of chemistries possible within these systems.

Contents

List of Figures

List of Publications

1. P. Donovan, A. Robin, M. S. Dyer, M. Persson and R. Raval, (**2009**) *Unexpected Deformations Induced by Surface Interaction and Chiral Self-Assembly of Co(II)-Tetraphenylporphyrin adsorbed on Cu(110): A combined STM and Periodic DFT study*, Journal of the American Chemical Society, Submitted.

Acknowledgements

I would firstly like to express my gratitude to my supervisor, Professor Rasmita Raval, for gambling and giving me the opportunity to expand my horizons by working in and contributing to her research group. Thanks must also go to all those who helped me get started, including Lisa Marnell, Vicky Smith, Mendel In't Veld, John Ledward and most of all, Sam Haq, who somehow found, and continues to find, the time to put others' problems first, no matter how small.

People have come and gone over the years but Abel 'Typically' Robin and Matt 'Pentagonal water?' Forster have made the majority of my time in the centre a great experience by offering their support and, most importantly, their humour. I think we made a really good team! Honourable mentions go to all the others in the centre for being a thoroughly decent bunch of people that I won't soon forget. You've all made the last couple of years a really good laugh.

Now down to business. A great effort and two years has gone into the countless revisions of the publication and thanks must first go to Abel for offering his advice and guidance from the very beginning. I also offer my sincerest thanks and respect to Matthew Dyer and Mats Persson for their extraordinary effort in performing the DFT calculations for the paper. The quality of the final product has surpassed all of my expectations thanks also to the valued proof-reading contributions of Matthew, Ras and Mats and the last minute LEED pattern from Sam. This manuscript has benefited greatly from the time and effort you all put in, including proof-reading and criticism from Sam Haq and Sue Barlow.

Finally, thanks to Dad and Graham for the support you've offered, especially over the last year. It's reassuring to know I can fall back on you if I

need to. Pints will definitely be on me, soon. A mighty 'Yerse!' and 'Nice work!' go to my good friends Marc 'waste-mooch' Mullin and Jonathan 'jonno' Westwood. I can't remember much, but those profoundly hilarious breaks from normality over the past few years were much needed.

And last but by no means least. I wouldn't have been able to accomplish all I have without the continued love and support from Lisa. Even through the really stressful times, you've put up with me and stuck by me. Thank you so much.

CHAPTER 1

Introduction

1.1. General Introduction

Surface and interface science is a multi-disciplinary field that spans physics, chemistry, biology and materials and clinical science. As a result, the field has found significant breadth of application, for example, in heterogeneous catalysis, corrosion, film growth and semiconductor electronics. Furthermore, recent advances in the biological sciences owe much to surface-sensitive analytical techniques.

There is a large body of information on small molecules adsorbed at solid surfaces, CO is a prime example[1-13], and the knowledge gleaned from these studies has provided the basis for larger and more complex systems to be approached. However, despite a growing number of studies on larger systems[13-20] it remains a complicated area of investigation and small changes to a system, e.g. the presence (or not) of side groups or metal ions in porphyrins, can result in striking and unexpected consequences, even when all other experimental conditions are maintained. One such class of complex molecule that is currently of great technological and scientific interest is the porphyrins[19,21-35]. Due to their versatility and functionality, they are a promising basis for realisation of the controlled assembly of molecular building blocks on defined substrates, which is one of the major keys in building functional molecular nano-devices and materials[34,36-39]. Indeed, the wide variation of functionalisation of porphyrins for specific electronic, magnetic and conformational properties that have already given rise to

promising technological applications in colorimetric gas sensors[40], organic solar cells[41], photonic wires, Field Effect Transistors (FTs), Light Emitting Diodes (LEDs), catalysts, optical switches[42,43] and data storage[44]. An interesting development is the possibility of technologies based on porphyrin monolayers, which would require nanoscale control and detailed understanding of all relevant interactions involved in their adsorption and self-assembly. However, the current understanding of porphyrin systems means that researchers are unable to directly transfer knowledge and expectation between closely related porphyrin systems – a deeper understanding is now the goal so that reliable predictions can be made. With modern surface science equipment and computational facilities, this is now becoming realistic.

A surface atom has fewer neighbours than an atom in the bulk, leaving dangling bonds, which present 'reactive sites'. The coordination of atomic or molecular species at these sites gives rise to myriad properties and functionalities. It is no surprise that, since the 1960s, there has been considerable interest in the nature of solid surfaces, be it single crystals, quasicrystals[45-47], alloys[48], or nano-particles[49,50], and their interactions with atomic and/or molecular species. This interest has seen investigation of the solid/liquid, solid/air, solid/solid (atomic or molecular layers) and solid/vacuum interfaces. Environments such as air or liquid enable the effects of real-world contaminants and disorder to be studied, but do not allow a fundamental understanding. Conversely, the use of vacuum, and Ultra High Vacuum (UHV) specifically, enables the researcher to selectively modify and control the system under scrutiny, thus allowing fundamental issues to be tackled. UHV itself presents problems, however, requiring expensive and bulky instrumentation, but the intrinsic costs are far outweighed by the gains. Thus, vacuum apparatus is now used in the study of a wide range of nano-scale systems. This is mainly due to the ability of the researcher to be able to introduce a substance that is known to be pure at a surface that is known to be clean: Even before experimentation, one can decisively characterise

aspects of the experiment that would otherwise remain unknown. Furthermore, when employed in the analysis of molecules that are adsorbed on solid surfaces, UHV techniques can provide detailed information about inter- and intra-molecular and molecule-substrate interactions that is simply not achievable under other conditions. Using this approach, models are constructed that are extremely important as they present a functional foundation for fundamental descriptions of real-world systems, which are typically too complicated for consideration.

The last thirty years has seen great advancements in the tools available for surface scientists. Improvements in vacuum technology and molecular/atomic deposition systems have coincided with the continued development of experimental techniques such as Reflection Absorption Infrared Spectroscopy (RAIRS) and Scanning Tunnelling Microscopy (STM)[51]. Using combinations of the 100+ surface sensitive methods that are available, it is now possible to obtain information pertaining to any chemical or physical property of the system (both molecules/adatoms and surface), although deciphering the output of many techniques remains extremely challenging. More recently, experimental data has been offered strong support by theoretical methods. Numerous small molecules on solid surfaces have benefited from calculations in one form or other[8,12,13,52,53] but larger systems have only come into focus more recently with the application of periodic DFT[54,55]. Despite the main drawback that this method is computationally demanding, requiring supercomputer facilities, it promises important and deep insight into adsorbed molecule systems that experimental methods cannot offer; from single molecules through to self-assembled monolayers or networks of interacting molecules.

1.2. Porphyrins

1.2.1. Structure

Porphyrins are based on a core ring structure, which, by itself, is known as a Porphine (Figure 1.2-1). The Porphine consists of four pyrrole

subunits that are linked by four methine bridges, and has 22 π-electrons. The conjugated system of alternating single and double bonds between carbons not only lowers the overall energy of the molecule, but also makes the compound chromatic, hence name 'porphyrin', which originates from the Greek word for purple.

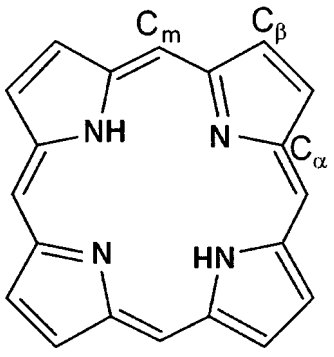

Figure 1.2-1. A porphyrin core, or porphine, showing the α, β and methine carbon designations.

The large range of functionality of the porphyrin family stems from this core, which permits the addition of chemical groups at the methine bridges (C_m), the β carbons of the pyrrole rings or via axial ligation at metal ions that can be coordinated in the central cavity. This diversity of functionality is the reason for their prevalence in nature. Two examples of porphine functionalisation are Tetraphenylporphyrin (TPP) and Phthalocyanine (Pc), shown in Figure 1.2-2. A porphine functionalised such as in TPP is called a porphyrin. In the porphyrin, the porphine is often referred to as the macrocycle.

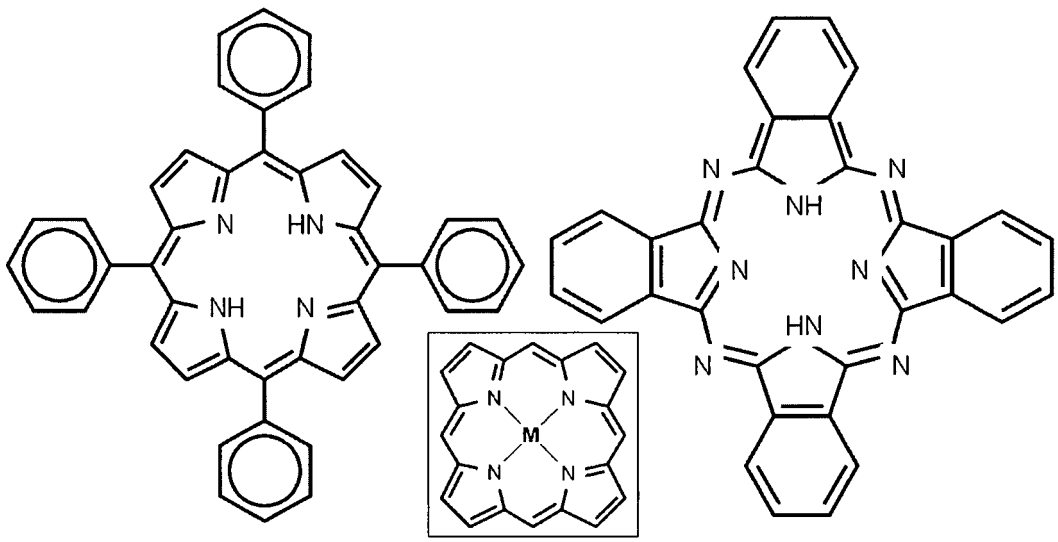

Tetraphenylporphyrin Phthalocyanine

Figure 1.2-2. Schematics of TPP ($C_{44}H_{30}N_4$) and Pc ($C_{32}H_{18}N_{80}$). Inset centre: Metal ion coordination in the core cavity. The two hydrogens must be lost in order for an ionic bond to be created.

Significant functionality can be introduced to metal-free, or free-base, porphyrins by the coordination of metal ions into the core cavity of the macrocycle (Figure 1.2-2 inset). This process is called chelation. Since metal ions such as iron exhibit an affinity for electro-negativity, the metal can be introduced into the cavity when the hydrogens bonded to the core nitrogens are removed, which makes the core negatively charged and suitable for ionic bonding. There have been several recent studies of porphyrin and phthalocyanine metallation[24,25,56-58]. Porphyrin chelation is shown to occur in two steps: firstly, the two pyrrolic hydrogens are transferred to the metal ion, then secondly, they are released as H_2 and the metal ion is incorporated into the porphyrin cavity[26,56,58]. There are numerous examples of metal ion functionality in nature, but they are most commonly associated with the all-important oxygen transport/storage and light harvesting functions[27,29,59,60]. These are mediated by iron- and manganese-coordinated molecules, respectively. Further examples are shown in Table 1.2-1.

Table 1.2-1. Porphyrin molecules in nature perform a wide variety of functions. They can be distinguished by their central metal ion. (table adapted from Smith[61]). Below are the examples of Heme, Chlorophyll and Vitamin B12 (reproduced from http://www.sigmaaldrich.com and http://en.wikipedia.org).

Tetrapyrrole	Metal Ion	Function	Protein Complex
Chlorophyll Bacteriochlorophyll	Mg	Light Harvesting	Chlorophyll-binding proteins
Heme	Fe	Respiration, Photophorylation, Removal of reactive oxygen species, detoxification, N_2-fixation, O_2-transport/Storage.	Cytochrome, Cytochrome P450, Catalyse, Peroxidase, Haemoglobin, Myoglobin
Phycobiline	Fe	Light Harvesting	Phycobilisomes
Phytochromobiline	Fe	Light Perception	Phytochrome
Siroheme	Fe	Sulfinate and nitrate reduction	Sulfinate reductase, Nitrate reductase
Corrinoids	Co	Coenzyme vitamin B12	Methylmalonyl coenzyme A mutase

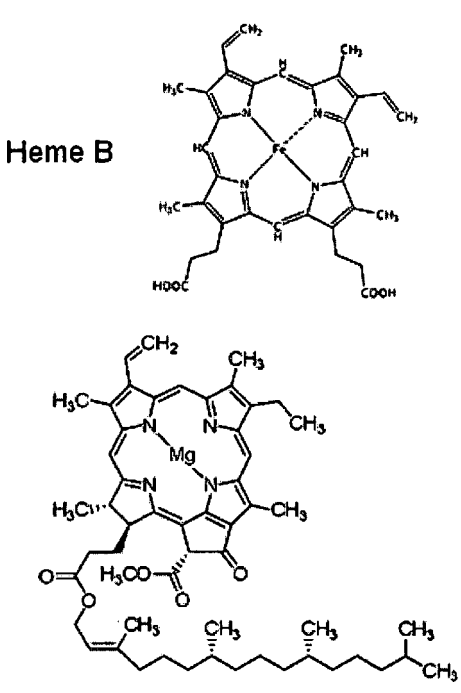

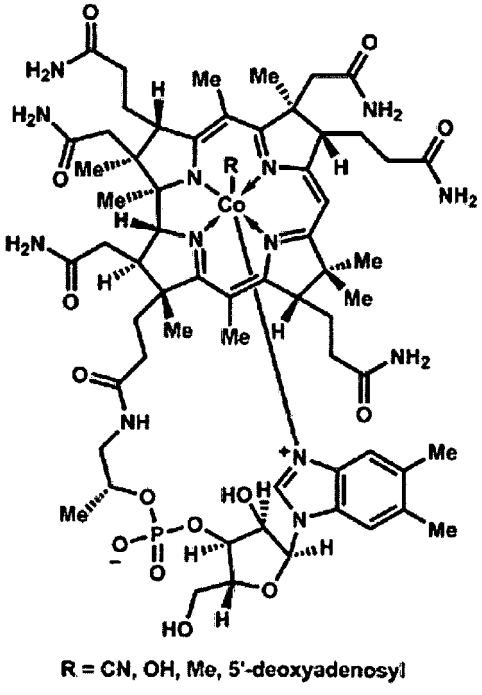

In the gas phase, there can be drastic alterations to the geometry of the molecule as chelates are formed. Although not strictly accurate, most porphyrins are considered planar. When metal chelates are formed from porphyrin molecules their geometry can be radically deformed because the metal ions do not fit exactly into the core cavity of the macrocycle. The discrepancy between the metal-nitrogen bond length and the core hole

diameter means the molecule has to adjust itself in order to accommodate the ion. Some ruffling or saddling may occur for small ions and larger ions induce doming deformations. These deformations are shown in Figure 1.2-3.

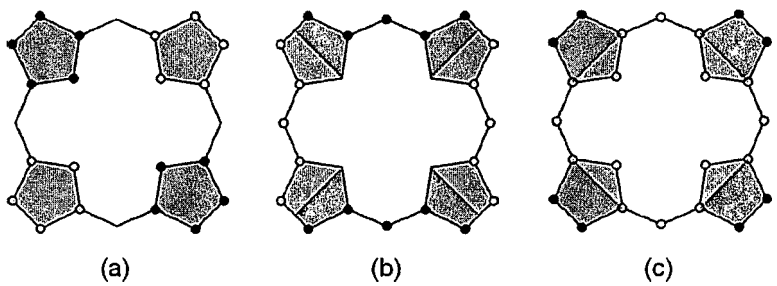

Figure 1.2-3. (a) Saddling, (b) ruffling and (c) doming macrocycle deformations caused by the coordination of metal ions. Open and solid circles represent points that lie below and above the mean plane, respectively. Adapted from Gruden-Pavlović, Grubišić and Niketić[62].

Cobalt(II)-TPP is an unusual molecule as it undergoes very little deformation despite the cobalt-nitrogen bond length being significantly shorter than the core cavity size. This enhanced resistance to deformation is attributed to the cobalt ion favouring a square-planar coordination geometry[32]. The conformation of the molecule is further affected by the size and nature of *ortho*-substituents on the methine bridges, such as the phenyl groups in TPP. These groups adopt orientations such that repulsive steric interactions caused by π-overlap with the pyrrole rings of the macrocycle are minimised. Upon adsorption, deformations of the molecule can be induced by the interaction between *ortho*-substituents and the surface, depending on the groups' size and the strength of the interaction with the substrate.

1.2.2. Adsorption and self-assembly on metal surfaces

Studies of porphyrin or phthalocyanine monolayers date back as far as the 1930s[63], but it wasn't until recently, during the early 1980s, in which work to understand the properties of porphyrin monolayers adsorbed on solid surfaces began. At this time, their electronic[64] and catalytic[65,66] properties were of greatest interest, however, as the techniques available to surface science developed, the focus has shifted from the properties of the film as a whole to the properties of its molecular constituents – the porphyrins

themselves. If understood, the relation between the molecular properties and the properties of the film is expected to allow for functionalisation of the molecule for specific properties, be it conformational, magnetic or catalytic properties, the preference for adsorption at specific sites or the ability to form tailored interactions that form functionalised monolayers, wires or networks[22,38,67-70]. A major problem with studying porphyrin monolayers is that it is difficult to endow functionality in a deliberate and effective way to a molecule that would likely react radically different after only small changes have been made, such as the introduction of metal atoms into their core[26,58,61,70].

Studies of ordered porphyrins and the related phthalocyanines have been conducted on metal surfaces in both solution[30,37,71] and in ultra high vacuum[23,26,29,36,67,70,72-76], involving the use of complementary surface sensitive techniques such as Near Edge X-Ray Absorption Fine Structure (NEXAFS)[36], X-Ray Photoelectron Spectroscopy (XPS)[26,29], and Scanning Tunnelling Microscopy/Spectroscopy (STM)/(STS)[37,74,77,78]. STM in particular has allowed a wide range of detailed electronic and geometric information to become available and shown its use in molecular manipulation[42,79,80] but publications only go back as far as the mid 1990s[77,78,81-85]. Jung *et al*[82], Hipps *et al*[77] and Lu *et al*[78] particularly laid the foundation for future work on organised porphyrin and phthalocyanine arrays at surfaces. Jung *et al*[82] reported the formation of a total four distinct surface phases from the adsorption and subsequent annealing of Cu-tetra[3,5 di-*t*-butylphenyl]porphyrin (Cu-TTBPP) on the Cu(100), Au(110) and Ag(110) surfaces.

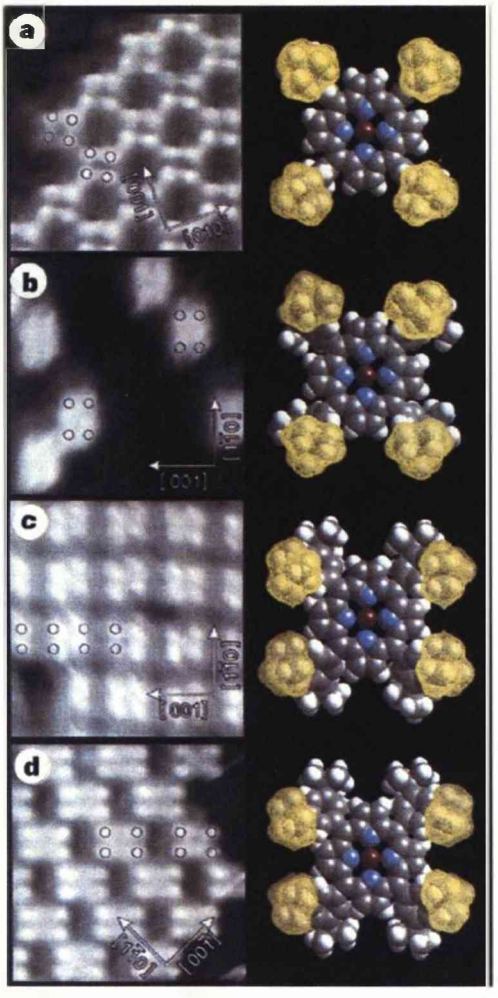

Figure 1.2-4. Four surface phases are observed across three single crystal surfaces upon the adsorption of Cu-TTBPP in work by Jung *et al*[82].

For each phase, the features in the STM images corresponding to one molecule were identified and the aspect ratio was calculated using those that corresponded to the topmost butyl groups (Figure 1.2-4). From there a molecular conformation was constructed that had phenyl twisting Θ and tilting Φ deformations (Figure 1.2-5) that fit the STM data. It was concluded from this work that all the observed conformations were driven by the molecule-surface interaction, where a greater interaction results in greater deformation of the molecule. It would be shown later that this study provided the first indications that the conformation of porphyrin molecules adsorbed both individually and in assemblies may involve molecular deformations that would be unfavourable in the gas phase[23,32,74], suggesting a strong influence of the molecule-surface interaction on the subsequent conformational adaptation.

For Cu-TTBPP on Cu(100)[82], this interaction partially takes the form of a weak chemisorption of the saturated butyl groups to the surface, to which the observed molecular mobility is attributed.

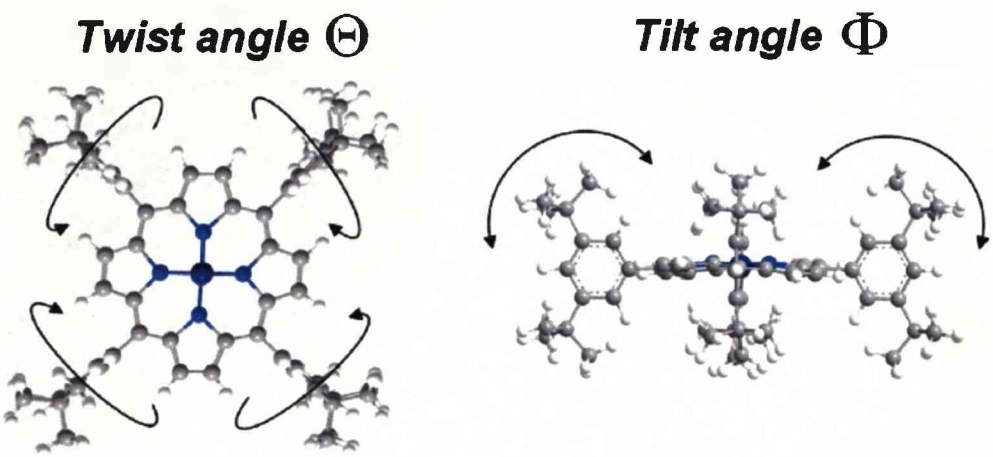

Figure 1.2-5. Phenyl twist and tilt deformations, taken from Buchner *et al*[23].

Severe surface-induced deformations have been documented more recently[23,36,72,74]. Strikingly, Buchner *et al*[23] present high resolution STM images of four distinguishable self-assembled structures from the sublimation of Co-TTBPP onto the Ag(111) surface, which was held at room temperature during deposition (Figure 1.2-6). As in the work by Jung *et al*, each conformation was fitted with a molecule that was deformed to accurately correspond with the aspect ratio measured from the STM images. Good agreement was, therefore, achieved.

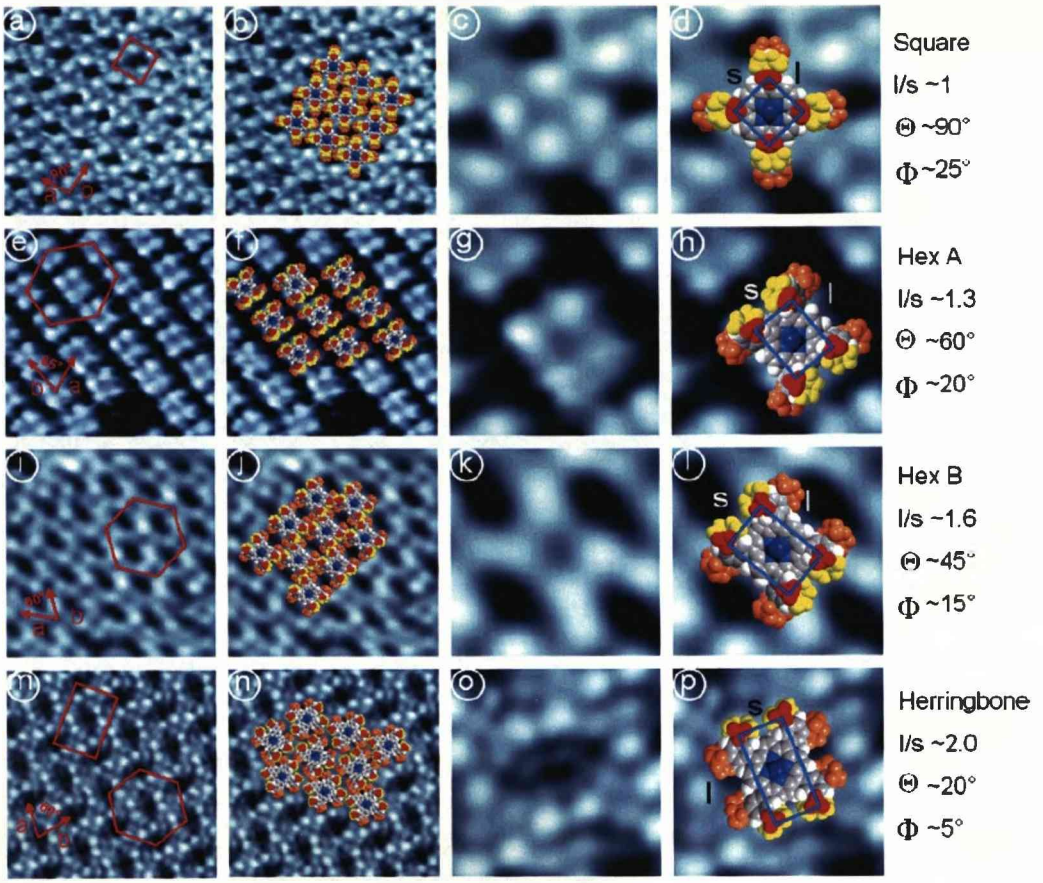

Figure 1.2-6. Four highly ordered structures form on the adsorption of Co-TTBPP onto the Ag(111) surface at room temperature[23]. The herringbone phase (bottom row) is concluded to be a thermally activated phase.

A further example of multiple structures that are formed from the adsorption onto the Cu(111) surface of a single type of porphyrin molecule, 5,10,15,20-tetrakis(3,5-di-t-butyl-4-hydroxyphenyl) porphyrin, TDtBHPP, is found in the work of Hill and co-workers[34,39,86]. It was found that the phase structure and, therefore, molecular conformation was determined by a trade off between steric repulsions between the *ortho*- groups and the macrocycle and attractive intermolecular interactions. The most energetically stable structure for adsorption was, therefore, not the most stable for the formation of extended structures. These works also encompass a description of the boundary between phases, which identifies the adaptability of adsorbed porphyrins to their local environment. This work is summarised in Figure 1.2-7.

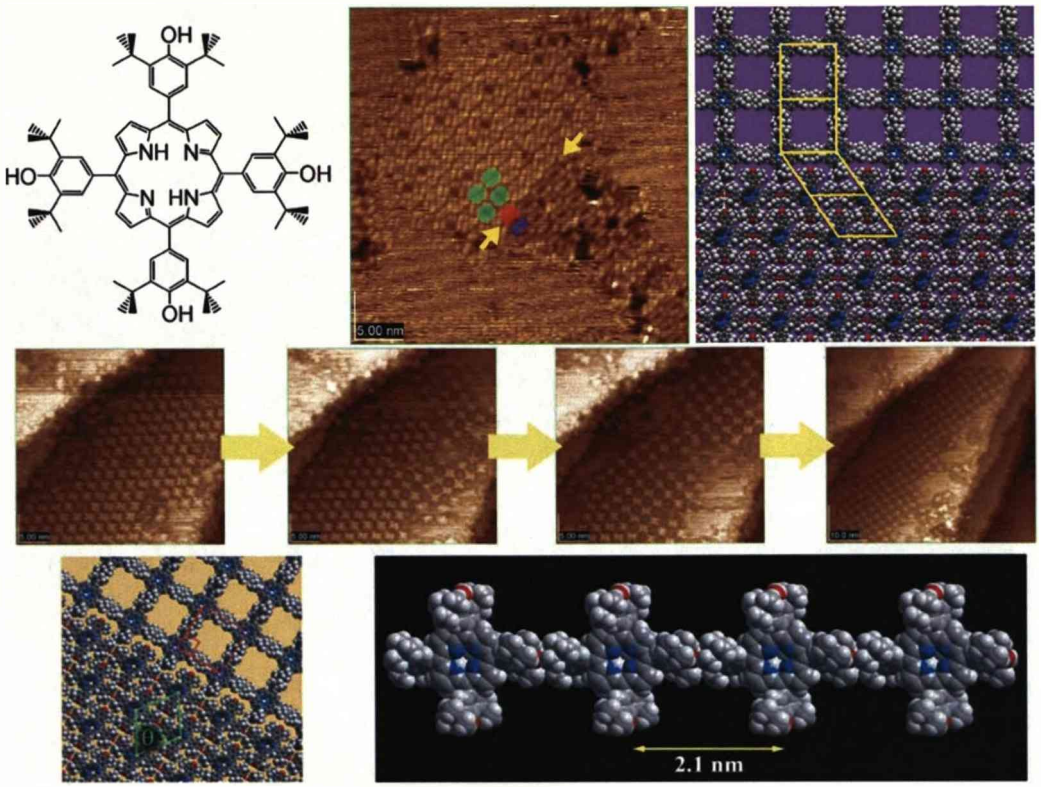

Figure 1.2-7. Summary of the work of Hill *et al*[39,86] and Ariga *et al*[34]. The molecule forms separate domains that rearrange to for the most energetically stable at room temperature. Domain boundaries highlight the adaptability of porphyrin molecules.

Importantly, researchers have identified that the conformation of the adsorbed molecule is a defining factor in determining its properties and self-assembly. However, it can be argued that a genuine understanding is absent from studies where the deformation of the molecule is done manually and based solely on the observed spread of electron density in the STM images, which can be deceptive. Furthermore, the deformations are only to the ortho-groups and not to the macrocycle, about which no conformational conclusions are generally given. It appears from the models in each work that a planar core is expected. Indeed, very little contribution to the STM images is observed from this region and this could be due to relative apparent heights, however, no assumptions are explicitly made. Another drawback of this method is that intermolecular interactions, and their geometric consequences, are ignored entirely, and the structures are consequently modelled as tightly packed groups of isolated molecules, rather than a network of connected units.

To push the understanding further, conclusions about molecular deformations must be made from experimental evidence. Work by Auwarter *et al*[21] and Weber-Bargioni *et al*[31] address this issue by applying NEXAFS to free-base Tetrapyridyl-porphyrin (H_2-TPyP) and Co-TPP adsorbed on Cu(111), respectively, to determine the distortions to both the core and outer groups. These data show strong distortions of each molecule on adsorption, but for different reasons. The adsorption of Co-TPP onto Cu(111) reveals self-assembly into chiral domains that are mirrored across each of the three main copper directions, thereby creating a total of six distinguishable domains. By combining STS with NEXAFS, a strong argument is forged for a saddle shaped conformer in the self-assembled domain (Figure 1.2-8).

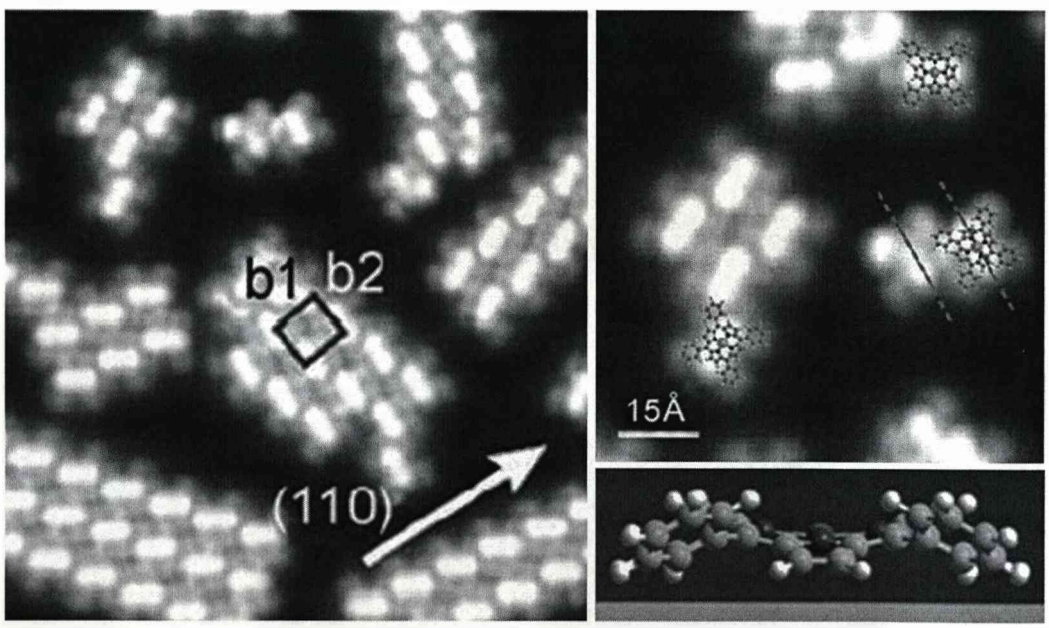

Figure 1.2-8. Results from Weber-Bargioni *et al*[31]. Organisational chirality is manifest in the Co-TPP/Cu(111) system. Domains are formed from molecules that are highly saddled and with phenyls that orient close to the surface plane.

A saddle shaped macrocycle is also described in other studies[21,27,87,88]. There is, however, no indication as to what role intermolecular interactions perform in the assemblies. For TPyP, the nitrogens in the pyridyl groups cause the entire molecule to distort significantly as they form strong bonds with the copper atoms of the surface. This is explained in terms of the strong affinity nitrogen has for copper. This is contrary to the same molecule on Ag(111), whose macrocycle retains its

planarity due to a weak molecule-substrate interaction[22,69]. In this case, intermolecular interactions dominate the assembly, which is seen from the non-integer values of the unit cell's matrix notation to have an incommensurate unit cell, to form a racemic structure consisting of rows of opposite mirror orientations of molecule (Figure 1.2-9). Alternating rows of differently oriented molecules are observed in assembled monolayers of TTBPP on Au(111) also[75], indicating strong macrocycle deformations induced by dominating intermolecular and molecule-surface interactions between the butyl substituents and the underlying copper lattice. Yokoyama *et al* also find an incommensurate unit cell, indicating a relatively weak macrocycle-surface interaction.

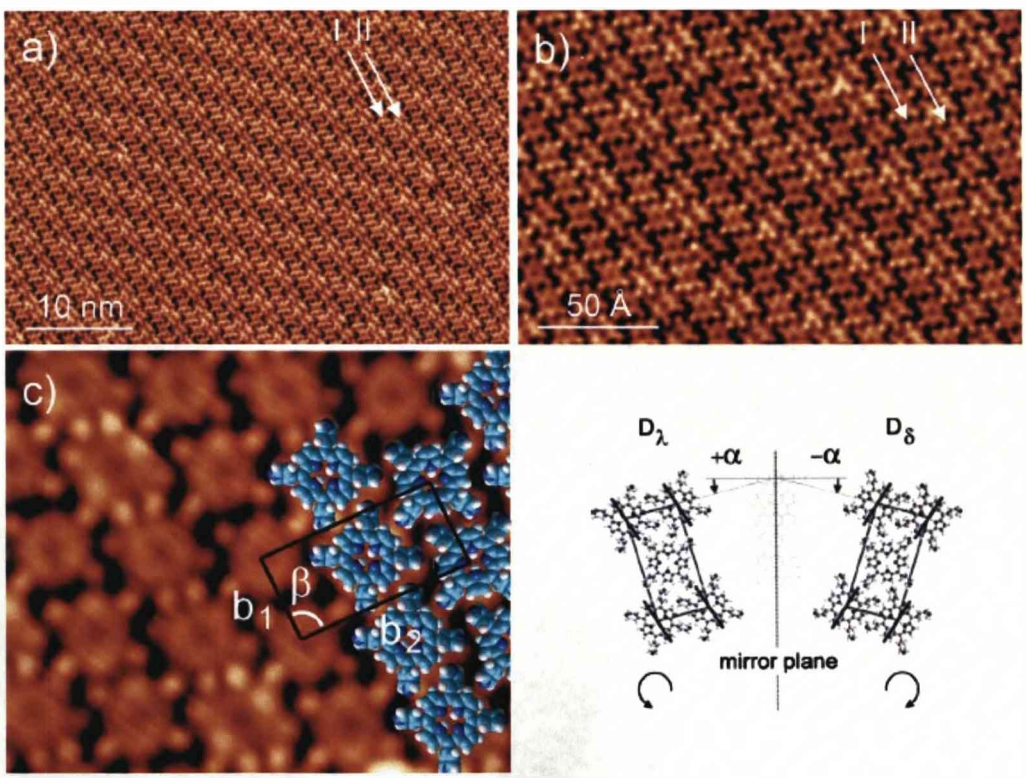

Figure 1.2-9. Results from Aüwarter *et al*[22]. TPyP molecules form a racemic structure consisting of rows of oppositely oriented molecules with respect to the surface symmetry axes.

Induced chirality in adsorbed porphyrins is rare and is not fully characterised in any study[22,73,89]. The induction of chirality from the adsorption of molecules onto a surface has been described in great

detail[14,90,91] and is summarised in the Appendix (section 0). In the work of Sekiguchi *et al*[73], the formation of twin superstructures of TTBPP on Cu(100) that are aligned at ±6° to the Cu[011] axis is concluded to be a result of butyl groups undergoing deformations in order to find an appropriate adsorption site (top in Figure 1.2-10).

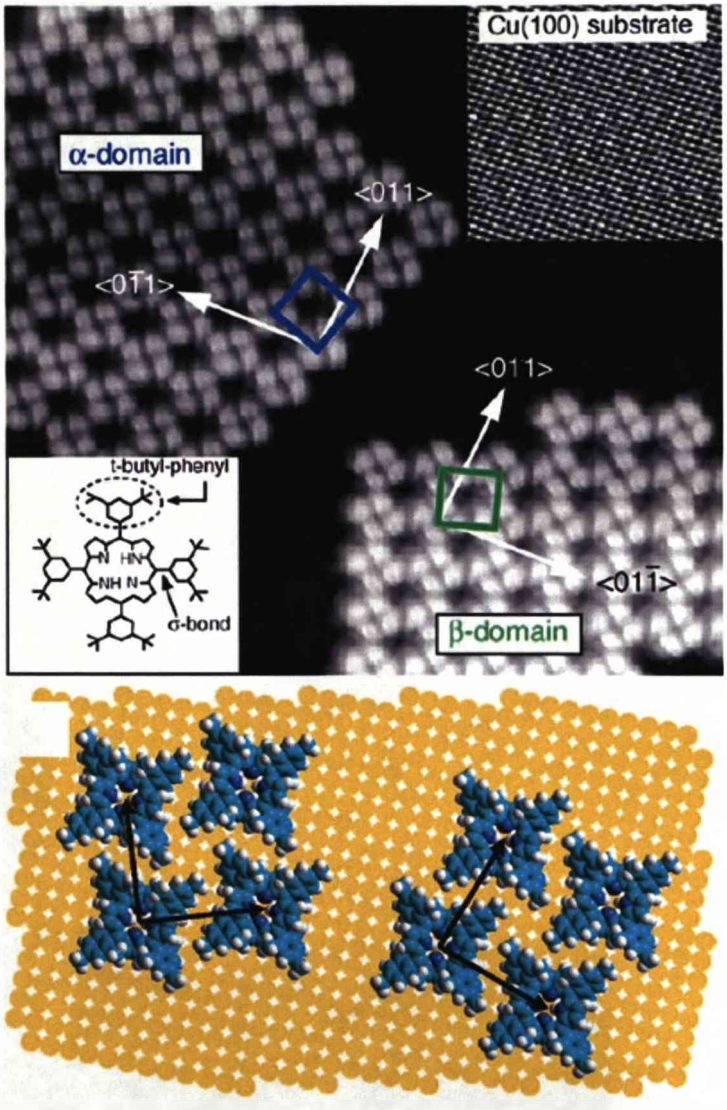

Figure 1.2-10. Chiral self-assembly from the adsorption of non-chiral porphyrins onto high-symmetry surfaces. Top image from Sekiguchi *et al*[73], bottom image from Ecija *et al*[89].

This is paralleled by Ecija *et al*[89], who observed the growth by molecular diffusion at room temperature of chiral mirror domains of Tetramesityl-porphyrin, also on Cu(100) (bottom in Figure 1.2-10). Unusually,

they surmise that the molecular overlayer is likely to be commensurate with the substrate lattice, although this appears to be purely through convenience. They continue to show that the molecules themselves are aligned with the copper substrate, revealing only organisational chirality and a globally racemic surface phase.

The planarity and stiffness of porphyrin molecules is shown to have an effect on the nature of the surface phase. Kamikado *et al*[70] show that, at low temperature, free-base TTBPP molecules have the flexibility to bridge over step edges and for creating molecular wires along them through intermolecular interactions. This bridging is accompanied by rotations and tilts of the butyl groups so that cost effective interactions can be formed with the substrate and nearby molecules. The same molecule will not form domains on narrow terraces and prefers to form these wires. 2D structures are observed on larger terraces. Under the same conditions, metal-TTBPP molecules would not form wires over and along the steps. This is attributed to the relative stiffness of the core in the presence of metal chelates. Metal porphyrins are known to exhibit greater resistance to deformation[32].

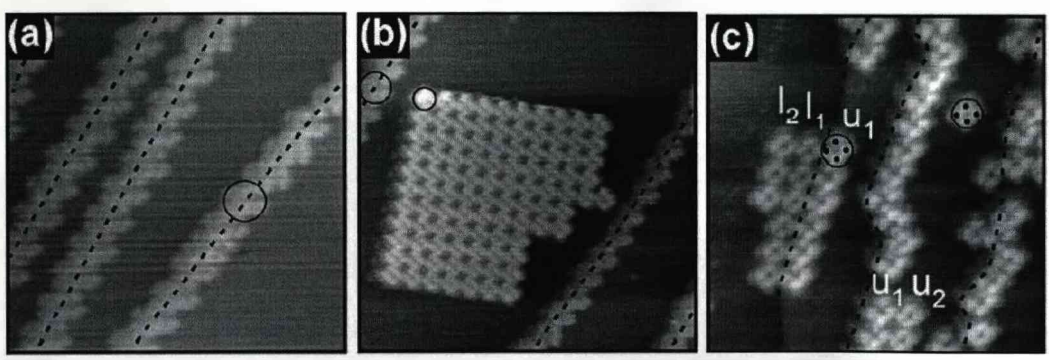

Figure 1.2-11. The adsorption of H_2- and Cu-TTBPP on Cu(100)[70]. (a-b) H_2-TTBPP bridges across steps. The molecule doesn't form domains on narrow terraces, only on larger terraces. (c) Cu-TTBPP situates either on top of or below steps. Its relative stiffness does not allow it to bridge over the step.

A further study in which intermolecular interactions dominate molecule-surface interactions is by Nishiyama *et al*[67], who observed the successful creation of molecular wires by functionalised carboxy-substituted TTBPP molecules on the Au(111) surface (Figure 1.2-12). In this study, the

carboxy groups formed hydrogen bonds with their neighbours. Interestingly, a monolayer could be formed that was so stable that subsequent layers could be added simply by dosing more molecules. The TTBPP molecule has undergone several functionalisations to yield similar results[92,93], and is directly compared to the non-functionalised TTBPP molecule. In an earlier work, Terui *et al* has shown the power of STM in chemical identification of adsorbed species[94].

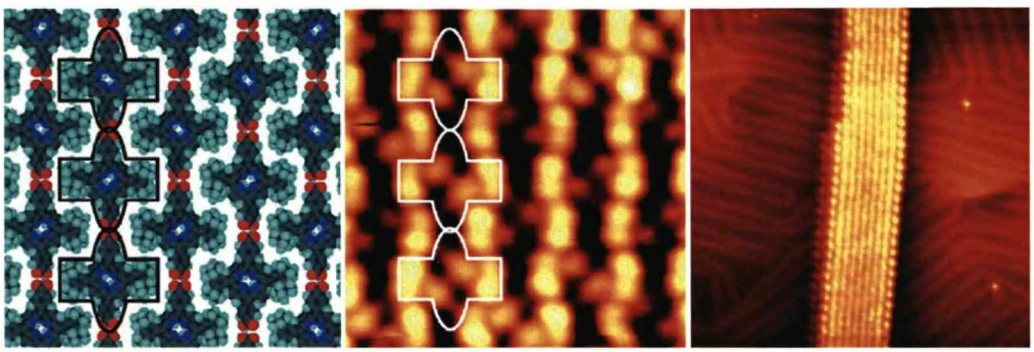

Figure 1.2-12. Chains of hydrogen bonded carboxy-substituted TTBPP molecules form wires which eventually form monolayers[67]. The interaction with the substrate is so weak compared to the intermolecular interaction that the reconstructed gold surface has no effect on the growth direction.

The conformation, orientation and self-assembly of adsorbed porphyrins can be manipulated by altering the deposition or crystal temperature. Distinct 2D and 1D phases of Pt-TTBPP on Ag(110) are shown by Yokoyama *et al*[95] to occur at temperatures above, at and below room temperature. A strong dependence of the molecular ordering on annealing temperature has also been shown by Klappenberger *et al*[96]. In this work, three distinct phases of TPyP on Cu(111) were observed over a temperature range of 300-500K. An altered bonding motif that occurs above 450K was concluded to occur as a result of a change in electronic structure of the molecules that is initiated by deprotonation of pyrrolic nitrogens in the core.

From conformational/geometric studies alone, it remains unclear precisely what forces drive the observed strong molecular deformations and, therefore, a detailed understanding of the interactions driving molecular adsorption, conformation and self-assembly of porphyrins at metal surfaces remains in its infancy. A comprehensive geometric study that includes all

involved interactions is necessary at this stage, although detailed information about other aspects of porphyrin/phthalocyanine adsorption and assembly has been gleaned.

The adsorption of Co- and Cu-Pc molecules on the Au(111) surface was investigated by Hipps *et al*[77] and Lu *et al*[78]. Co-adsorption of the two molecules resulted in a randomly mixed film. Both molecules adsorbed flat on the surface and, from the similar nature of pure and mixed films, it was deduced that lateral interactions were effectively the same for each type. In the mixed film, the chemical identification of each type was 'trivial' as the nature of the coordinated metal ion in the core endowed each molecule with a different signature when read by STM (Figure 1.2-13). This signature was identified in the pure films of both species and it was easily shown that the Co atom images bright and the copper imaged dark. The difference in the way Co- and Cu-Pc are imaged by STM is clear, and it was tentatively established that, although several processes are described that could lead to enhanced tunnelling, the large number of cobalt d-orbitals, which are missing in the copper due to the filled d-band, are responsible for the relative brightness; thus creating an enhanced tunnelling pathway.

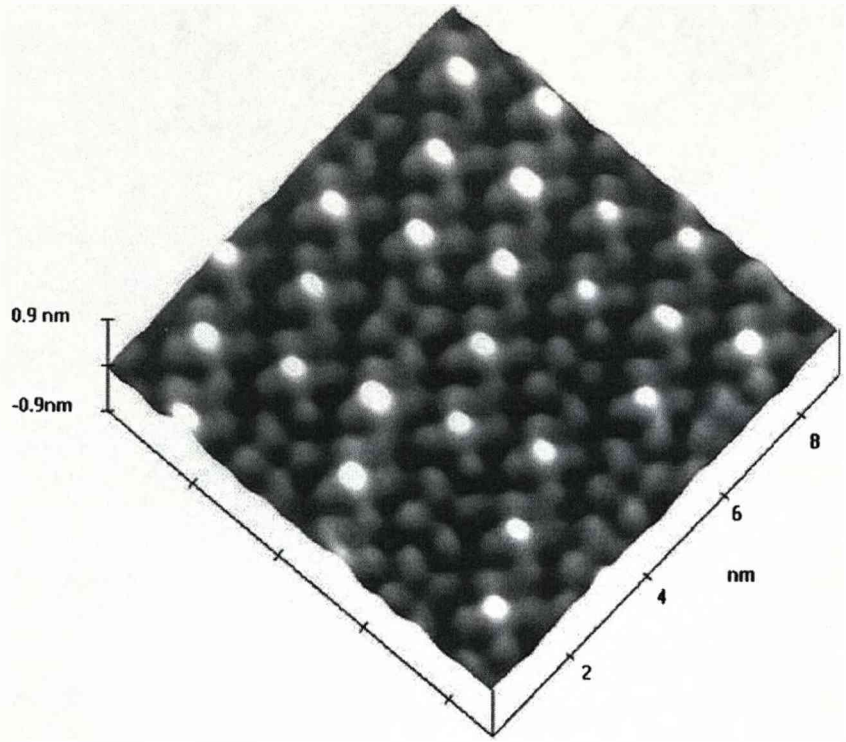

Figure 1.2-13. The co-adsorption of Co- and Cu-Pc onto Au(111) reveals a different electronic structure for each species[77]. Co-Pc is imaged with a bright core.

This conclusion of Hipps *et al* and Lu *et al* are supported by others[37,97-100]. The work of Comanici *et al*[101] on the adsorption of TPP and Co-TPP on Ag(111) shows that the contrast mechanism for co-adsorbed porphyrins is not as 'trivial' as previously thought and that the STM images are strongly bias dependent; often showing little or no difference between the two different molecules. The cause of the contrast changes was attributed to differences in the (un)occupied states in the molecule, primarily due to the Co atom in the core. This is supported also by a combined STM and theoretical study on Co-TPP on Ag(111) by Buchner *et al*[35], who showed the contrast difference between co-adsorbed species is directly caused by a direct orbital interaction of the adsorbed molecule's Co d_{z2} with the Ag 5s orbital. It is stressed that the explicit inclusion of the Ag(111) substrate in the calculation resulted in good agreement with experimental STM data.

A more detailed investigation into the electronic interaction between the metal ion and the metal substrate specifically was carried out by Lukasczyk *et al*[29], who employed photoelectron spectroscopy on the Co-TPP

and Co-TTBPP on Ag(111) system. It was found that electron transfer occurred from the silver surface to the cobalt atom in the core via the singly occupied Co $3d_{z2}$ orbital. Furthermore, it is shown that the closer the core Co atom is to the surface, the greater the interaction. This is due to increased orbital overlap.

The interaction of the central metal ion with underlying features has been investigated by Inada *et al* also[102]. The adsorption of the chiral bis(3,5-di-t-butyphenyl)(4-ethynylphenyl)(methylthiophenyl)porphyrin (EMTTBPP) onto the TiO_2(110) surface showed that the molecular core preferentially adsorbed on top of surface oxygen atoms. On adsorption, a strong attractive molecule-surface interaction induces a change in conformation, but produces no interesting chiral properties. The overall adsorption geometry is a compromise between steric interactions between butyl groups and the molecule-surface interaction.

Overall, the porphyrins and related molecules have the ability to be functionalised in a meaningful and deliberate manner. At present, researchers are unable to properly capitalise on this and make valid predictions about how any particular molecule will react to any given substrate. This is primarily due to the fact that there has been no study to date that has incorporated information about all of the involved interactions, and not least the molecule-surface interaction, which has not been broached in any detail.

1.2.3. Theoretical studies of porphyrins

At present, there has been little focus by theoreticians on this class of large molecule. A major obstacle remains in the understanding of large and complex systems that is attributed to the molecule-substrate interaction, which is highly challenging to describe. It is now apparent that the most effective approach to address this issue is by periodic Density Functional Theory (DFT) calculations, which allows precise insight into substrate contributions and the overall electronic and geometric properties of the assembled system, but has the drawback of being computationally demanding. The situation is further compounded by the fact that, at present,

no theoretical approach can include all relevant interactions, such as covalent, substrate-mediated, and dispersion interactions[103-107], but, theoretical methods have been shown to perform well when describing chemisorbed molecules on relatively reactive transition metal surfaces, despite a general underestimation of van der Waals and π–π interactions. In the gas phase, computational studies have been performed on conformational flexibility of metallo-porphyrins[32], porphyrin metalation[58] , porphine stacking by van der Waals interactions[108] and, with specific importance to this work, the nature of the benzene-benzene interaction[32,103-107]. Periodic DFT calculations have been reported, detailing the adsorption characteristics of Fe- and H_2-Tetrapyridile porphyrins weakly adsorbed in a self-assembled layer[22,69] and Pd- and Mn-porphines weakly adsorbed on the Au(111) surface[55]. Most recently, a periodic DFT and STM study on several porphyrins on both Cu(111) and Au(111) has indicated that the adsorption of single molecules and their self assembly is determined primarily by the phenyl groups and their interactions with each other and the surface[54]. A saddled geometry of the molecules is found to be induced by an attractive molecule-surface interaction and there is observed a consequent reaction of the *ortho-* groups in the form of strong twisting. Inter-molecular interactions are identified as T-type phenyl-phenyl interactions and these are estimated to contribute about $-24 kJmol^{-1}$ to the net adsorption energy. This T stacking was suppressed by the addition to the molecules of altered functional groups that showed a greater affinity with the surface. The molecule–surface interaction is defined in terms of the orientation of the single molecule and the induced saddle conformation, which is not favourable in the gas phase, however, the effect of the core metal ion is found to be negligible. Good agreement is observed between experimental and theoretical methods.

Thus far, systems possessing strong molecule-surface interactions have not been broached in detail, and remain ill understood.

1.3. *Summary of presented study*

Presented herein is a systematic study combining STM, RAIRS, LEED and periodic DFT (carried out by Matthew Dyer of the group of Mats Persson of the University of Liverpool's Surface Science Research Centre) to investigate the geometric and electronic characteristics of the adsorption and self-assembly of Co(II)-Tetraphenylporphyrin (Co-TPP) on the Cu(110) surface at room temperature. The Co-TPP/Cu(110) system allows for a significant macrocycle-surface interaction and is sufficiently simple to apply periodic DFT modelling since it possesses no reactive substituent groups that could strongly influence the porphyrin assembly[30].

STM data reveal a wealth of organisation and the formation of three highly ordered structures is observed – Structures 1, 2 and 3. In support of the experimental data and due to its simplicity relative to the other structures, Structure 1 has been subject to a periodic DFT study and a comprehensive picture of the fully assembled molecule-surface system is presented, including detail on the adsorption, chiral self-assembly, molecular conformation, and a quantitative description of energetic costs and gains of all the relevant interactions. Structures 2 and 3 are distinguished by their constituent intermolecular interactions which make up two- and four-molecule unit cells respectively. On a molecular level they are closely related to Structure 1 and have, therefore, each been modelled as a modified Structure 1 and their respective differences characterised individually.

Each of the three major structures exhibits further complexity in the form of transition or boundary structures, which are alterations to the intermolecular interaction pattern, and are modelled also as a modified Structure 1.

Additional to the organised structures is a separate phase in which isolated molecules exhibit three distinct interactions with the substrate that are characterised by differences in the molecule's orientation and by the electronic structures observed by STM. One of these, whose symmetry axes

align with those of the underlying copper surface, has been addressed by periodic DFT, also by Matthew Dyer and Mats Persson.

With the exception of the single molecule phase, the three major structures have been ordered (and numbered) according to the number of molecules constituting their unit cell and all have been linked and discussed under the umbrella of six distinct intermolecular interactions:

- Structure 1: Unit cell, DFT calculations, geometry, energy balance and chirality.
- Structure 2: Organisation, unit cell, model and intermolecular interactions.
- Structure 3: Model, unit cell, symmetry, intermolecular interactions and adatoms.
- Transition and boundary structures: Detailed characterisation.
- Single molecule: Characterisation and DFT calculations.
- Discussion of domain formation from single molecules. Phase summary with discussion of the relationship between dose conditions and observed structure.
- Conclusions.

CHAPTER 2

Theory

Surface scientists attempt to describe the interactions and processes that occur at surfaces and they do this using a multitude of experimental techniques that glean insight into the topography, composition and structure of the surface itself, as well as the electronic and chemical structures, interactions and conformations of atomic or molecular layers, both self-assembled and otherwise, adsorbed at the surface. Many surface sensitive analytical techniques measure the response of a system to a stimulus, which is often in the form of incident electrons, photons or ions. There are an increasing number of available techniques that include spectroscopic (described above), microscopic and theoretical methods, and the specific questions asked of a system by a researcher dictate the combination of methods and physical principles that need to be exploited to achieve understanding.

For a comprehensive analysis to be undertaken, an experimentalist must understand the theoretical basis of the techniques. Only then can their versatility be fully exploited, their limitations worked around and their output properly interpreted. This chapter details the physical and chemical foundations onto which the techniques used for this study, Scanning Tunnelling Microscopy (STM) and Low Energy Electron Diffraction (LEED), are built. A description of the intricacies of the chosen substrate is included, as is a general discussion of vacuum.

2.1. Vacuum

An important prerequisite to a fundamental level of understanding is that the system under scrutiny can be fully characterised. That is, disregarding properties or effects specific to the system, *all* information about the state of the system can be determined prior to experimentation, including the purity of the adsorbate and the precise nature of the surface onto which the molecular adsorption takes place. This has two requirements:

- A sample surface must be prepared to atomic cleanliness in an environment such that the cleanliness may be maintained for the duration of the experiment.

- An adsorbate that is free of contaminants must be introduced at the surface and probed in such a way as to retain the cleanliness of the chamber and sample surface.

Both of these points are discussed from a practical standpoint in Chapter 3.

From the kinetic theory of gases, the collision rate r ($m^{-2}s^{-1}$) of atmospheric molecules onto a surface is:

$$r = \frac{p}{(2\pi k_B T m)^{1/2}}, \qquad \textbf{2-1}$$

where p is the local atmospheric pressure (Nm^{-2}), k_B is the Boltzmann constant (JK^{-1}), T is the local temperature (K) and mass m is measured in ($kgmol^{-1}$). The adsorption rate is also determined by a sticking probability $S(\theta)$, where θ is coverage, defined as the probability that a given molecule will adsorb at the surface on collision, as opposed to simply deflecting. Consider the extreme case of $S(\theta) = 1$, i.e. all collisions result in adsorption. At atmospheric pressure, a small molecule such as N_2 or CO has a collision frequency of 3×10^{27} m^{-2} s^{-1} that, when colliding with a metal surface consisting of approximately 10^{19} atoms m^{-2}, results in a time of less than 10^{-8}

s for monolayer formation. Clearly, this will not suffice for experimental surface science, which can require several hours of clean conditions for completion of an experiment.

The answer to this problem lies in increasing the time in which the surface can be considered free from contamination, which, from Equation 2-1, can be achieved most easily by decreasing the atmospheric pressure to which the surface is exposed. To use the correct terminology, we increase the vacuum. There are varying degrees of vacuum that have been arbitrarily defined as:

Rough Vacuum	1000-1mbar
Medium Vacuum	$1\text{-}10^{-3}$ mbar
High Vacuum	10^{-3} - 10^{-9} mbar
Ultra High Vacuum	10^{-9} mbar and below

In order for experiments to be performed with any chance of success they must be performed using UHV. Under this regime, clean conditions may be maintained for 10^3 - 10^5 s, and, for N_2 or CO, with only 1-2% surface contamination.

A procedure aimed at maintaining the cleanliness of the UHV chamber's atmosphere is the bake, which is done prior to experimentation. Baking is a sustained heating of the entire instrument that releases gases that are trapped on the walls of the chamber itself (outgassing), normally at or above 120°C and lasting for 18 or more hours. These gases would otherwise be slowly released, causing problems with the vacuum and, by extension, the cleanliness of the surface. This issue is compounded by the fact that many apparatus, including ion gauges, ion guns and Titanium Sublimation Pumps (TSPs) operate at high temperatures, thus heating and releasing gases from their own components and the nearby chamber wall.

2.2. *Scanning Tunnelling Microscopy (STM)*

2.2.1. Introduction

Subsequent to its invention in 1982, the Scanning Tunnelling Microscope (STM) quickly proved to be a powerful tool in the study of surfaces[109-114]. Consequently, its inventors, Gerd Binnig and Heinrich Röhrer of the IBM Zürich Laboratories[115], received the quickest award of the Nobel Prize in Physics ever, just four years later. Clean surfaces, as well as isolated adsorbates and thin films, have been studied by STM. Ordered arrays of atoms and disordered atomic features have also been observed on numerous metal and semiconductor surfaces, and in a variety of environments including UHV, air and various liquids, and at temperatures ranging from liquid helium to above room temperature.

The power of the tunnelling microscope lies in its ability to spatially and energetically resolve the electronic states of surfaces or adsorbed species. Spatially, the states can be observed with atomic resolution; a 5Å lateral resolution is routinely achieved and features on the 3Å scale can be resolved under favourable circumstances.

Details of the geometric arrangement of atoms on the surface are reflected in the spatial distribution of electronic states, and the STM thus provides a probe of the atomic structure of surfaces. Although the connection between the local electronic states and the atomic structure depends on the type of system, for metals the states generally follow the atoms in a fully predictable manner, and so the STM can be used to effectively provide a topographic view of the surface. This does not hold true for semiconductors, for example, and one must be careful when interpreting data from such systems[116].

One powerful aspect of the STM is its ability to allow the user significant control over a large number of variables that include tunnelling current, voltage, tip-sample separation (z position), and lateral (x,y) position on the sample. This ability leads to a number of variations in the techniques used in acquiring the data.

Since its conception, Scanning tunnelling microscopy (STM) has rapidly continued its evolution and development and now the commercial availability of STM devices, coupled with the depth and breadth of information that can be gleaned about a system, have made STM one of the most common techniques used to characterise structural, electronic and chemical properties of conducting surfaces.

2.2.2. Basic principles of operation

STM works on the quantum mechanical principle of electron tunnelling, that is, the ability of electrons to traverse energy barriers that in classical physics would be impossible. In STM, a probe tip is scanned over a sample surface (the electrode) at a height of 5-10Å. The vacuum gap between the two is the barrier across which the electrons must pass in the STM experiment.

Electron tunnelling is a quantum mechanical phenomenon that occurs when two conducting electrodes move close enough together so that their respective wavefunctions overlap, thus allowing a current to flow between them. This will be discussed in more detail in section 2.2.4.

The probe is a sharp tip, made of either W or Pt-Ir wire that is electrochemically etched or cut, respectively. The tip is positioned close to the sample surface so that when a bias voltage is applied between them, a current flows as electrons tunnel through the gap. When tunnelling is achieved, i.e. a current is measured, the tip is scanned in a raster pattern across the sample surface.

STM has two main operational modes; constant current and constant height. In constant current mode, the bias voltage is maintained and, as topographical and/or electronic features are encountered, the feedback circuit alters the tip height z so that the tunnelling current remains constant. Electronic features such as a workfunction of an adsorbed species that is different to that of other nearby features causes changes in the z direction to maintain the tunnelling current. Features with the same, or similar topographic properties may, therefore, be imaged very differently due to their

dissimilar electronic properties. This will be discussed later. The output from an STM operating in constant current mode, as shown roughly in Figure 2.2-1, is a record of the tip height for each (x,y) position in the scanning area. Operating in the latter mode, constant height mode, has the tip height z maintained over the sample surface. As surface features are encountered the tunnelling current I alters as the tip-surface separation changes. The changing current is therefore output to a PC to produce the image. As in constant current mode, constant height mode images are subject to the electronic properties of the sample. Constant height mode has the disadvantage that the feedback circuit does not respond to major changes in sample height and tip crashes are therefore more likely.

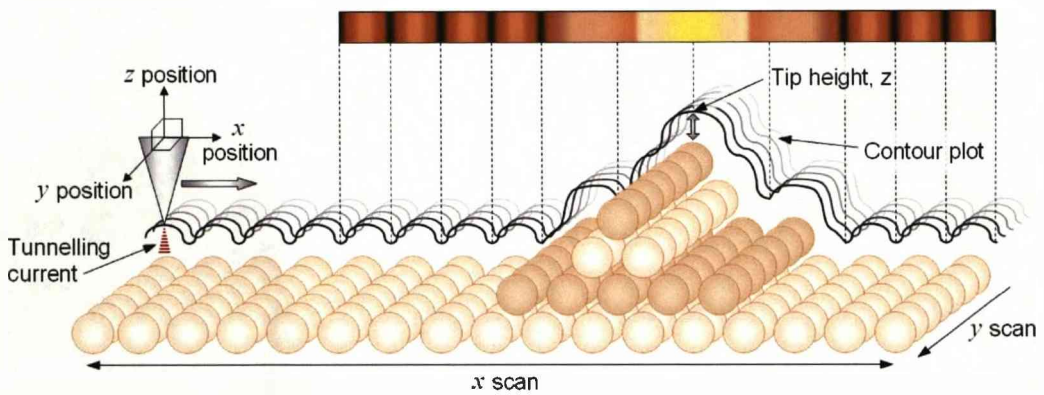

Figure 2.2-1. Schematic diagram showing the scanning process in constant current mode. The tunnelling current I is kept constant throughout the scan. The bar at the top is a representation of the output from the STM, also shown by rows of contour plots. Each contour shows the change in z over the extent of the x scan and each line is for a separate y value.

In simplistic terms, the tunnelling current can be regarded as a measure of the overlap, in the vacuum gap, of wavefunctions of the two electrodes (the tip and sample). Consequently, the resultant current is a function of the electrode separation and the nature of the involved electronic states. This is corroborated by one-dimensional tunnelling theory, which for free electrons tunnelling through a planar barrier at small voltage the current density J, depends strongly on the distance between the two electrodes s and an average inverse decay length of the wave-function density outside the surface k_0:

$$J \propto \exp(-Ak_0 z), \qquad \text{2-2}$$

where A is a constant and k_0 is given by;

$$k_0 = \sqrt{\frac{1}{2}\phi_2\phi_1}\,, \qquad \text{2-3}$$

where ϕ_1 and ϕ_2 are the work functions of the electrodes. The exponential dependence of J on z is the physical principle behind the simplest interpretation of STM images – that of a purely topological representation. For example, a constant current image is a plot of the z position of the tip along the x direction, thus forming a contour. As the tip is raster scanned over the surface, contours for each y value are plotted together, thus forming a 3D image of the surface (Figure 2.2-1).

In reality, however, STM images are a complex convolution of the electronic structure of the tip, the electronic structure of the surface and the tunnelling barrier function. It is only under the condition that the electronic properties of both tip and sample surface are uniform that this interpretation strictly holds true, although in many circumstances it provides an adequate approximation. In cases where this approximation is ineffective, there still remains an exponential dependence of J on some effective tip-surface separation barrier height, z.

2.2.3. Instrumentation

The STM is designed in three main parts:

1. The tunnelling and scanner unit,
2. The vibration isolation system,
3. The electronics and controllers.

Problems with the STM that impede the collection of high quality data can often be attributed to the instrument itself, and are generally related to the vibration isolation mechanism, or more frequently, the physical and/or chemical state of the tip. Sharpness and stability are two aspects of the tip

that are directly related to lateral resolution, e.g. a lateral resolution below 100Å requires tip radii of the order of 100Å. To achieve atomic resolution in a consistent and reproducible manner, therefore, a sharp tip with very small radius is required. A perfect tip has, amongst other features, just a single atom at its tip.

An important technical feature of the STM concerns unintentional spatial drift between tip and sample. This drift typically amounts to movement of a few angstroms per minute, in any of the x, y or z directions. At this rate, the drift often amounts to a significant fraction of an image size in the time required to acquire the image. Sources of the drift include thermal expansion and creep of the piezoelectric elements. Several hours are normally required for the scanner to fully relax.

2.2.3.1. Tunnelling and scanner unit

The tunnelling and scanner unit are collectively known as the head. For a tunnelling current to flow, the electrodes must be positioned just a few angstroms apart. This is normally achieved in two stages; first using a coarse positioner and then using a z piezodrive. The coarse positioner is used to make the first rough approach, after which the fine approach to the tunnelling separation is performed automatically using the piezodrive, which functions by the piezoelectric effect: a voltage applied to the drive induces a strain in the piezo, and vice versa. A piezo tube is typically used as a piezodrive for fine control of mechanical movements. By sectioning the surface of a piezoelectric tube into regions and connecting them to electrodes, it becomes possible to apply voltages to the tube in various specific directions. By applying voltages in mutually perpendicular radial directions across the tube it becomes possible to induce distortions in two mutually perpendicular dimensions (x and y), while voltage applied axially controls the position in the third dimension (z). The fine approach terminates when the tunnelling current, which is continually monitored, reaches a user-preset limit.

Once the tip and the sample have been brought together within a few angstroms and there is tunnelling current flowing between them the scanning process is controlled by the piezo tube. Applying a sawtooth voltage on the x

piezo and a ramped voltage on the y piezo the tip scans over the x-y plane. In constant current mode, a feedback circuit is employed to control the z position of the tip. Tunnelling current is measured, amplified and converted to a voltage, which is compared with a user-determined reference value and the difference is used as an output signal to control the z position of the tip appropriately. This process allows the equipment to establish an equilibrium z position, which is then stored for every x point creating a contour plot. The same process is repeated throughout the entire scan creating a contour plot for every y position.

2.2.3.2. Vibration isolation

The typical corrugation amplitude for STM images is about 0.1 Å (z direction); therefore the disturbance from external vibrations must be reduced to less than 0.01 Å. The desired lateral resolution is 1.0 Å (x and y direction), this imposes lateral noise levels of less than 0.1 Å. In a functional STM this can be exceeded by mechanical coupling of the instrument to its surroundings. Vibrations can be transmitted to the head of the STM from the building, the ground where the chamber system is sat, the chamber or the microscope itself and the air.

Different methods of vibration isolation system have been used. The first generation of STM in the IBM laboratories used a vibration isolation system by superconducting levitation. The second and third generations used a two stage spring system and additional eddy-current damping with permanent magnets and in the fourth generation, viton dampers were used[117].

2.2.3.3. Electronics

The electronics that control and support the mechanical components are a vital component of the STM. A simplified representation of a typical electronic control system is outlined below in Figure 2.2-2.

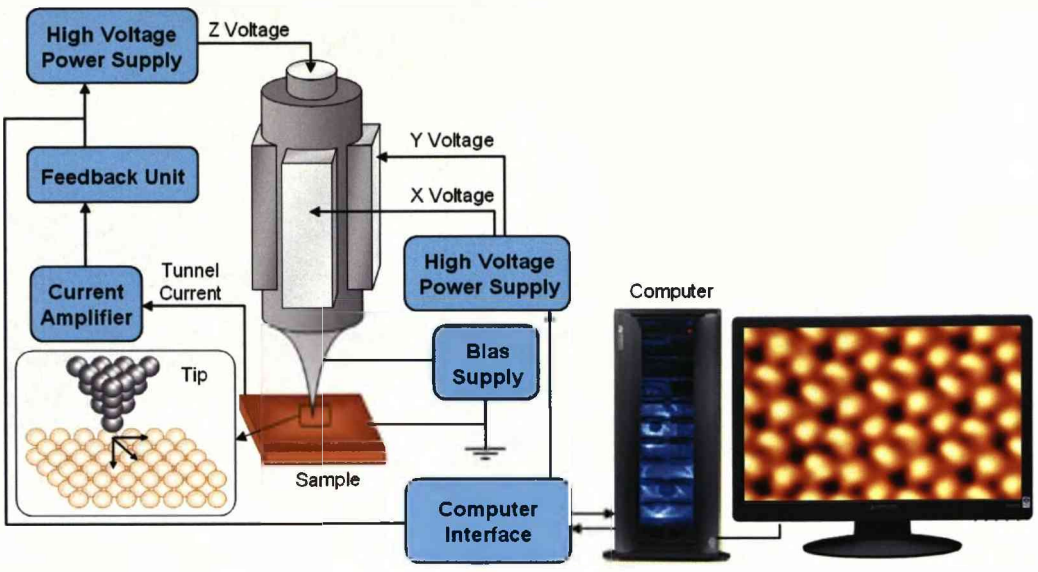

Figure 2.2-2. Scheme of the essential elements in the electronics and control of the STM.

A high voltage power supply controls the x and y piezoelectric elements. A current amplifier reads and amplifies the tunnelling current, which is typically between 0.01 and 50nA, and converts it to a voltage. The output of the current amplifier is sent to a feedback circuit, which controls the response of the z piezo to the measured tunnelling current by means of a high voltage power supply. This power supply alters the tip height according to the user-defined reference voltage. A low voltage power supply is needed to provide the bias voltage between the sample and the tip. Typically all the electronics and controls are connected to a pc interface that facilitates their control. The computer interface reads the feedback control unit output (an equilibrium z value) and the x-y position of the tip and the information is plotted as a 3D surface image.

2.2.3.4. The STM tip

The quality of the tip determines, to a large degree, the quality and reproducibility of the image(s) produced by the STM. Various methods are used to fabricate tips; the most common is grinding or etching of tungsten wires. It is impossible to tell whether a tip is good quality without scanning with it, and tip conditioning is therefore performed *in situ*. Although it can be somewhat unpredictable, the most common procedure is voltage pulsing with

up to 10V, which is used to forcibly 'drop' foreign material from the tip onto the surface, whilst simultaneously reforming and sharpening the tip. Further in situ sharpening of the tip is often acquired by applying high voltages up to 100V to the tip (field emission, described in section 3.1.2) or by controlled collision of the tip with the surface. The tip treatment is not well understood and is controversial. A perfectly smooth tip would not provide atomic resolution immediately and sometimes atomic resolution happens spontaneously and unexpectedly. STM tips are directly affected by a number of things, for example, foreign species such as oxygen or even molecules or vibrations, which affect long and/or thin tips more. Ideally, the tip should be thick (0.5mm to 1mm) and come to a point rapidly. Mini tips are normally created at the end and the extreme dependence of the tunnelling current on the distance between the tip and surface results in the mini tip closest to the surface being the one that produces transmits the tunnelling current. A tip consisting of widely separated mini tips which are all close to the surface is not useful as it may cause double or multiple copies of single features or distorted images as well as changes during scanning. The chemical identity of the tip is important also. It has been proposed that tips of materials with strong d-band character like W and Pt achieve higher resolutions since electrons in d-bands are more strongly localized than s-band electrons but there is no known experimental correlation between tip material and resolution. Moreover, it is almost impossible to know the exact chemical identity of the tip as the tunnelling can be made through an impurity at the end of the tip adsorbed from the gas phase or from the sample surface.

2.2.4. Theory

The basic principles of tunnelling can be described with an elementary one-dimensional model. In classical mechanics in one dimension (denoted z), an electron with energy E moving in a potential U(z) is described by;

$$E = \frac{p_z^2}{2m} + U(z) \qquad \textbf{2-4}$$

where m is the electron mass, 9.109×10^{-31} kg and p_z is the momentum in z.

In regions where the energy of the electron is greater than the potential barrier, i.e. $E > U(z)$, the electron has a non zero momentum. Conversely, the electron cannot penetrate into regions where the potential is bigger than its energy, i.e. there is a potential barrier to penetrate into a region with $E < U(z)$, thus, this is a region forbidden in classical mechanics. In quantum mechanics the state of the same electron is described by the wavefunction $\psi(z)$, which satisfies Schrödinger's equation:

$$E\psi(z) = U(z)\psi(z) - \frac{\hbar^2}{2m}\frac{d^2}{dz^2}\psi(z) \qquad \textbf{2-5}$$

A simplification is achieved when an average rectangular barrier $U(z)$ is considered (Figure 2.2-3). In reality, the potential across the gap may not be constant, however, the approximation serves adequately as a simple representation.

The solution of Schrödinger's equation for an electron in the region where $E > U(z)$ is:

$$\psi(z) = \psi(0)e^{\pm ikz} \qquad \textbf{2-6}$$

where k is the wave vector;

$$k = \frac{\sqrt{2m(E-U)}}{\hbar}. \qquad \textbf{2-7}$$

In quantum mechanics the region $E < U(z)$, forbidden in classical mechanics, has a solution,

$$\psi(z) = \psi(0)e^{-kz}, \qquad \textbf{2-8}$$

where,

$$k = \frac{\sqrt{2m(U-E)}}{\hbar} \qquad \textbf{2-9}$$

is a decay constant that describes a state of the electron decaying in the $+z$ direction.

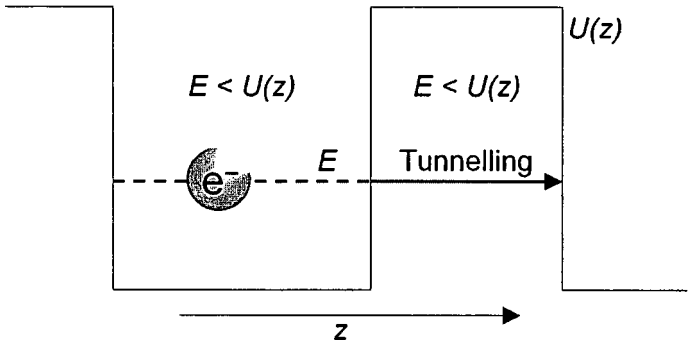

Figure 2.2-3. Schematic of a rectangular barrier in one dimension.

The probability density of observing an electron near a point z is proportional to $|\psi(0)|^2 e^{-2kz}$, which has a non-zero value in the barrier region, thus a non zero probability to penetrate the barrier. Another solution, $\psi(z) = \psi(0)e^{-kz}$, describes an electron state decaying in the $-z$ direction.

The model in Figure 2.2-3 explains the basic features of a practical metal-vacuum-metal tunnelling system. The potential barrier corresponds to the vacuum gap, and the sample and the tip (electrodes) are the ends of the barrier represented as semi-finite pieces of free-electron metals (Figure 2.2-4). The work function ϕ of a metal surface is defined as the energy required for an electron to escape from the bulk of the metal into the vacuum level. In the simplest case the work function corresponds to $U-E$. Neglecting any thermal excitation, the Fermi level E_f is the upper limit of the occupied states in a metal. Taking the vacuum level as the reference energy level (E = 0), it can be seen that $E_f = -\phi$. According to the probability density of Equation 2-8, an electron in the sample can tunnel into the tip and vice versa, however, without a bias voltage there will be no net tunnelling current.

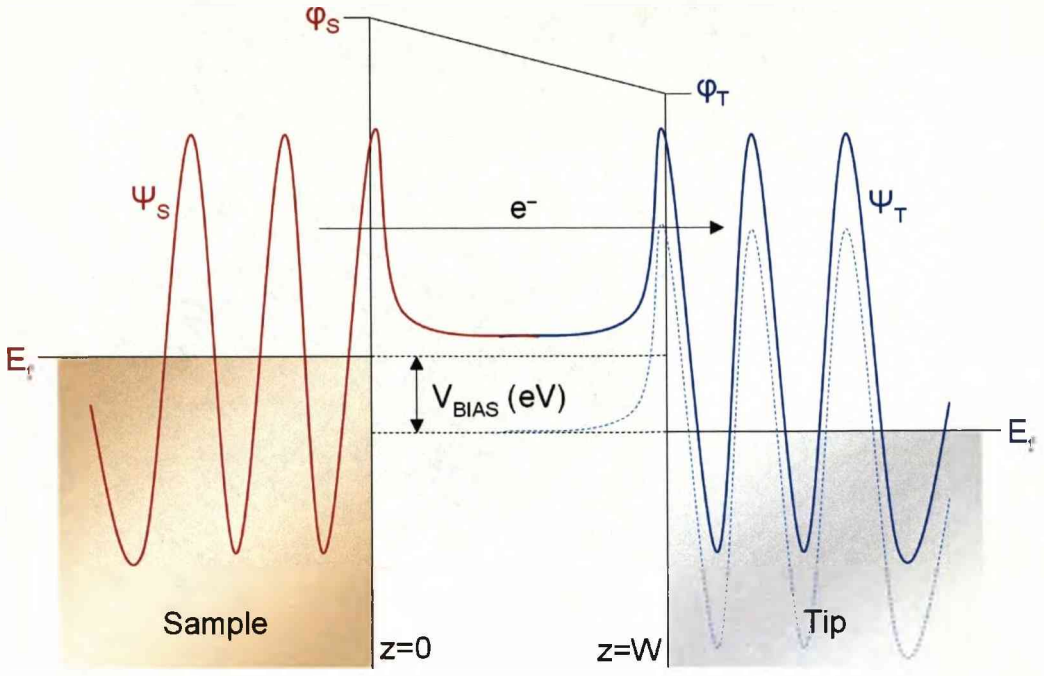

Figure 2.2-4. A one-dimensional metal-vacuum-metal junction. Red indicates association with the sample, blue the tip. The Bias voltage raises the wavefunction energy for the tip from its original value (blue dotted line) to an energy such that overlap occurs with the sample wavefunction, thus allowing tunnelling.

When a bias voltage is applied between the tip and sample, a net tunnelling current occurs. A sample state ψ_n with energy level $E_F - eV < E_n < E_F$ i.e. with E_n lying between $E_f - eV$ and E_f, has a chance to tunnel into the tip. Under the assumption that the bias voltage is much smaller than the work function, the energy level of all sample states are very close to the Fermi level, that is $E_n \approx -\phi$. The probability *w* for an electron in the *n*th sample state to be present at the tip surface z=W, is:

$$w \propto |\psi_n(0)|^2 e^{-2kW} \qquad \textbf{2-10}$$

where $\psi_n(0)$ is the value of the *n*th sample state at the sample surface, and,

$$k = \frac{\sqrt{2m\phi}}{\hbar} \qquad \textbf{2-11}$$

is the decay constant of a sample state near the Fermi level in the barrier region.

Using eV (electron Volt) as the unit of the work function and $Å^{-1}$ as the unit of *k*, Equation 2-11 becomes;

$$k = 0.51\sqrt{\phi(eV)}\ Å^{-1}. \qquad \textbf{2-12}$$

In an STM experiment, the tip is scanned continuously over the surface and, if the tip condition is stable enough during the scan, the tunnelling electrons coming to the tip surface have a constant velocity. This current is directly proportional to the number of states on the sample surface within the energy interval *eV*. These states are responsible for the tunnelling current, which is given as;

$$I \propto \sum_{E_n=E_F-eV}^{E_F} |\psi_n(0)|^2 e^{-2kW} \qquad \textbf{2-13}$$

If the *eV* is small enough that the density of electronic states does not vary significantly within it the sum in Equation 2-13 can be written in terms of the local density of states (LDOS) at the Fermi level. At a location *z* and energy E the LDOS $\rho_S(z,E)$ is;

$$\rho_S(z,E) \equiv \frac{1}{\epsilon} \sum_{E_n=E-\epsilon}^{E} |\psi_n(z)|^2 \qquad \textbf{2-14}$$

The tunnelling current can be written in terms of the LDOS of the sample;

$$I \propto V\rho_S(0,E_F)e^{-2kW} \approx V\rho_S(0,E_F)e^{-1.025\sqrt{\phi}W} \qquad \textbf{2-15}$$

The exponential dependence of the tunnelling current with respect to distance is a measure of the tunnelling barrier height (W), or the work function ϕ. By scanning the STM tip over the surface a topography image is generated which is a constant Fermi-level LDOS contour of the sample. This argument is adequate as long as the conditions imposed for a simple one-dimensional model can be adequately satisfied.

The extreme dependence of the tunnelling current on electrode separation and wavefunction decay length is the basis of the STM. The tunnelling current decays an order of magnitude for every 1Å of vacuum gap, for typical work function values (4-5eV). Tunnelling current can therefore be experimentally observed only for very small vacuum gaps. These considerations determine the stringent tip control and vibration isolation requirements for a practical STM experiment.

2.3. Crystals, surface symmetry and molecular overlayers

2.3.1. Crystals and surface symmetry

Single crystals can be cut in specific directions to reveal well defined crystallographic planes, which can be either atomically flat, consisting of large terraces, or vicinal and consisting of short atomically flat terraces separated by atomic spaces. Although there are seven different crystal structures, only one has been used for this work and so only one will be discussed here; the cubic crystal, of which there are three forms: bulk simple cubic (s.c.), face-centred cubic (f.c.c) or body-centred cubic (b.c.c.). In s.c. crystals, only the vertices are atomic positions. In f.c.c crystals, the centres of each face and the vertices of the cube have an atom, whereas the centre of the cube and each vertex of the cube is an atomic position in a bcc crystal. Since in this work only copper single crystals have been used, only the f.c.c formation will be exemplified (Figure 2.3-1).

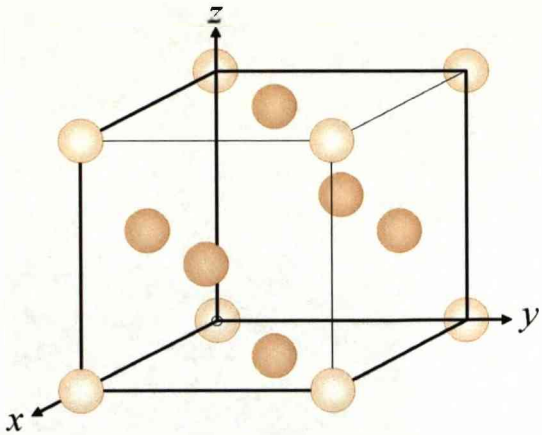

Figure 2.3-1. The f.c.c crystal structure of copper. Atoms located at the faces are represented by the darker shade.

When defining a direction (or vector) within a crystal it is first important to specify an origin from which the vector is measured. The vector can then be determined in terms of the unit cell dimensions a, b and c. If one or more from a, b or c are fractional, all three must be multiplied (or divided) by a common factor so that all are integer values. These values are denoted u, v and w and written in square brackets, [uvw]. Examples are given in Figure 2.3-2. Crystallographic equivalent directions are denoted by angular brackets, i.e. [100] = [010] = [001] = $[\bar{1}00]$ = $[0\bar{1}0]$ = $[00\bar{1}]$ = <100>, where negative values indicate a reversal in direction, also shown as 1bar (see Figure 2.3-2).

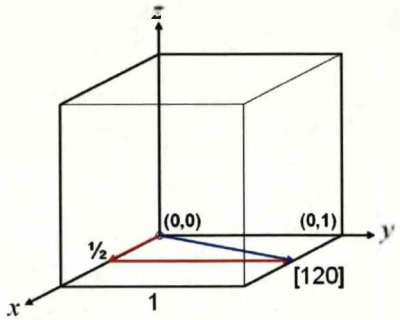

	x	y	z
a,b,c	½	1	0
×2	1	2	0

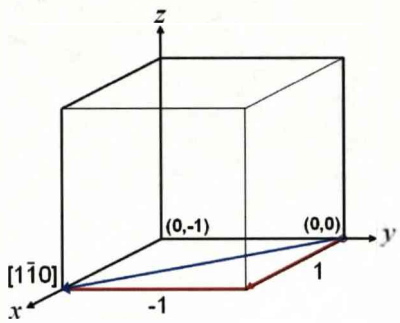

	x	y	z
a,b,c	1	-1	0
×1	1	-1	0

Figure 2.3-2. Definition of the [120] and [1-10] directions in a cubic crystal.

When defining a crystal plane the Miller index is used. The Miller index is used to describe the most common crystallographic forms consists of three integers (x, y, z) for materials adopting cubic structures. The Miller indices correspond to the reciprocal values of the interceptions of the described plane with the x-, y- and z-axes of the crystal. The plane cannot pass through the origin however as the resultant Miller index would be ∞ for that coordinate, and a parallel plane must be used if it does so. For example, considering the crystal plane shown in Figure 2.3-3, it can be seen that the intercepts are found at (a b c) = (1 ∞ ∞). The reciprocal values defining the plane are therefore (1 0 0). This plane can be seen to be parallel to the equivalent plane passing through the origin (shown dark red in Figure 2.3-3).

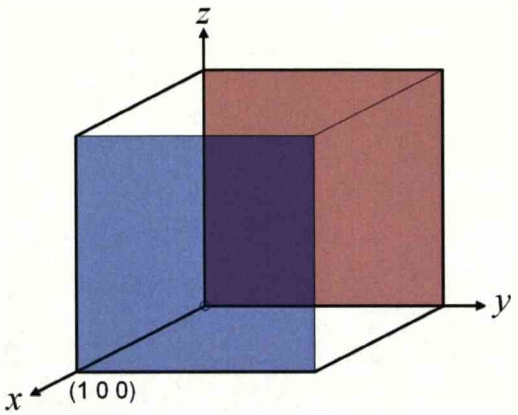

Figure 2.3-3. The (100) plane of a cubic crystal. The plane cannot run through the origin, as shown by the dark red plane. Instead, a parallel plane should be used (blue). The origin is marked by the small o.

In the case where the reciprocal values are fractional, they must be multiplied or divided by a common factor to achieve the smallest possible integer values. Crystal planes are denoted in round brackets, i.e. (hkl). Some further examples are shown in Figure 2.3-4.

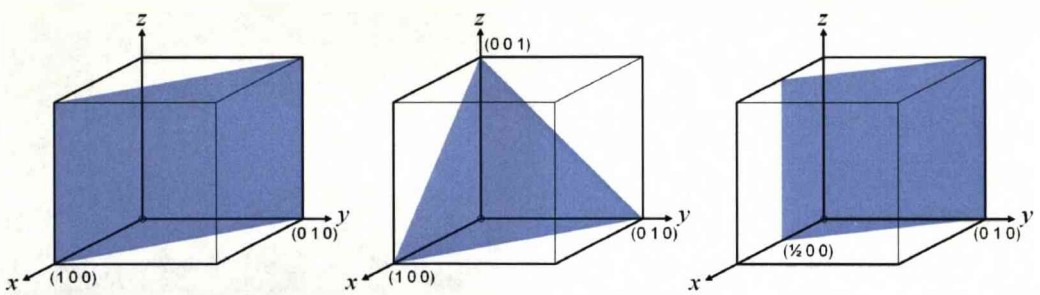

Intercepts (1 1 ∞)
Miller Index (1 1 0)

Intercepts (1 1 1)
Miller Index (1 1 1)

Intercepts (½ 1 ∞)
Miller Index (2 1 0)

Figure 2.3-4. Examples of Miller index notation for different cubic crystal planes.

Crystal planes exists that are essentially equivalent. These are grouped and collectively denoted by curly brackets, as follows:

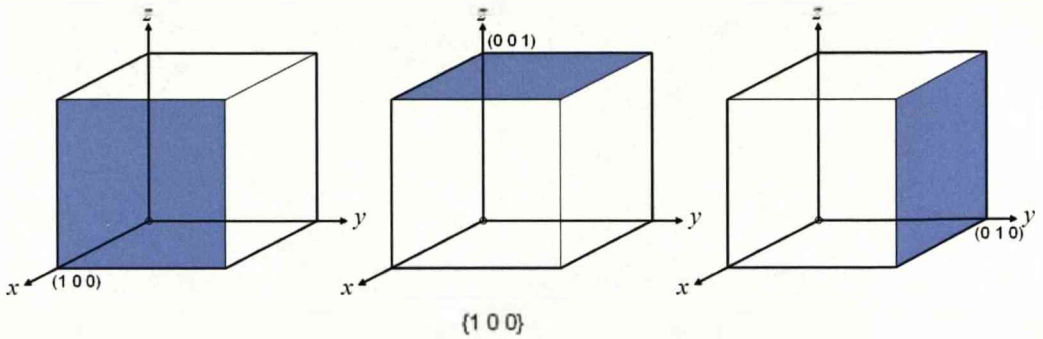

Figure 2.3-5. The {100} planes of a cubic crystal consists of the (100), (010) and (001) crystal surfaces (shown) and their respective negative counterparts.

Crystalline surfaces possess translational symmetry in the plane parallel to the plane surface. Additionally, they exhibit several point and line symmetry operations, involving rotations or reflections in planes that are parallel to the surface. These symmetry operations are, one-, two-, three-, four- and six-fold rotation axes (five-fold and more than six-fold axes are not compatible with two dimensional translational symmetry), mirror reflection in a plane perpendicular to the surface and glide reflection (involving reflection in a line combined with translation along the direction of the line by half of the translational periodicity in this direction).

2.3.2. Molecular overlayers

A molecular overlayer is defined in terms of the underlying substrate[14], which is described by the real space vectors a_s and b_s. a_s and b_s are separated by the angle γ (Figure 2.3-6). Important points to note are;

- The co-ordinate system is right-handed (RH), i.e. the defining axis system is such that x goes to y, y goes to z and z goes to x in an anticlockwise direction. Likewise, the substrate vectors a_s and b_s are such that a_s goes to b_s in an anticlockwise direction through the angle γ.

- a_s points downwards and b_s points to the right,

- $|a_s| \leq |b_s|$,

- Angle γ between a_s and $b_s \geq 90°$.

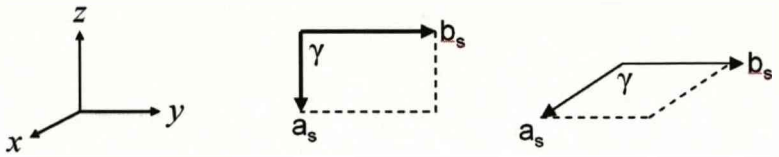

Figure 2.3-6. Definition of the RH axis system and assignment of substrate vectors a_s and b_s.

Overlayer vectors a_0 and b_0 are defined in the same way as for substrate vectors, i.e. a_0 is found clockwise from b_0 through the angle between them. A general rule for defining overlayer vectors is;

- A RH axis system is used,
- a_0 points downwards and b_0 pointing to the right if possible,
- Angle γ between a_0 and b_0 ≥ 90° and < 180°.

Figure 2.3-7 is an example defining the substrate and a molecular overlayer.

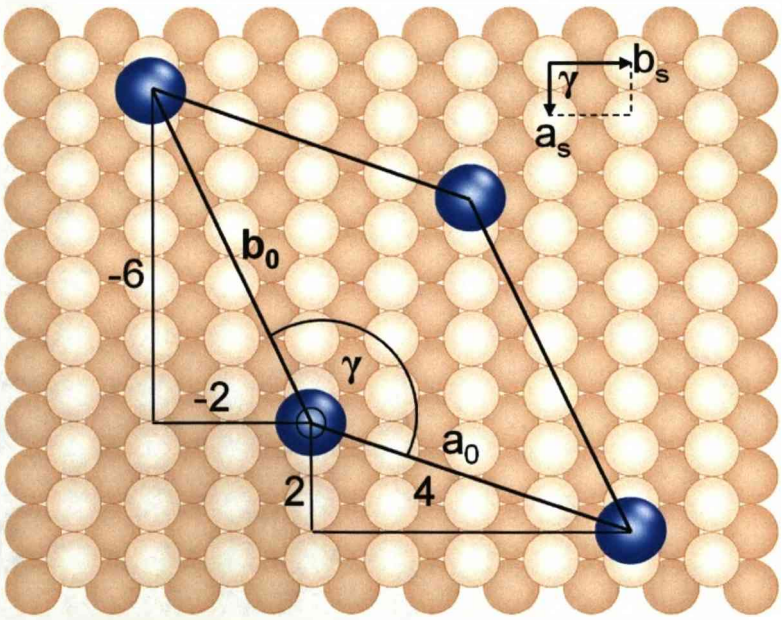

Figure 2.3-7. Definition of substrate vectors and an overlayer with the associated matrix notation.

In matrix notation, molecular overlayers are described by:

$$\begin{bmatrix} a_0 \\ b_0 \end{bmatrix} = \begin{bmatrix} m_{11} & m_{12} \\ m_{21} & m_{22} \end{bmatrix} \begin{bmatrix} a_S \\ b_S \end{bmatrix} \quad \textbf{2-16}$$

In the text the matrix notation is written as:

$$G = \begin{bmatrix} m_{11} & m_{12} \\ m_{21} & m_{22} \end{bmatrix} \quad \textbf{2-17}$$

From the matrix notation the surface molecular density of the overlayer (the coverage) can be calculated by:

$$\frac{1}{Det\ M} \text{ (mols per atom),} \quad \textbf{2-18}$$

where,

$$Det\ M = m_{11}m_{22} - m_{12}m_{21} \text{ (atoms per mol).} \quad \textbf{2-19}$$

From Equation 2-16, the matrix notation for the example overlayer shown in Figure 2.3-7 is given by;

$$\begin{bmatrix} a_0 \\ b_0 \end{bmatrix} = \begin{bmatrix} 2 & 4 \\ -6 & -2 \end{bmatrix} \begin{bmatrix} a_S \\ b_S \end{bmatrix}$$

The corresponding coverage is calculated as:

$$\frac{1}{Det\ M} = \frac{1}{(2\times -2) - (4\times -6)} = \frac{1}{20}$$

i.e. there is one adsorbed molecule for every 20 top-layer substrate atoms (20 atoms per molecule).

2.4. *Low Energy Electron Diffraction (LEED)*

LEED is used in surface science to ensure either the cleanliness or quality of the crystal prior to experimentation, or to determine the periodicity of ordered molecular adlayers. The technique allows the experimentalist to analyse electrons that have been elastically back-scattered from a sample surface, and not the bulk. This surface sensitivity was demonstrated by the early work of Farnsworth[118-121] and ensured by the use of low energy monochromatic electrons in the energy range 20-1000eV, which limits their inelastic mean free path to between ~5 and 20Å.

The apparatus required for LEED experimentation are designed in such a way that a sample with long range periodicity results in beams of scattered electrons whose spatial distribution directly reflects the ordered nature of the sample[122,123]. A diagram of a typical UHV LEED apparatus is shown in Figure 2.4-1. This setup is known as the rear view LEED arrangement.

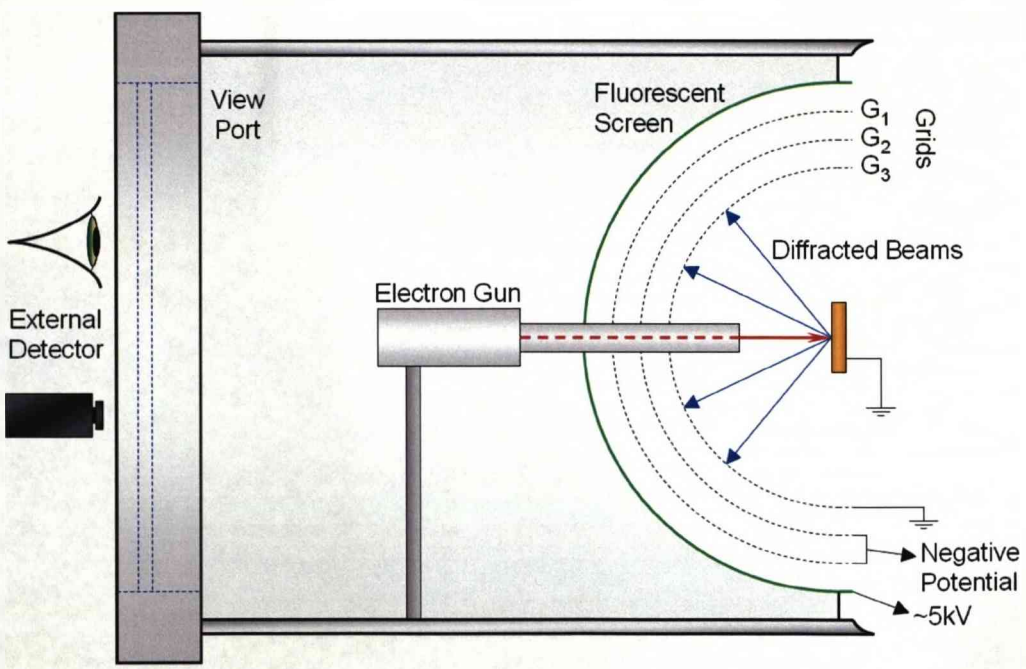

Figure 2.4-1. Schematic of a UHV LEED system.

The primary electron beam E_P is generated by an electron gun and is incident normal to the sample surface, which must be a conductor that is grounded. Subsequent to diffraction, a series of concentric spherical grids filter out those electrons that have been inelastically scattered. The detector is a fluorescent screen located behind the grids that accelerates elastically scattered electrons into it by a large positive potential of typically several thousand Volts, thus producing bright spots on the screen. The resulting diffraction pattern is a projection of the reciprocal surface net at a magnification determined by the incident electron energy. The nature of the observed spots is a direct indication of the nature of the sample surface. For example, a sample that has uniform periodicity over a long range (compared with the wavelength of the incident electrons) will produce sharp spots. A sample with a small amount of order or containing impurities will produce diffuse spots, as will a highly stepped surface.

2.4.1. One-dimensional diffraction

The main principle underlying LEED is electron diffraction[124]. To begin with, a periodic one-dimensional array will be used to exemplify the basic theory.

An electron beam incident on a periodic array of lattice constant *a* exhibits diffraction, with beams scattered at angle θ_a (Figure 2.4-2). The Laue condition relates the directions of the incident and diffracted beams to the interplanar spacing and electron wavelength in real space. The condition for constructive interference is given by the Bragg condition, which states that the path difference Ψ must equal an integral number of wavelengths:

$$\Psi = n\lambda, \qquad \textbf{2-20}$$

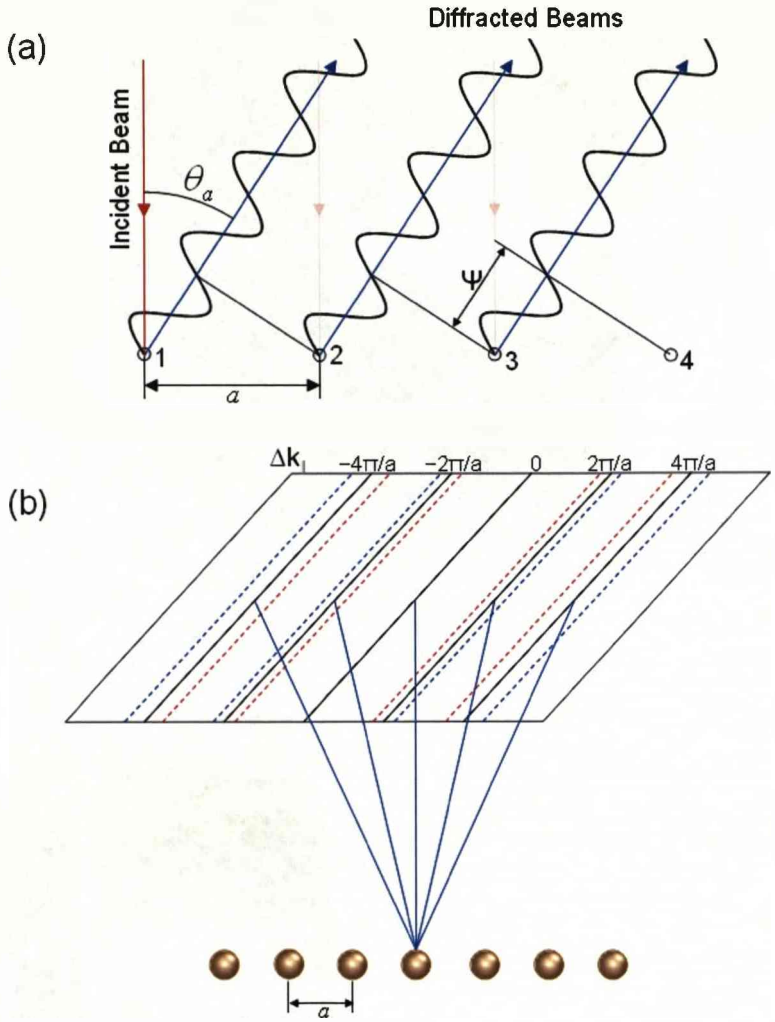

Figure 2.4-2. Schematic showing diffraction of a primary electron beam (solid red lines) at normal incidence to the sample surface (a), and the observed pattern from one dimensional scattering (b). In (b), increasing or decreasing the kinetic energy of the primary beam results in decreasing (red dotted line) or increasing (blue dotted line) separation between the lines of the pattern.

From Figure 2.4-2, it can be seen that;

$$\Psi = aSin\theta_a, \qquad \textbf{2-21}$$

and, due to the Bragg condition,

$$aSin\theta_a = n\lambda, \qquad \textbf{2-22}$$

where *n* can take values 0, ±1, ±2, ±3,... A simple rearrangement leads to:

$$Sin\theta_a = \frac{n\lambda}{a}, \qquad \textbf{2-23}$$

thus for fixed wavelength λ and surface lattice spacing a, each value of *n* corresponds to a well defined value of θ_a for constructive interference.

The diffraction pattern from a one-dimensional array is shown in Figure 2.4-2(b) and is made up of equally spaced lines, the separation of which is inversely related to the lattice spacing of the sample, i.e. an increase in lattice space results in a decrease in diffraction line separation for the same incident beam energy. The pattern can also be described in terms of electron wave vectors and the reciprocal space lattice vector. The magnitude of the incident wave vector of an electron ($|k_0|$) is given by:

$$|k_0| = \frac{2\pi}{\lambda}, \qquad \textbf{2-24}$$

Rearranging equation 2-23 for λ and substituting into 2-24 gives:

$$|k_0| \sin\theta_a = \frac{2\pi}{a} n \qquad \textbf{2-25}$$

where $|k_0| \sin\theta_a$ is the component of momentum parallel to the surface ($k_{\|}$) and $2\pi/a$ is the magnitude of the reciprocal lattice vector.

A primary beam whose wave vector is normal to the surface has no component parallel to the surface, however, for diffracted beams to arise (for the electron to undergo a change of direction) the electron must exchange parallel momentum with the one-dimensional lattice (i.e. momentum is conserved). This can be expressed as:

$$\Delta k_{//} = |k_0| \sin\theta_a = \frac{2\pi}{a} n \qquad \textbf{2-26}$$

where $\Delta k_{//}$ represents the change in parallel momentum in quantised units of $2\pi/a$.

2.4.2. Two-dimensional diffraction

In a real LEED experiment, the diffraction pattern for a two-dimensional array, or surface, is observed. A surface has two mutually perpendicular axes, and two lattice constants, a and b, that are repeated in line with the axes. In this case, the Bragg condition for constructive interference holds for both directions:

$$\sin\theta_a = \frac{n\lambda}{a} \qquad \textbf{2-27}$$

and,

$$\sin\theta_b = \frac{m\lambda}{b}. \qquad \textbf{2-28}$$

where *m* and *n* are integral numbers. Two sets of mutually perpendicular diffracted beams are obtained, one from the periodicity in *a*, and another from the periodicity in *b*.

The periodicity in both dimensions restricts parallel momentum exchange to:

$$\Delta k_{//} = |k_0|\sin\theta_a = \frac{2\pi}{a}n \qquad \textbf{2-29}$$

and,

$$\Delta k_{//} = |k_0|\sin\theta_b = \frac{2\pi}{b}n. \qquad \textbf{2-30}$$

For diffraction to be observed from a 2D array, both Equations 2-29 and 2-30 ***must*** be satisfied, thus, two-dimensional diffraction is allowed only at the intersection of the two one-dimensional reciprocal lattice rods generated in *a* and *b* directions. The resulting LEED pattern will then consist of spots corresponding to the points of intersection.

Accordingly, the exchange of parallel momentum is restricted to a two-dimensional reciprocal lattice vector G:

$$G = \Delta k_{//} = n\frac{2\pi}{a} + m\frac{2\pi}{b} \qquad \textbf{2-31}$$

The reciprocal lattice vector can be related to a real space lattice vector using the following set of rules:

$$G = na^* + mb^*, \qquad \textbf{2-32}$$

and,

$$|a^*| = \frac{2\pi}{|a|};\ |b^*| = \frac{2\pi}{|b|};\ a \cdot b^* = a^* \cdot b = 0 \qquad \textbf{2-33}$$

where *a* and *b* are the elementary vectors of the surface two dimensional unit cell and *a** and *b** are the elementary vectors of the corresponding reciprocal cell. These equations imply that a large (small) distance in the real space becomes a small (large) distance in the reciprocal space, and in addition, that *a* and *b* are perpendicular to the direction of *a** and *b**, respectively (Figure 2.4-3).

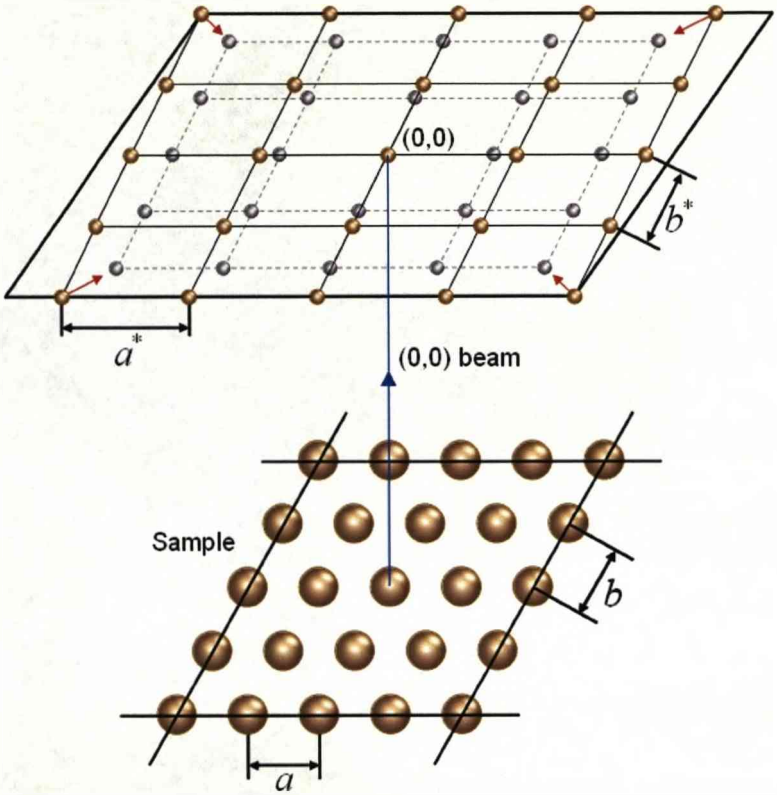

Figure 2.4-3. Diffraction pattern observed from a two-dimensional array. Note that a decrease in the wavelength of the incident beam 'contracts' the reciprocal lattice towards the (0,0) beam.

The condition for diffraction is the conservation of parallel momentum:

$$k_0^{//} = k_s^{//} \pm G \qquad \textbf{2-34}$$

where $k_s^{//}$ is the parallel component of the wave vector of the scattered electron.

The Ewald sphere construction is a method that is used to find the number of diffracted beams emerging from a three-dimensional periodic array at a given energy. The method can be applied to a 2D periodic array (surface) by reducing the sphere to a circle. The Ewald circle construction is created using the following steps:

a) Using the modified de Broglie equation the wavelength of the electrons is calculated using the energy of the incident electrons:

$$\lambda = \left(\frac{150.6}{E}\right)^{1/2} \qquad \text{2-35}$$

where λ is in Å and E in eV. Using λ, the corresponding wave vector can be estimated from Equation 2-24.

b) A scaled image of the reciprocal lattice has to be constructed using the conditions in Equation 2-33 and any lattice point is chosen as the origin (0,0).

c) Finally, a scaled circle of radius $|k_0|$ centred at the origin is drawn.

The total number of diffracted beams emerging from the surface is equal to the number of reciprocal lattice points contained within the circle. An example of the circle model construction is given in Figure 2.4-4(a). As the energy of the primary electron beam increases, so does the incident wave vector k_0. This is represented in Figure 2.4-4 by an increase in radius of the circle (red dotted line), which, as a consequence, leads to more spots being enclosed by the circle. This is essentially the same contraction towards the centre diffraction feature that is described in Figure 2.4-2(b), but in two dimensions.

The angle made by a diffracted beam with a particular real space direction can be calculated by constructing a variation on the Ewald circle model. The reciprocal lattice in this case can be considered that of diffraction from a one-dimensional array, hence a series of equidistant lines, rather than the pattern of spots corresponding to diffraction from a two-dimensional array (Figure 2.4-4(b)). It should be noted that, in the figure, the distance between the lines of the reciprocal lattice is equal to *a* so this specifically corresponds to diffraction from a one-dimensional array with lattice spacing a. If $a = b$, then the angles of the diffracted beams in the two mutually perpendicular directions parallel to the surface will be equal, however, if $a \neq b$ as in Figure 2.4-4, two different angles will be observed and the circle construction must be performed twice: once for *a* and once for *b*. In Figure 2.4-4(b), the intersections of the reciprocal lattice rods for a with the circle generated by

$|k_0|$ are the points at which the condition of the momentum conservation (Equation 2-34) is satisfied.

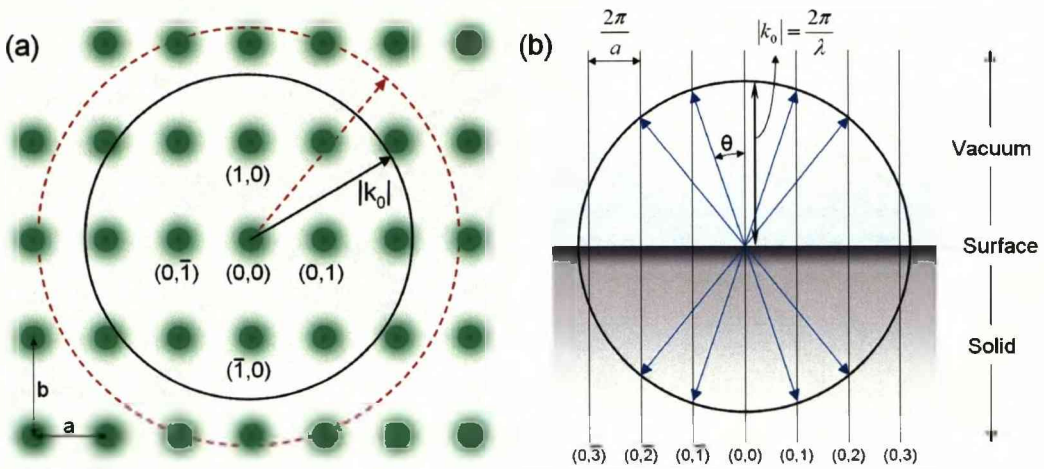

Figure 2.4-4. (a) The Ewald circle construction. The grid is anisotropic and distances a and b are defined. (b) The Ewald circle construction for diffraction from the array with lattice spacing *a*. The construction must be repeated for a lattice spacing b, which will be different as $a \neq b$. Beams penetrating the solid are not detected by LEED.

2.4.3. Description of overlayer structures from LEED

The adsorption of molecules onto a surface may result in the formation of ordered assemblies, which may or may not be commensurate with the underlying atomic lattice of the surface. It is appropriate to describe an ordered overlayer by relating it to the Bravais net of the substrate, and this can be done using two different notations, the most convenient of which for adsorbate arrangements is the one proposed by Park and Madden in 1968, involving a vectorial construction[125]. The reciprocal unit cell vectors of the overlayer a_o^* and b_o^* can be related to their reciprocal space substrate counterparts a_s^* and b_s^* by;

$$a_0^* = G_{11}^* a_s^* + G_{12}^* b_s^* \qquad \textbf{2-36}$$

and,

$$b_0^* = G_{21}^* a_s^* + G_{22}^* b_s^* \qquad \textbf{2-37}$$

where the G^*_{ij} are four coefficients which form a matrix G^*:

$$G^* = \begin{pmatrix} G_{11}^* & G_{12}^* \\ G_{21}^* & G_{22}^* \end{pmatrix} \qquad \textbf{2-38}$$

The conversion between reciprocal space and real space is possible by taking the inverse transpose of the matrix G*;

$$G = \left(\left[G^*\right]^{-1}\right) = \frac{1}{\det G^*}\begin{bmatrix} G_{22}^* & -G_{21}^* \\ -G_{12}^* & G_{11}^* \end{bmatrix} \qquad \textbf{2-39}$$

where,

$$\det G^* = \left(G_{22}^*.G_{11}^*\right) - \left(G_{21}^*.G_{12}^*\right) \qquad \textbf{2-40}$$

The adsorbate and substrate real space meshes are related by:

$$\begin{pmatrix} a_o \\ b_o \end{pmatrix} = G\begin{pmatrix} a_s \\ b_s \end{pmatrix} \qquad \textbf{2-41}$$

The type of surface structure can be classified according to the value of the determinant of G (det G), which is the ratio of the areas of the adsorbate and susbstrate meshes[126]:

a) If det G is integral and all matrix components are integral then the two meshes are simply related; the adsorbate mesh has the same translational symmetry as the whole surface.

b) If det G is a rational fraction or det G is integral and some matrix components are rational then the two meshes are rationally related. In this case the structure is still commensurate but the true surface mesh is larger than either the substrate or the adsorbate mesh. This surface mesh has a size dictated by the distances over which the two meshes come into coincidence at regular intervals.

c) If det G is irrational then the two meshes are incommensurate and no true surface mesh exists. The substrate is simply providing a flat surface on which the adsorbate can form its own two-dimensional structure.

CHAPTER 3

Experimental Details

This chapter introduces the equipment used in this study, including detailed descriptions of three UHV chambers used – the Specs STM, the RAIRS/LEED chamber and the Omicron VT-STM. The functions and operation of each and their supporting instruments are distinct and are described.

3.1. UHV Chambers

3.1.1. RAIRS/LEED chamber

LEED experiments were carried out on a single chamber dedicated primarily to RAIRS (Figure 3.1-1). The chamber is equipped with LEED optics, a Hiden Analytical Quadrupole Mass Spectrometer (including the control unit, the RF generator and the analyser), standard sample preparation techniques, including an Ar^+ Ion Gun for sample sputtering, and powder sublimation dosing system that is isolated from the main chamber by a gate valve. Dosing of gases and liquids is possible through a leak valve on the gas lines, shown in Figure 3.1-1. Cleaning techniques are described in greater detail in section 3.4. The chamber is pumped so that it operates at a base pressure of ~$2x10^{-10}$ mbar, which is primarily achieved and maintained by a diffusion pump (Diffusion pump A). Diffusion pumps operate by heating extremely viscous and high molecular weight silicone oil so that it evaporates. The vapour rises by convection and is deflected in the pump, accelerating it to supersonic velocities so that the oil molecules impart their

momentum on gas molecules in the atmosphere. The silicone oil condenses on the water-cooled chamber wall, and the captured gases are released at an outlet that is pumped by a dedicated rotary pump: Backing A. Diffusion Pump A remains on at all times, and, as with the rotary pumps, can be completely isolated from the chamber during a vent. Diffusion pump A is equipped with a cold trap that, in the event of difficulties achieving UHV, can be filled with liquid nitrogen that forces atmospheric gases to condense, thus improving the performance of the pump. The use of the cold trap is unnecessary under normal conditions. A titanium sublimation pump (TSP) aids in the attainment of UHV. The TSP is fired every 30mins in the short period after the bake as it is most effective in removing hydrogen from the chamber's atmosphere. Afterwards, a fire every 6 hours or more is sufficient to maintain UHV. A second rotary pump (Backing B) is used to roughly pump the KBr windows, the gas lines, the manipulator and the main chamber. A secondary diffusion pump is located on the gas lines but is not required in normal operation of the chamber.

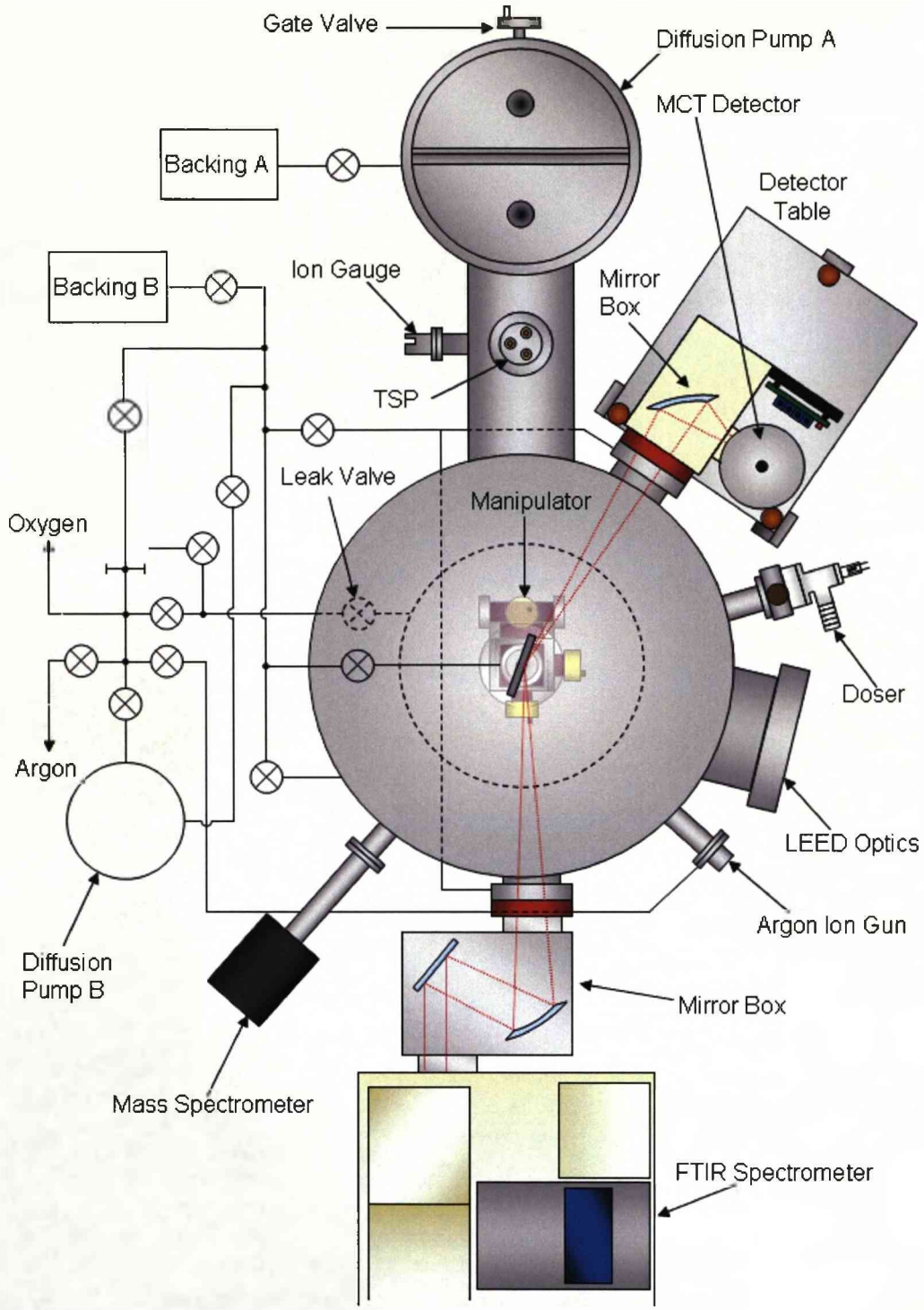

Figure 3.1-1. Schematic representation of the RAIRS/LEED UHV chamber showing the IR beam path from the spectrometer at the bottom to the detector (top right).

Subsequent to baking, the Mass Spectrometer, detector table and mirror box are carefully positioned. The alignment of the optical components must be extremely accurate in order for the IR beam to reflect off the sample

surface and then reach the detector – small changes in the positions of these components have a large effect on the signal strength.

The crystal is mounted on an X-Y-Z-θ manipulator (Figure 3.1-2) that is positioned on top of the chamber. Two sets of feed-throughs on the manipulator allow an electrical link between the crystal and electronic equipment outside the chamber such as power supplies (for resistive heating) or thermometers. Temperature is measured by use of a thermocouple that can be inserted into spark eroded holes in the crystal. Through the centre of the manipulator is a cold finger probe into which liquid Nitrogen can be funnelled to cool the sample. During cooling, thermal energy is required to pass through several individual components of the manipulator (shown in Figure 3.1-2), and the transfer across these boundaries and through the different materials makes cooling a long process that must commence at least 1hr prior to the beginning of an experiment. The crystal sample is attached to the manipulator by means of two tantalum wires (∅0.25mm) that are typically spot-welded to the crystal at several points along the edges (close up in Figure 3.1-2). When cooling the sample, heat must be transferred away from the crystal through the welds alone. More importantly, the welds are the only points of transit of the electric current that passes during annealing, which can cause significant local heating and breakages of the links. This is also the case for the join between the tungsten wires and the molybdenum rods of the manipulator. The greatest contact surface area is desired to reduce the current density and promote the transfer of thermal energy.

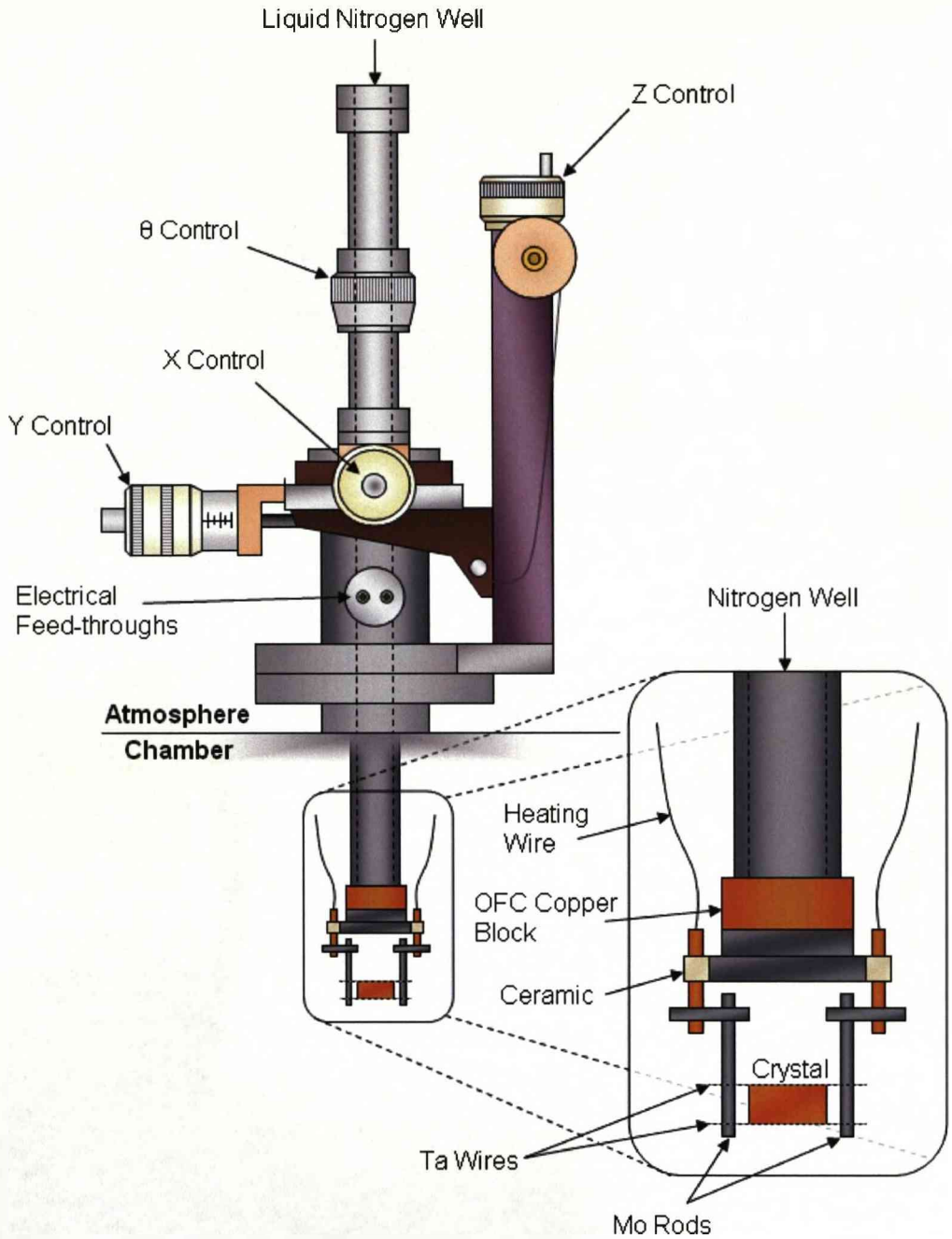

Figure 3.1-2. Schematic of the X-Y-Z-θ manipulator and crystal holder of the RAIRS/LEED chamber.

The LEED apparatus on the chamber is a reverse view Vacuum Science Instruments LEED/Auger combined instrument with a transparent fluorescent screen and a three-grid assembly. The instrument is design in such a way that the miniaturised shielded electron gun obstructs only a minimal part of the LEED pattern. The gun has an operational energy range of 0-1000eV and has a standard cathode filament of LaB_6 (lanthanum

hexaboride) that has specially cut microfaces. Three mounted concentric hemispherical Mo grids are coated with Au and have a common centre that is aligned with the gun. The fluorescent screen is coated on both sides with metal; the grid side is coated with P43 cadmium-free phosphor. LEED images are normally captured using a charge coupled device (CCD) TV camera but a mobile phone-mounted digital camera has proved adequate in some conditions.

3.1.2. Specs STM chamber

The Specs STM chamber is differentially pumped to UHV using a Pfeiffer Balzers turbo-molecular pump that is backed by a rotary pump, and a Varian Vaclon Plus 300 Ion Pump. Ion pumps operate by ionising atmospheric gas molecules in a magnetically held cloud of electrons. The gas molecules are then accelerated by a large electric field towards a reactive, high-surface-area electrode in which they become embedded. The ion pump is only used at UHV pressures to avoid saturation of the honeycomb electrode by embedded molecules, which would render the pump ineffective. The turbo-molecular pump is used alone during higher pressure procedures such as dosing. A single TSP is fired every 8hrs after UHV is achieved and more frequently shortly after baking the chamber. The TSP and ion pumps are ideal for use with STM chambers due to their vibration free function. A base pressure of $2x10^{-10}$ mbar was typical during the experiments.

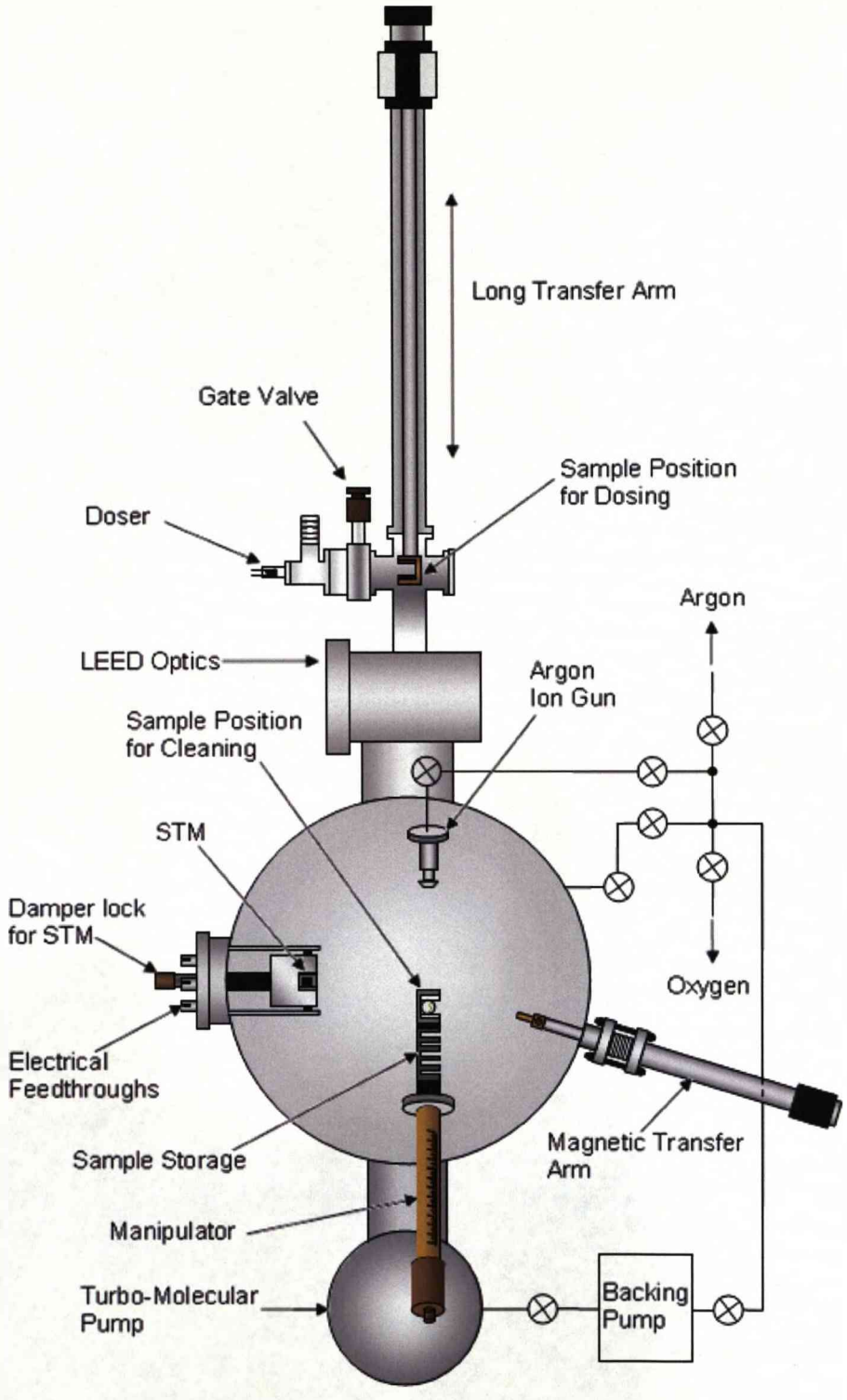

Figure 3.1-3. Schematic of the Specs STM UHV chamber.

The apparatus comprises a single chamber in which the STM, manipulator, transfer arms, LEED optics and cleaning apparatus are located. There is no way to retrieve or replace tips or samples without first bringing

the chamber up to atmospheric pressure and consequently up to 5 samples can be stored on the manipulator at any time. The manipulator only moves in a linear fashion and is used to position the sample for either transfer or preparation. Using the magnetic transfer arm, which allows x/y/z and rotational (θ) motion of samples within the chamber, the sample can be transferred to either the STM or the long transfer arm, which allows z and θ movement through the length of the chamber. The long transfer arm is used for positioning the sample for both LEED experiments and dosing procedures.

The primary STM used in this study is a Specs GmbH Aarhus STM150, which is mounted on a massive metal block that itself is mounted on a cradle. The metal block can be filled with liquid nitrogen to cool the sample. The STM has two dedicated damping systems that protect the system from unwanted vibrations caused by mechanical coupling to the environment. The first is the block itself, which is suspended by springs that counter low frequency vibrations in the range of 1-3Hz. The second type is adjustable and protects against higher frequency vibrations in the range 5-200Hz. Correct adjustment of the damping systems can achieve a stability of less than 5 picometers at all frequencies.

STM requires an extensive electronic control system. For this STM, an SPC 20 controller controls the following equipment:

- Preamplifier – Amplifies the tunnelling current and converts it to a voltage,
- Variable temperature controller VTC 20 (unused for this study),
- Monitor-Digipot – Manual control of the motor and scanner head (unused for this study),
- Filter box – Filters signals from the SPC 20 to the approach motor and reduces crosstalk between the tunnelling current and the approach motor,
- ISA Interface Card – Allows data collection using a PC.

The electronics controlling the STM movement and power are linked directly to the STM via electrical feed-throughs on the STM flange. This allows precise control using the Specs software, which is used to approach

or retract the tip to or from the sample and to perform the STM experiments. The scanner approaches using a worm at a fast rate of around 1mm/min. The Specs software is used to determine the conditions under which the approach is done, including the step size, which on approach can result in a tip crash if set too high. A smaller step size increases the time to approach/retract however so a larger step is used for the retraction where there is no risk to the experiment. Control of the tip position and the tunnelling conditions is controlled via the Specs software also, as is tip conditioning: the process of clearing the tip of unwanted material and forming an atomically sharp assembly of atoms by means of voltage pulses and, if necessary, tip crashes.

In extreme cases in which the tip simply won't allow tunnelling to produce a high enough quality image, a high voltage field emission clean can be performed. This involves deliberately crashing the tip into a clean surface while 100V is applied between the tip and surface. On retraction, the electric field removes unwanted material from the tip by forcing it towards the surface. To form the new tip, the tip is crashed again into a clean area of surface and the field direction reversed, thus bringing new material – the surface atoms – to the tip as the tip is retracted. A short period of tip conditioning is usually necessary for the tip to become suitable.

The Specs software is used for the enhancement and calibration of images. The calibration is simply an expansion or contraction of the x and y axes of the image by the amount input into the program. This does not take into account any inherent skew in the uncalibrated image. This is addressed by third party software such as Image SxM. The STM was calibrated to better than 5% accuracy by measuring distances in the (2×1) superstructure resulting from the introduction of oxygen onto the clean Cu(110) surface. The response of the scanner changes slightly between different scanning scales and calibrations are consequently performed on 20×20nm, 30×30nm, 50×50nm, 70×70nm and 100×100nm images.

3.1.3. Variable Temperature (VT) STM/LEED UHV chamber

The VT-STM is a commercially available STM that is manufactured by Omicron Vacuum Physik GmbH. It has been designed in three main sections - the Fast Entry Lock, Preparation Chamber and the Analysis Chamber, and is shown in Figure 3.1-4. Separation of the sections by gate valves allows them to be used independently of one another and permits a base pressure below $2x10^{-10}$ mbar to be maintained (after systematic degassing) where it is needed while samples or tips can be safely introduced into other sections of the STM. The Preparation Chamber and, when the middle gate valve is open, the Analysis Chamber is pumped by a Balzers TPU300 turbo-molecular pump that is backed by a rotary pump. The turbo-molecular pump is isolated by a pneumatic gate valve that automatically closes in the event of a power failure, thus retaining vacuum. The turbo pump is used to evacuate the Argon and Oxygen gas lines and can also be used to pump the Preparation Chamber through the Fast Entry lock. UHV is attained and maintained by the use of two Varian Ion Pumps that respectively pump the Preparation and Analysis chambers, and two Vacuum Generators (VG) TSPs that are in the same configuration. The turbo-molecular pump can be the cause of undesirable vibrations. The pumping configuration allows the STM to operate with the turbo disabled and the Ion Pumps and TSPs holding the vacuum. The pumping configuration on the VT-STM is very versatile and can account for any eventuality.

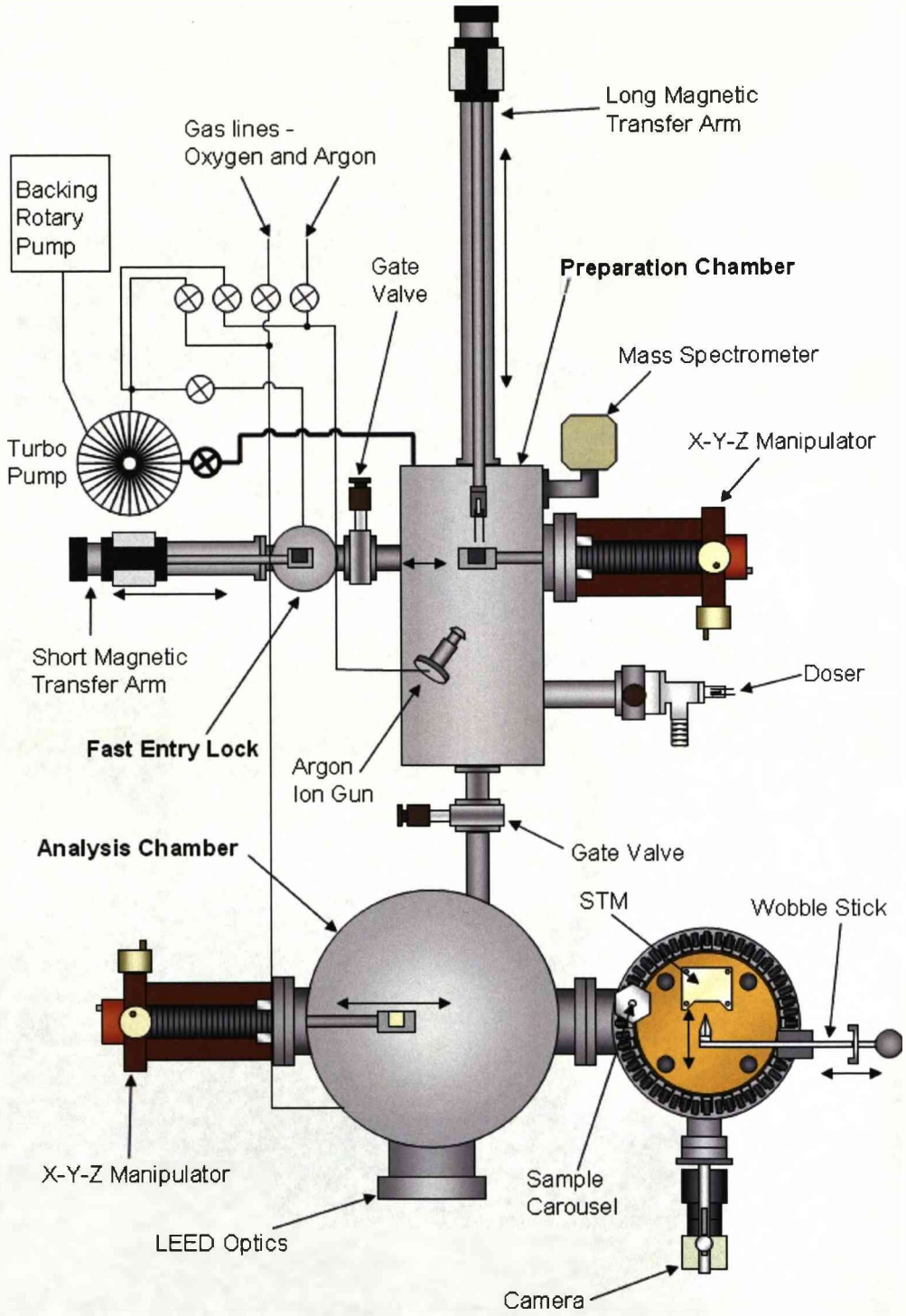

Figure 3.1-4. Schematic of the Omicron VT-STM chamber showing the three main parts: the Fast Entry Lock, the Preparation Chamber and the Analysis Chamber.

The Fast Entry Lock is used for the insertion of samples and STM tips (see Figure 3.1-5) into the chamber without compromising the vacuum. Crystals are secured on standard sample plates that are made of

Molybdenum or Tantalum (see Figure 3.1-5) using strips of Ta foil that are spot-welded to the plate and held in tension over the ends of the crystal. Stainless steel tip carriers are designed as a double-decker. The bottom tier is where the tip is held by a magnet. The top tier completes the protective 'cage' around the tip, and is essentially the same design as the sample plate, albeit with holes in. This configuration allows the tip to be held securely as transfers take place.

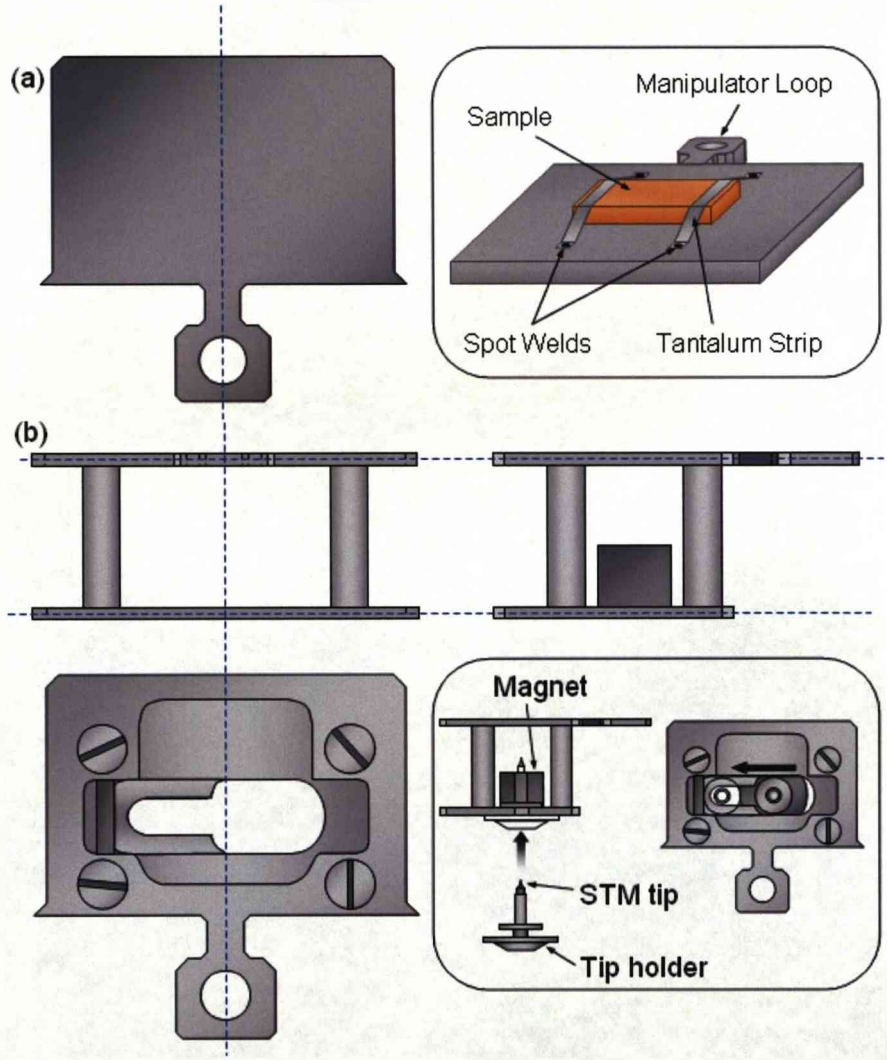

Figure 3.1-5. Schematics of a sample plate and tip carrier. (a) The sample is held on the sample plate by spot-welded tantalum foil strips. The manipulator loop is gripped by a hammer on the end of the long transfer arm to secure the plate during transfer through the chamber. (b) The STM tips are inserted into a magnetic holder to ensure their safe transfer through the chamber.

The Fast Entry Lock can be vented with Nitrogen, a sample placed in and the lock pumped to UHV using the turbo-molecular pump in just a few hours, thus saving the disruption of a complete vent, and this can normally be done whilst other operations are carried out. It is especially useful in the replacement of STM tips, which can be damaged under normal operating conditions.

The Preparation chamber, to which the Fast Entry Lock links directly via a gate valve, comprises standard sample preparation techniques, the Mass Spectrometer and the dosing line. Samples are transferred from the fast entry lock to the Preparation Chamber by means of the short magnetic transfer arm, shown in Figure 3.1-4, where it is transferred to the long magnetic transfer arm. When on the long transfer arm the sample can be transferred to the X-Y-Z-θ manipulator, positioned for dosing, or transferred to the Analysis Chamber. For sample cleaning, i.e. sputtering and annealing cycles, the sample is transferred to the manipulator, which is then set in a pre-determined position. The manipulator has, on the atmosphere side, electrical feed-throughs for connecting high voltage (HV) power supplies and Thermocouples (TC)/digital Voltmeters (DVMs) for measuring temperature or drain current respectively.

The second section, the Analysis Chamber, is a two piece chamber with LEED/Auger optics, an Ion Gauge and an X-Y-Z-θ manipulator in one part and the STM in the other. Numerous ports allow customisation of the chamber to suit the experiment. Samples and tips are transferred to this chamber from the long transfer arm to the X-Y-Z-θ manipulator and the gate valve between the sections is closed to prevent contamination. Typically, the Analysis Chamber is maintained at a lower base pressure than other sections because gases are not regularly introduced into it, however, oxygen is occasionally dosed in small quantities (≤5L) as a necessity for calibration of the sample lattice parameters (see section 3.4).

The cleanliness of the Analysis Chamber is further improved by the ability to store samples on the sample carousel, which can store any combination of 12 tips and samples on two hexagonal tiers, removing the need for exposure to contaminants from other sections of the chamber when changing the crystal or tip. Excess material in the chamber's atmosphere acts to contaminate samples and can cause the user to have to condition the STM tip for some time before high quality images can be obtained. From the manipulator, LEED experiments can be done or the sample can be positioned for transfer into the sample carousel or STM using the pincer-grip wobble stick.

The STM is housed in a bell chamber and is damped against vibration by two methods. Firstly, the stage on which the STM in mounted is locked by a push-pull mechanism (PPM) that, when released, drops the stage so that it hangs from four vertical springs that are accommodated in tubes that protrude through the stage and are positioned equidistant from each other. The PPM remains locked at all times other than during STM experiments. The springs are supported by an eddy current damping system in which copper fins fitted around the circumference enclose a rigid ring of strong permanent magnets fitted to the chamber itself, shown in Figure 3.1-6 below. The combination of the stiffness of the springs and strength of the induced Lorentz force on the Copper fins results in a steady scanning table for the STM that effectively reduces vibrational noise.

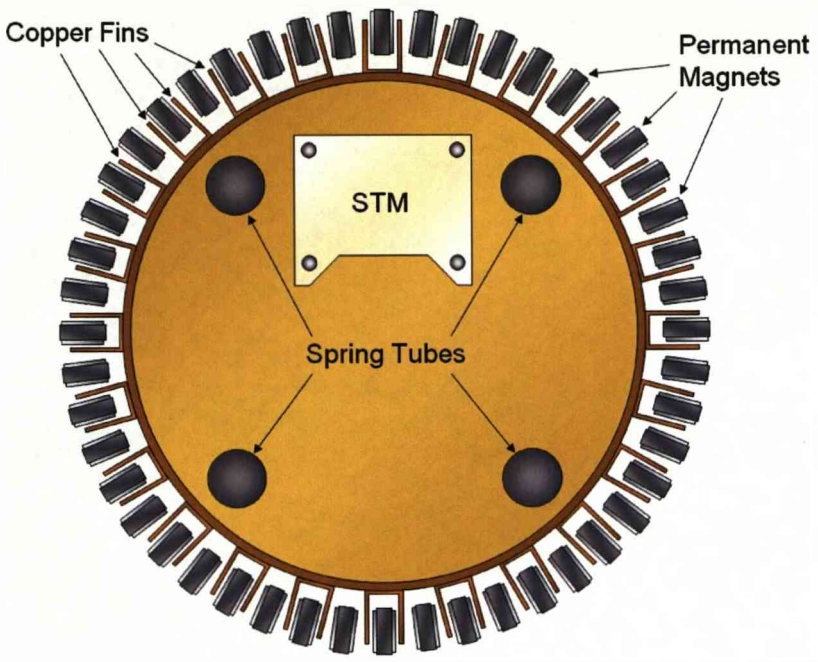

Figure 3.1-6. Schematic showing the VT-STM damping system.

The STM head consists of a single tube scanner that employs a piezo-tripod to scan the sample. The tube has a maximum scanning range of 12μm with a z range of 1.5μm and z resolution of 0.1Å or better.

The approach of the STM tip towards the crystal is done in two stages – manual then automatic. The manual stage uses a coarse controller that controls a rapid movement piezo louse. The tip is positioned as close to the crystal without crashing with the aid of a CCD camera that is linked to a black and white TV. With a light source positioned suitably and the camera focussed well the tip can be approached during this stage so that the time taken for the automatic stage to complete is greatly reduced. The fine approach to tunnelling height is done by the SCALA PRO program on the interfaced PC. The user must first specify a tunnelling current that, when reached, signals an end to the approach. It is occasionally the case that tunnelling cannot commence after the approach because the tip is still too far away from the sample. Often, a manual step forward solves the problem but a re-approach is occasionally necessary. Typical approach time is in the range of 5mins.

Operation of the STM is controlled by an Omicron STM control unit, which has an integrated 68010 microprocessor that is interfaced to a pc. The workstation can be operated either locally or remotely. Local control is directly from the instrument panel, whereas the remote mode allows full control of the imaging and scanning procedures via an IEEE-488 interfaced PC. Both local and remote modes support constant current and constant height STM operation modes as well as full dI/dz and dI/dV spectroscopy. In remote mode, operation of the instrument is performed using the SCALA software, which can also be used to perform rudimentary analyses of data and image enhancements for presentation. The software also comprises several filters that can be used to reduce or entirely eliminate artefacts and/or noise in the data. Care must be taken when carrying out these procedures as real features may also be affected. Normally, the data will be analysed using third party software such as WSxM[127] or Image SxM. As with STM data from the Specs STM, images must first be calibrated.

3.2. *Adsorbate*

A single molecule has been employed for the entirety of this study; Co(II)-Tetraphenylporphyrin (Co-TPP) (Sigma-Aldrich, UK) (Figure 3.2-1), which was used as purchased and sublimed onto a Cu(110) surface that was held at room temperature during deposition. A detailed description can be found in section 1.2.

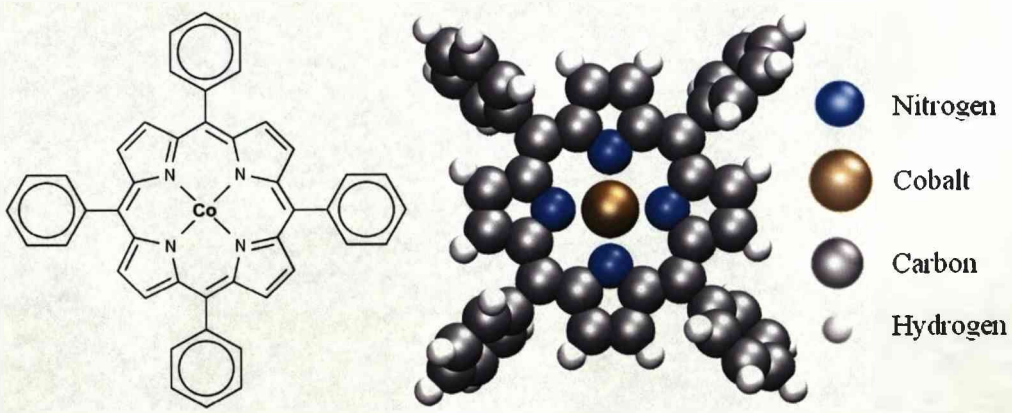

Figure 3.2-1. Chemical and structural representations of Co-TPP.

3.3. *Doser and dosing procedure*

Dosing the Co-TPP molecule was done using a sublimation doser (Figure 3.3-1). The sublimation doser consists of an electrical feed-through flange containing two copper power electrodes and two thermocouple electrodes. Stainless steel barrel connectors are attached to the top of each copper electrode. The barrel connectors secure the ends of a 0.25 mm Ta filament wire which is evenly wrapped (7 turns) around a small glass tube in which the granular molecule is contained. By carefully constructing the doser, its response to the applied current can be accurately judged by the doser power without the need for a thermocouple. This can be advantageous as the presence of a thermocouple on the tube can create a temperature gradient that causes molecules to condense at the opening, thus promoting the adsorption of more molecules in the tube. The end of the Ta filament is secured by the second barrel connector, thus completing the circuit. In this study, Co-TPP molecules have been dosed under several conditions to achieve different coverages. These are described below:

1. 1.4A – Low molecular flux condition for slow domain growth.
2. 1.45A – Medium flux condition.
3. 1.5A – High flux condition.

Experimental requirements dictate which of the above conditions is used; however, the exact temperature of the tube is unknown, incurring some degree of uncertainty in the procedure. The temperature has been measured to be in the range 150-165°C. During sublimation, the pressure in the chamber reaches up to 2×10^{-9} mbar, depending on the dose conditions and the degas status of the molecule. The conditions of the dose depend on the build quality of the doser. Consequently, there is normally a calibration period for a new doser in which doses are initially attempted using a low power, usually 1.6W, and increased by 0.1W to achieve effective and reliable dosing conditions. By following this procedure, not only is the molecule safe from decomposition, but the doser receives a thorough degassing. Between

experiments, a power of roughly 0.2W below the minimum dose requirement is used for a continual degas of the tube.

It should be noted that the dose rate is strongly dependent on the shape of the chamber into which the molecule is dosed, for example, the RAIRS chamber opens into a large volume a significant distance before the sample and so the flux reaching the surface is relatively low compared to that of the STM chambers, in which the doser and sample are close and in an enclosed space. The dose rate is estimated using the chamber pressure, and confirmed by the experimental data, i.e. coverage estimations from STM.

There is a minor error in the estimations of the dose times that can be attributed to the time taken to open and close the gate valve between the doser line and the main chamber. Although the impact on the analysis of the experimental data has been minimal due to the coarse definition of low, medium and high coverage only, it is noted that 10s dose time in some STM experiments may have an intrinsically high error of ±2s, although this still remains in the low coverage regime.

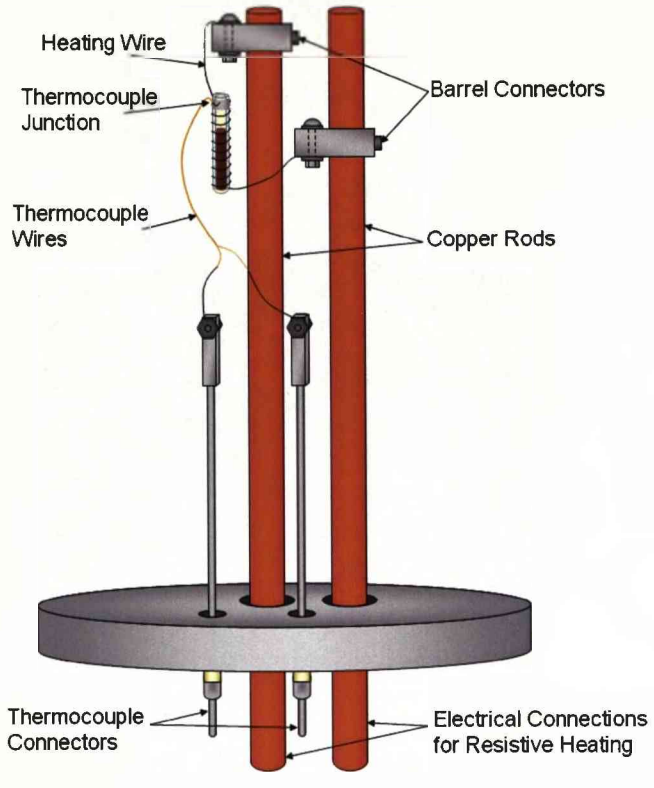

Figure 3.3-1. Schematic of a sublimation doser used for dosing Co-TPP.

The dosing line is pumped to rough vacuum first by a rotary pump, then to UHV (~10^{-8} – high 10^{-9}mbar) by a turbo-molecular pump, shown in Figure 3.3-2. The dosing line is isolated from the chambers by a gate valve, allowing degassing of the doser to be done independently of the chamber conditions. This also has the benefit of allowing molecule changes or maintenance to be carried out in a time-effective manner and without the need to disrupt the conditions in the main chamber.

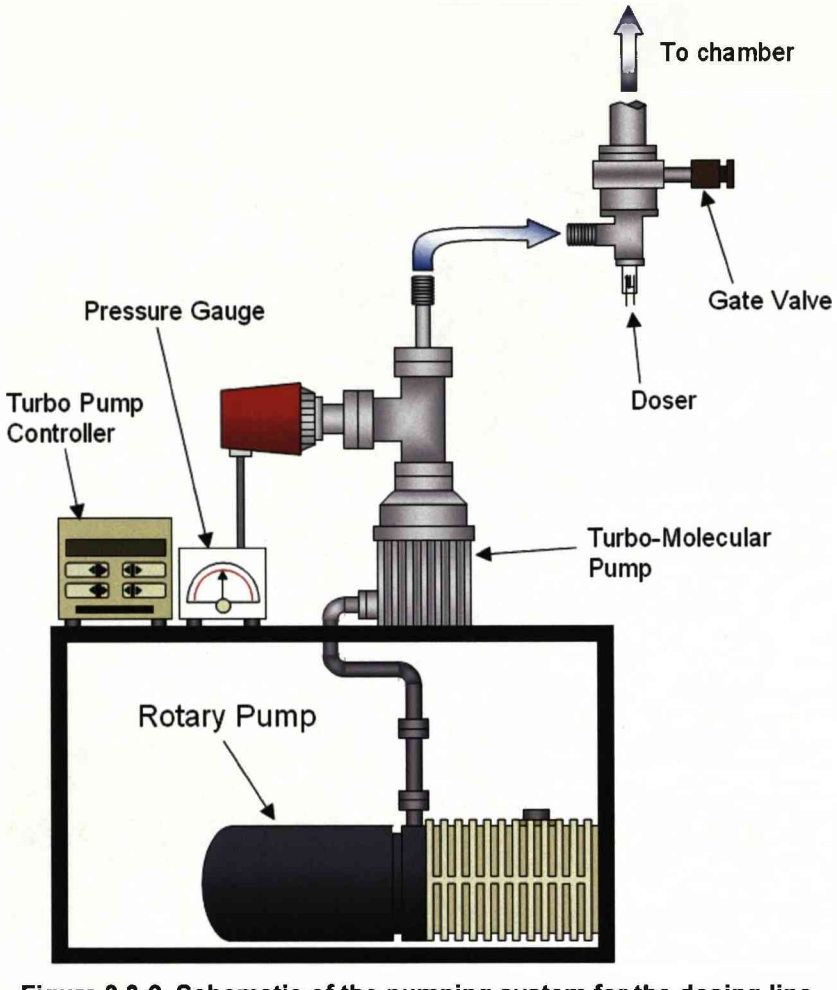

Figure 3.3-2. Schematic of the pumping system for the dosing line.

3.4. Crystal and preparation

All experiments in this study were performed on a Cu(110) crystal, of which two have been used. The specification of each is as follows:

- VT-STM: A single crystal copper (Cu) sample, cut in the (110) plane to better than 0.2% accuracy and reported to be 99.999% pure. The crystal is of dimensions 9×3×2mm and was purchased from Surface Preparation Laboratory (NL).

- Specs STM: A single crystal copper sample, cut in the (110) plane to an accuracy of 0.1° and reported to be 99.999% pure and scratch free at 800× magnification. The crystal, of dimensions 8mm diameter and 1.8mm thick, was purchased from Surface Preparation Laboratory (NL).

The Cu(110) surface is characterised by a rectangular array that is created by a diagonal 'cut' through the face-centred cubic (f.c.c) unit cell, as shown in Figure 3.4-1.

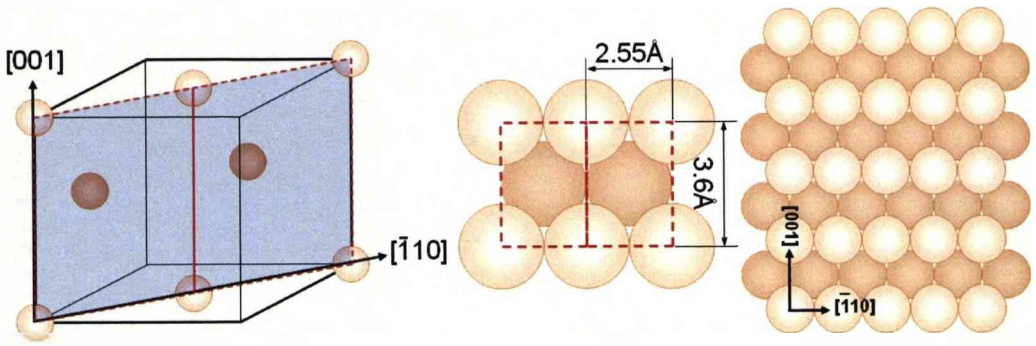

Figure 3.4-1. A diagonal cut through the cubic unit cell creates the (110) surface of the f.c.c copper. The result is an anisotropic surface with a rectangular unit cell of dimensions 3.6Å×2.55Å. Lightly coloured atoms are those of the top layer, darker are the second layer (middle and right). Dimensions in the 3D crystal (left) are inaccurate.

The use of UHV chambers permits the preparation of atomically clean and flat samples that are prepared using cycles of argon ion sputtering and annealing. Sputtering is the process of bombarding the surface with argon ions (Ar^+) that are accelerated toward the surface by an electric potential (Figure 3.4-2a), thus destroying and removing the top layers of molecules, adatoms and the crystal itself. Acceleration energies typically range between 500 and 1keV, but can exceed this depending on the quality of the surface and the nature of adsorbed species. Sputtering is known to damage KBr windows and they must be protected in the RAIRS chamber by a movable shield. During the sputtering process, argon is introduced into the chamber at a pressure of $2x10^{-5}$ mbar. In a parallel with the molecular flux during dosing (see section 3.3), the effectiveness of the sputter differs between UHV chambers and this is reflected in the drain current – the passage of electrons that counter the effect of the positively charged argon ions bombarding the surface. This is a direct measure of the number of argon ions arriving at the surface and, in the RAIRS chamber, there is observed a typical drain current of ~3-4μA compared with a drain current of 7-9μA in the STM chambers for equivalent acceleration energies. Argon for sputtering is changed regularly to ensure cleanliness, which is checked by Mass Spectrometry – any significant

changes during the introduction of argon to the chamber in peaks other than 18, 19, 20, 36, 38 and 40 are considered contamination. Peaks 18, 19, 36 and 38 are isotopes. The Ion Pump and TSP in the STM chambers are disabled as they can become unnecessarily saturated by argon. The turbo-molecular pump in this case can hold the desired pressure and, due to its purely mechanical operation, is able to handle larger numbers of molecules with no drop in performance. In the RAIRS chamber, the diffusion pump performs the same function, having no realistic capacity for saturation.

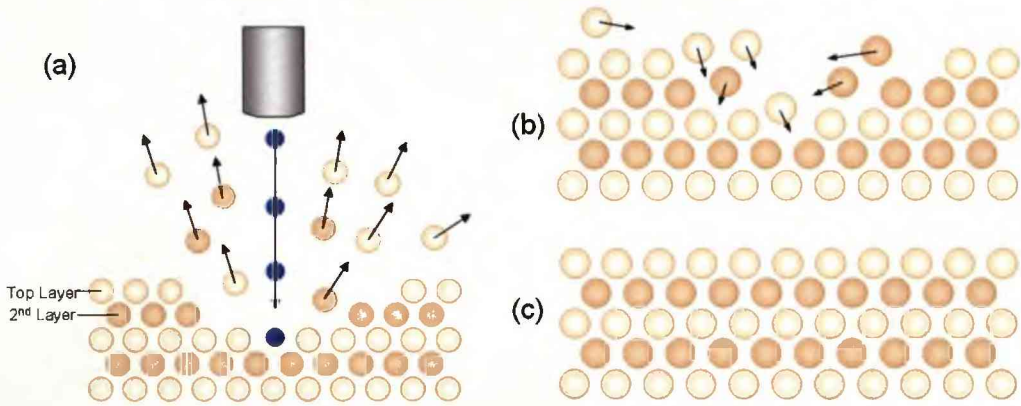

Figure 3.4-2. Sputter-anneal cycles prepare the crystal for experiments. (a) Sputtering by argon ion (blue) bombardment destroys the surface, including any molecules present. The figure shows a simplified view. (b) Subsequent annealing rearranges surface molecules, leaving flat, or approximately flat, terraces (c).

Sputtering is followed by a 550-600ºC anneal for copper (Figure 3.4-2), which provides the surface atoms with enough thermal energy so that they can rearrange themselves in order to minimise the total number of defects at the surface. In the RAIRS chamber, annealing is done by passing a current through the wires securing the crystal, thereby inducing heating in the wires that heats the crystal conductively. As the resistance in the wires increases, the crystal will inevitably constitute the path of least resistance, thus forming part of the circuit through which the current flows, and will therefore be resistively heated also. The temperature is reached slowly by this method and the crystal is subsequently cooled by conductive (sometimes with the aid of liquid nitrogen) and radiative heat loss.

Annealing to elevated temperatures requires the electron beam (e-beam) heater in the STM chambers. A current is passed through the filament(s) on the manipulator on which the sample plate is situated. This begins radiative heating of the sample, which only allows temperatures of below 400°C to be reached. The path of the current is shown as red lines in Figure 3.4-3 below. To initiate e-beam heating a potential difference must be applied between the filaments and the sample, which is grounded and insulated by ceramics. This causes the electrons escaping from the glowing filaments to accelerate towards the sample plate, which is heated resistively as a consequence of the electrons' transit to ground through the HV wire, shown as blue dotted lines in Figure 3.4-3. Sample temperature is estimated with the aid of a Pyrometer, despite glass ports on the chambers not being entirely transparent to IR. The emissivity for the sample was set manually on the Pyrometer to gain the most accurate reading. A secondary method of gauging the temperature that comes only with experience is to closely watch the colour of the crystal as it heats, knowing that its temperature will be 550-600°C when it starts to glow a dull red. The sample is held at this temperature for 15-20mins before being cooled.

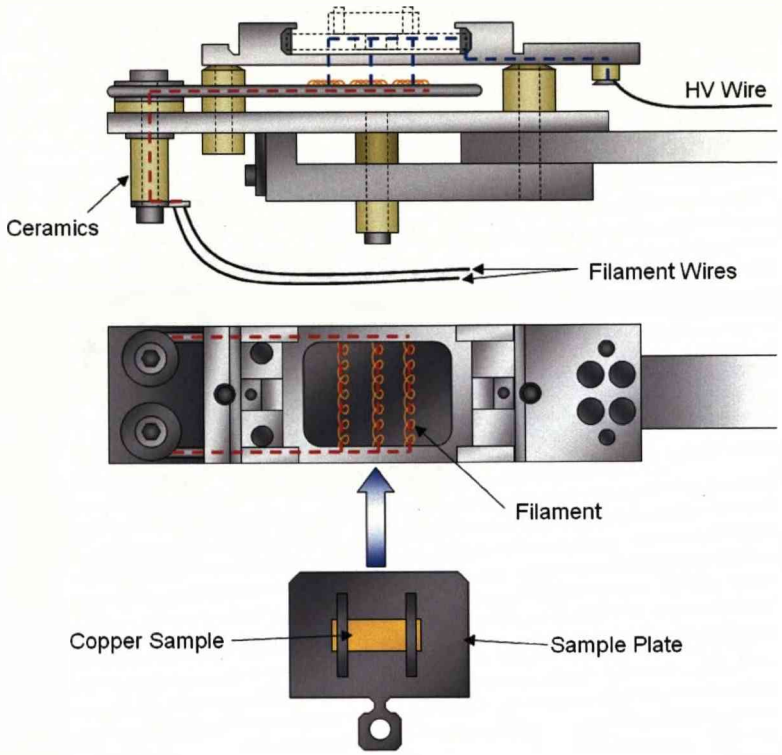

Figure 3.4-3. Schematic of the VT-STM manipulator sample holder and sample. The top section where the sample is held is isolated from the rest.

It should be noted that thoriated (thorium coated) wire is preferential for this application. Thorium acts to decrease the work function of the wire, thereby making it easier for electrons to escape the material. A smaller current would then be required to give the same emission of electrons that could be manipulated for e-beam heating.

Effective sputter-anneal cycles leave a surface with large flat terraces (Figure 3.4-2), depending on the original state of the crystal – a highly stepped crystal may require removing from the chamber and polishing to reach a state fit for experimental surface science. The state of the crystal is evaluated in the chamber by LEED and STM. Under normal conditions only three cleaning cycles are required.

A final method of sample preparation is an oxygen treatment. The crystal is held at 250°C while oxygen is introduced into the chamber, which is maintained at a pressure of 2×10^{-8}mbar. This oxidation-reduction step is used to ensure desorption of surface carbon in heavily contaminated crystals.

CHAPTER 4

The single molecule unit cell chiral organisation (Structure 1)

Structure 1 appears in most of the STM data on this system, however, it is only at very low flux that it is observed it in its purest form, i.e. without distortion by transition structures (see section 5.3). Structure 1 is the simplest of all the observed structures and was chosen for a theoretical study for this reason.

4.1. Characterisation

Structure 1 is the predominating assembly arising from the self-organisation of Co-TPP on Cu(110), forming over a large coverage regime. A pure phase can be achieved at room temperature under low flux conditions.

Large area STM data of Structure 1 are presented in Figure 4.1-1a and show the coexistence of two mirror domains whose growth directions diverge from the Cu[001] axis by ±(20°±2°) respectively. The system, therefore, possesses chiral domains, denoted λ and δ. Typically, these organized domains are observed to nucleate and grow with time following deposition at room temperature and are capable of reaching dimensions of $1\mu m^2$.

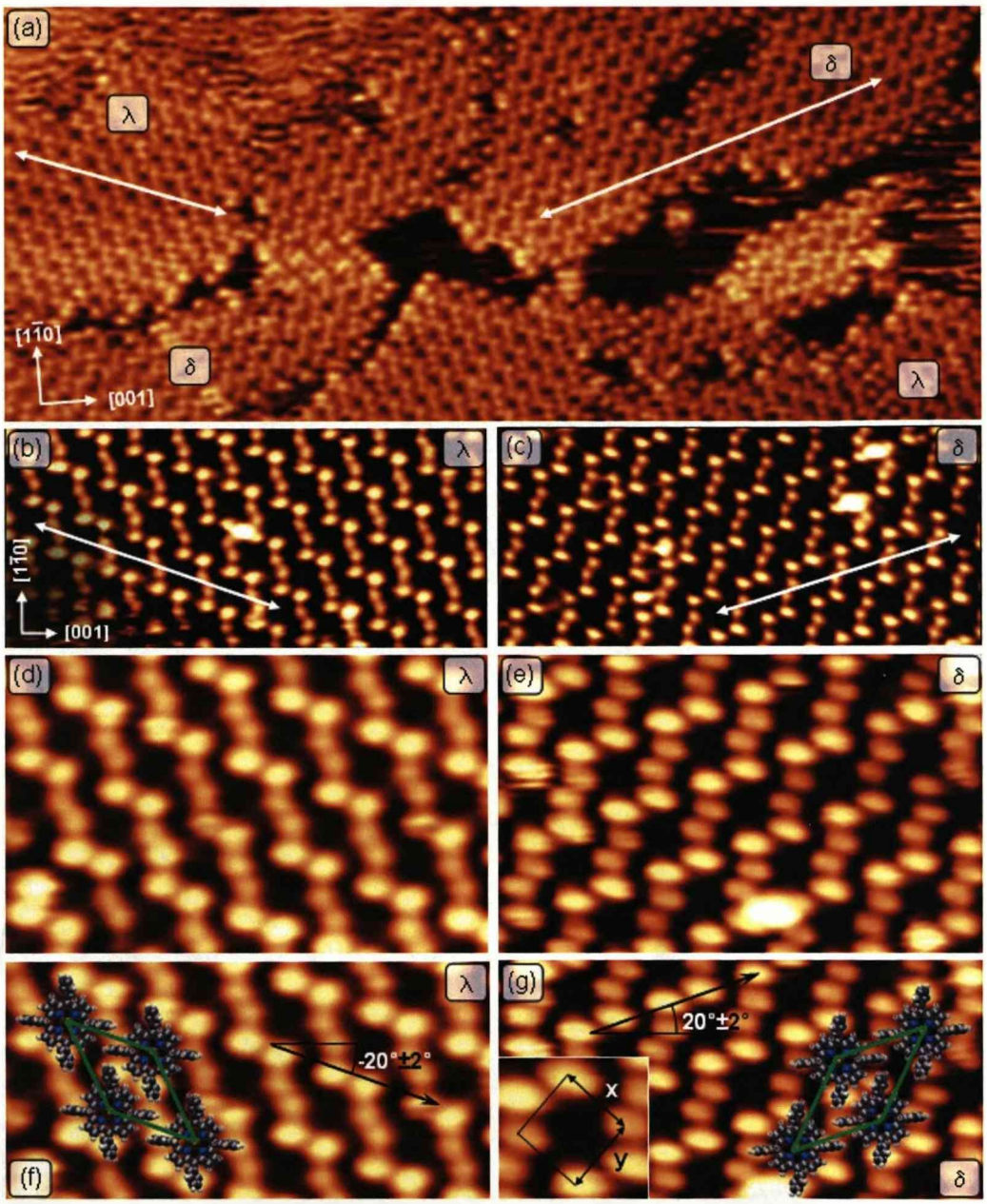

Figure 4.1-1. Co-TPP assembly on Cu(110): λ and δ chiral domains of Structure 1. Bright spots represent significant contributions from the phenyl rings (discussed later) while the porphyrin cores image much darker. Arrows represent the main growth directions of the two chiral domains. (a) Large area (542×242Å^2) image showing coexisting chiral domains I_T=0.48nA, V=1250mV. The total surface coverage of Co-TPP during this scan was roughly 10%. Detailed images of the two chiral domains are shown in (b) 140×65Å, I_T=0.32nA, V=670.5mV, (c) 140×65Å, I_T=0.49nA, V=670.5mV, (d) 80×50Å, I_T=0.38nA, V=734.8mV, (e) 80×50Å, I_T=0.21nA, V=611.3mV. (f) – (g) Molecules overlaid on sections of (d) and (e) respectively, showing the unit meshes. The copper axes in (b) apply to all subsequent images. Chiral directions are shown relative to the Cu[001] axis. Inset in (g) defines the aspect ratio of adsorbed Co-TPP.

Figure 4.1-1b-e display detailed, small area STM images obtained from each chiral domain. These reveal a highly organized domain structure. From the regular patterns observed, the repeat unit mesh can be identified directly from calibrated STM images, as shown in green in Figure 4.1-1f and g. Both chiral domains possess structures that are fully commensurate with the substrate and, using standard convention[14], are described by $G^{\lambda} = \begin{bmatrix} 2 & 4 \\ -6 & -2 \end{bmatrix}$ and $G^{\delta} = \begin{bmatrix} -6 & 2 \\ 2 & -4 \end{bmatrix}$. This is corroborated by the analysis of LEED data (Figure 4.1-2). Using the reciprocal space vectors shown in Figure 4.1-2, the matrix *G** (Equation 2-38) is found to be;

$$G^* = \begin{bmatrix} G_{11}^* & G_{12}^* \\ G_{21}^* & G_{22}^* \end{bmatrix} = \begin{pmatrix} -\frac{2}{10} & -\frac{1}{10} \\ -\frac{1}{10} & -\frac{3}{10} \end{pmatrix}.$$

Taking the inverse transpose of the matrix G* yields the conversion between reciprocal space and real space (Equation 2-39);

$$G = \left(\left[G^*\right]^{-1}\right)^t = \frac{1}{\det G^*}\begin{bmatrix} G_{22}^* & -G_{21}^* \\ -G_{12}^* & G_{11}^* \end{bmatrix}$$

$$= 20\begin{bmatrix} -\frac{3}{10} & \frac{1}{10} \\ \frac{1}{10} & -\frac{2}{10} \end{bmatrix}$$

$$G = \begin{bmatrix} -6 & 2 \\ 2 & -4 \end{bmatrix}\begin{bmatrix} a_s \\ b_s \end{bmatrix}$$

where the determinant is found using Equation 2-40:

$$\det G^* = \left(G_{22}^*.G_{11}^*\right) - \left(G_{21}^*.G_{12}^*\right)$$

$$= \left(-\frac{3}{10}\cdot-\frac{2}{10}\right) - \left(\frac{1}{10}\cdot\frac{1}{10}\right) = \frac{1}{20}.$$

The blue spots in the simulation conclusively correspond to the δ domain of Structure 1.

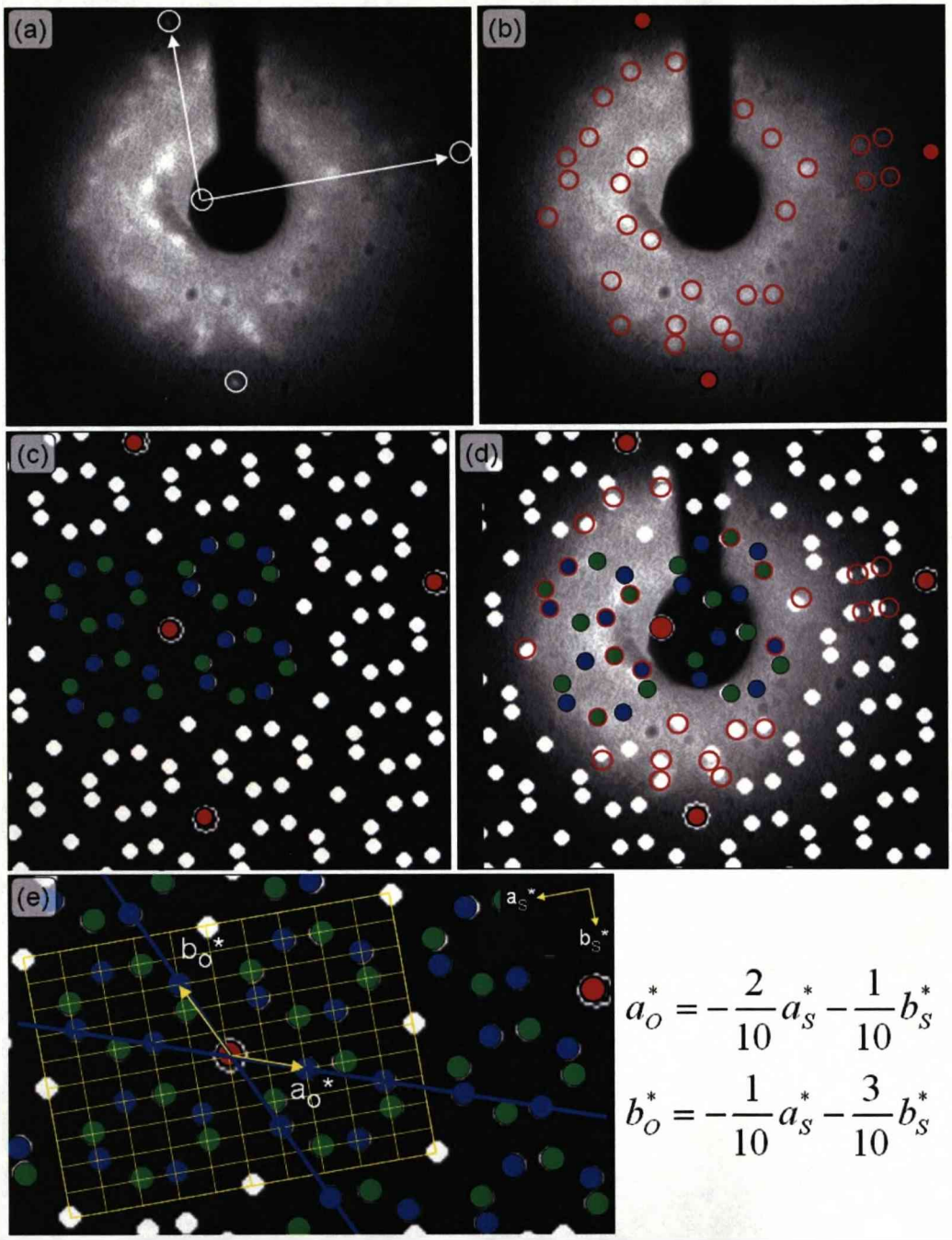

$$a_O^* = -\frac{2}{10}a_S^* - \frac{1}{10}b_S^*$$

$$b_O^* = -\frac{1}{10}a_S^* - \frac{3}{10}b_S^*$$

Figure 4.1-2. (a) Experimental LEED data of the Structure 1 overlayer at 37eV, with the major features of the pattern highlighted in (b). (c) The Structure 1 LEED pattern as created by The LEED pattern simulator (K. Hermann (Fritz-Haber Institute) and M. A. Van Hove (Lawrence Berkeley National Laboratory). Green and blue spots represent each chiral domain, where blue is found to represent the δ domain. (d) The simulated pattern overlaid on the experimental image shows good registry with the features shown in (b). (e) A 10×10 grid overlaid on the simulation shows spots only at the intersections and, therefore, allows the reciprocal space vectors to be obtained for the blue spots.

Each unit mesh accommodates a single Co-TPP molecule, and each molecular position is, therefore, associated with a number of bright protrusions and a dark area in the STM image. By positioning the Co-TPP molecules onto STM images such that each protrusion corresponds to one phenyl group a highly ordered and close packed layer is obtained in which the molecules appear with reasonable dimensions when compared with the gas phase conformation, Figure 4.1-1f-g.

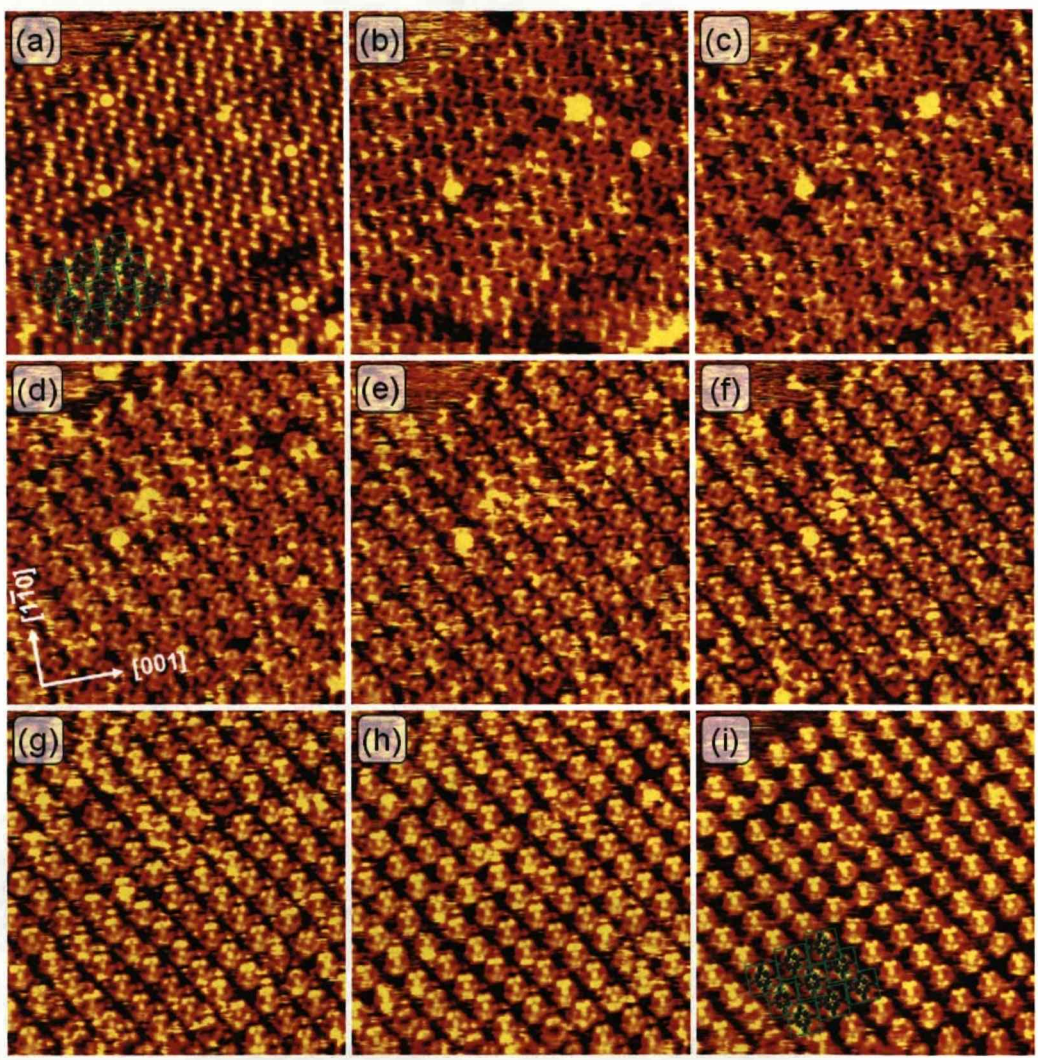

Figure 4.1-3. Identification of molecules within Structure 1. (a)-(i) shows the same area, but with a clear transition in the way the structure is imaged. Frames (a) to (i) were taken consecutively, and a 3×3 molecule matrix is highlighted in green in (a) and (i). (a) shows the normal imaging, with phenyls being prominent. Some core structure is observed also in (a). In (i), only the molecular cores are shown and the phenyls are not observed. Copper axes in (d) apply to all images. Image conditions: (a) I_T=–0.51nA, V=–1201.1mV, (b) V=1698.6mV, (c) V=1010.1mV, (d) V=1428.5mV, (e) V=1201.1mV, (f) V=1010.1mV, (g) V=849.3mV, (h) V=714.1mV, (i) V=600.6mV. (b-i) I_T=0.49-0.53nA. All images are 152×154Å.

In this configuration, it is observed that the STM images show little or no contribution from the Co-TPP core, although some negative bias images show a protrusion at the Cobalt position. Imaging Structure 1 by STM is often unpredictable, however, and a changeable STM tip can alter the observations dramatically (Figure 4.1-3). In general, and in contrast to Comanici *et al*[101], it is found that the STM images are largely bias independent. Using the centres of the bright protrusions associated with individual phenyl rings to determine distances x and y as shown in the inset in Figure 4.1-1g, the molecular aspect ratio (x/y) in Structure 1 is calculated to be 1.1. This overall model is corroborated by the results from the periodic DFT calculations discussed in the following sections. Finally, the fact that Co-TPP orders in registry with the underlying Cu(110) surface suggests a significant molecule-surface interaction. It is also noted that the Co-TPP/Cu(110) system displays relatively high molecular diffusion during domain growth and, therefore, the assumptions that a strong(weak) molecule-substrate interaction generally leads to low(high) molecular mobility has been carefully reconsidered. Figure 4.1-4 shows this dynamic growth of a Structure 1 domain at room temperature and shows the result – a structure covering the largest part of a $1\mu m^2$ area (Figure 4.1-4h).

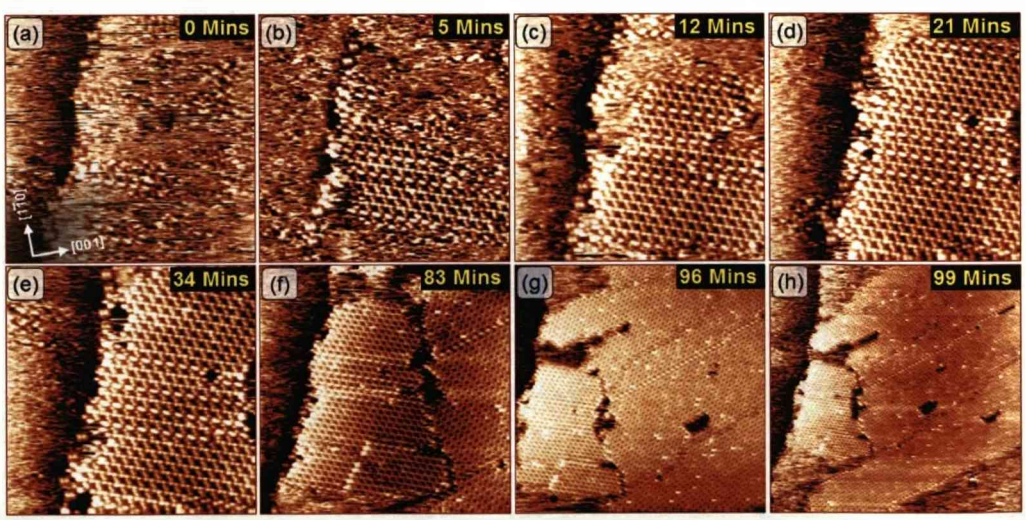

Figure 4.1-4. (a) to (e) are time lapse images of λ domain growth of Structure 1. (f) to (g) show the result of the growth over an extended period of time. Images (b) to (h) were taken at +5, +12, +21, +34, +83, +96 and +99mins after (a). Image conditions: (a) to (e) are 306×303Å, (f) 510×505Å, (g) 714×707Å and (h) 918×909Å. V=611.3mV and tunnelling currents are in the range I_T=0.24-0.3nA for all images. The copper axes in (a) apply to all images.

4.2. DFT introduction

In order to derive the specific adsorption site for Co-TPP in Structure 1 and to obtain further insight into the bonding and conformation of the adsorbed Co-TPP molecule the unit mesh of the λ domain is utilised to perform periodic DFT calculations of the full system. The DFT calculations were performed by Matthew Dyer of the group of Mats Persson at the University of Liverpool's Surface Science Research Centre.

In the following, special attention will be given to the molecule-metal and molecule-molecule interactions that drive the observed chiral self-assembly. Details of the calculations can be found in the Appendix.

4.3. Adsorption site, molecular deformations and STM simulations

DFT calculations using periodic boundary conditions were carried out to find the energetically preferred adsorption sites for the Co-TPP molecules within Structure 1. There is found a strong preference for molecular adsorption at the short-bridge site, shown in Figure 4.3-1, with adsorption at the top and hollow sites calculated to be less stable by +32.5 and +67.0kJmol^{-1}, respectively. Further calculations have been performed that show adsorption at the long-bridge site to be considerably less stable.

The calculations show large molecular deformations away from the preferred conformation in vacuum when Co-TPP adsorbs at the short-bridge site, Figure 4.3-1. Porphyrin deformations can occur both within the macrocycle and in the attached side functional groups.

Considering the macrocycle first, our calculations also reveal that the adsorbed molecule shows only minor deformation from planarity. Cobalt porphyrins have been shown to possess enhanced resistance to distortions of the macrocycle, even in the gas phase[32]. This planarity is additionally favoured by the nature of the interaction between the macrocycle and the copper surface, discussed later. Interestingly, the cobalt atom in the core is

held just 2.1Å above the surface plane (shown in Figure 4.3-1) and significant deformations in the phenyl groups are consequently observed. These, in turn induce small deformations in the macrocycle as steric repulsion acts between neighbouring hydrogens. This small deformation may lie within the accuracy of the calculation, but it is consistent around the ring. This contrasts the observations made by Zotti *et al*[69], in which a weak molecule-substrate interaction between H_2-Tetrapyridylporphyrin (TPyP) and the Ag(111) surface results in a large molecule-surface separation of 5.6Å and largely preserves the original conformation of the molecules.

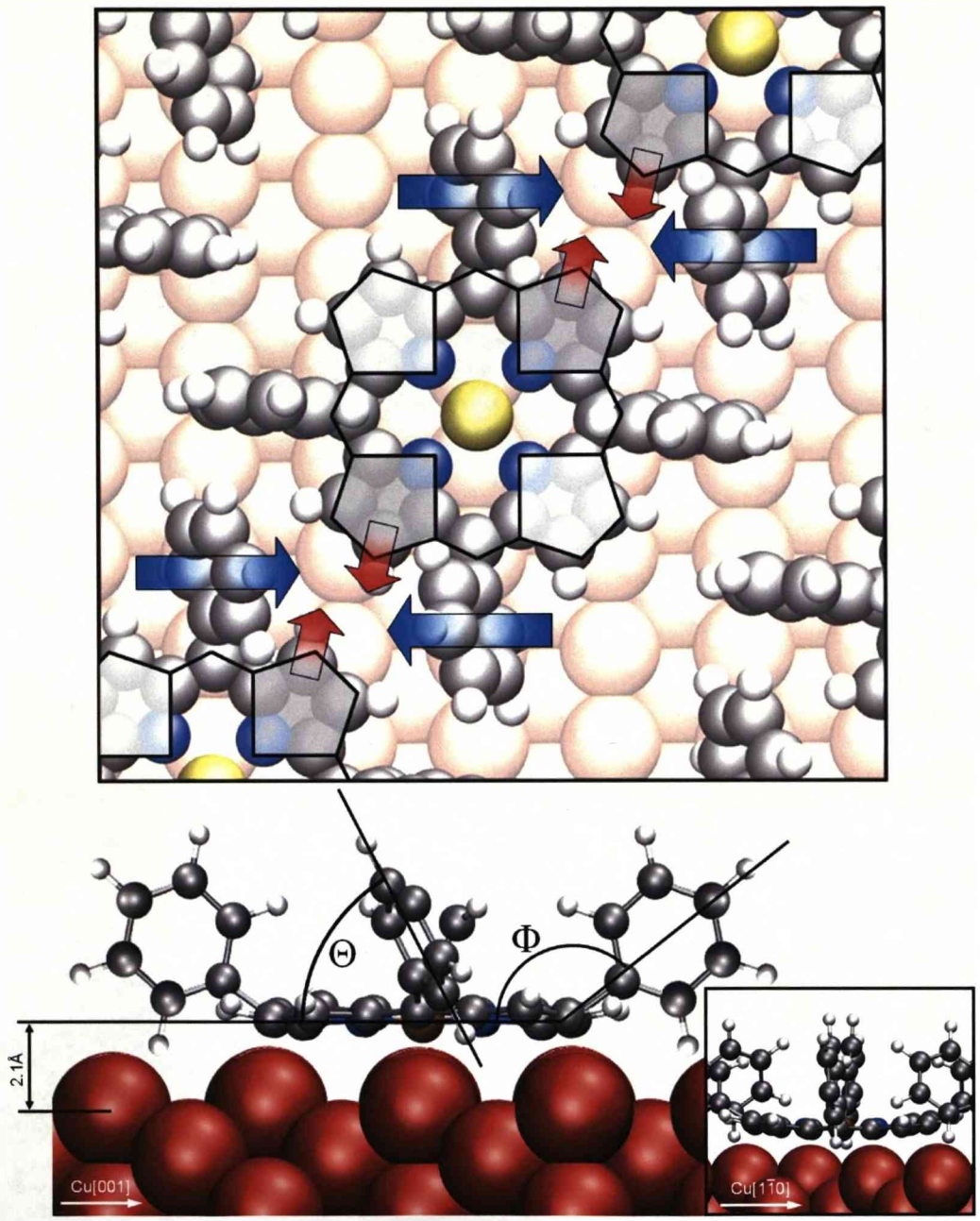

Figure 4.3-1. Molecular conformation of Co-TPP within Structure 1. Top: Adsorption site of the minimum energy conformation calculated by DFT. The twisting of the phenyls relative to the core (arrows) give the molecule a chiral propeller-like conformation. As the phenyls twist over the macrocycle, small deformations occur due to steric repulsion. Bottom: Side view along the Cu[1-10] axis of Co-TPP adsorption and conformation– tilt Φ and twist Θ angles are altered significantly with little observable deformation of the core. Inset: Side view of Co-TPP when viewed along the Cu[001] axis.

Turning now to the deformation of the phenyl groups; DFT calculations of Wölfle *et al*[32] give a useful insight into the energy cost of various distortions in the gas phase for selected metal-TPP molecules, and

consistency is retained with this literature[32] in defining the tilt angle, Φ, as the angle between the plane of the macrocycle and the σ bond connecting phenyl rings to the core. Twist (dihedral) angles, Θ, describe the rotations of the phenyl rings around the same σ bond and are defined as the angle between the phenyl ring plane and the surface plane (Figure 4.3-1). In the lowest energy configuration calculated for the isolated molecule in the vacuum, one finds that tilting distortions are energetically costly and the gas phase system displays only a small distortion with Φ=176°. In contrast, twist distortions are less costly and a large range of angles between 90° to 60° can be tolerated in the gas phase[32]. The deformations observed for Co-TPP on Cu(110) are due to a compromise between two interactions: an attractive interaction between the Co-TPP core and the surface and a repulsive interaction between the phenyl rings and the surface. When adsorbed in the short-bridge site, the phenyl groups align with and accommodate themselves in the corrugations of both Cu[001] and Cu[1-10] rows by a combination of tilting and twisting. Due to the intrinsic anisotropy in the system endowed by the substrate, two pairs of diametrically opposite phenyls exist that are clearly identified by their different twist angles, as can be seen in Figure 4.3-1. Our calculations show that the first pair of phenyls, aligned with the Cu[001] rows, show a twist angle Θ of 86° which lies within the range of values that can be expressed in the gas phase conformation. However, the proximity of the surface causes a substantial and costly tilt Φ of 144° in this pair, which is over 32° away from the vacuum configuration. The interaction between the second phenyl pair and the substrate is significantly different. Here, the adsorption site dictates that the phenyl centres align on top of the close packed Cu[1-10] rows. The calculated twist angles Θ of 64°-65° are close to those adopted in the vacuum[32], and are sufficient to move the H atoms away from the copper atoms (Figure 4.3-1). The surface corrugation allows a slightly less costly tilt angle Φ of 148°-149° in this pair. This conformation, as observed by STM, is consistent across the entirety of the domain, including the outer row of molecules that each have a single free phenyl. Although seemingly extreme, the deformation of the molecules in the Structure 1

domain is in the range of those estimated in other studies, shown in Table 4.3-1.

Table 4.3-1. Summary of porphyrin deformations from published work[22,23,31,73,75,82].

		Phenyls		Phenyls		Core	
Porphyrin	Surface	Tilt angle 1	Tilt Angle 2	Twist angle 1	Twist Angle 2	Saddle 1	Saddle 2
Co-TBPP	Ag(111)	25	25	90	90		
Co-TBPP	Ag(111)	20	20	60	60		
Co-TBPP	Ag(111)	15	15	45	45		
Co-TBPP	Ag(111)	5	5	20	20		
TPyP	Ag(111)			60	60		
H2-TBPP	Cu(100)	46	46	49	49		
Cu-TBPP	Au(110)			65	65		
Cu-TBPP	Au(110)			45	45		
Cu-TBPP	Cu(100)			90	90		
Cu-TBPP	Ag(110)			30	30		
TPyP	Cu(111)	0	0	30	30	40	40
Co-TPP	Cu(111)			35	35	20	20
H2-TBPP	Au(111)			20	20		

It is important to note that, due to the large number of degrees of freedom with such a large molecule, there are many similar conformations with very similar energies that correspond to nearby local minima on the potential energy surface and an exhaustive search for the global minimum within these is not feasible. Several symmetric adsorption conformations were also found with the cobalt atom above the short-bridge site that were within a few $kJmol^{-1}$ of that presented below. Nevertheless, all the low energy conformations of Co-TPP adsorbed at the short-bridge site had qualitatively the same adsorption geometry, both in terms of the deformation of the macrocycle and the orientation of the phenyl substituents and the conclusions are not affected by choosing any of these structures – in fact it can be concluded from this analysis that several conformations, only slightly different in geometry and energy, exist simultaneously at RT. Data from an alternative stable conformation with the cobalt atom situated above the short-bridge site is shown in the Appendices for comparison.

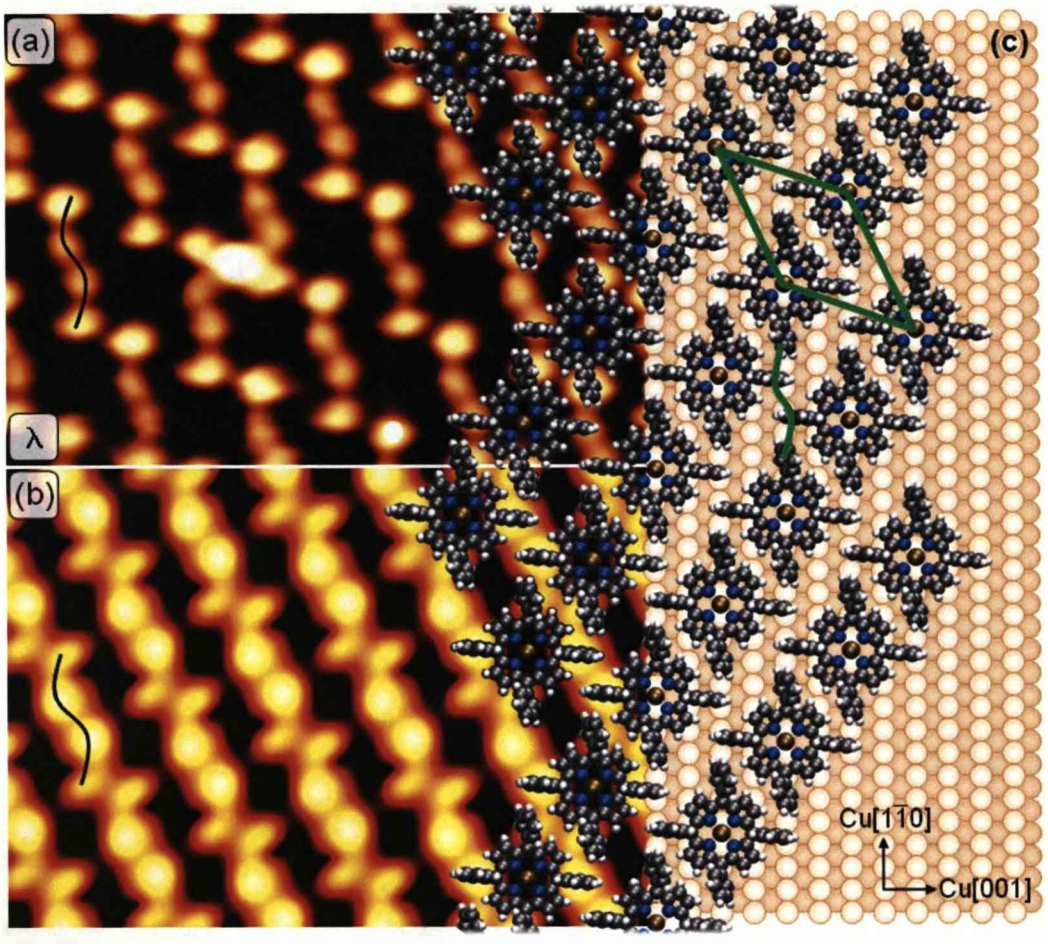

Figure 4.3-2. A good agreement is observed between experimental and simulated STM images for Structure 1. (a) λ domain STM image, data taken at V=449.8mV, I_T=0.32nA. (b) The corresponding STM image of the structure calculated at 450mV. The contour range for (b) is 9.5-10.75Å. (c) The molecular overlayer on real space model of the self-assembled λ □domain of Co-TPP/Cu(110) shows good overlap with both (a) and (b). The unit cell and the S-like Structure 1re shown in green.

In addition to the deformation of the molecule away from its preferred conformation in vacuum, the positions of the atoms in the underlying copper substrate are also seen to change upon adsorption (Figure 4.3-3). The largest substrate deformation is observed directly below the porphyrin macrocycle. The ten top-layer copper atoms (red) directly below the carbon atoms in the macrocycle are drawn out of the surface and towards the carbon atoms by up to 0.1Å. The two top- and six second-layer copper atoms (green) below the centre of the macrocycle move down into the surface by a similar distance. The four top-layer copper atoms below the phenyl rings also move down into the surface by 0.1Å and show some additional lateral

displacements, the remaining two top-layer copper atoms in the unit cell have only negligible displacements away from their clean surface positions.

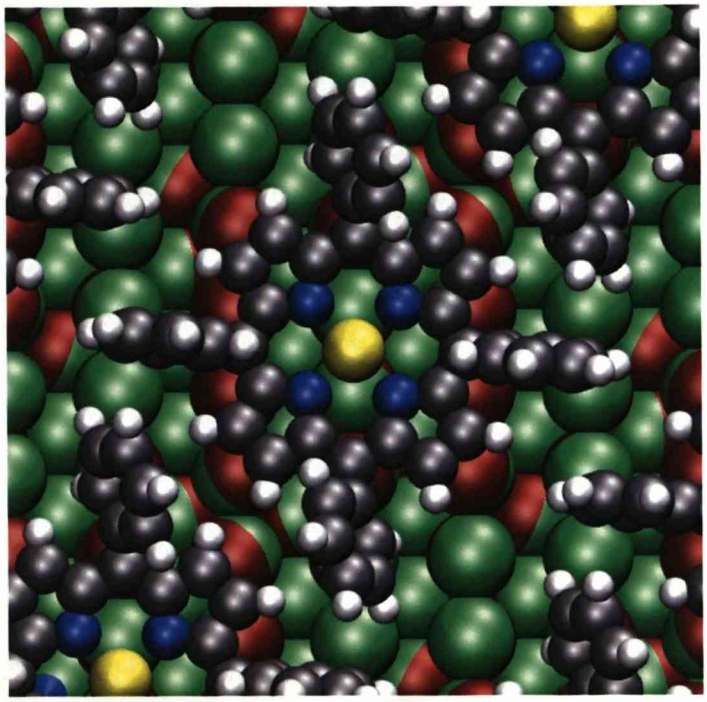

Figure 4.3-3. The displacement of copper atoms following adsorption of the Co-TPP molecule. The positions of copper atoms in the relaxed clean copper surface are shown in green, and those of the copper atoms with the Co-TPP molecule present in red. As a result copper atoms appear red when they have moved out of the surface. Where atoms are part green, part red this represents a lateral motion away from the green position, towards the red.

The Co-TPP/Cu(110) structure shown in Figure 4.3-2 provides a good basis for understanding the features observed in experimental STM data. First, due to the large phenyl tilt angles of the adsorbed Co-TPP, the lack of discernible core structure in the STM images can be attributed to a largely topographical origin – a result of the greater height of the phenyl groups relative to the core. This conformation is maintained in all molecules constituting the assembly, including those at the domain edge, and is the cause of the general bias independence of the assembly observed in the experimental STM data. There is generally good agreement between experimental and calculated STM data for the short-bridge adsorption site within the $\begin{bmatrix} 2 & 4 \\ -6 & -2 \end{bmatrix}$ assembly of the λ domain (Figure 4.3-2). Both the

stretched S-like structure consisting of phenyl groups from four neighbouring porphyrins and the characteristic dark porphyrin cores are well reproduced by the calculated STM images (Figure 4.3-2). From the calculated structural model, there is found a (10×10) copper-aligned supercell for this structure that is identified, also with good agreement, in the experimental STM images (Figure 4.3-4). This is effective for obtaining an accurate calibration of the experimental STM data by measuring the distance between widely spaced molecules that are known to occupy the same copper row.

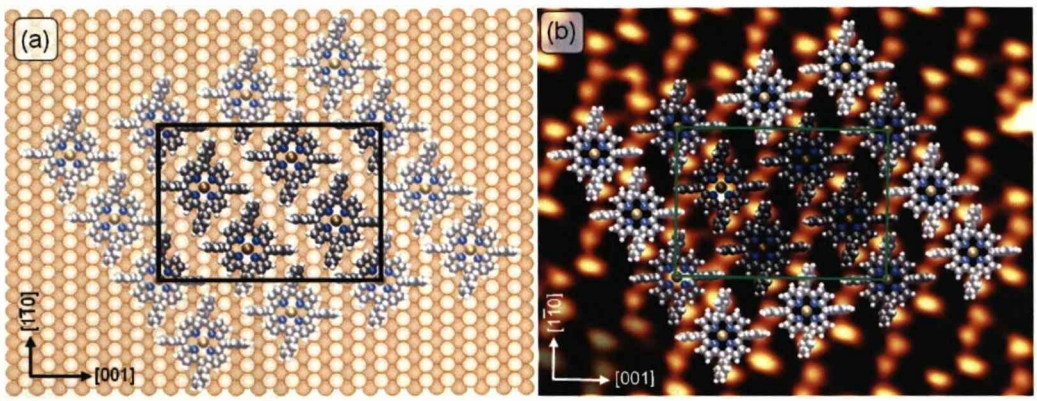

Figure 4.3-4. (a) A 4×4 matrix shows the 10×10 copper-aligned supercell for Structure 1. Image conditions: 126×70Å, I_T=0.49nA, V=670.5mV. (b) The real space model for (a). This supercell means a high accuracy calibration of the STM data can be performed by measuring large distances that are known to follow a single copper row.

There is some divergence in the agreement for negatively biased calculated STM images however but all features observed in the experimental STM data remain present across the entire range of the calculation – between ±1500mV (Figure 4.3-5).

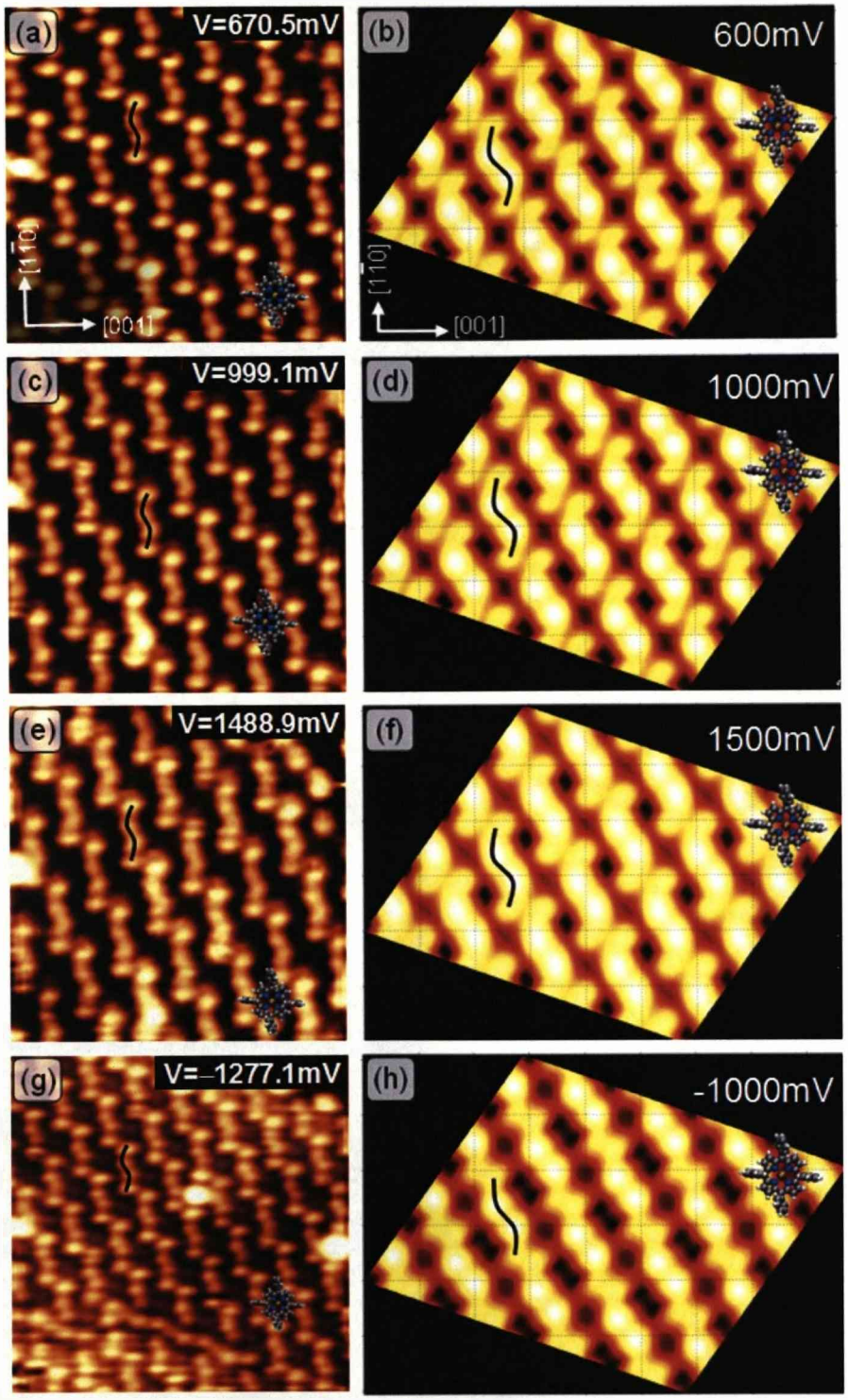

Figure 4.3-5. Agreement between experimental STM (a), (c), (e) and (g) and calculated STM (b), (d), (f) and (h) images. From the top, the experimental STM images were taken at V=670.5mV, V=999.1mV, V=1488.9mV and V=–1277.1mV. Tunnelling currents are in the range 0.26-0.34nA and I_T=–0.24nA for (g). The corresponding calculated STM images were calculated at 600mV, 1000mV, 1500mV and -1000mV respectively. There is good agreement across all positive biases but, although all the features remain present, the agreement is not as good for negatively biased images. Copper axes in (a) and (b) apply to the whole of their respective columns. Molecular conformation is assumed.

The calculated aspect ratio of 1.1, using the topmost hydrogen atoms from each phenyl ring, agrees with the value derived from STM images (Figure 4.3-6). It can be seen from Figure 4.3-1 that the deviation from square is a result of the different twist angles of the two pairs of phenyl rings and not from core macrocycle distortions.

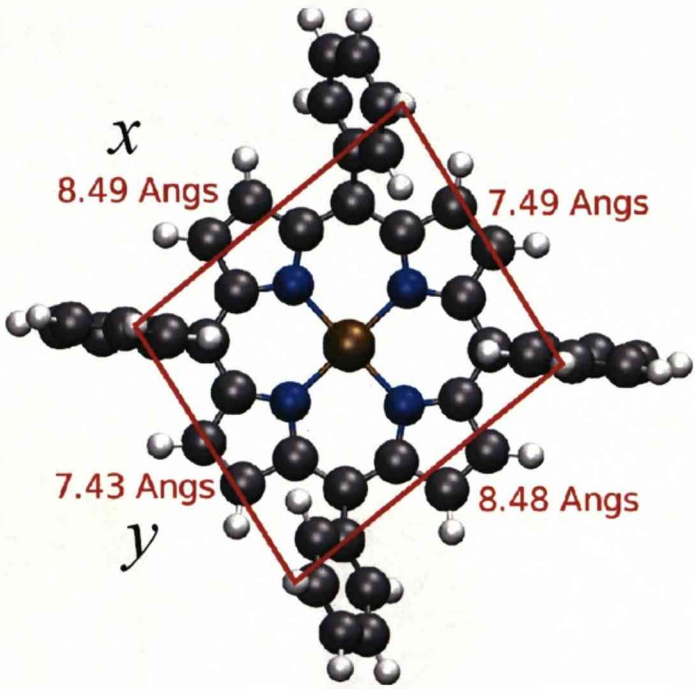

Figure 4.3-6. The calculated aspect ratio of Structure 1 Co-TPP agrees well with the experimentally determined value of 1.1.

The calculated energy cost to deform the molecule from its optimized vacuum conformation[32] to its adsorbed conformation within the self-assembled Structure 1 on Cu(110) is +229.7kJmol^{-1}. This is somewhat greater than the value estimated from Wölfle et al[32] of +187kJmol^{-1} and this discrepancy is expected primarily to be due to the incorporation of the copper surface into the calculations. The results of Wölfle *et al*[32] for Co-TPP are summarised below in Figure 4.3-7.

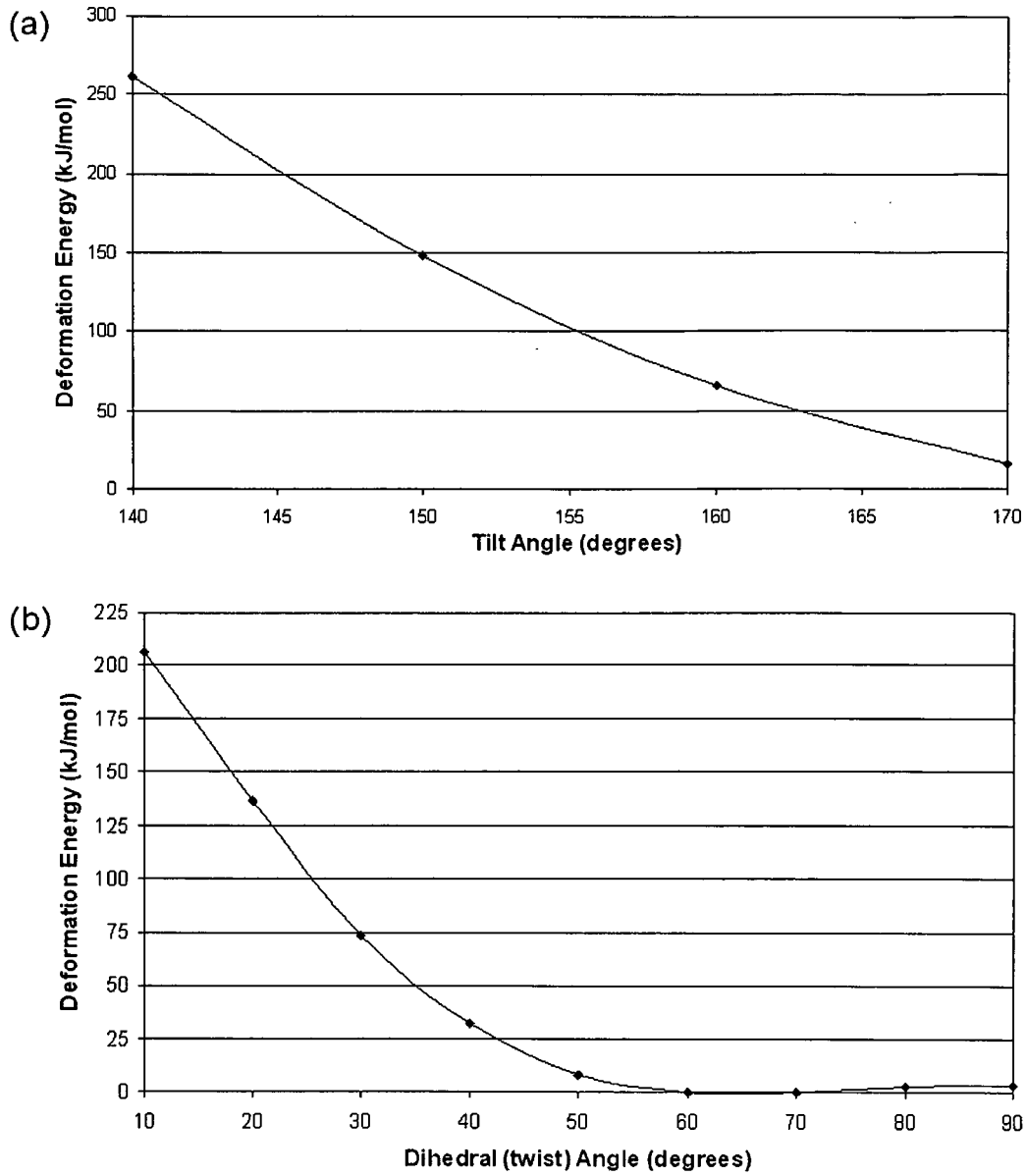

Figure 4.3-7. Plots of the Co-TPP deformation data of Wölfle *et al*[32] showing the energy costs of phenyl tilt and twist distortions. (a) Even minor tilting deformations have a significant energetic requirement, while twisting (b) of the phenyl groups is not as costly. Twists between 50 and 90° are energetically similar and are likely to occur in the gas phase also, with the minimum occurring at 60°.

In addition, a concomitant deformation of the copper surface occurs at a cost of +38.6kJmol^{-1}, leaving the total cost of deformation of the molecule and substrate as E_{COST} = +268.3kJmol^{-1}. The necessity to include a deformable substrate in theoretical approaches to energetic analyses of adsorbed porphyrins is clearly highlighted by the significant difference the addition of the surface reconstruction makes to the total cost. Importantly, there must be a substantial energy gain by the molecule-surface interaction

to afford this large deformational energy cost, as discussed in the next section.

4.4. Molecule-surface interaction

The nature of the attractive molecule-substrate interaction was examined by DFT, which shows an increase in electron density between the uppermost rows of copper atoms and both the cobalt atom and the macrocycle. This localisation of electron density between the molecules and surface stabilises the system, as is the case in a conventional covalent bond, and is also responsible for maintaining the planarity of the macrocycle. It should be noted that the nitrogen atoms of the macrocycle pyrroles play no part in the adsorption. A detailed analysis shows that, upon adsorption in Structure 1, the d_{z^2} molecular orbital (MO) becomes fully occupied. This eliminates the enhanced tunnelling pathway observed in STM studies of similar systems[26,37,77,78] and contributes to the lack of core structure in the STM data.

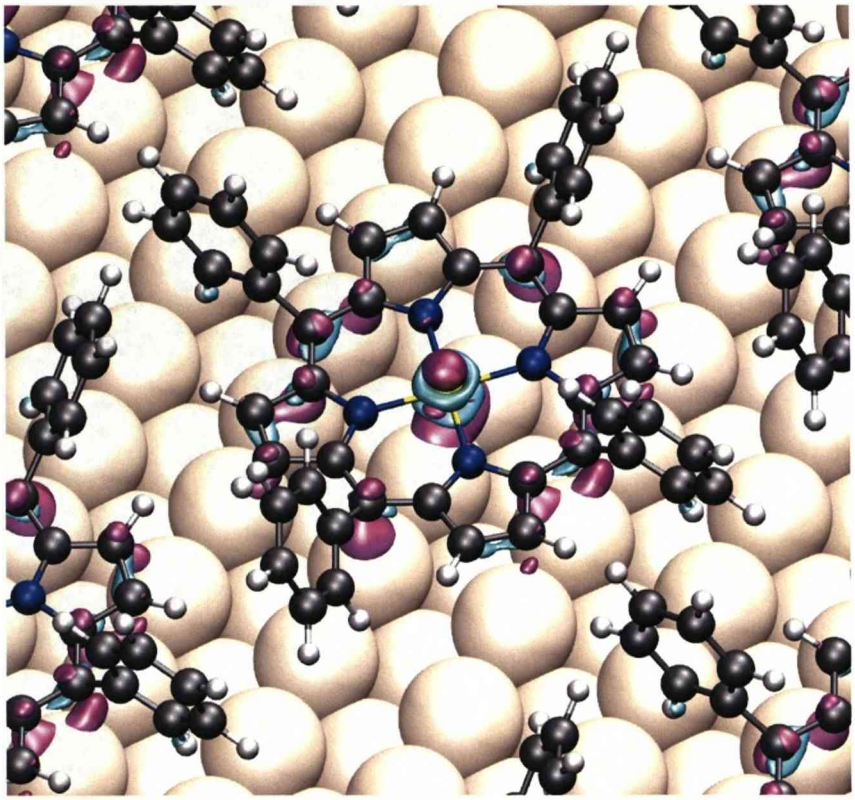

Figure 4.4-1. The interaction of MOs with the metal surface. The pink (light blue) areas show the increase (decrease) in electron density.

The electron transfer and the interaction of the MOs with the metal surface, as shown in Figure 4.4-1, give rise to strong chemisorption with both ionic and covalent character. These bonding interactions with the d_{z^2} and other orbitals are the source of the large attractive interaction energy, calculated at $E_{MOL\text{-}SUR}$ = –363.7kJmol^{-1}, between the isolated molecule and bare surface in the same deformed configurations as when the molecule is adsorbed. The large magnitude of $E_{MOL\text{-}SUR}$ more than recuperates the considerable energy cost E_{COST} = +268.3kJmol^{-1} calculated for the conformational deformations.

4.5. Intermolecular interaction

Structure 1 is constructed by an anisotropic network of intermolecular π–π interactions that occur between phenyl groups of adjacent molecules. The precise nature of the interaction is dictated by the intermolecular separations between molecules in the assembled structure, which in turn

defines two phenyl inter-centroid separations. The phenyl ring centroid is defined as the centre of mass of the carbon ring. In organised structures there are two such separations: one top-bottom (TB) (between the top and bottom phenyl groups), TB-1, and one left-right (LR) (between left and right phenyl groups), LR-1, as exemplified by the Structure 1 interactions in Figure 4.5-1.

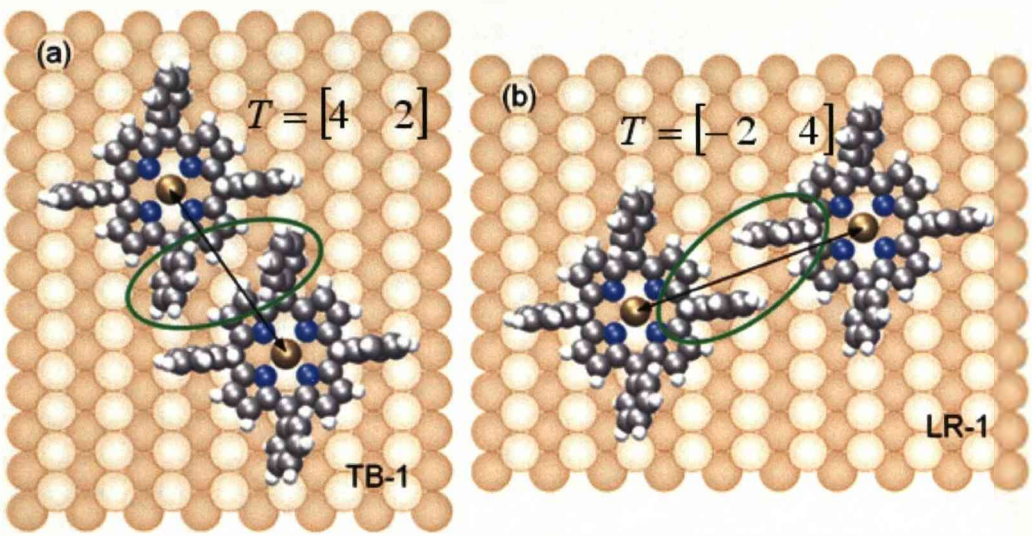

Figure 4.5-1. Phenyl inter-centroid separations in Structure 1. (a) The Top-Bottom (TB) and (b) Left-Right (LR) phenyl-phenyl interactions are shown. Mirroring the images would represent the opposite chiral domain without altering the definitions.

The benzene dimer has been used as a model system to estimate the energies of the π–π interactions, which are poorly described by DFT, between the phenyl groups in the Structure 1 domain. Due to the cost of wavefunction based calculations, there have been a very limited set of studies of non-equilibrium benzene dimer configurations similar to those present in this system. Contributions are estimated from work employing Coupled-Cluster calculations with Single, Double and perturbative Triple excitations {CCSD(T)}, which has produced highly reproducible results across several studies[105,107]. It should be noted that the estimates for the following contributions represent upper bounds of their magnitudes.

Attractive interactions between phenyl groups in Structure 1 occur in different configurations, and are classified as T, Parallel Displaced

(PD)[103,105,107] and combinative PD/T interactions, as shown in Figure 4.5-3b for the δ domain.

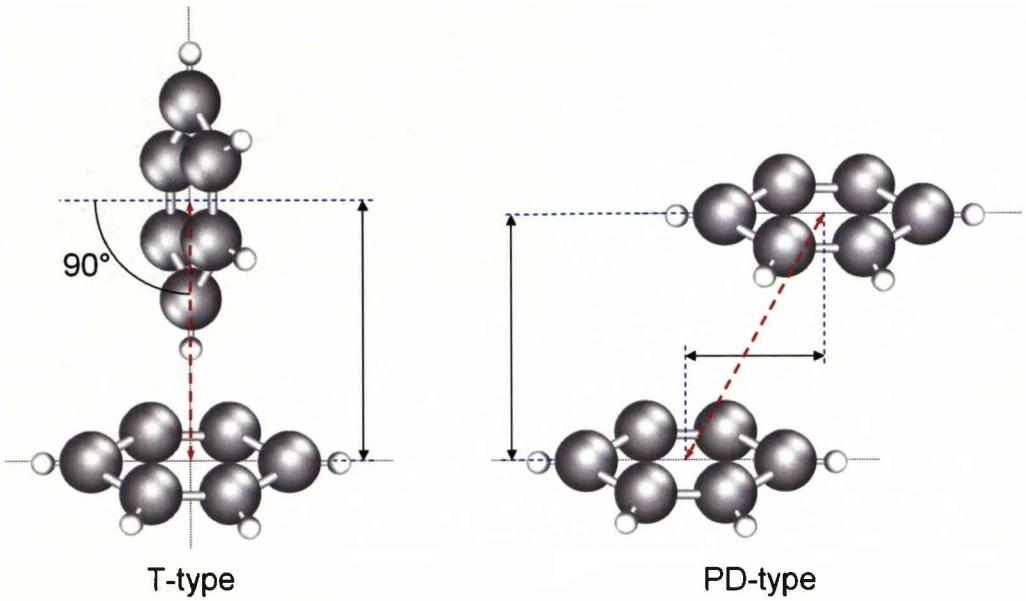

Figure 4.5-2. Intermolecular interaction types in Structure 1. The T-type interaction is defined by an axial separation and a 90° rotation of the ring plane about a mirror symmetry axis of one phenyl. The PD interaction is defined by an axial separation and a parallel offset (right).

The net interaction is maximised by involving each phenyl ring in two of the three interaction configurations, thus forming staggered rows of high interaction that are symbolised by the S-like structure shown in Figure 4.3-2 and Figure 4.5-3 below.

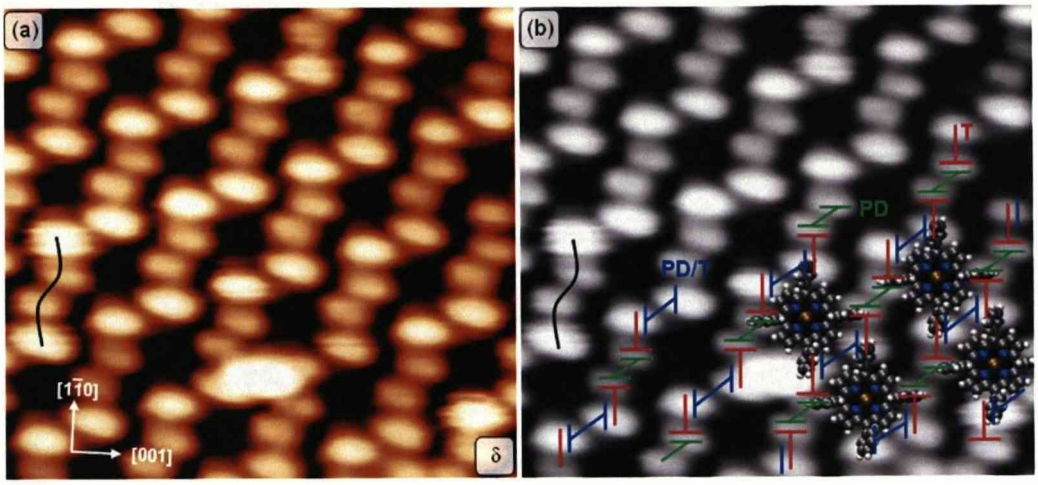

Figure 4.5-3. Intermolecular interactions in the δ domain of Structure 1. PD (green lines), T (red lines) and PD/T (blue lines) phenyl-phenyl interactions form lines of high interaction that correspond to the S-like structure indicated (cf. also Figure 4). Image conditions: 58×56Å, V = 650mV, I = 0.52nA.

Estimates of the interaction energies have been obtained by calculating inter-centroid distances and comparing to benzene dimer data[103,105,107]. The phenyl ring centroid is defined as the centre of mass of the carbon ring. Calculated at 4.9Å, the inter-centroid separation for the T configuration of phenyls in Structure 1 (red lines in Figure 4.5-3(b)) is identical to the minimum energy separation for benzene dimers[103,105,107], however, the combined effect of both tilt and twist angles and the relative ring positions on this interaction is unknown. The T configuration in the work of Sinnokrot *et al*[105] and Tsuzuki *et al*[107] is assumed to provide an adequate approximation to the T configuration in Structure 1 with an energy gain of E_T = –10.4kJmol^{-1} per interaction. There is expected to be a repulsive component of the T-type interaction that would be manifest between the phenyls and macrocycles of adjacent molecules. The inter-centroid separation for the PD configuration (LR-1) (green lines in Figure 4.5-3) of 5.4Å is greater than the 3.75Å quoted for the optimised configuration[105,107]. From the work of Tsuzuki *et al*[107], the total interaction energy from PD type configurations is estimated at E_{PD} = –2.5kJmol^{-1}. The LR-1 interaction may, therefore, be the most optimised overall, given its relative magnitude and lack of any repulsive component. This may explain the general elongation of domains along the direction of the intermolecular separation for this interaction. This interaction is also present throughout all of the observed

structures, possibly for the same reason. This will be discussed in a later section. All other phenyl-phenyl configurations have a significantly larger inter-centroid distance and their interactions are almost negligible. For instance, the PD/T configuration (blue lines in Figure 4.5-3), has an inter-centroid separation of 7.6Å that is far greater than the energetic minimum for either the PD or the T configuration. At this distance both the PD and T configuration have a maximum attractive interaction energy[105] of $-1 kJmol^{-1}$.

The T-type interaction becomes a dominating feature in situations where an associated PD interaction cannot form. In such cases, the line of high interaction, indicated by the S-like structure in Figure 4.5-3, is broken and the distribution of electron density becomes confined to a single interaction. This predominantly occurs at domain edges, as shown in Figure 4.5-4.

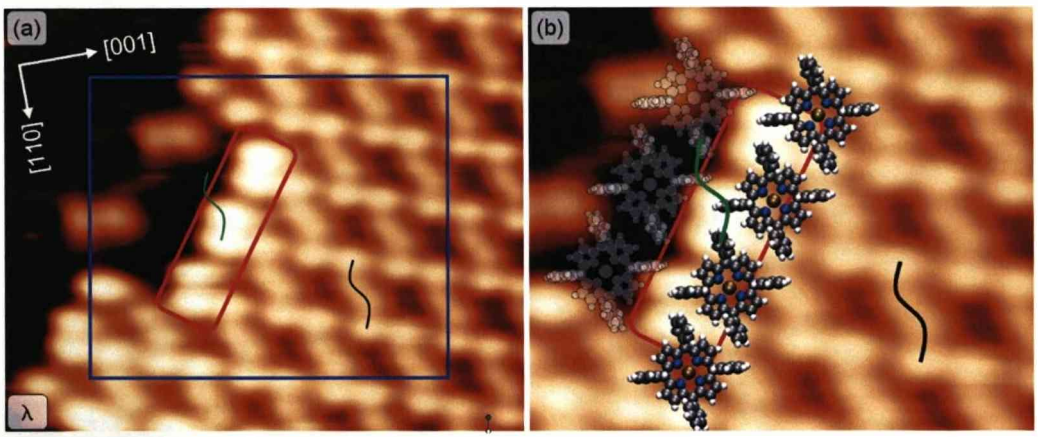

Figure 4.5-4. Disruption of the line of high interaction results in transference of electron density to the T-type interaction along a domain boundary. The three bright features on the domain boundary in (a) (highlighted in red) are representative of T-type interactions. (b) The area indicated by the blue box in (a). Both the positions of molecules within the domain (solid) and the positions of the molecules that would form the PD interaction (wire frame) are shown. Copper axes in (a) apply to both images. Molecular conformation is assumed.

Thus, the total energy gain from the π–π interactions involved within the self-assembled Co-TPP/Cu(110) structure is obtained using Equation 4-1.

$$E_{PH-PH} = 2E_T + E_{PD} + E_{PD/T} \qquad \textbf{4-1}$$

Using the estimates above the total energy gain from intermolecular interaction is calculated to be $E_{PH\text{-}PH}$ = –24.3kJmol^{-1}. This is of roughly the same magnitude as has been observed previously for just T-type interactions between porphyrin molecules in a highly ordered array[54]. As will be discussed in conjunction with isolated molecule adsorption (Chapter 7), this energy gain is responsible for the preferential domain formation at room temperature.

4.6. Net energy balance

By substituting the interaction energies derived in the previous sections into Equation 4-2 below the net interaction energy E_{NET} (or the negative adsorption energy) can be calculated. This is defined as the difference in energy between the adsorbed system and the fully relaxed isolated molecule and bare substrate:

$$E_{NET} = E_{MOL-SUR} + E_{PH-PH} + E_{COST} \qquad \textbf{4-2}$$

Using the energies from our calculations, the net interaction energy for Structure 1 is E_{NET} = –363.7kJmol^{-1} – 24.3kJmol^{-1} + 268.3kJmol^{-1} = –119.7kJmol^{-1}. Disregarding the contribution from intermolecular interactions, the substantial gain from the macrocycle's interaction with the copper substrate alone recuperates by far the total cost of both molecule and substrate deformations. In fact, this gain is so considerable that even greater molecular deformations would be accessible and it is assumed that strong molecule-substrate interactions have the potential for unlocking even more severe conformational distortions and, thus, different and unexpected chemistries for other porphyrin/surface systems. Indeed, for systems in which a considerable molecular deformation has already been characterised[23,31], the underlying molecule-substrate interaction and its implication on the energy balance is vital to explain the observations.

4.7. *Chirogenesis*

Chirogenesis – the induction of chirality from intrinsically achiral components – is observed within Structure 1 that occurs on both local and supramolecular levels. The distinct pattern of phenyl-phenyl interactions around individual molecules in the organized structure, as shown in Figure 4.7-1, explains the induction of supramolecular chirality: The directionality of these interactions, indicated by the green and blue lobes in Figure 4.7-1, determine whether the domain orients at +20°±2° or –20°±2° with respect to the Cu[001] axis, thus the repeat mesh of the organization breaks both mirror-symmetry planes of the underlying Cu(110) surface.

From the DFT calculated molecular conformation (Figure 4.3-1), it can be seen that the twisting deformations of the phenyls break the local mirror symmetry of the system. The twist is small for the pair of phenyls aligned along the [001] rows, however, the substantial and matching (anti)clockwise twists of the second phenyl pair endow each adsorbed molecule with a distinctive propeller-like conformation and lead to a strong expression of chirality at the individual molecule level. Prior to 2D assembly, the phenyls aligned with the Cu[1-10] axis are presumably free to choose between energetically equivalent twists of about ±65° to accommodate the substrate corrugations. However, upon the formation and optimisation of all PD, PD/T and T interactions, the phenyl pairs are forced to twist in the same sense, i.e. clockwise or anticlockwise, as repulsive forces between molecules are minimised. This pins each molecule in the well-defined propeller-like conformation shown in Figure 4.3-1; signalling the induction of molecular, or local, chirality. Symmetry breaking by the adsorption of achiral porphyrins has only been observed in a few other systems[22,73,89]. To our knowledge, this is the first report of the detailed origins of supramolecular and local chirogenesis in such systems.

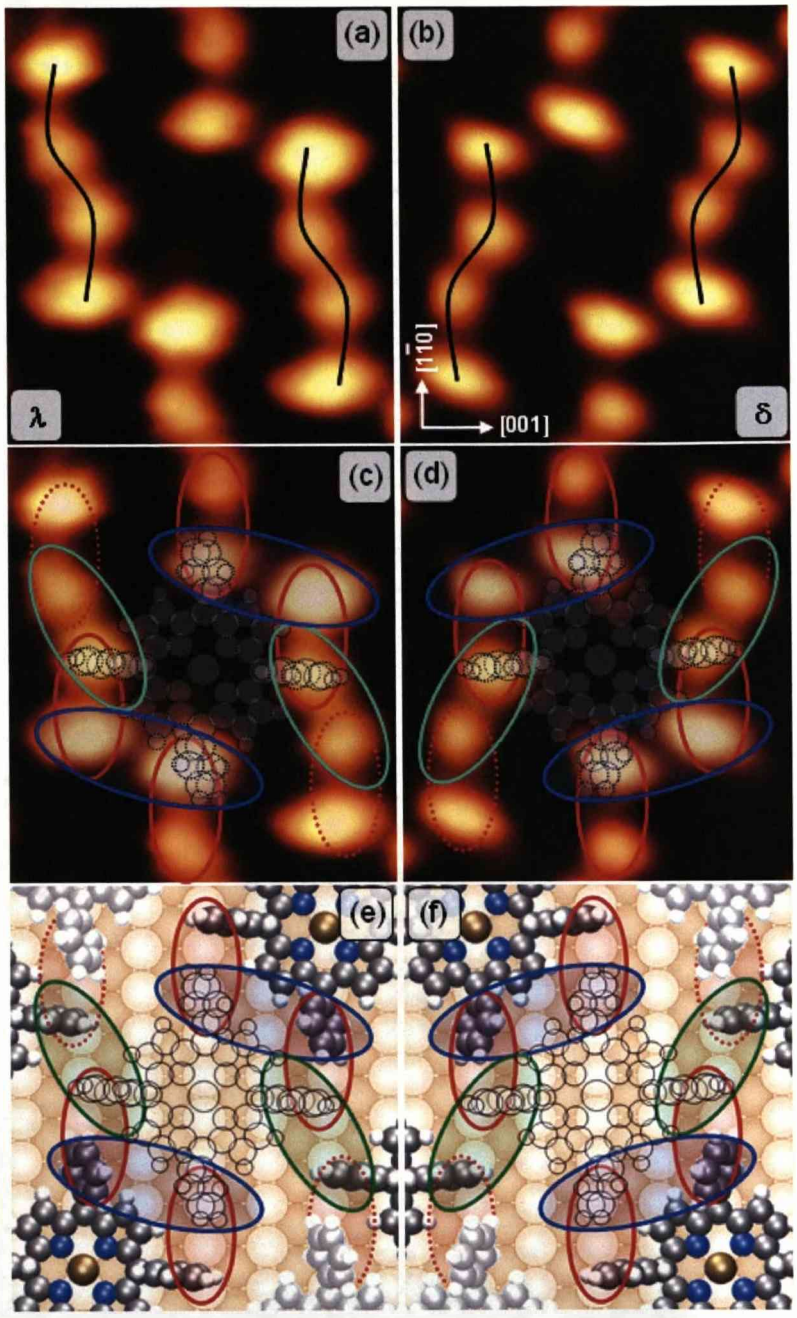

Figure 4.7-1. Expression of chirality in Structure 1. Enlarged sections of STM images from Figure 4.1-1b and c show individual molecules from (a) λ and (b) δ domains. Lines of high interaction are indicated. (c) and (d) overlay the PD interactions as green lobes, PD/T interactions as blue lobes and T-type interactions as red lobes for single molecules in both domains. Dotted red lobes are T-type interactions that are not associated with the central molecule. The same interactions are shown on the real space structures (e) and (f). The copper axis in (b) applies to all figures.

4.8. *Image artefacts*

Scattered throughout the data on Structure 1 are features that do not correspond to normal Structure 1. These take the form of bright protrusions in the STM data and occur in two configurations, shown below in Figure 4.8-1.

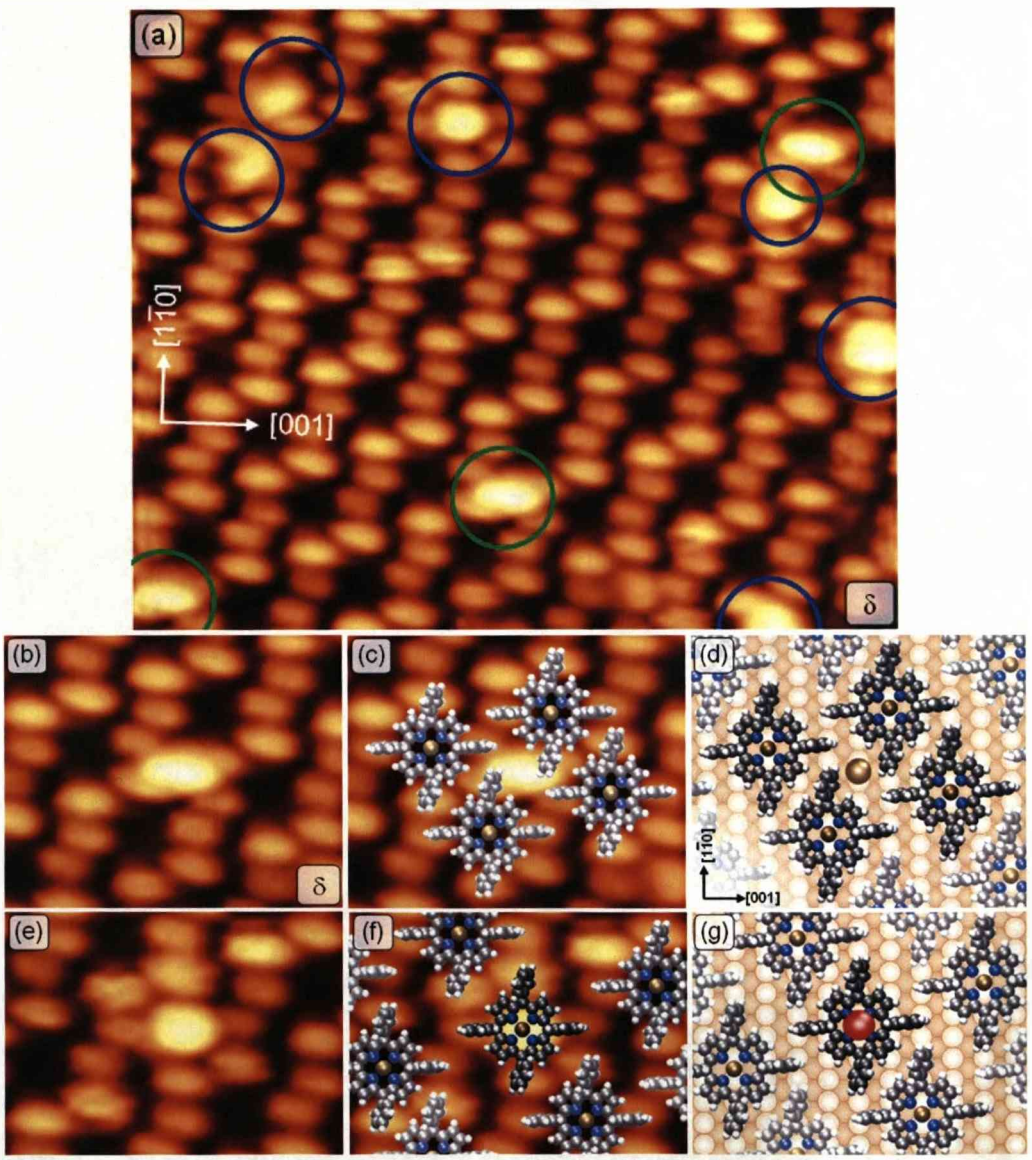

Figure 4.8-1. Artefacts in Structure 1 occur randomly throughout the STM data. (a) Two types exist that are shown by green and blue rings. 97×87Å, V=650mV, I_T=0.52nA. (b-d) The most common type, shown by the green rings in (a), suggest the possible presence of adatoms between molecules in the structure. The real space structure (d) shows the short-bridge adsorption site as the most likely position of the feature. (e-g) The second type is a bright protrusion at the core cobalt position. This indicates axial ligand coordination, possible by atmospheric oxygen, shown in red in the real space image (g). Molecular conformation assumed in (f). Copper axes in (a) apply to all but (d) and (g), where the axes in (d) apply.

There are a number of candidate atmospheric molecules that could form interactions with the core cobalt atom to form the features shown ringed in blue in Figure 4.8-1, atmospheric oxygen in particular, but at present, the coordinated species is unknown. The features ringed in green are expected to be copper adatoms, as there is evidence for adatoms locating at the short-bridge site[128] on copper surfaces.

CHAPTER 5

Higher-order and distorting structures

In addition to Structure 1, there are two other highly organised structures and several complex formations that are produced by Co-TPP on Cu(110). This chapter details their characteristics.

5.1. The 2-molecule unit cell chiral organisation (Structure 2)

The self-assembly of Structure 2 occurs when Co-TPP is dosed at high sublimation rates, i.e. using the greatest doser power. Like Structure 1, Structure 2 is prone to defects (section 5.3) but its integrity is seen to increase with higher coverage. This structure occurs in two chiral domains, denoted λ and δ, and has main directions oriented at $\pm 22° \pm 1°$ to the crystallographic axes of the underlying copper (Figure 5.1-1). Chiral micro-domains of Structure 2 have been observed.

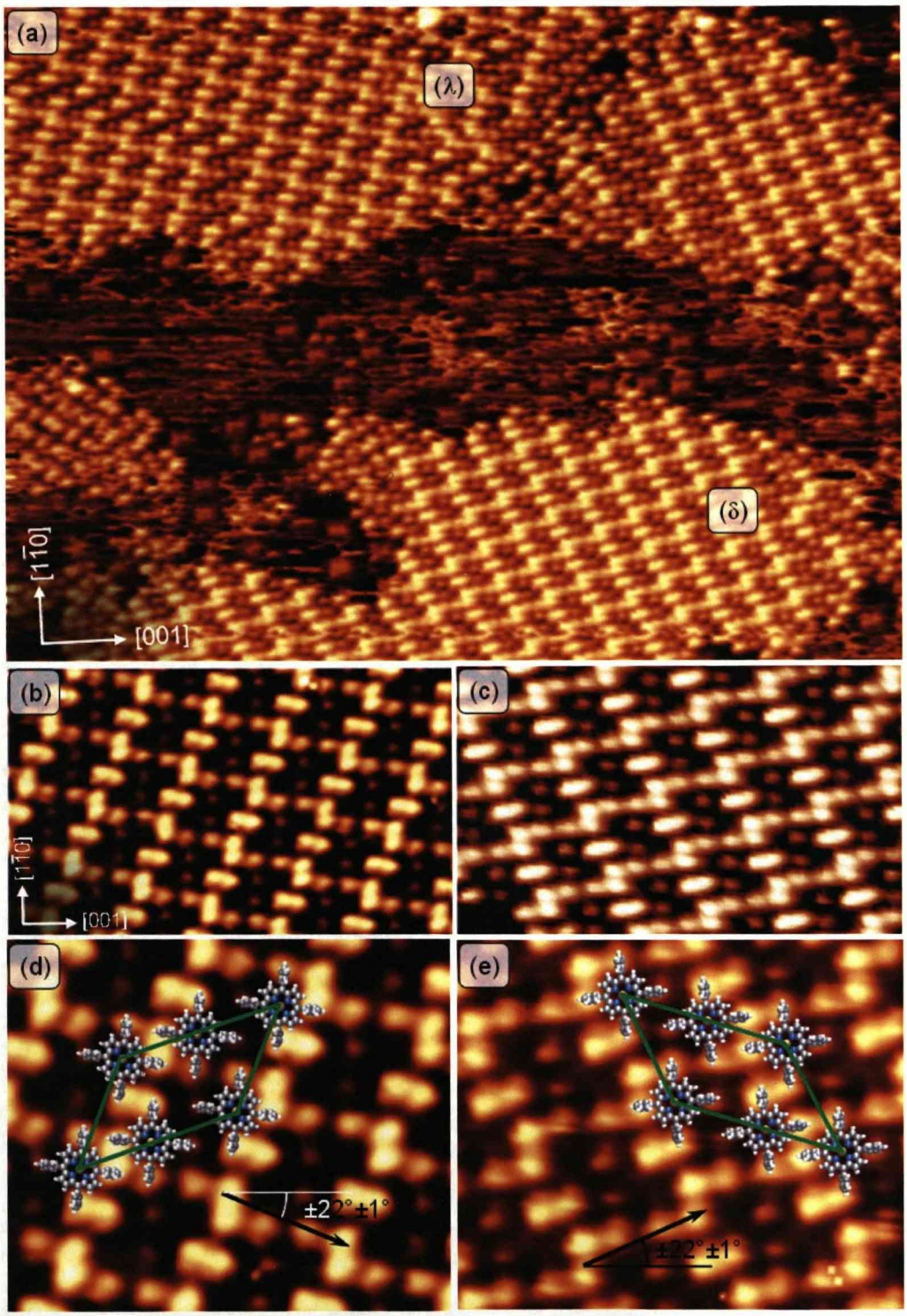

Figure 5.1-1. (a) λ and δ domains of Structure 2. (b) and (c) are close up images of Structure 2. Copper axes in (b) apply to (c) also. (d) and (e) the unit cells of the λ and δ domains of Structure 2 respectively. Spots represent contributions from the phenyl rings. The main directions of the domain with respect to the Cu[001] direction are shown on the images by black arrows. Molecular conformation is not accurate. Image Conditions (a) 447×460Å^2, I_T=0.21nA, V=611.3mV, (b) 130×83Å^2, I_T=0.48nA, V=1250mV, (c) 130×84Å^2, I_T=0.41nA, V=781.5mV, (d) 68×61Å^2, I_T=0.56nA, V=1250mV, (e) 68×61Å^2, I_T=0.41nA, V=781.5mV.

Structure 2 is observed forming, growing and disintegrating in the presence of other domains, although a stable and pure phase can be achieved at room temperature. Heating the surface breaks up domains from the edges, as with Structure 1. Figure 5.1-1 shows images of the two chiral domains of the structure, from which it can be seen that Structure 2 exhibits the same pattern of dark patches and bright spots in the STM data as Structure 1. It is, therefore, deemed a reasonable assumption that both structures have the same adsorption site and similar conformational and electronic properties. It should be noted that precise conformations of Structure 2 molecules are not available at the time of writing due to computational limitations. Molecules have therefore been positioned on the STM images in a way that accommodates the phenyl groups whilst retaining the molecule's adsorption site and molecular dimensions. From the STM images, it is found that Co-TPP molecules in Structure 2 form a highly ordered assembly with a unit cell that contains two molecules and is described by the matrices $G^{\lambda} = \begin{bmatrix} 4 & 7 \\ -7 & -2 \end{bmatrix}$ and $G^{\delta} = \begin{bmatrix} -7 & 2 \\ 4 & -7 \end{bmatrix}$[14]. LEED data on Structure 2 has been obtained by Smith[61] (Figure 5.1-2), and spots in the data fit well with the simulated images, however, a commensurate unit cell matrix cannot be established from the LEED data alone for Structure 2. A commensurate unit cell is assumed.

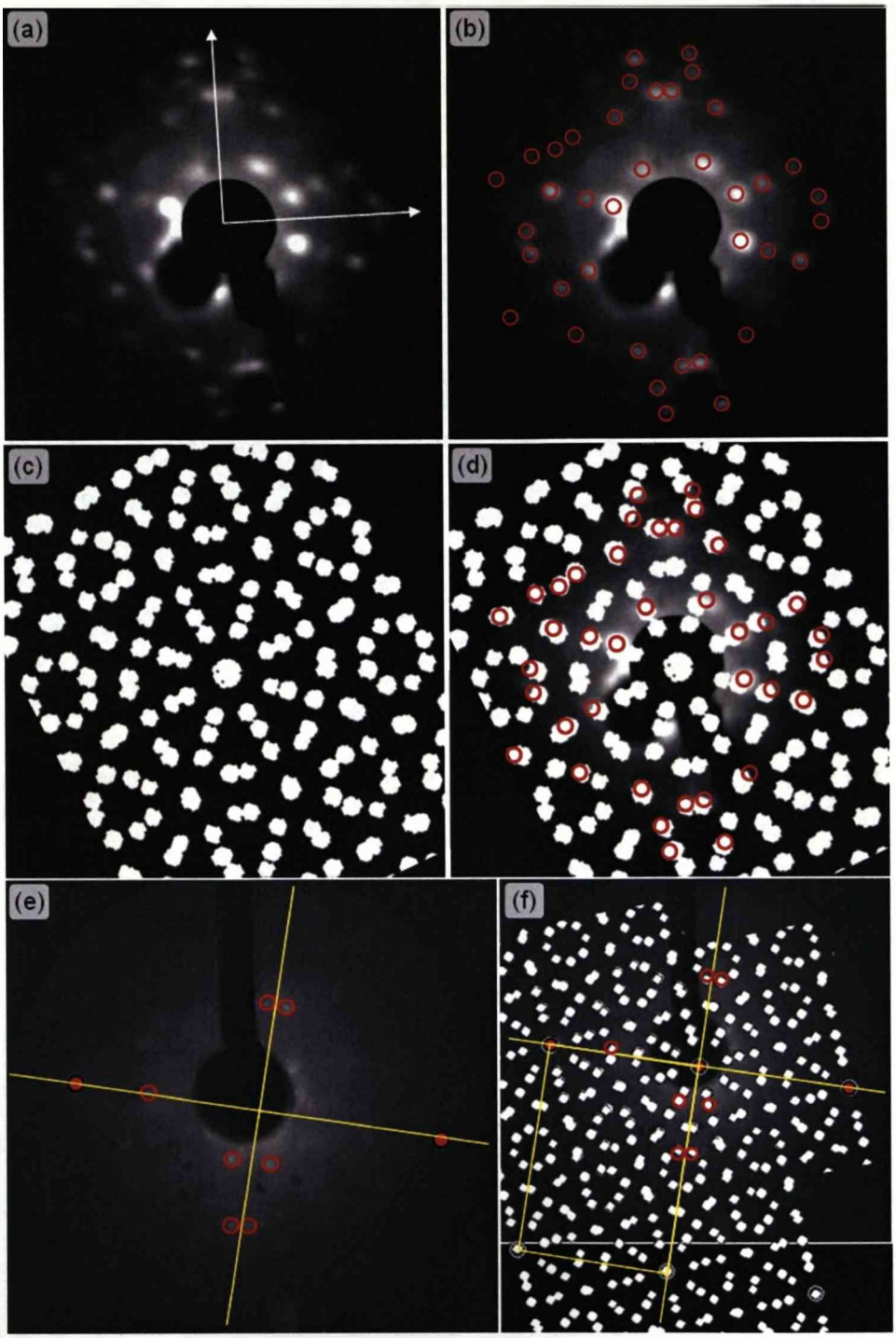

Figure 5.1-2. (a) Experimental LEED data for Structure 2, taken by Smith[61]. The beam energy is unknown but is around 23eV. (b) shows the observed spots in (a). (c) the simulated LEED pattern for Structure 2, with contributions from both chiral domains. (d) Good agreement is observed between the simulated and experimental STM data. All the observed spots (ringed red) correspond closely to spots in the simulation. (e) Experimental LEED data taken at 34eV. Two surface spots are visible and again all observed spots agree with simulation. (f) Despite good agreement, there are not enough spots observed with the surface spots to conclusively obtain a reciprocal space matrix. The image has been extended artificially to draw the unit cell.

The expected commensurability of the overlayer is indicated in the model in Figure 5.1-3(a), which has been constructed as a modified Structure 1 due to the strong similarities between the structures. This also assumes a short-bridge adsorption site, which has proved impossible to conclusively attain due to the disordered nature of the surface phase containing both Structure 1 and 2. The model's dimensions and angles are accurate to the calibrated STM images to within 2% and 2° respectively and have therefore allowed a retrospective calibration of STM data, shown in Figure 5.1-3(b) and (c), using the exact distances between molecules that are situated on the same copper row. This calibration does not represent a copper-aligned unit cell (Figure 5.1-3b), and the measurement must begin at the lower molecule of the unit cell (ringed green in Figure 5.1-3c). Note, the pattern of two molecules up(across) then one molecule across(down), two up(across) then one across(down) and finally one molecule up(across) gives the next molecule adsorbed on the Cu[1-10](Cu[001]) row. The 29 Cu[1-10] lattice spaces gives an intermolecular separation of 73.95Å and the 21 Cu[001] lattice spaces gives an intermolecular separation of 75.6Å. A fully commensurate copper-aligned unit cell of (41×42) lattice spaces (104.55×151.2Å) exists that can also be used for an extremely accurate calibration that is independent of the starting molecule. The 41 is made up by the large 29 plus the shorter 12-row measurement shown by the short blue line in Figure 5.1-3c. The calibration of the data presented here is simplified by the image axes being very close to the copper axes, i.e. simply altering the *x* and *y* of the image without a rotation or skew induces only a minimal error in the calibration that can be adjusted easily to achieve an accuracy of less than 2% in both main crystallographic directions.

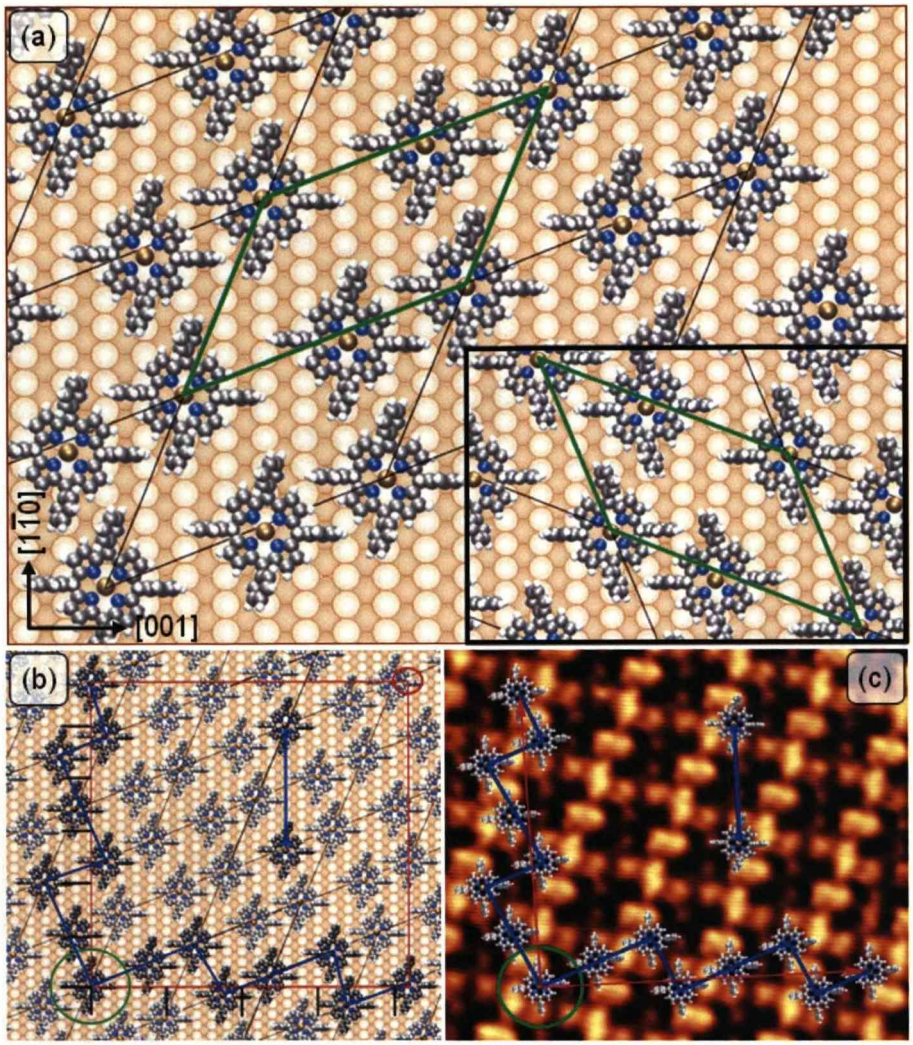

Figure 5.1-3. (a) Model showing the unit cells of the λ domain of Structure 2. The δ domain is shown inset. The overlayer is expected to be fully commensurate with the substrate. Molecules are therefore shown with the same adsorption site as Structure 1. (b) The model has allowed easy calibration of STM images by highlighting molecules lying on the same copper rows. (c) Calibrating an STM image. The copper rows are shown by red arrows. The shorter distance for calibration of the [1-10] row is also shown, and consists of 12 lattice spaces. Image conditions I_T=0.56nA, V=1250mV. Molecular conformation is that from the Structure 1 calculation, except in (c) which shows an arbitrary conformation and orientation. Molecular dimensions have been reduced for clarity.

A comparison between the unit cells of Structure 2 and those of Structure 1 shows that Structure 2 is only marginally less dense than Structure 1, with 20.5 surface atoms for each molecule. The high density of the assembly is mainly due to strong phenyl-phenyl interactions creating lines, or 'spines,' through the structure that consist of alternating shorter-range (compared to Structure 1 and the TB-3 interaction described below) LR

and TB interactions (Figure 5.1-4). LR and TB interactions have been defined in Chapter 4.

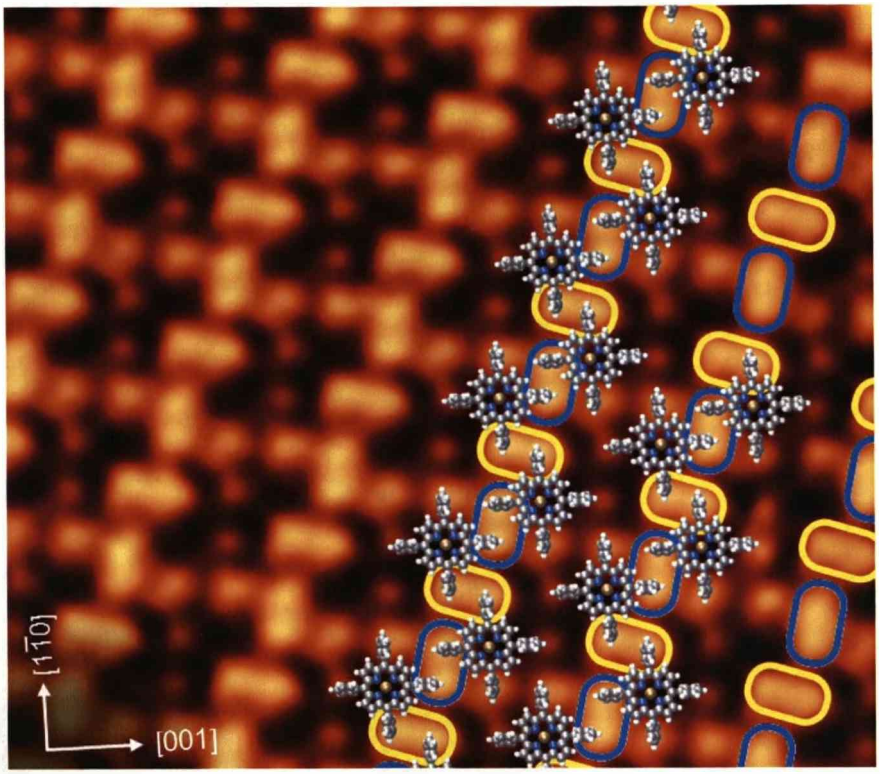

Figure 5.1-4. Spines of high intermolecular interaction in Structure 2 create a high density self-assembled structure. Close range LR (ringed blue) and TB (ringed yellow) interactions make up the spines. Image conditions 107×96Å^2, I_T=0.56nA, V=1250mV. Molecules are scaled down for clarity and are shown in an arbitrary conformation.

The spines arrange side by side to form the 2D structure, forming long-range interactions, and thus reducing the overall molecular density. The spines themselves show greater contrast than other features, and this creates the highly distinctive pattern of bright and dark features observed in the data.

An interesting feature of this structure is that there is only one molecular conformation and interaction pattern despite there being two molecules in its unit cell. To achieve the configuration of the second molecule in the unit, the first must be rotated by 180°, as shown in Figure 5.1-5.

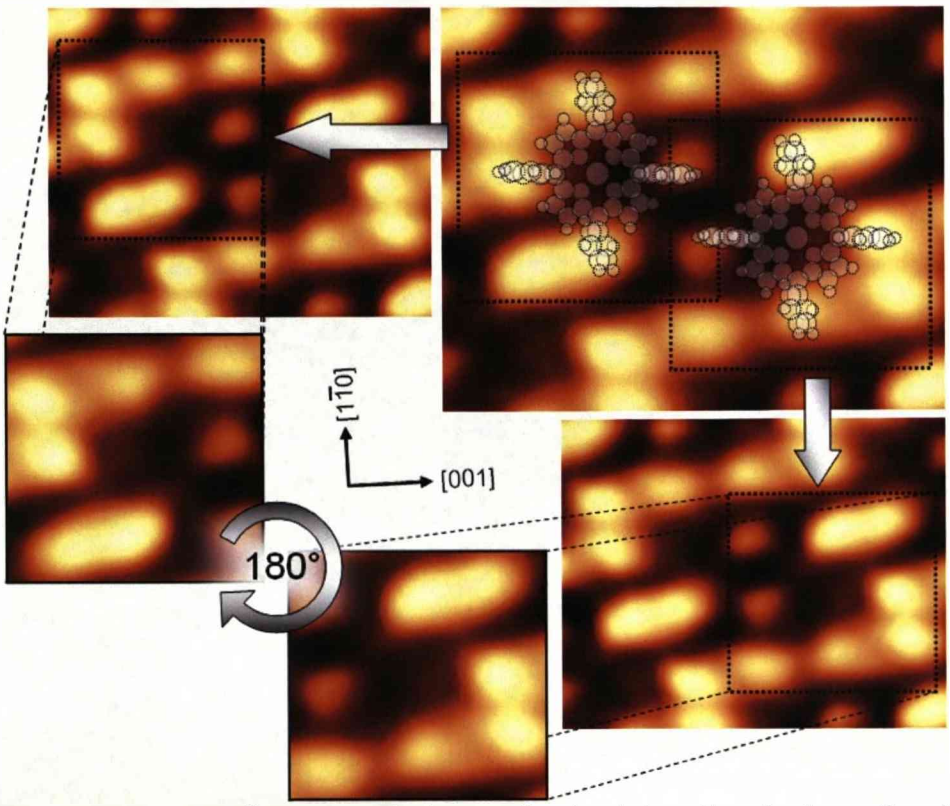

Figure 5.1-5. Rotationally symmetric intermolecular interaction in the unit cell of Structure 2. A rotation of 180° is required to change one form into the other. The original image with overlaid molecules is shown at the top-right. Molecular conformation is arbitrary.

The interactions in Structure 2 are described below and shown in Figure 5.1-6, which also shows the positions of each type on the STM image.

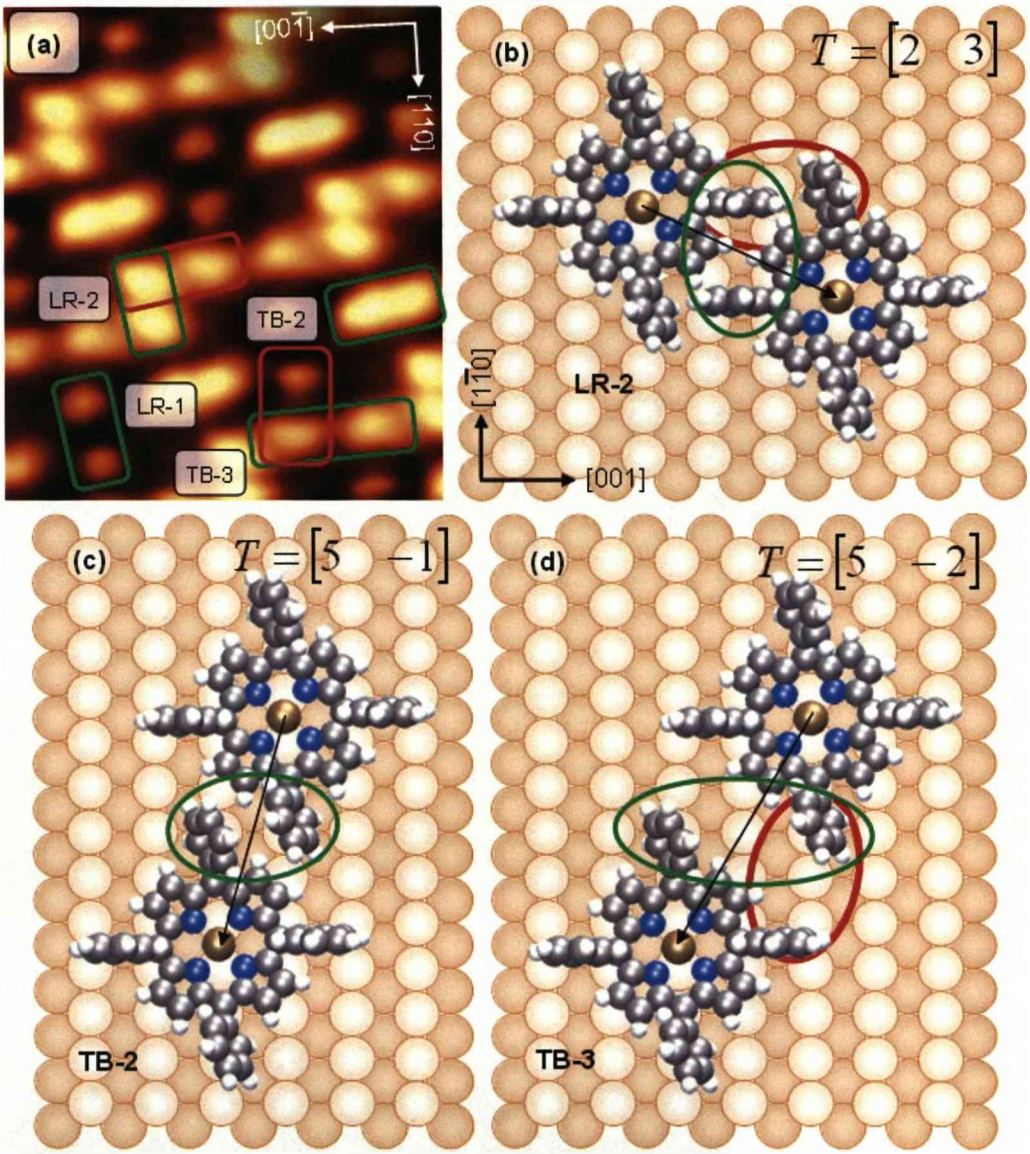

Figure 5.1-6. Intermolecular interactions in Structure 2. (a) The four main interaction types shown green and a secondary T-type in red. The spine-joining LR-1 interaction, constituting the dim spots in the dark region, has been characterised already in section 4.5. Image Conditions 39×48Å^2, I_T=0.43nA, V=1238.7mV. (b) The spinal LR-2 interaction (with matrix notation) and weaker T-type interaction (red), (c) the spinal TB-2 interaction (with matrix notation) and (d) the spine-joining TB-3 interaction (with matrix notation). Molecules in the models are rotated by 6° from the Structure 1 orientation to minimize overlap between phenyl and pyrrole groups of adjacent molecules. This therefore does not present an accurate representation of the true system.

The LR-2 and TB-2 interactions, being the close proximity bonds that form the spine, are unique to the phase and have phenyl-phenyl separations measured from the STM data of 2.6Å±0.3Å. As with intermolecular interactions in other structures, the bond itself is expected to alter the

observed position of the phenyls, meaning these measurements could differ from the real inter-centroid separation of the phenyls. In the case of the LR-2 interaction, the model (Figure 5.1-3) indicates that the electron density is situated entirely between the phenyl rings, whose inter-centroid separation is roughly 5Å. The expected twisting of the TB-2 phenyls gives them a separation of roughly 4Å in the model, again suggesting that the interaction itself affects the STM images. Regardless of the interpretational ambiguity in the measurements, these interactions nevertheless are close range and it is therefore likely that some conformational adaptation would have to occur in order for phenyl and pyrrole overlap and also steric repulsion to be avoided. This adaptation has been created artificially in the model with a 6° rotation of the molecules but the adaptation could be in the form of macrocycle deformations and/or a rotation. According to the model of Figure 5.1-6(b), a consequence of these changes is that the phenyls involved with LR-2 bonds have a T-type interaction (Figure 4.5-2) with phenyls of the TB-3 bond. The model's prediction is corroborated by the experimental data, although the discernibly reduced electron density at the T-type indicates a substantially weaker interaction than the LR-2[107]. The TB-3 interaction is imaged weaker still, with even less localised electron density. The STM data suggest the LR-1 interaction is different in Structure 2 than in Structure 1. The protrusions are relatively weak in Structure 2 despite the same intermolecular separation. This implies that the electronic structure of the participating phenyls is different in the two phases. This is supported by STM data collected under other imaging conditions, from which it can be seen that the electronic structure is significantly different to that of LR-1 configuration in other phases (Figure 5.1-7). Also from Figure 5.1-7, there can be seen a feature imaged at the bottom phenyl of the TB-3 interaction that is highlighted by the blue dotted ring in (c). It is unclear what it represents at the present time. There is no corresponding feature at the other involved phenyl.

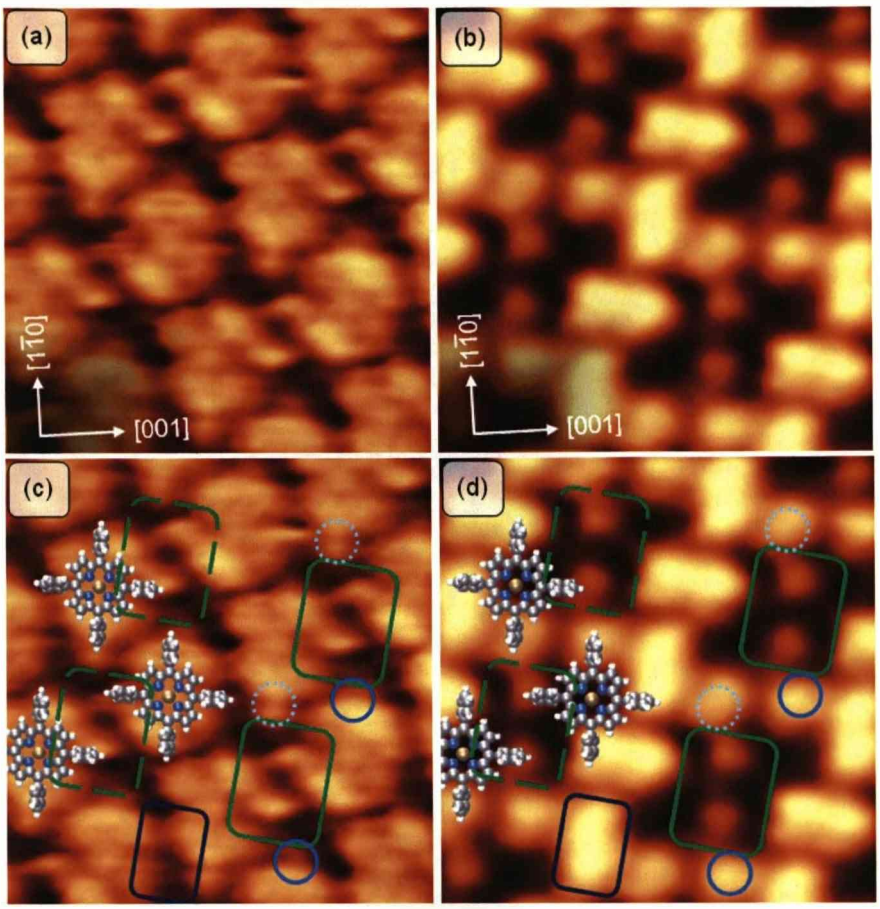

Figure 5.1-7. (a) and (b) STM tip effects reveal the Porphyrin core structure and the interaction structure for the same areas. (c) and (d) Distinct electronic features are observed at the weak LR-1 (green boxes) and long-range TB-3 (blue dotted rings) interactions in Structure 2. Dark blue rings represent the location of the other phenyl of this TB interaction. Interestingly, there is little or no feature at this location. The dark blue box represents the shorter-range LR-2 interaction. All images are 43×48Å^2 with conditions (a) and (c) I_T=0.49nA, V=1250mV and (b) and (d) I_T=0.40nA, V=1250mV.

5.2. The 4-molecule unit cell racemic organisation (Structure 3)

Structure 3 is an anomalous phase that is sporadically observed across the middle range of dose currents. Its characteristic feature is a distinct herringbone pattern (Figure 5.2-1(a)). Structure 3 is yet to be observed as a pure surface phase despite it rarely being distorted by transition or other structures (see section 5.3). A nearly pure phase was observed after a 45s dose at 1.45A, which consisted of small scattered domains. When left for a period of roughly 12hrs the small domains

coalesced to form larger structures. The addition of more Co-TPP molecules created regions of Structure 1.

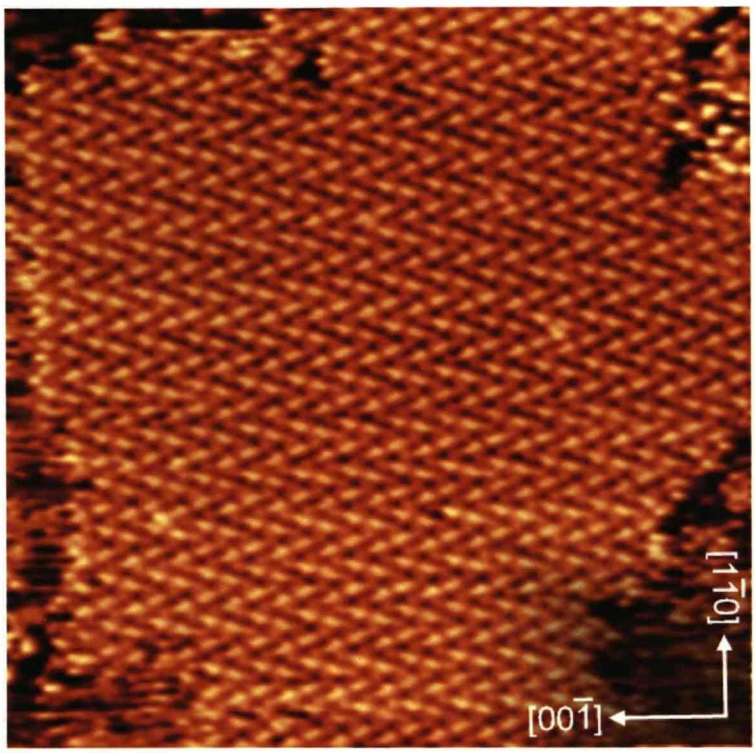

Figure 5.2-1. The distinct herringbone pattern of Structure 3. Image Conditions: 451×440Å^2, I_T=0.48nA, V=1250mV.

When Structure 3 molecules are imaged by STM, they show the same response to the applied bias as Structure 1. STM images are also comprised of a similar pattern of bright and dark features, strongly suggesting that the short bridge adsorption site is maintained and that the same electronic and topographical features make up the structure. The phase also exhibits a disintegration of the domain, and not the molecules themselves, on annealing. This structure has, therefore, been modelled as a modified Structure 1 (Figure 5.2-2), as with Structure 2. The model's dimensions and angles are accurate to the calibrated STM images to within 2% and 2°, respectively, but molecular conformation is assumed as there has been no computational study on this assembly. The model has allowed a retrospective calibration of STM images that is consistent with the original calibration for Structure 3.

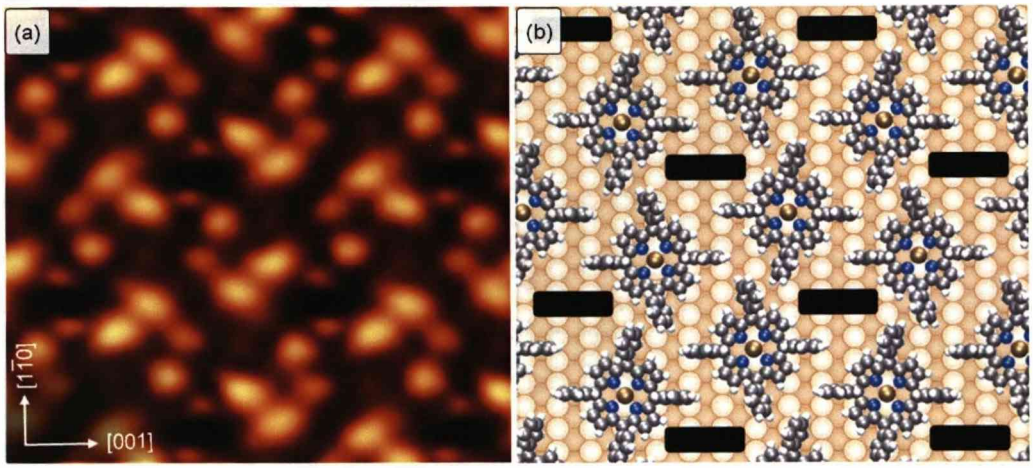

Figure 5.2-2. Structure 3 has been modelled as a modified Structure 1. (a) The original STM image. Image Conditions: 57×52Å^2, I_T=0.36nA, V=1238.7mV. (b) The model uses a preliminary calculated conformation for Structure 1 and two mirror forms of molecule have been used to avoid overlap. The short-bridge adsorption site and molecular conformation of Structure 1 has been retained.

The model shows good agreement with the STM images and it has therefore been used to determine the unit cell. Using standard convention[14], Structure 3 is described by a single unit cell, $G = \begin{bmatrix} 12 & 0 \\ 0 & 8 \end{bmatrix}$ or (12×8), that aligns with the crystallographic axes of the substrate and consists of four molecules. The unique feature of this phase is that, despite requiring only one unit cell to describe the entirety of the structure, the single cell can be tiled from two separate and meaningful locations on the overlayer to do this, where the corner of one represents the centre position of the other. At these corner and centre positions, Structure 3 features empty regions that reduce the overall molecular density to 24 surface atoms per molecule, the lowest of the three main structures. The two cell positions are highlighted by the green and blue cells in Figure 5.2-3, which is a lower resolution image in which each protrusion represents a single molecule.

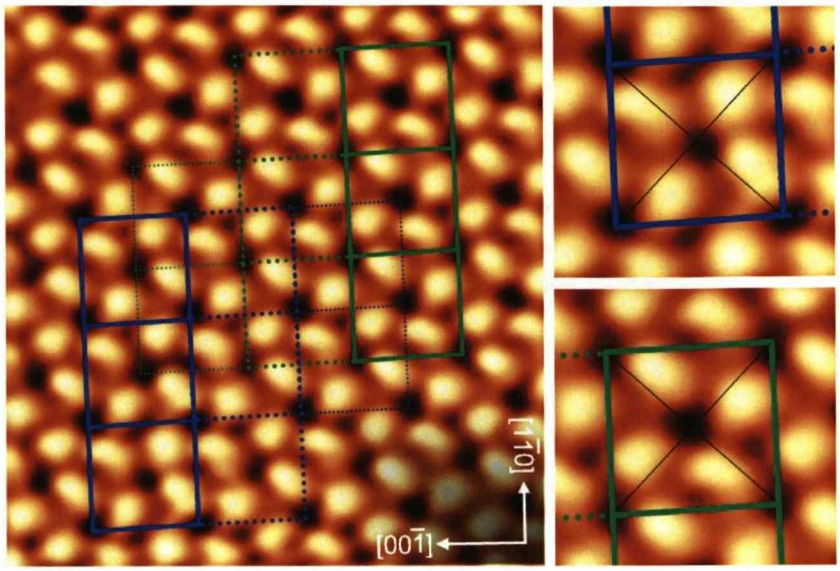

Figure 5.2-3. The two ways of tiling the unit cell of Structure 3. Different imaging conditions mean that each bright feature is a single molecule. The smaller images show the rotational offsetting of the molecules in the two units. Image Conditions: 151×159Å^2, I_T=0.42nA, V=1250mV.

The two units are distinguished by their symmetry characteristics; a simple translation and/or rotation of one cannot make the other. The aforementioned figures reveal that the four Co-TPP molecules that are located in each cell are offset from the cell's diagonals in either a clockwise (green cell) or anticlockwise (blue cell) direction (Figure 5.2-3). This opposite rotational offsetting of molecules has the consequence of making the two cells mirror, or chiral, opposites, with the axes of reflection shared by that of the underlying copper lattice. The rotational symmetry of the cells is further highlighted by the yellow horseshoe features in Figure 5.2-4, which clearly show each cell to be mirrored.

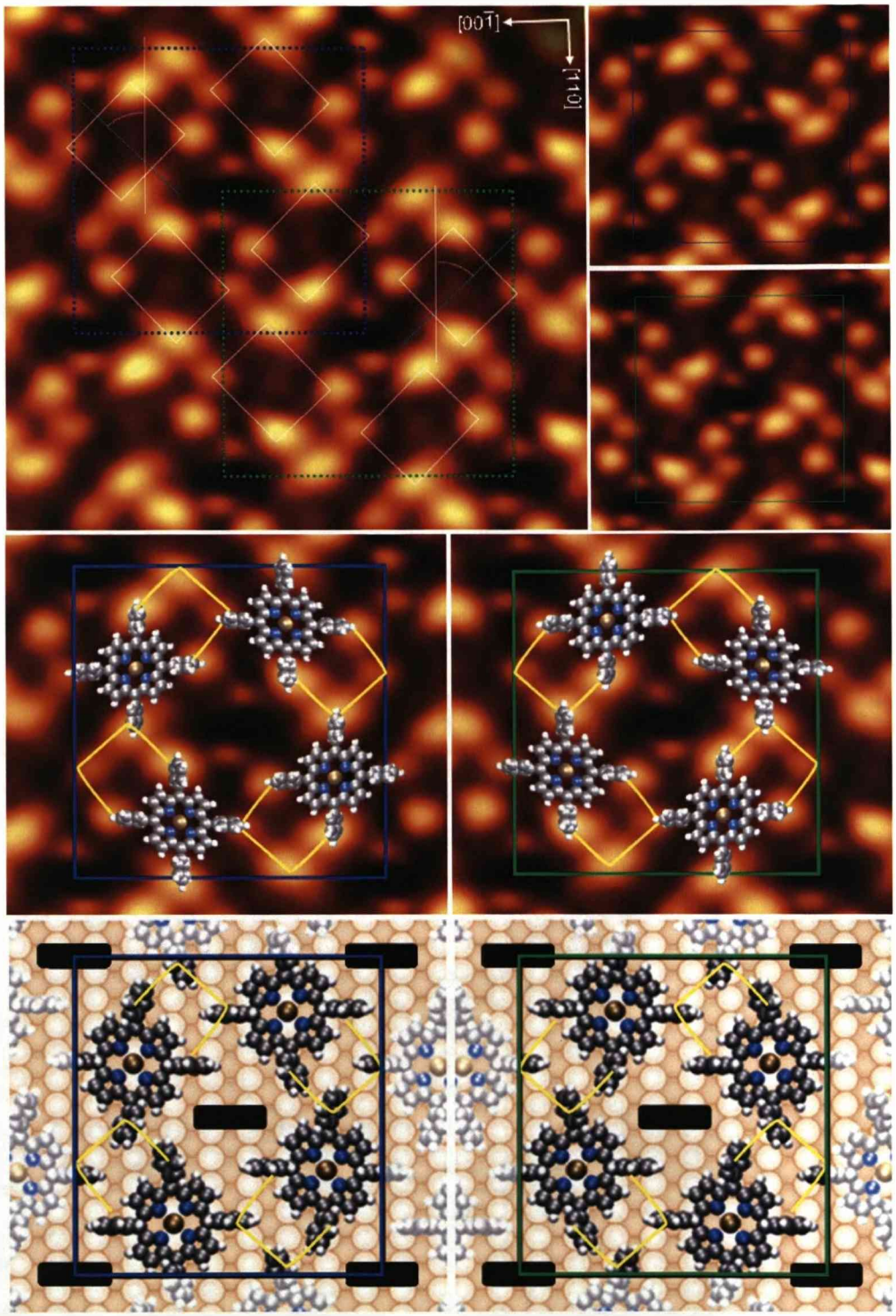

Figure 5.2-4. Mirrored unit cells of Structure 3. The two cells each contain four molecules. Each cell can describe the structure as a whole. White boxes (top left image) show the orientations of the molecules comprising the cell, both of which are described by the angle between the Cu[1-10] axis (vertical dotted white line) and the molecule's symmetry axis (dotted green line). Yellow horseshoes show the pattern of intermolecular interaction. In the large image some macrocycle structure can be seen as a core protrusion and a feint cross. The cells are well reproduced by the model. Molecular conformation is assumed. Image Conditions: 57×52Å^2 (large) and 41×39Å^2 (small), I_T=0.36nA, V=1238.7mV.

Further investigation of the high resolution images reveals that there are two orientations of molecule in Structure 3 that are rotated by ±46°±2° with respect to the Cu[001] axis, shown in the top image of Figure 5.2-4. Equal numbers of each orientation in the assembly permit the definition of a 2D racemic crystal to apply for this phase. Each orientation has the same aspect ratio of 1.12±0.1, making them very similar in size and orientation to molecules from both of Structure 1's chiral domains. Indeed, a similar bonding pattern (discussed later) has been observed in distorted Structure 1 domains (discussed in section 5.3) so the similarity is expected.

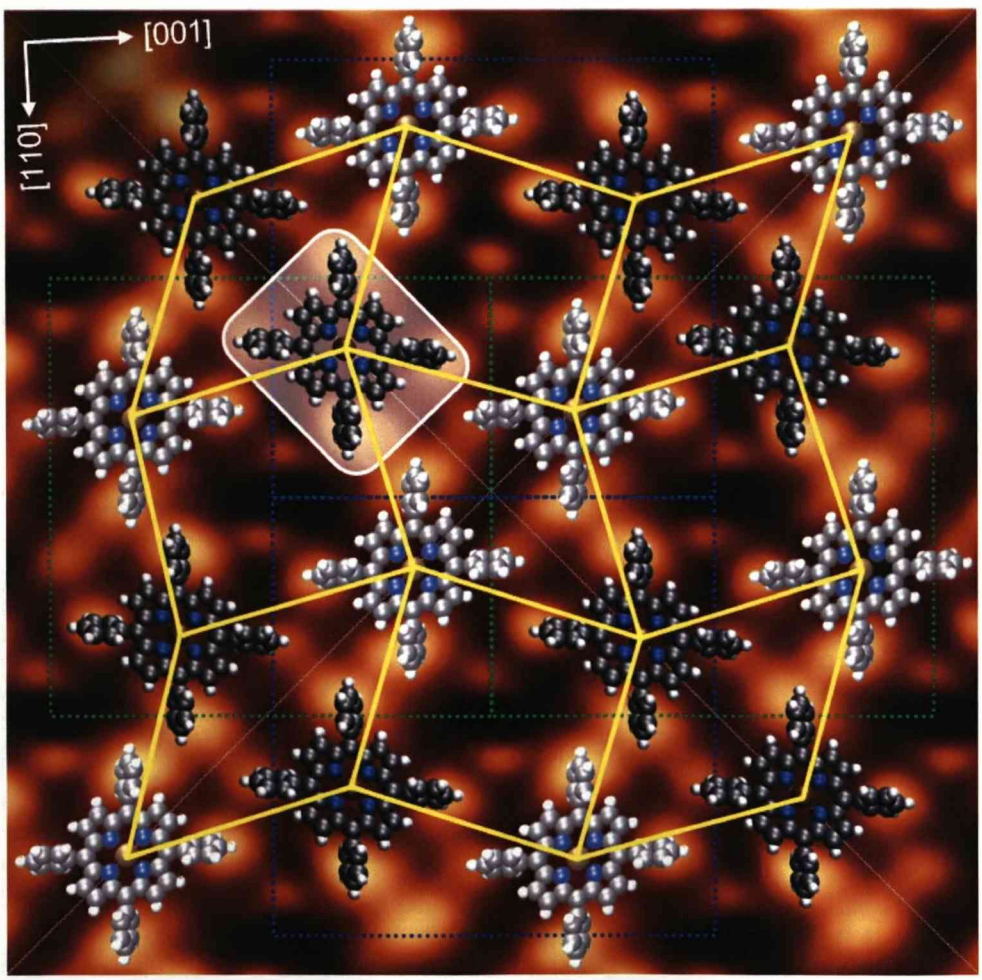

Figure 5.2-5. A 4x4-molecule image showing the distinct pattern of Structure 3. Alternately oriented (white and black) molecules form zigzagging rows that follow both of the crystallographic directions of the copper. This ordering gives the domain itself two lines of symmetry (shown by diagonals in image) that aren't related to the unit cells, which are shown as green and blue dotted boxes. The highlighted molecule will be used for further analysis. Molecules are scaled down for clarity. Image Conditions: 70x70Å^2, I_T=0.36nA, V=1238.7mV.

Molecules in Structure 3 form zigzagging rows of alternating, oppositely oriented molecules whose general direction defines the orientation of the unit cells, shown in Figure 5.2-5. In the figure, the two orientations are distinguished by different shades.

As with the other structures created by the adsorption of Co-TPP on Cu(110), each molecule forms phenyl-phenyl bonds with its four nearest neighbours, however, the alternating molecular orientations following the copper directions means that, for any given molecule, its four nearest neighbours are always of the opposite orientation. This is demonstrated in Figure 5.2-6 using the highlighted molecule from Figure 5.2-5. In Figure 5.2-5, one can identify three further molecules in the core of the 4×4 matrix (on the central diamond) that have identical nearest neighbour interactions to the highlighted molecule in Figure 5.2-6. There are two configurations, based on whether the target molecule is black or white, and there are key differences between them. The primary difference is the direction of the symmetry line, indicated by the black arrow in Figure 5.2-6, which points to the top-left for the black molecules and to the top-right for the white molecules. Secondly, the intermolecular interactions, i.e. the features indicated by the yellow horseshoes in Figure 5.2-4, are mirrored for the interactions surrounding either black or white molecules. This will be discussed in greater detail later.

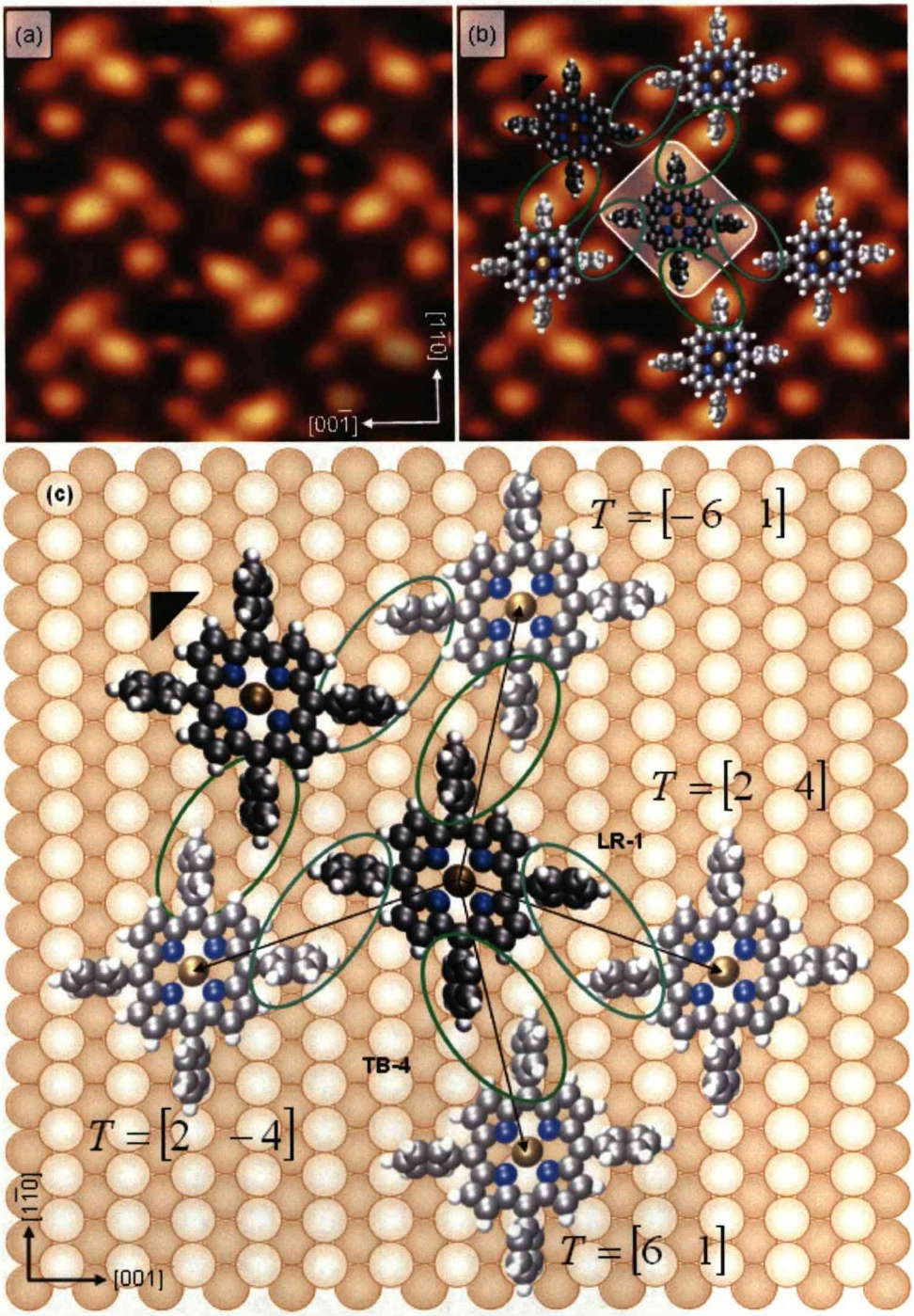

Figure 5.2-6. Nearest neighbour bonding in Structure 3. (a) A segment of image surrounding the highlighted molecule in Figure 5.2-5. Image Conditions: 44×47Å^2, I_T=0.36nA, V=1238.7mV. (b) Molecules overlaid onto (a) showing all nearest neighbour interactions. (c) Two interactions create zigzagging lines that follow the copper axes. The TB-4 interaction (ringed in light green) occurs in two mirror forms, as does the LR-1 interaction (ringed in dark green). The black arrow near the top left of the image indicates the direction of this configuration's mirror symmetry line (discussed in text and shown in Figure 5.2-5). An arbitrary molecular conformation is presented with molecules scaled down for clarity.

Four main interactions create Structure 3, however, it is impossible to identify exactly what form they all take. The LR-1 interaction has been observed previously and it is believed to be appropriate to assume it adopts the same form as in Structure 1 as there is no strong evidence to suggest otherwise. There is ambiguity in the assignment of the TB-4 interaction though. From the analysis of Structure 1, it is known that the TB phenyls reach their minimum conformational energy by aligning in the surface corrugations. In Structure 3, the phenyls forming the TB-3 can both adopt a near-Structure 1 conformation whilst forming a T-type intermolecular interaction that has a similar configuration to that in Structure 1 (although between different phenyls). In Structure 1, the T-type interaction was shown to display the greatest energy gain (section 4.5). This is, therefore, the likely molecular conformation, and is shown below in Figure 5.2-7.

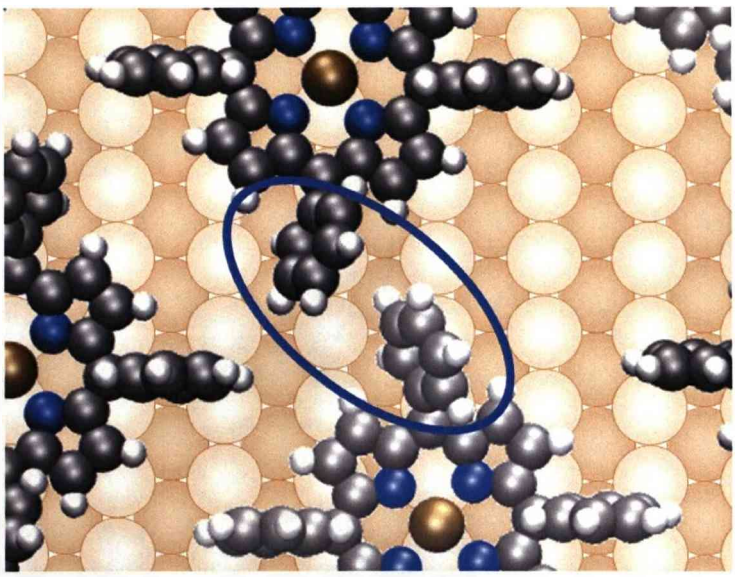

Figure 5.2-7. Predicted T-type TB-4 interaction of Structure 3. The molecules in the figure are in their mirrored Structure 1 conformations and are, therefore, an assumed representation of the real system.

The separation of the phenyls protrusions measured from the STM data returns values of 5Å±0.3Å. When comparing this to the measurements from the model, 5.69Å±0.3Å, they are found to be in good agreement. This is therefore a nearly-optimised T-type interaction[107]. Other TB-4 configurations involving phenyls in their Structure 1 conformation show phenyls that are either too close, and therefore overlapping, or so far apart that they greatly

conflict with the inter-centroid separation measured from the STM data. Considering the potential for macrocycle distortions, there could be a number of potential combinations of phenyl and core deformations that form T, PD type or combinative interactions. At the time of writing, a conclusive characterisation of the TB-4 interaction remains pending; a fact that serves well to highlight the limitations of a model based on Structure 1.

Pairs of interactions form the distinct horseshoes observed in Figure 5.2-4 and Figure 5.2-8, where the brighter half (bright green outline) represents the TB-4 interaction and the dim half (dark green outline) represents the weaker LR-1 interaction. Additional to the two main interactions is a third interaction that links the two main bonds (red outline in Figure 5.2-8), thus creating the horseshoe. This is the only interaction between like-oriented porphyrins but without knowing the precise conformation of the molecules, it is impossible to clarify its nature.

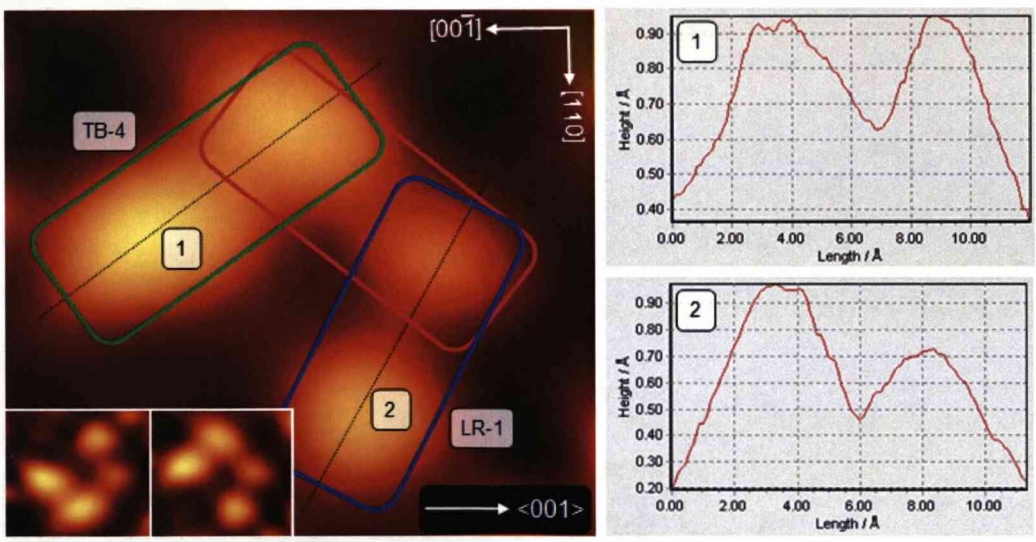

Figure 5.2-8. Intermolecular interactions create a horseshoe pattern in Structure 3, that consists of one TB-4 interaction (green), one LR-1 interaction (blue) and a linking T-type interaction (red). Image Conditions: 16×14Å^2, I_T=0.36nA, V=1238.7mV. Inset: The original image (left) and its chiral opposite (right). Line scans 1 and 2 are marked on the image.

The identification of the conformational properties of the phenyls is made all the more difficult by changes in observed electron density around the horseshoe. Three of the phenyl groups appear to be equivalent with

respect to the signal from the STM but one phenyl is clearly distinguished by its noticeably reduced height. This imparts chirality on the horseshoe which is repeated along lines of domain symmetry (arrows in Figure 5.2-6). The opposite chiral feature occurs along the opposite line of domain symmetry, i.e. they are mirrored for interactions associated with black and white molecules respectively. There is currently no explanation for the decrease in apparent height of the single phenyl of the LR-1 interaction other than that particular phenyl ring reorienting flatter with respect to the surface..

Another defining, and therefore distinguishing, feature of this structure is the possible presence of adatoms, which are confined to the empty regions marking the corners/centers of the unit cells (Figure 5.2-9). There are two features per hole, of which one or both are occasionally seen to occupy positions in the centre of the hole. It is unknown how many configurations exist for the two features, but four have been observed experimentally (Figure 5.2-9a-d). Despite being imaged away from the hollow site, it is expected that this would be the preferred site for all features, as has been observed for copper adatom capturing around H_2-Porphines on Cu(110)[129]. This does not coincide with a similar feature seen in Structure 1, primarily because Structure 1 does not provide a similar possible adsorption site. However, the features of the preferred configuration (Figure 5.2-9a and b) do adopt similar positions relative to the molecule's phenyl rings. At present there is no proof that these are adatoms and the nature of the forces holding them in position is unknown, but similar features have been observed elsewhere[21,129], suggesting a moat-like potential well surrounding adsorbed porphyrins and related molecules.

In Structure 3, the two features are indicative of the chirality of the unit cell in which they appear at the centre of. For example, Figure 5.2-9(a) and (b) represent the centres of green and blue cells respectively and have the corresponding mirror symmetry between them. It should be noted that these features eliminate much of the intrinsic symmetry in Structure 3, leaving only the mirror unit cells that, despite being aesthetically interesting, are unnecessary to evoke in a description of Structure 3.

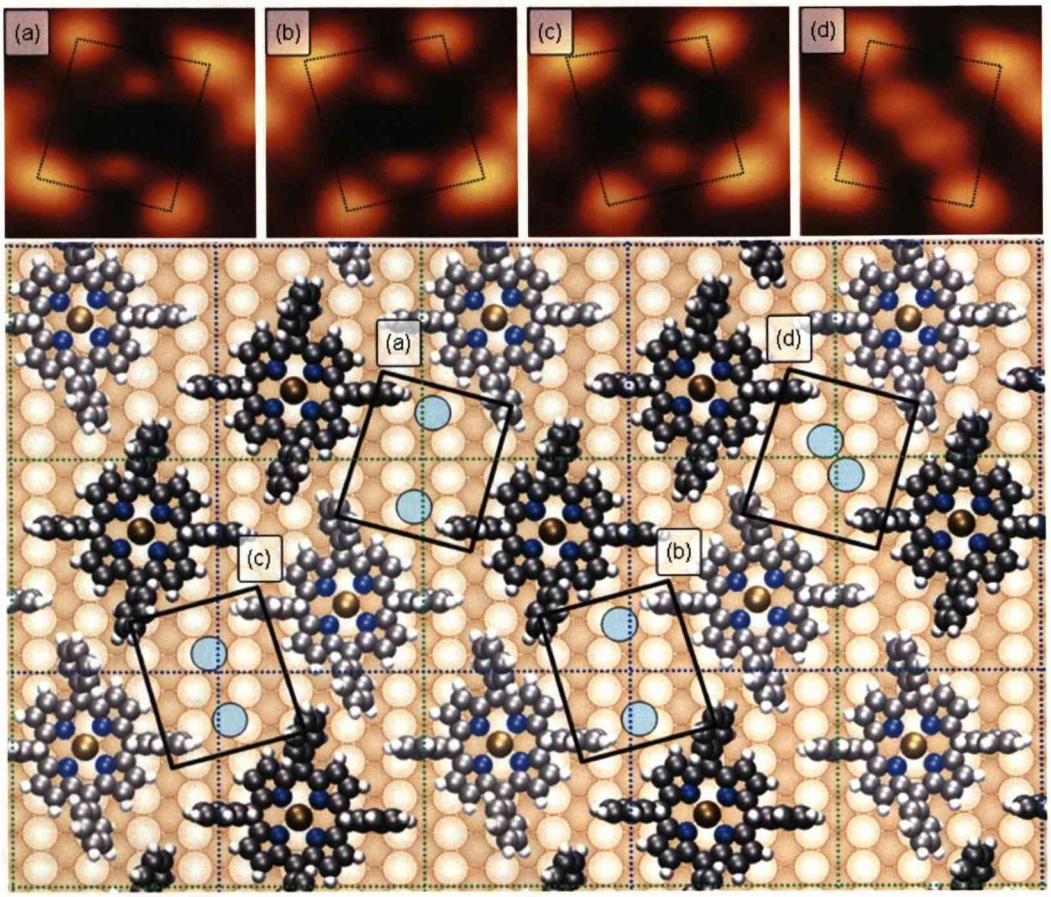

Figure 5.2-9. Possible adatom capturing in Structure 2. (a) and (b) are the two normal holes with spots at the top and bottom of the hole. Lines between the spots are oriented in a non-symmetry direction of the copper substrate. (c) Movement of one spot towards the centre of the hole and (d) movement of both spots towards the centre. In (d) the observed electron density is broadened. Image conditions for (a) to (d): 17×16Å^2, I_T=0.36nA, V=1238.7mV.

5.3. Transition and boundary structures

In the majority of the STM data of the three organised structures lines (1D) or regions (2D) of distinct intermolecular interactions that interrupt and break up the host bulk domain are observed. These are transition or boundary structures. Transition structures are distortions to Structure 1 only and their frequency of occurrence is related to the molecular flux arriving at the surface during the dose (discussed in Chapter 7). Other structures are observed to exhibit discontinuities also, typically in the form of boundary lines, which are observed when out-of-phase domains join. This is observed in other porphyrin systems and is commonly referred to as lattice mismatch[39].

Some boundary structures take the same form as transition structures and their assignment is consequently often difficult to establish with certainty.

This section will show how the intrinsic flexibility of Co-TPP molecules endows the assembled structures with the ability to adapt to varying conditions. These adaptations take the form of changes to the intermolecular separation that, when modelled, are shown to retain the commensurability of the overlayer with the underlying copper lattice whilst potentially maximising the total energy gain by populating the greatest number of intermolecular phenyl-phenyl interactions. It should be noted that no computational study has been undertaken on the following structures and the conformation and dimensions of presented molecules and structures are not as accurate as those that have been calculated. Also, the calculations of Structure 1 show that there is induced in the copper substrate a minor reconstruction that amounts to around $+39kJmol^{-1}$ (section 4.3), suggesting the same might happen with these structures. Both Structures 1 and 3 are also suspected to invoke movements of surface atoms by integrating them into the molecular assembly (Figure 4.8-1(a-d) and Figure 5.2-9). Although impossible to establish for this work, it has not been ruled out that the transition and boundary lines do not also induce or are, in fact, the adaptation of the domains to a unique deformation of the copper surface.

5.3.1. Transition structures

Transition structures are limited only to Structure 1, in which they appear in much of the STM data. In fact, it is far less common to find domains that are entirely free of them. A Structure 1 transition line is roughly defined as a long range 1D modification to intermolecular interactions that retains the chiral direction of the host structure, i.e. only the TB interaction is altered; the LR-1 interaction is always maintained. The modification occurs during Structure 1 domain growth. New molecules that join the domain interact with the bulk domain differently to the TB-1 interaction and the new interaction is maintained along the chiral direction. this, in turn, maintains the LR-1 interaction. There are two main types of transition structure present in Structure 1; primary and secondary, and both are observed to form 1D and

2D assemblies in both λ and δ domains. Primary and secondary transition lines (1D) are shown in Figure 5.3-1.

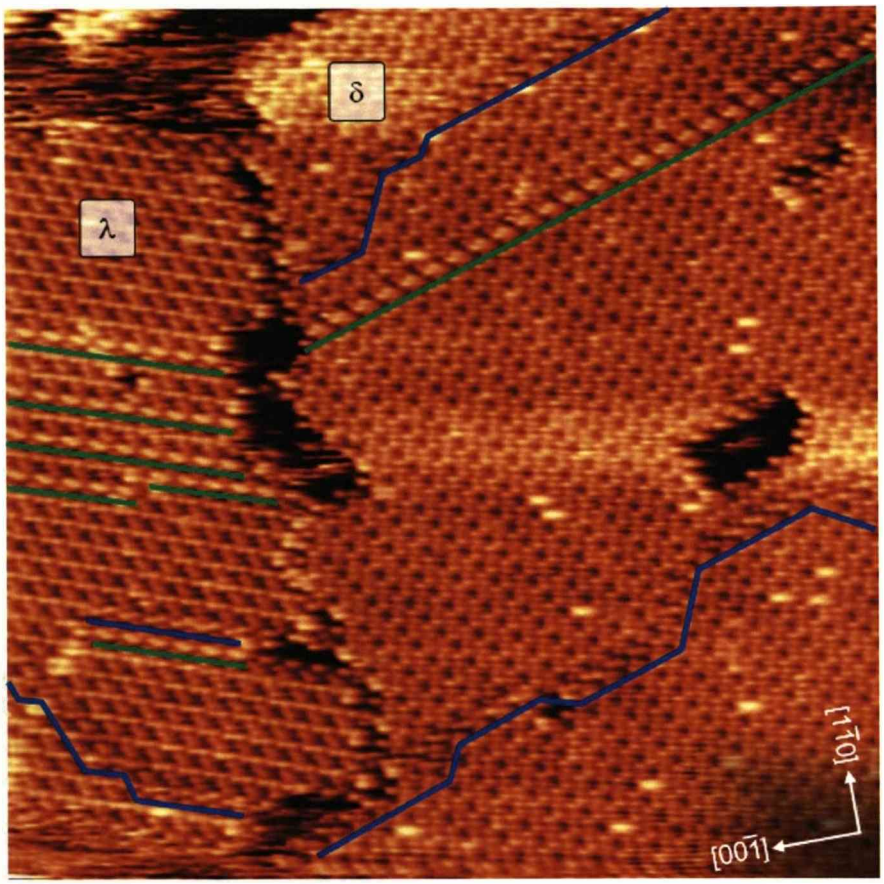

Figure 5.3-1. Primary (blue underline) and Secondary (green underline) lines in both λ and δ domains of Structure 1. Image conditions: 510×525Å^2, I_T=0.21nA, V=611.3mV.

Primary transition lines are a row of TB-3 interactions through a Structure 1 domain, resulting in a line of stepped features of reduced brightness (Figure 5.3-1). The TB-3 interaction is normally found as part of Structure 2's spine links and has been characterised already (Figure 5.1-6). Considering the whole assembly, the primary transition line can be described as the shift of one lattice space in the [1-10] direction of a section of bulk domain that is cut off along the chiral direction (Figure 5.3-2). This acts to increase the distance between phenyls of the TB interaction (comparing Figure 4.5-1(a) and Figure 5.1-6(d)). Unit cells for each chiral line were evaluated from the model in Figure 5.3-2(c) as $T_P^{\lambda} = \begin{bmatrix} 2 & 4 \\ -7 & -2 \end{bmatrix}$ and

$T_P^{\delta} = \begin{bmatrix} -7 & 2 \\ 2 & -4 \end{bmatrix}$. The single molecule unit cell across the line (shown in red in the figure) has a density of 24 surface copper atoms per molecule; the equal lowest for the whole system.

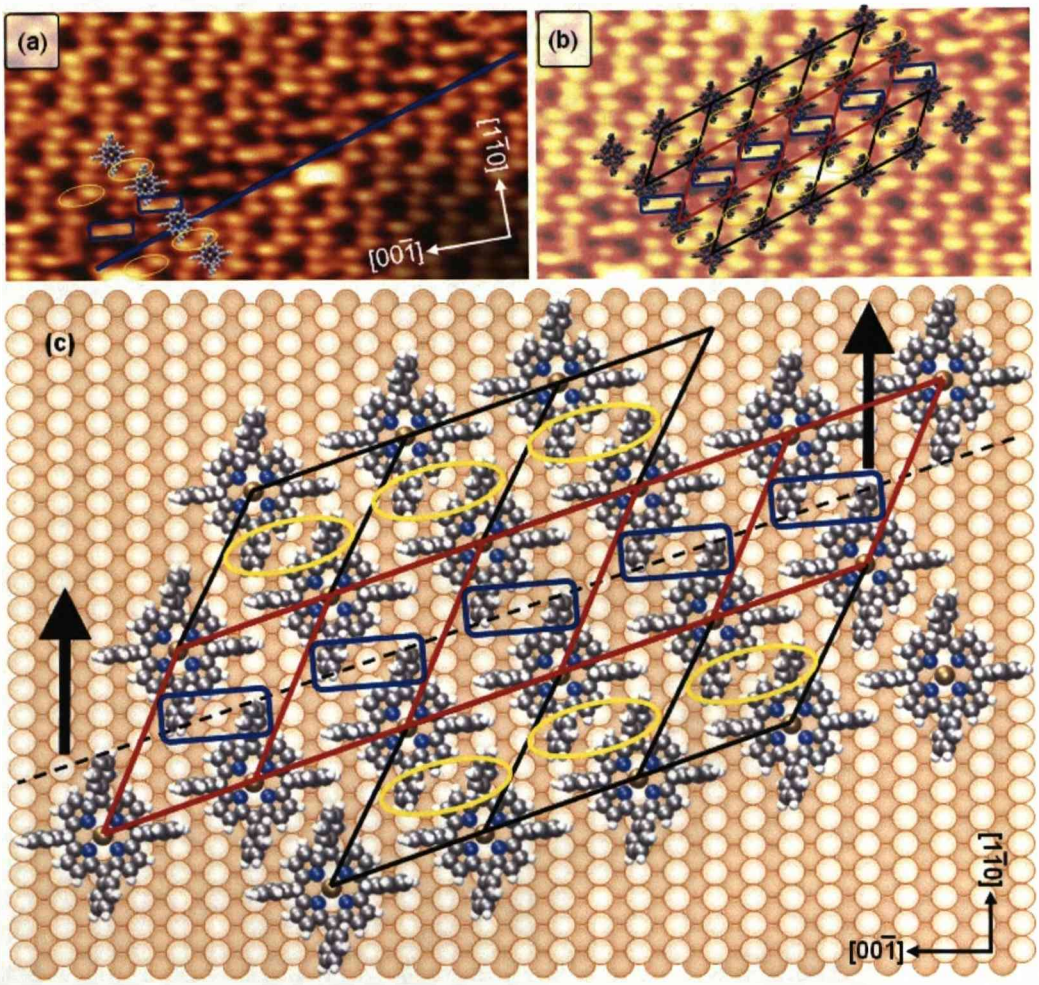

Figure 5.3-2. Primary transition lines in Structure 1. (a) The transition line is underlined in blue. Part of the model (c) is overlaid. (b) The model in (c) is overlaid in its entirety. Blue boxes surround the distinctive primary transition line TB-3 bond, yellow ovals highlight the normal Structure 1 bonding pattern. Black arrows in (c) show the direction of the shift of one group relative to the other (across the dotted line). Image conditions: 144×74Å^2, I_T=0.14nA, V=611.3mV.

Changes in direction of primary transition lines (Figure 5.3-3) result in a non-uniform distortion through the domain. The flexibility of the intermolecular interactions can compensate for this but the line must span the extent of the domain for the bulk structure to resume as normal on either side, i.e. the distortion must affect the entire domain for the compensation to

be uniform. When this doesn't happen, a block deformation occurs. Figure 5.3-3 clearly shows the effects of primary transition lines when they span only a small part of their host domain. Deformations are observed that force T type interactions between adjacent domain that are offset (or out-of-phase) by a small amount.

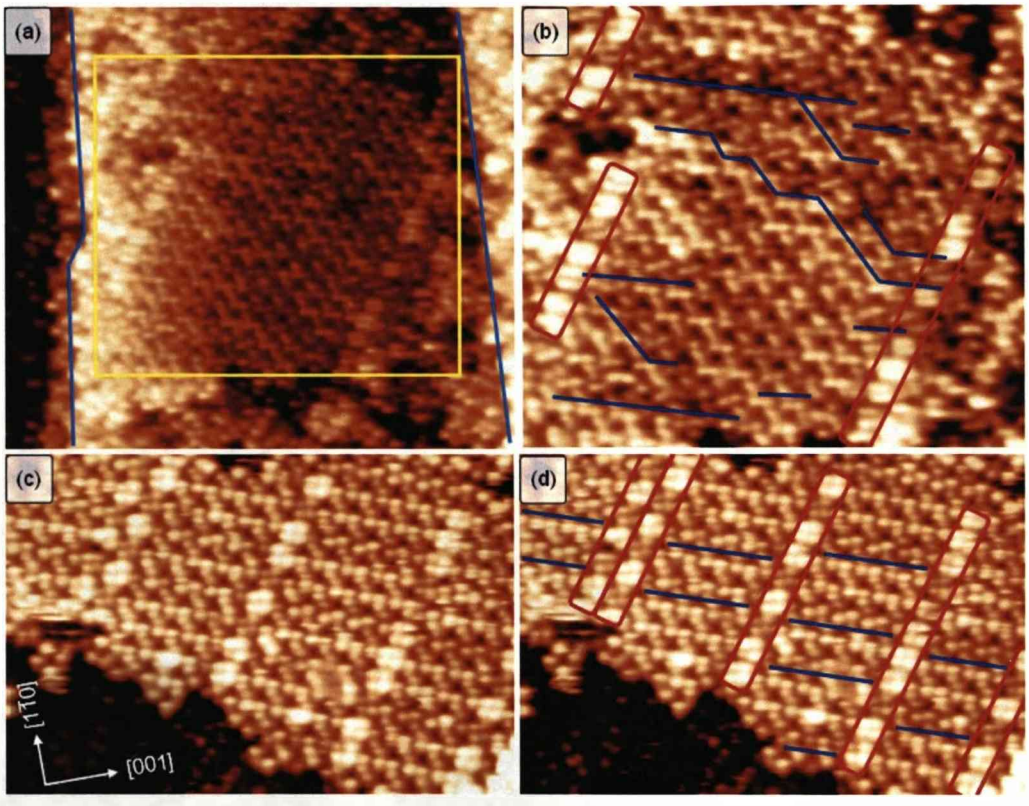

Figure 5.3-3. Primary transition lines in Structure 1 domains form block deformations when they span only a small part of their host domain. The surface is quite highly stepped here and the domains have had to form on small terraces. (a) a narrow terrace on which a Structure 1 domain has formed. Steps are shown as light blue lines. The yellow box highlights the area covered in (b), which shows primary transition lines (blue lines) and block deformations (red boxes). (c) and (d) show a different region in which the same features occur. Bright and dark regions of the block deformations indicated the degree of offsetting, where brighter regions are caused by domains joining that are more out of line than for the dark. Copper axes shown in (c) apply to all images. Image conditions: (a) 310×274Å^2, I_T=0.41nA, V=557.5mV, (b) Image conditions: 250×170Å^2, I_T=0.42nA, V=883.8mV.

Although uncommon, primary transition lines form 2D structures (Figure 5.3-4). The rarity of primary transition lines amplifies the rarity of the 2D phase. The figure, therefore, shows one of the few occurrences of significant scale.

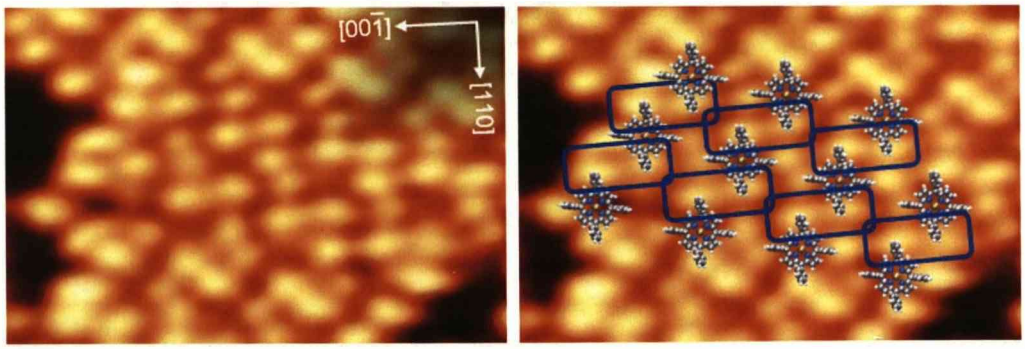

Figure 5.3-4. (a) A 2D primary transition structure in Structure 1. (b) Overlaid molecules are shown and the bond highlighted. Molecular conformation is assumed. Image conditions: 61×37Å^2, I_T=0.48nA, V=1238.7mV.

Secondary transition lines in Structure 1 are very common, and are shown in Figure 5.3-5. These are distinguished by a row of bright TB-4 interactions that are observed, although less often, as the bright half of the horseshoes of Structure 3 (Figure 5.2-6). Like the primary lines, these are created by a shift of one bulk group relative to another. For secondary transition lines, the shift is by one lattice space in the [001] direction. This is a larger shift than for the primary lines and a consequence of this is that the interaction ceases to be between the same two molecules as for the TB-1 interaction, thus removing the rotational directionality of phenyl-phenyl bonding around the involved molecules. The unit cells have been evaluated from the models as $T_S^{\lambda} = \begin{bmatrix} 2 & 4 \\ -6 & -1 \end{bmatrix}$ and $T_S^{\delta} = \begin{bmatrix} -6 & 1 \\ 2 & -4 \end{bmatrix}$, resulting in a density of 22 surface atoms per molecule. It is expected that a computational study of this single molecule unit cell will shed light on the nature of Structure 3's intermolecular interactions.

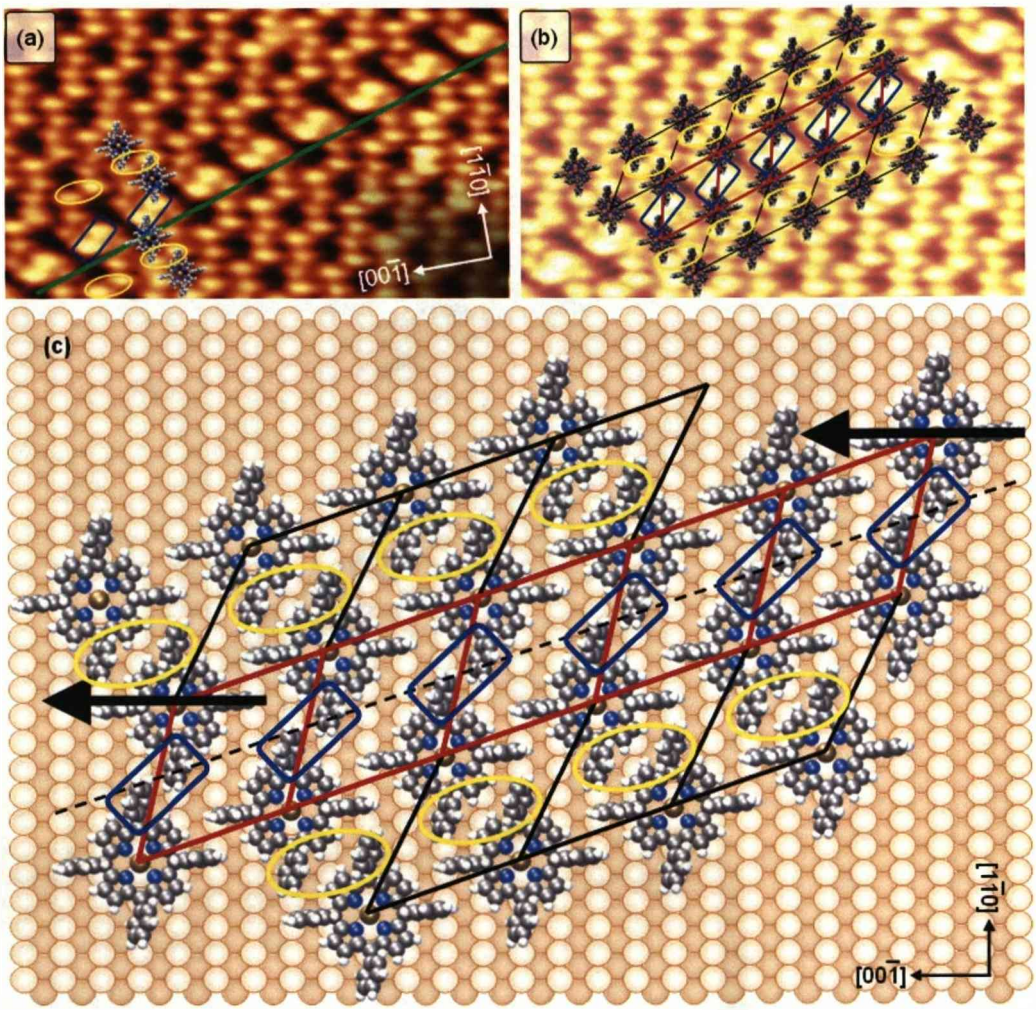

Figure 5.3-5. Secondary transition lines in Structure 1. a) The transition line is underlined in green. Part of the model, (c), is overlaid. (b) The model, (c), overlaid in its entirety. Blue boxes surround the distinctive secondary transition line TB-3 bond and yellow ovals highlight the normal Structure 1 bonding pattern. Black arrows in (c) show the direction of the shift of one group relative to the other (across the dotted line). Image conditions: 131×73Å^2, I_T=0.14nA, V=611.3mV.

An interesting feature of secondary lines is their ability to hold within the domain, retaining their position during domain growth and becoming a discontinuity within the bulk. Why some secondary transition lines hold their position in the domain while others disintegrate to form the normal structure 1 domain is unknown, however, when positioned in a bulk domain they are not always confined to a single row and may adjust their position, as shown in Figure 5.3-6.

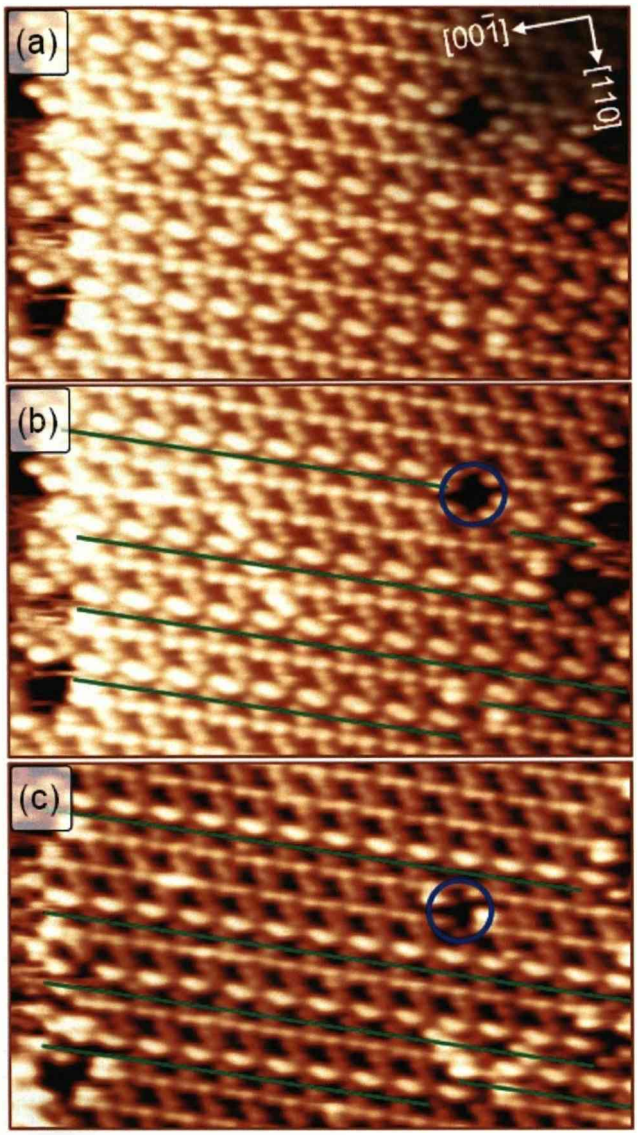

Figure 5.3-6. Secondary transition lines in a Structure 1 domain. (a) These lines formed then held their position during domain growth and are not the result of joining domains. Image conditions: V=611.3mV, I_T=0.26nA, 210×130Å^2. (b) The image from part (a) with secondary transition lines highlighted by green underlines. A hole caused by a missing molecule (ringed in blue) splits the uppermost transition line, leaving either side between different rows of molecules. (c) A molecule moves into the free space, making a hole elsewhere. This allows each side of the transition line at the top of (b) to form a single feature across the entire domain. Image conditions: V=611.3mV, I_T=0.21nA, 210×130Å^2. Copper axes in (a) apply to all images.

Secondary transition lines extend into two dimensions relatively readily and 2D structures are widespread at higher dose rates (Figure 5.3-7). These 2D structures create horseshoe structures similar to those observed in Structure 3. Interestingly, the same interactions that make up Structure 3 also make up the 2D secondary transition phase, the difference being the lack of

alternating bond directions in the secondary transition phase. This close link will be further discussed later in this section. Creation of the 2D phase affects the nature of the LR-1 interaction. The interaction becomes very similar to the same interaction in Structure 2, with almost completely independent regions of electron density for each phenyl. A change in orientation of the involved molecules is unlikely and would be so slight as to have made it impossible to differentiate between this and an altered interaction from the STM data.

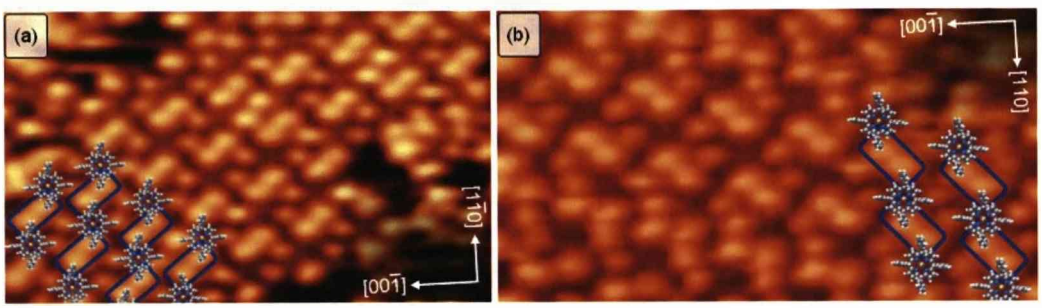

Figure 5.3-7. (a) and (b) 2D secondary transition structures in both domains of Structure 1. Image conditions: (a) 116x74Å^2, I_T=0.53nA, V=1238.7mV, (b) Image conditions: 101x61Å^2, I_T=0.5nA, V=1238.7mV.

There are rare appearances of primary-secondary transition line combinations in which part of the domain exhibits a dislocation resulting from single lattice space shifts along both [1-10] and [001] axes. This results in sections of the domain that are out of phase, with block deformations occurring at the phase boundary, shown in red boxes in Figure 5.3-8. In the figure, the static bulk section is at the top, so the shifts caused by the transition lines only affect the molecules below them. The adaptability of the domain is emphasised here as all phenyls remain involved in intermolecular interaction, with the brighter regions of the block deformation characterised by strong T-type interactions. Length measurements of the interaction from the STM data are in good agreement with the model.

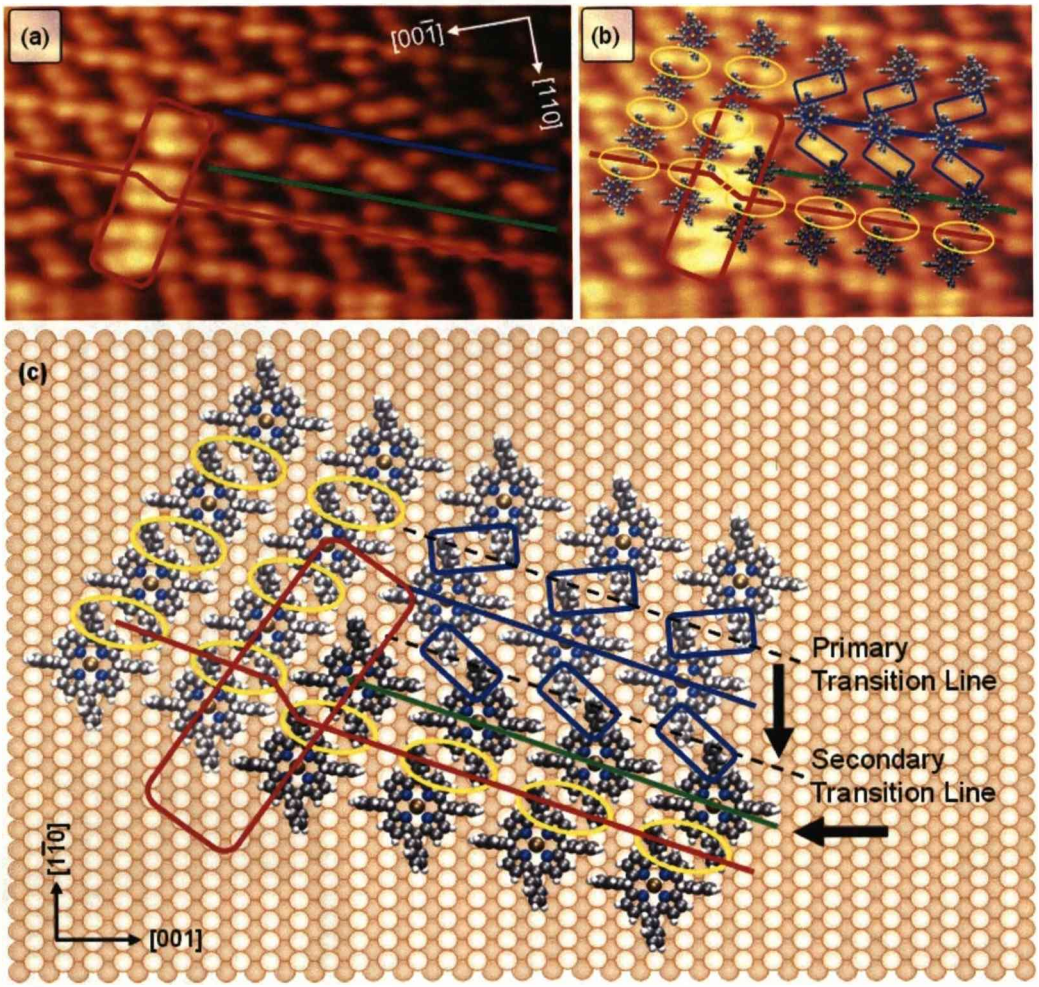

Figure 5.3-8. A primary/secondary transition line combination in Structure 1 causes a block deformation (red boxes). (a) A block deformation exists between the area affected by the transition lines (underlined) and the bulk outside this area. Image conditions: 111×69Å^2, I_T=0.22nA, V=611.3mV. (b) The model from (c) overlaid on part of the STM image in (a). (c) Molecules in the model that are shown darker than the rest are those affected by the resultant offset. Molecular conformation is assumed.

The final instance of a 1D invasion in Structure 1 is shown in Figure 5.3-9. This figure shows the only observation of this line in Structure 1, which is suspected to only be possible as a result of a highly distorted region containing numerous transition lines and an adjacent Structure 2 domain of the correct chirality and in the correct relative position. The interaction forming this line is Structure 2's spinal TB-2 interaction (Figure 5.1-4 and Figure 5.1-6).

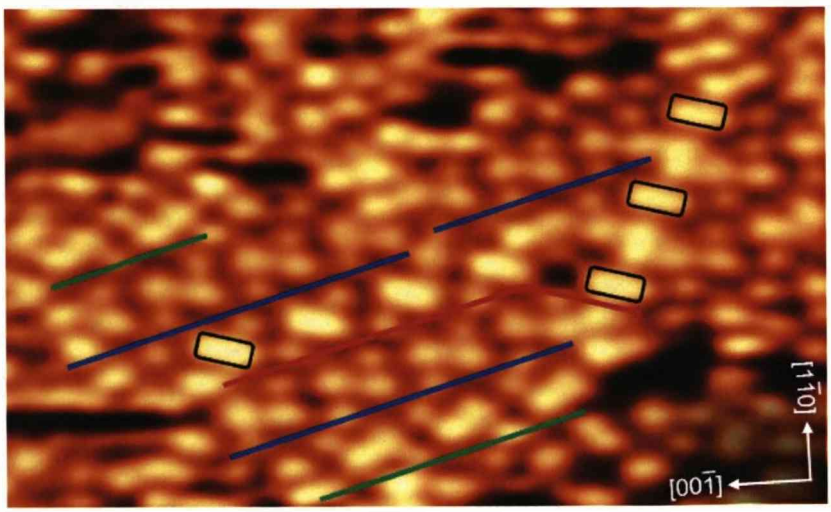

Figure 5.3-9. TB-2 line invasion in a highly distorted composite phase of transition lines. Black boxes outline the bonds in the Structure 2 spine (right) and at the end of the Structure 1 TB-2 row (left). The row is underlined in red (Primary and secondary lines in blue and green respectively) and continues into the adjacent Structure 2 spine. Inter-molcular spacing of the LR interaction in all rows following the chiral direction bond remains the same as in Structure 1. Image conditions: 137×87Å^2, I_T=0.53nA, V=1238.7mV.

The characteristic herring-bone pattern of interaction in Structure 3 is so strictly dependent on the precise pattern of interaction that any alteration to it changes the domain to the extent that it ceases to be Structure 3. One such alteration is a special case of a Structure 1 transition structure (Figure 5.3-10). These assemblies contain inter-mixed lines resembling secondary transition lines of both chiral domains of Structure 1. The assembly additionally exhibits some of the zigzagging pattern of Structure 3 between them, and two distinct orientations of molecule that are identified by the angle between the L and R phenyls of individual porphyrins. In this phase the TB-4 interaction, characteristic of both Structure 3 and the secondary transition line, is dominant. The mesh of nearest-neighbour lines (green in Figure 5.3-10) creates two orientations of both diamond and square, albeit in a slightly distorted manner due to the random formations of both molecular orientations (Figure 5.2-5 and Figure 5.3-10). A point of interest is the absence of the possible adatoms (Figure 5.2-9), although this could be explained by the absence of well defined gaps in the structure where the features would normally situate. This fact, the linearity of large sections of the structure and the consistent direction of the LR-1 interactions sees this classified as a Structure 1 transition structure.

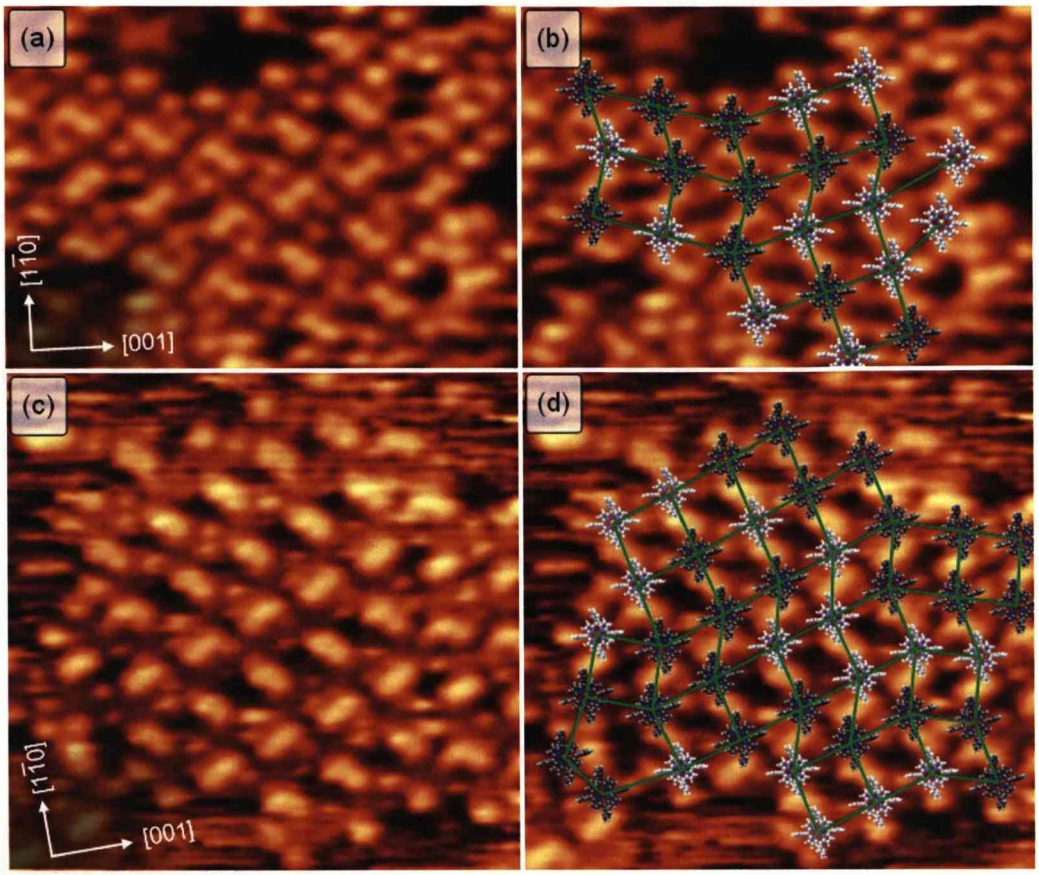

Figure 5.3-10. Structure 1/3 transition phase. (a) and (c) Regions of unusual transition line formation in Structure 1. In (b) and (d) the two orientations of molecule are higlighted in dark and light. The zigzagging pattern of Structure 3 is present but not consistent, as shown by the green nearest-neighbour mesh. This is similar to that seen in Figure 5.2-5. Image conditions: (a) 113×84Å^2, I_T=0.39nA, V=1238.7mV, (c) 117×117Å^2, I_T=0.48nA, V=1238.7mV. Molecular conformation is assumed.

5.3.2. Boundary structures

The more complicated two- and four-molecule unit cell structures are less susceptible to deformation than Structure 1. Their long-range periodicity makes distortion by other shorter-range periodic structures difficult, if not impossible. The intrinsic flexibility in Co-TPP assemblies however permits out-of-phase domains to join, forming unusual regions of interactions called boundary lines.

The versatility of TB interactions between Co-TPP molecules can explain some of the occurrences of possible secondary transition lines in Structure 1. In some instances the lines do not represent transitions in line with the definition discussed in section 5.3.1. Instead, the intrinsic shift in the

[001] direction makes the involved molecules act as 'bridging' components that allow out of phase domains to join (Figure 5.3-11). The use of this feature as a transition and boundary line by Co-TPP probably accounts for the frequent appearance of this feature relative to the primary transition line.

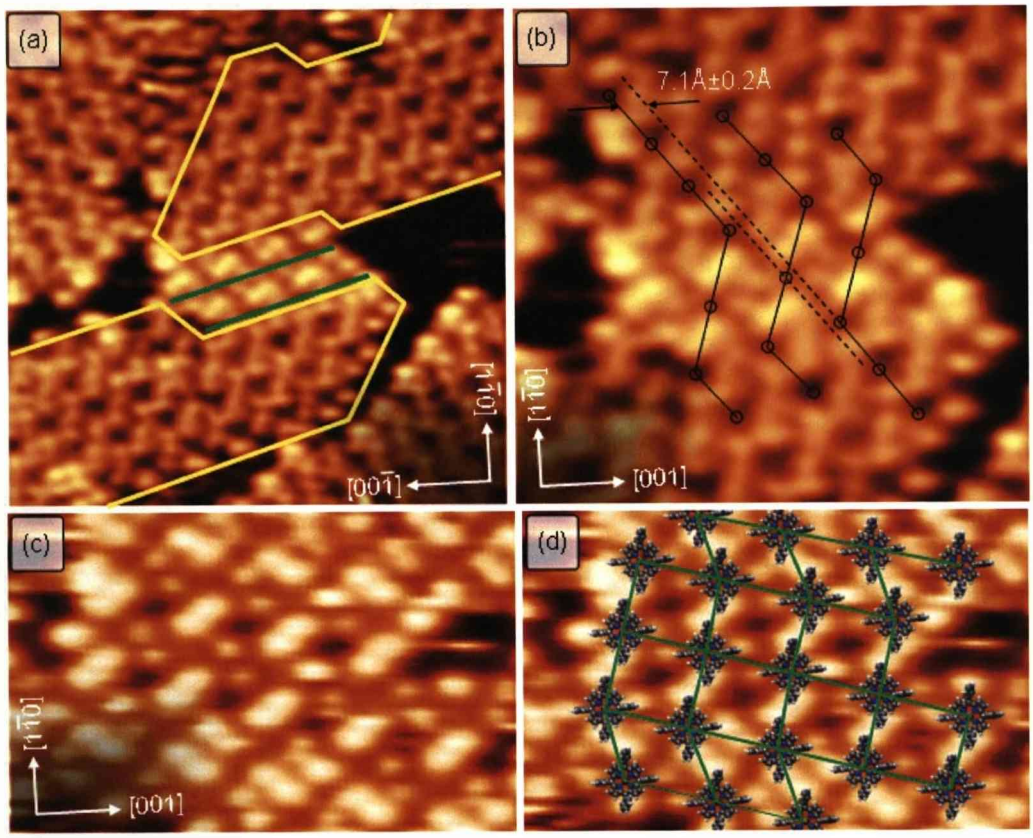

Figure 5.3-11. (a) Structure 1 boundary lines (underlined in light green) separate two out-of-phase domains (enclosed by yellow lines). Image conditions: 157×170Å^2, I_T=0.48nA, V=1250mV. (b) The total offset of two [001] lattice spaces is made up at the boundary by two lines that are identical to secondary transition lines. Circles in (b) indicate molecular centers. Image conditions: 78×77Å^2, I_T=0.48nA, V=1250mV. (c) The combinative Structure 1/3 transition line has been incorporated between two secondary transition phases to bridge the gap. Image conditions: 87×59Å^2, I_T=0.53nA, V=1238.7mV. (d) The mesh of nearest-neighbour interactions closely resembles the structures in Figure 5.3-10 but there is only one orientation of molecule involved.

In the other direction, a block deformation is frequently employed to join out-of-phase domains (Figure 5.3-3 and Figure 5.3-8). A further example of bonding being adapted to form bridging components for Structure 1-based assemblies can be seen in Figure 5.3-11(c) and (d). In the figure, a region of bonding identified by consecutive rows of square nearest-neighbour mesh allow two distorted regions of secondary transition phase to join. This is the

lowest density and also one of the rarest structures observed to be created by this system, with 26 surface atoms per molecule. It is also represented as a transition phase in Figure 5.3-10(c).

The effect that substrate features have on the deformations by transition/boundary line intrusion of Structure 1 has not been clarified. Although not always, it has been observed that these features are connected with steps. In the case of next row growth initiating at a step edge, the shape of the step may only allow the molecule to adsorb in an altered position (relative to the TB-1 configuration) in which the only permitted intermolecular TB interaction would be that of a transition or boundary line.

Structure 2 exhibits strong adaptive properties also, however, the clear difference between spinal and spine-joining interactions makes alterations to the structure extremely unlikely or impossible. As such, deformation of Structure 2 has only been observed in the form of the 2D primary transition phase of Structure 1, whose defining characteristic is Structure 2's spine-joining TB-4 interaction. This interaction is the weaker of the Structure 2 TB interactions and is therefore the best location for 2D phase invasion, requiring the least energy to form (Figure 5.3-12).

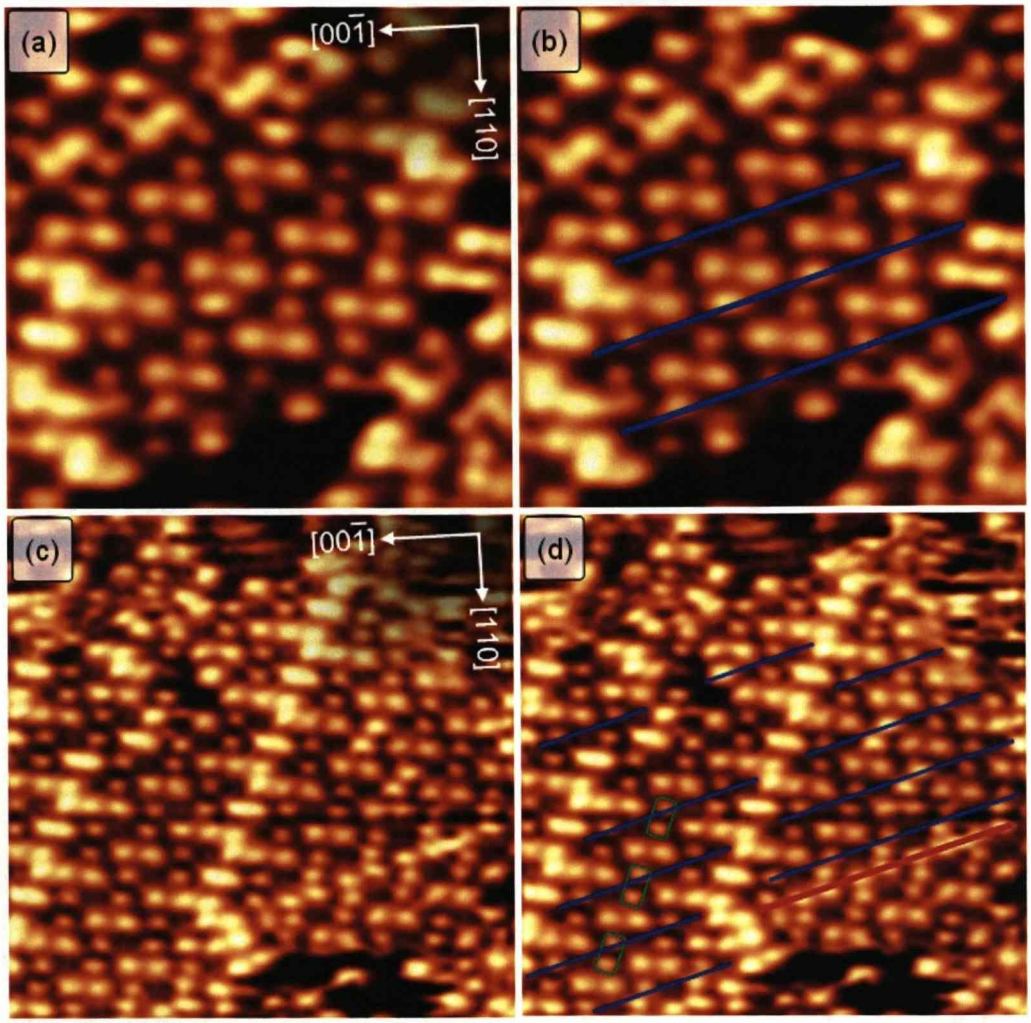

Figure 5.3-12. 2D phase invasion in Structure 2. (a) and (b) show a small phase filling the gap between two Structure 2 spines. These lines are identical to the primary transition phase. Image conditions: 62×62Å^2, I_T=0.50nA, V=1238.7mV. (c) and (d) show a more complex region of Structure 2 spinal sections between which are invasion phases. Green boxes outline where the offset is manifest. The LR-1 interaction has formed instead of the Structure 2 spinal LR-2 interaction. The red line in (d) is on a row of TB-1 interactions from Structure 1. The Structure 2 spine changes to the mirror form (and direction) as the TB-1 row joins. It isn't known whether the transition phase on the right is part of Structure 1 or 2. Image conditions: 100×100Å^2, I_T=0.49nA, V=1238.7mV.

A further Structure 2 adaptation to out-of-phase domains joining is shown in Figure 5.3-13(a) and (b). The bottom left corner of these images shows a domain that is offset in both of the crystallographic directions from the surrounding domain, forcing two lines of bridging components. This incompatibility was observed to repair itself over time. A further example of the adaptability of Co-TPP structures on Cu(110) is shown in Figure 5.3-13(c)

and (d). A row of T-type interactions similar to the block deformation form the bridge between two adjacent domains.

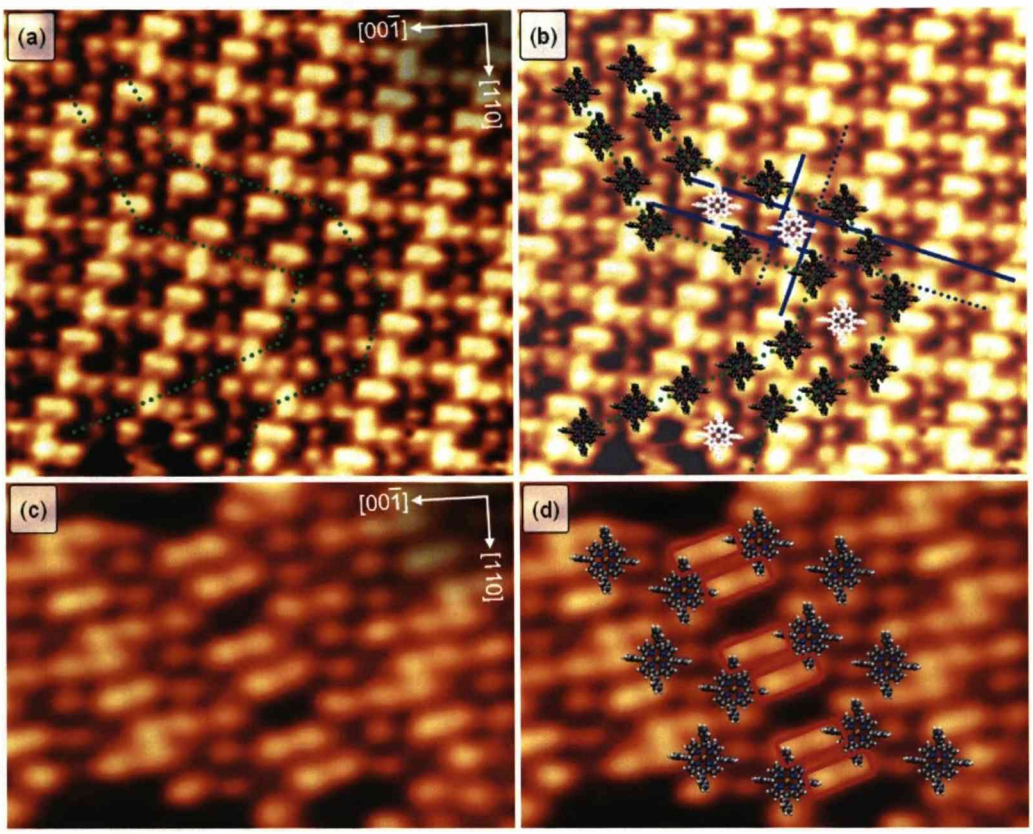

Figure 5.3-13. (a) and (b) A segment of Structure 2 domain (bottom left) situates in a position offset in all directions from a surrounding Structure 2 domain. Green lines indicate domain boundaries by joining the molecule centers. Blue lines show the offset between the domains to be large enough to accommodate a single bridging molecule (white) along the whole boundary. Image conditions: 98×93Å^2, I_T=0.34nA, V=1250mV. (c) and (d) Two Structure 2 domains join by means of six T-type interactions, shown by red boxes. Image conditions: 65×45Å^2, I_T=0.39nA, V=1238.7mV. Molecular conformation is assumed in (b) and (d).

Structure 3 is very similar to Structure 2 in terms of deformation and foreign structure invasion. Figure 5.3-14 shows the boundary between two domains that are offset by 4 Cu[1-10] lattice spaces. In this case there are linear groups, i.e. a breaking of the zigzag across the boundary that shows the same pattern as the structures in Figure 5.3-10. This is because the length and direction of the offset is such that the intermolecular LR interaction at the boundary is reversed in the [1-10] direction. Despite the successful formation of a bridge in this case, the author suspects that there may be Structure 3 domains that are offset by such a degree so as not to allow as

simple a connection as observed in the image. In any case it is unlikely that there would not be some form of bridging component, such as a T-type interaction.

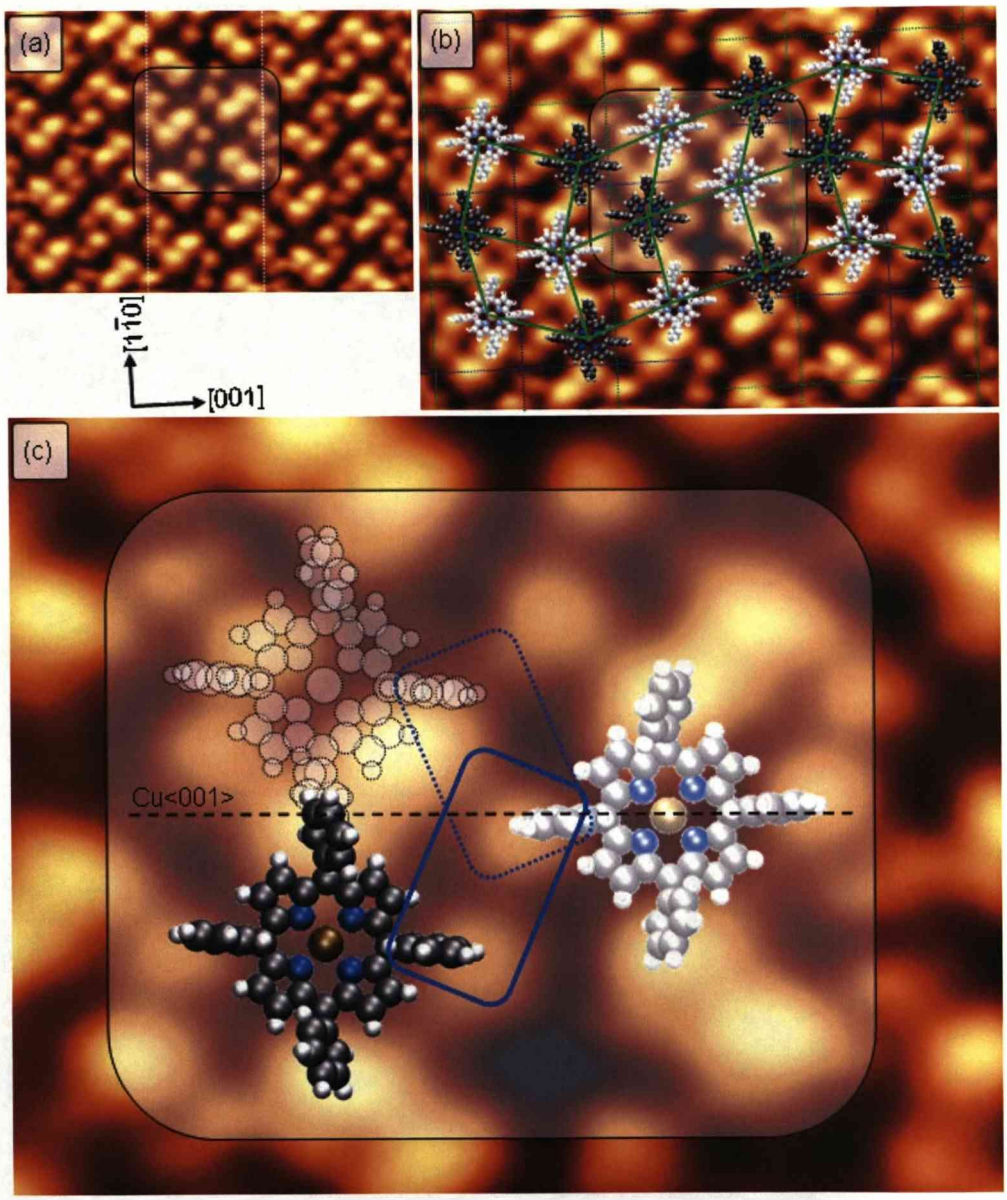

Figure 5.3-14. (a) Structure 3 domains joining, forming a boundary between the dotted lines. Image conditions: 73×52Å^2, I_T=0.48nA, V=1250mV. (b) A linear structure across the boundary compensates for a 10.2Å offset. The shaded region is detailed in (c). (c) The bridging interaction in this case (solid blue box) is a mirror image of the normal LR-1 interaction at that position, whose mirror axis is the Cu[001] axis. The position of the would-be Structure 3 molecule is shown by the wire frame model. Inset: The shaded region on (a). Image conditions: 34×28Å^2, I_T=0.48nA, V=1250mV. Molecular dimensions are reduced for clarity and molecular conformation is assumed.

CHAPTER 6

The single molecule phase

Single molecules, i.e. those molecules that are not part of a highly organised structure of two or more molecules, are frequently observed in the STM data of Co-TPP on Cu(110). They preferentially occupy steps but are found in large numbers on terraces, usually in areas where organised domains are present (Figure 6-1). Single molecules are imaged differently to those in a domain in that they generally show core structure. They are also observed in three main orientations; one whose symmetry axes align with the substrate and two exhibiting local chirality.

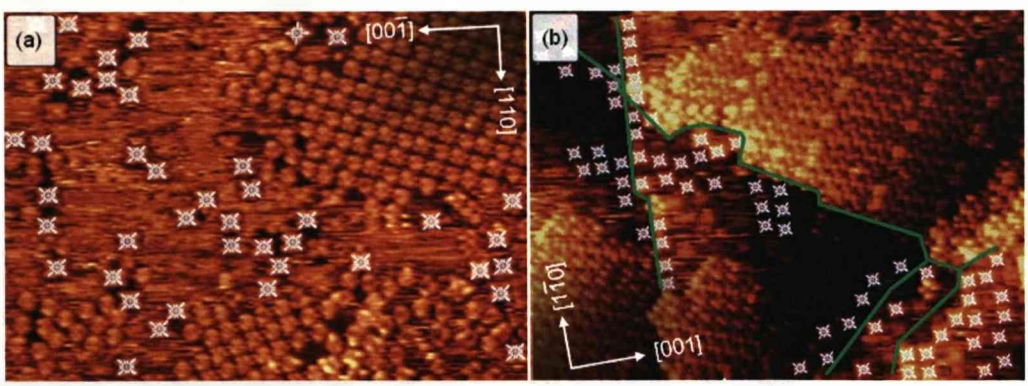

Figure 6-1. Adsorption of single molecules. Individual molecules are found scattered throughout all of the STM data. (a) In this case, between Structure 2 domains. (b) Preferential adsorption is at or near step edges (green lines), in the presence of several distorted Structure 1 domains. Image conditions: (left) 300×211Å^2, I_T=0.43nA, V=1250mV, (right) 444×312Å^2, I_T=0.48nA, V=1250mV.

6.1. Substrate-aligned single molecule

The substrate-aligned conformation of single molecule is the most common. Large numbers of substrate-aligned molecules are observed when there is a high local density of both single and domain-bound molecules,

(Figure 6.1-1). Under these conditions, individual molecules are confined to a small area in which they are unable to reorient themselves or diffuse; a situation that is suspected to hinder the formation of large domains to some degree.

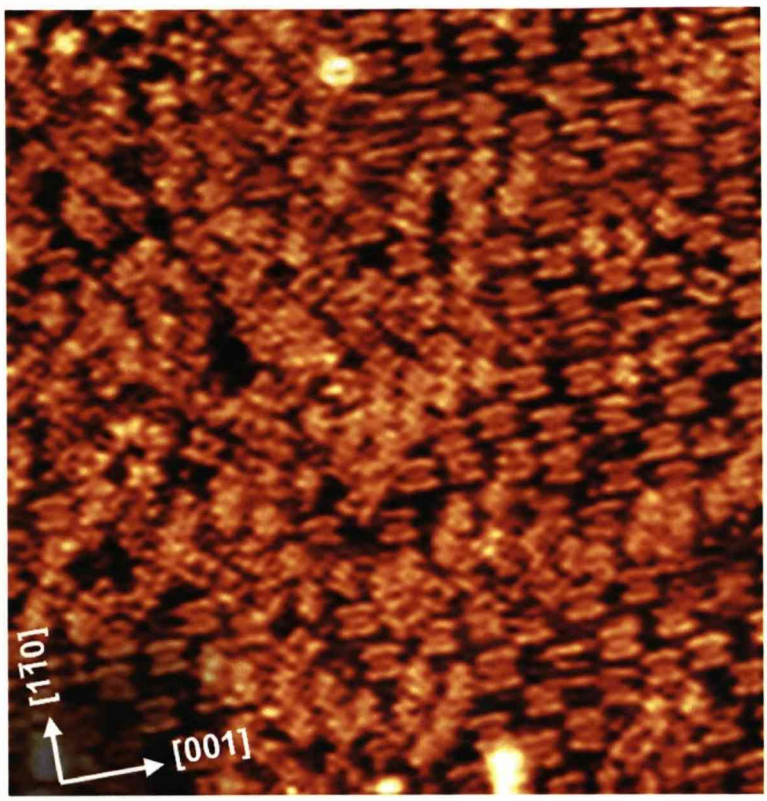

Figure 6.1-1. Substrate-aligned single molecules cluster in regions of high molecular density. Image conditions: (left) 279×287, I_T=0.44nA, V=630.5mV, (right) 502×386Å^2, I_T=0.40nA, V=630.5mV.

The substrate-aligned molecule shares its main symmetry axes with those of the copper. An aspect ratio of 1.2±0.1 has been deduced from the STM images, which is indicative of significant distortions (Figure 6.1-2).

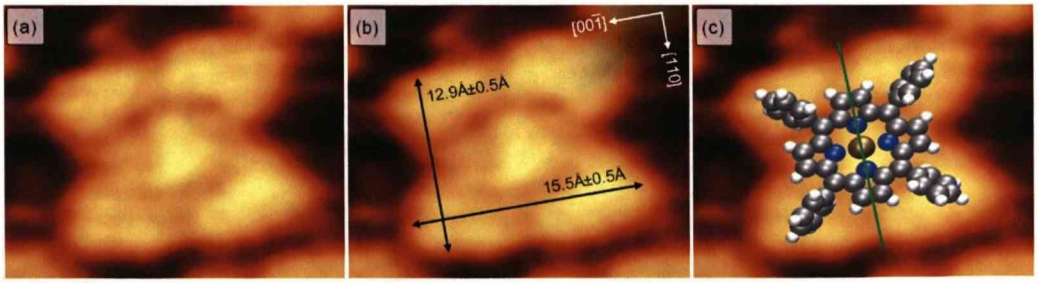

Figure 6.1-2. (a) The substrate-aligned orientation of individual Co-TPP molecule on Cu(110). The dimensions of the molecule are shown in (b), while (c) shows the position of the molecule relative to the STM image. The green line in (c) shows the orientation of the molecule. An arbitrary molecular conformation is shown in (c). Image conditions: 23×18Å^2, I_T=–0.44nA, V=–773.0mV.

The adsorption site of the achiral molecules has been determined. Using the model of Structure 2 (Figure 5.1-3), molecules that occupy the same copper row have been identified and this has allowed the grid of the top layer of copper atoms to be placed onto an STM image containing both Structure 2 and the single molecules. From the resulting image, which is shown below in Figure 6.1-3, it is concluded that the substrate-aligned single molecules most likely adsorb at the long-bridge site of the copper substrate (shown inset). There is some uncertainty in the assignment of the adsorption site for some isolated molecules and this is expected to be due to a tip-induced movement of the molecule along the Cu[1-10] direction during the scan.

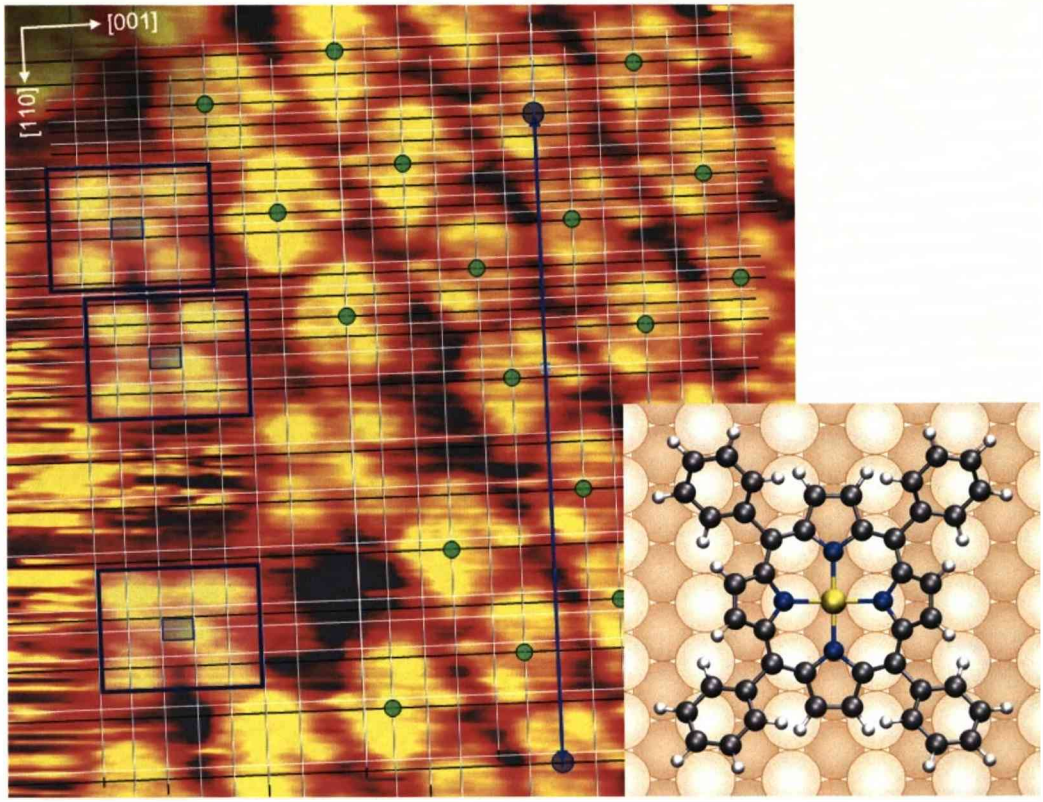

Figure 6.1-3. (a) Determination of the adsorption site of the substrate-aligned single molecule. Black lines link the assumed short-bridge adsorption sites (shown by green spots) of Structure 3 Co-TPP molecules. White rows are the copper rows. The measurement between molecules occupying the same copper row that was compared to the model is shown by the blue line, of which an accuracy of better than ±0.3° was achieved. The ratio of short to long lattice parameter measured using the grid is accurate to within 3%. Dark blue boxes enclose single porphyrins, with smaller boxes inside surrounding the Co centres. The long-bridge adsorption site is shown inset. Image conditions: 84×83Å^2, I_T=–0.49nA, V=–1250mV.

Molecules in close quarter confinement adhere to strict rules governing their interactions, resulting in a number of intermolecular separations that are dictated by repulsive forces, illustrated in Figure 6.1-4. The smallest observed separation is between molecules that are roughly aligned in the Cu[1-10] direction. The small lattice space of 2.55Å allows for 'fine-tuning' of the intermolecular separation in this direction, as opposed to the Cu[001] lattice space, which only allows larger jumps of 3.6Å. A jump of a single lattice space in the Cu[001] direction can result in strong repulsion by overlapping of phenyls. As is the case for the minimum separation (shown in the blue box in Figure 6.1-4), precise separations are also determined by the interlocking of phenyl groups, in which phenyls from different porphyrins situate between each other. This interlocking has already been observed in

ordered Co-TPP structures on Cu(111)[31]. The adsorption site locus, the line representing the nearest possible adsorption site of nearby molecules, (Figure 6.1-4(c)) shows the scope of the separation changes with respect to the copper surface. The combination of 'fine-tuning' and interlocking of phenyls in the Cu[1-10] direction is clearly seen as minima in the distance of the locus from the porphyrin core.

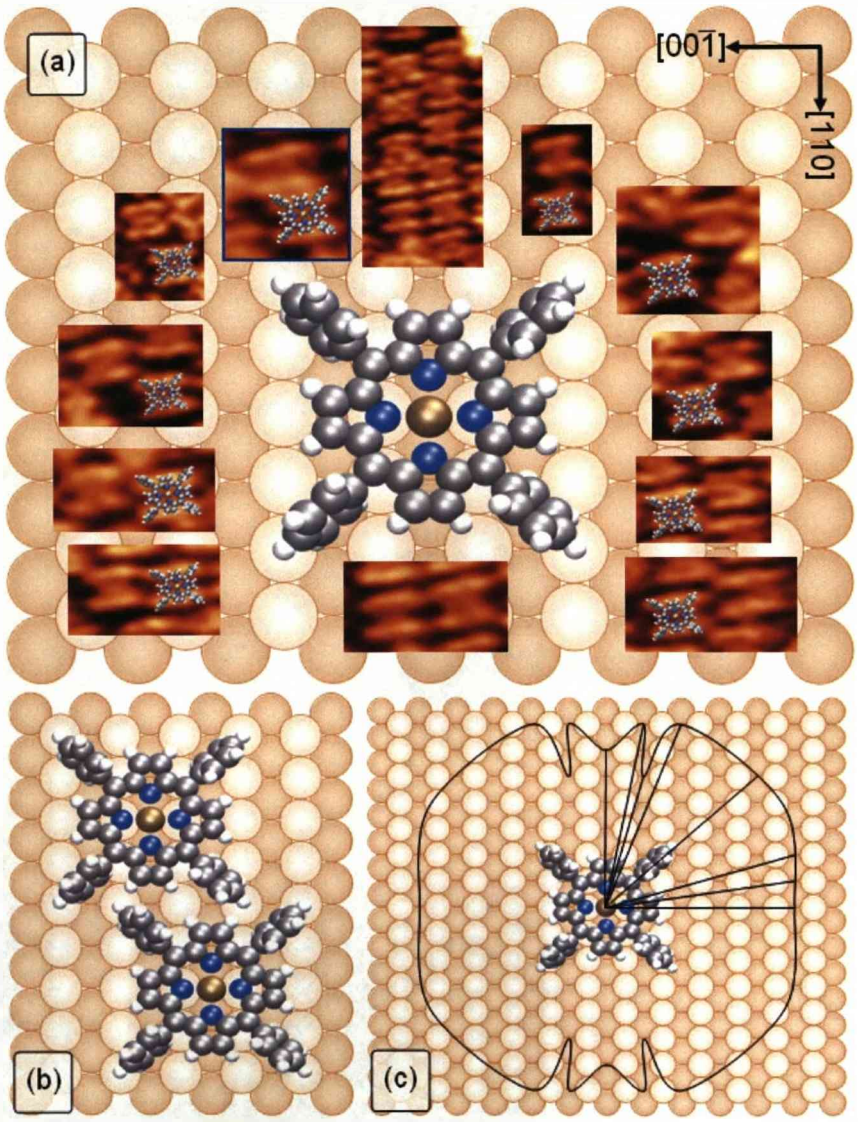

Figure 6.1-4. (a) Selected intermolecular separations observed for the substrate-aligned single molecule. The molecule in the centre represents the overlaid molecule in the small images. (b) The conformation shown by the blue-highlighted image in (a) is the smallest possible intermolecular separation for the achiral molecule, the model of which is shown on the right. (c) Adsorption site locus for substrate-aligned Co-TPP on Cu(110). The boundary represents the nearest possible adsorption site for other achiral Co-TPP molecules. Lines inside the locus show observed intermolecular separations. Molecular conformation is assumed.

Single molecules in the substrate-aligned configuration often have at least one other molecule on or very near its adsorption site locus. This clustering can be seen in Figure 6-1. The character of any present intermolecular interactions between substrate-aligned molecules is unknown at the time of writing although it is assumed that the interactions are attractive due to the number of immobile clusters at the surface.

An unusual and presently unexplained observation in the substrate-aligned molecules is that of an asymmetric distribution of electron density within the core, as shown in Figure 6.1-5. This effect is not always observed and it is thought to be a tip-related effect; a suggestion that is supported by its appearance in only one data set. The density is always imaged to the right of the molecule's centre. The significance (if any) of the observed electron density asymmetry in Co-TPP therefore has not yet been established although well defined switching and asymmetric core intensity has been observed, but not explained, in other unpublished work on cobalt porphyrins on Cu(110).

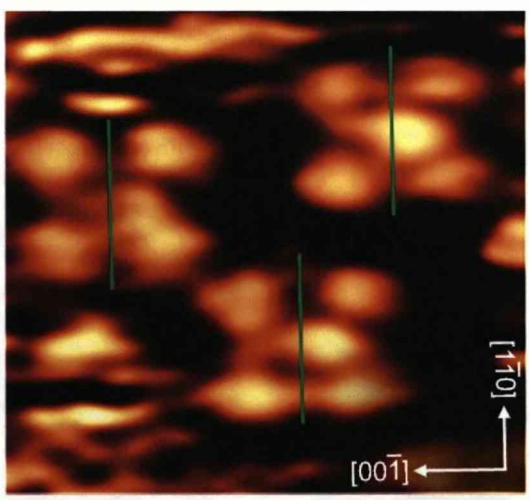

Figure 6.1-5. Asymmetric electron density in the macrocycle of individual substrate-aligned molecules. Core density is shifted to the right of the molecule's vertical symmetry axis (green line). Image conditions: 43×39, I_T=0.46nA, V=1250mV.

There are features observed around some of the substrate-aligned molecules that resemble the suspected adatoms detailed for Structure 1 and 3, indeed, their position relative to the molecule is similar. These features

occur only rarely and their appearance is not understood. Figure 4.8-1 and Figure 5.2-9 show these features alongside a model depicting their position relative to the molecules.

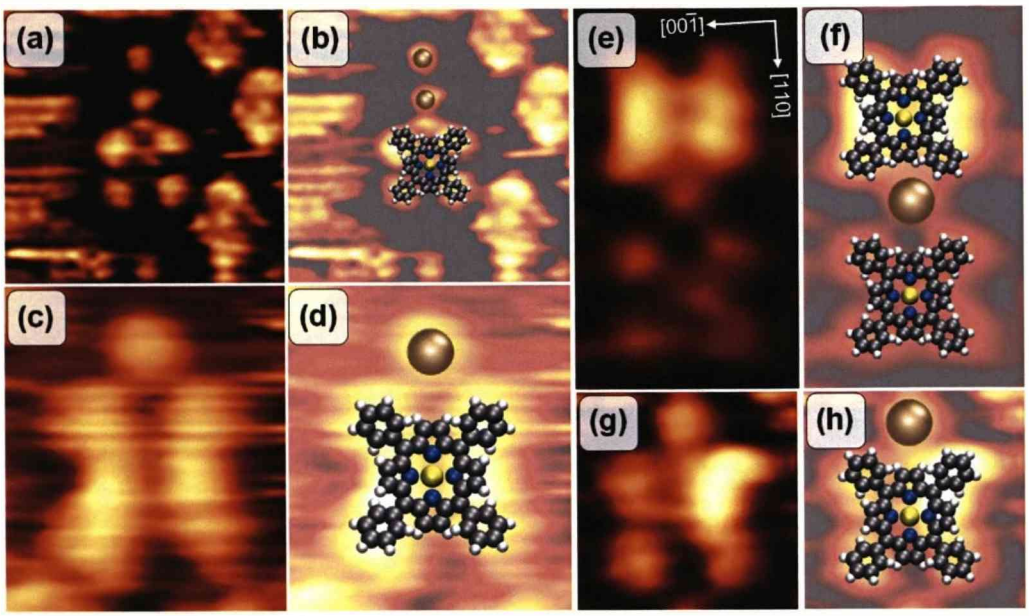

Figure 6.1-6. Possible presence of adatoms around substrate-aligned molecules. (a) and (b) Two features are observed above a single molecule. Other domain-bound molecules can be seen nearby. (c) and (d) Molecules with different electronic and/or conformational properties attract the features also. (e) and (f) Trapping of features between molecules. (g) and (h) Another appearance of the feature. The suspected Cu atom is shown oversized in (b), (d), (f) and (h). Molecular conformation is assumed and the copper axes in (e) applies to all images in the figure. Image conditions: (a) 51×46Å^2, I_T=0.49nA, V=1250mV, (c) 20×25Å^2, I_T=0.49nA, V=1250mV, (e) 21×43Å^2, I_T=0.52nA, V1250mV, (g) 24×26Å^2, I_T=0.37nA, V=1250mV.

6.1.1. Substrate-aligned molecule DFT calculations

To determine the adsorption characteristics of substrate-aligned molecules adsorbed at the long-bridge site identified in Figure 6.1-3, periodic Density Functional Theoretical calculations have been performed on this configuration by Matthew Dyer of the University of Liverpool's Surface Science Research Centre. The calculated molecular conformation is shown in Figure 6.1-7.

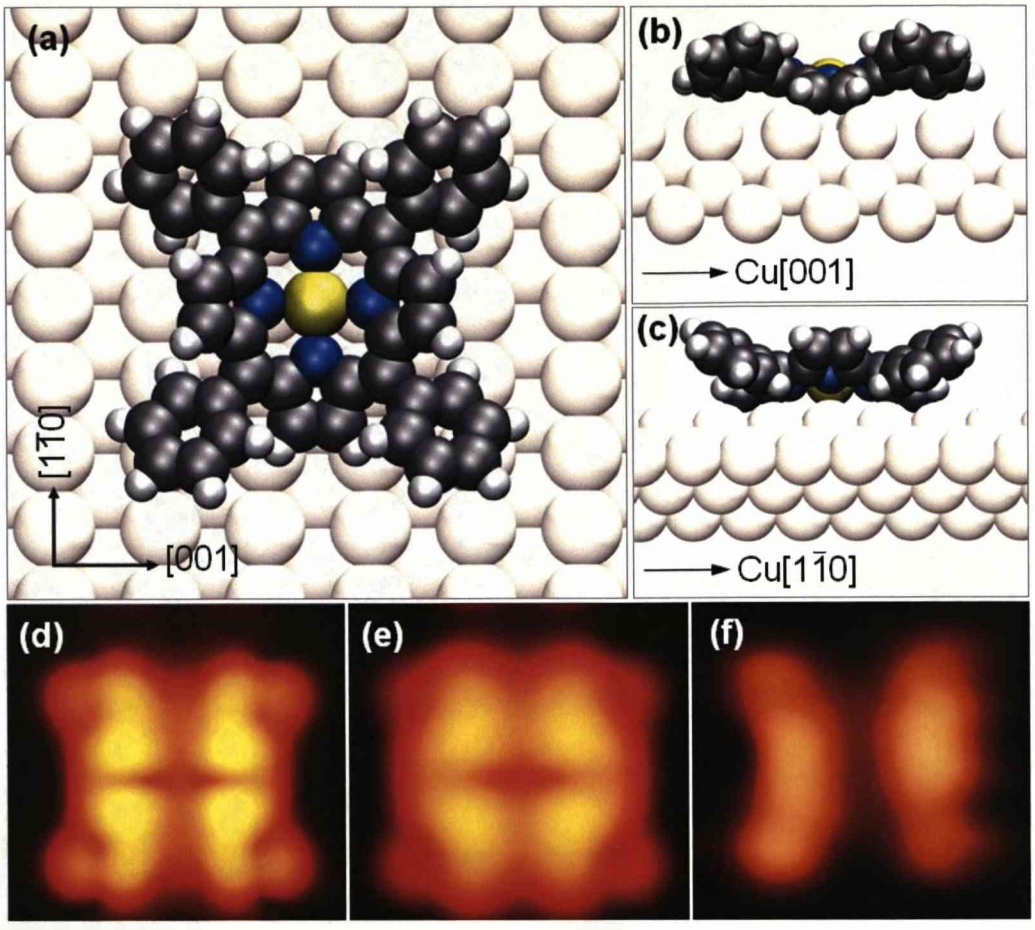

Figure 6.1-7. DFT calculation of the adsorption of a substrate-aligned Co-TPP molecule at the long-bridge adsorption site of Cu(110). (a) the top down view shows the extent of the twisting of the phenyl rings. (b) The molecule, when viewed along the [1-10] axis and (c) along the Cu[001] axis, show the large saddling of the core and twisting /tilting of the phenyls. Calculated STM images of the molecule at 1250mV at tip-surface heights of 7Å and 10Å, respectively, are shown in (d) and (e). (f) Experimental single molecule image at V=1250mV, I=0.4nA (19×20Å^2). Copper axes in (a) apply to (d) – (f).

The calculated lowest energy configuration is a molecule that undergoes considerable distortion on adsorption. Saddling of the macrocycle is induced despite the relative stiffness of the core[32]. Significant bending of core pyrrole groups results, with groups aligned with the Cu[001] axis tilted upwards by 32° (Figure 6.1-7(c)) and the Cu[1-10]-aligned pyrroles tilted down by 11-12° (Figure 6.1-7(b)), both with respect to the surface plane. Pyrrole bending deformations of 20°, 35° and 45° have been observed elsewhere[21,22,31]. Pyrrole bending was determined by calculating the angle between the normals to the pyrrole and the surface planes. The pyrrole groups themselves are distorted away from planarity so the plane through

their nitrogen and both β carbons has been used for the calculation. Tilting and twisting (defined in section 4.5) of the phenyl groups combine to situate them almost flat against the substrate, explaining the broadened features observed in the STM data. Despite the shared symmetry of the preferred adsorption site and the molecule, the calculation has each phenyl exhibiting a slightly different distortion, with tilt and twist angles in the ranges of 167-170° and 29-30° respectively.

The saddling of the core is proposed to be a consequence only of steric repulsion from the phenyl rings, rather than a direct result of the core's interaction with the substrate. In a strong parallel to the Structure 1 calculations, the Co atom in the core is situated very close to the substrate atoms, at only 2.4Å (vertical distance from the plane through the top layer of copper atoms). As the molecule adsorbs the phenyl rings experience a repulsive interaction with the substrate, having induced in them a pairwise disrotary twist[23,32] that is characterised by the two pairs of diametrically opposite rings twisting in opposite directions to each other. According to Wölfle *et al*[32], twisting is more favourable than tilting of the phenyl rings (Figure 4.3-7) and without the presence of significant intermolecular interactions, the isolated molecules adapt to the surface by this method, incurring the least losses as it does so. As the phenyl twist angle continues to decrease, steric repulsion begins to force the macrocycle pyrroles up where the phenyls twist under them and down where the phenyls twist over, as shown in Figure 6.1-8. Additionally, it is expected that the saddle is exaggerated by the small but notable tilts of the phenyls. The total cost of deformation for the single substrate-aligned molecule is has been calculated to be E_{DEF} = +117kJmol^{-1}. The total cost of all deformations will be summarised in the next section.

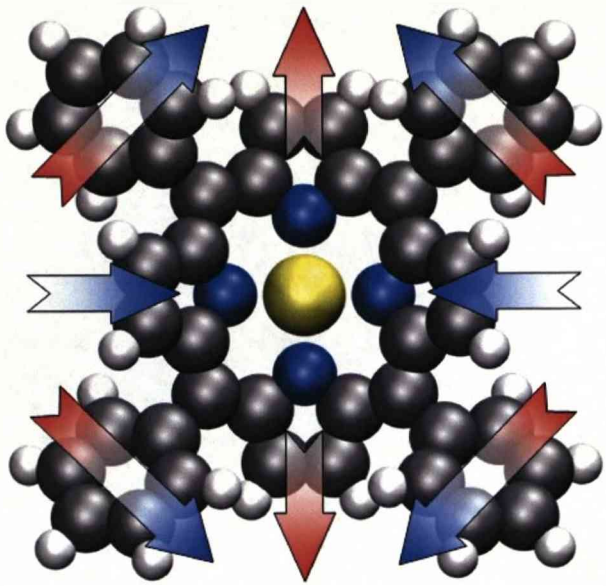

Figure 6.1-8. Adsorption induced conformation of an isolated Co-TPP molecule on the Cu(110) surface. Blue indicates parts of the molecule that are above the molecular plane and red represents parts of the molecule that are below. The arrows indicate the direction of tilt/twist. The core pyrroles react repulsively to the twisting of the phenyls, rising above the molecular plane as the phenyls twist below (left/right) and dropping below the molecular plane as the phenyl twists over (top/bottom). The result is an conformationally adapted molecule.

Topographical information for the single molecule cannot be deduced directly from the STM data. As observed in the Structure 1 TB-1 interaction (Figure 4.5-1 and Figure 4.5-3), the phenyls of the single molecules appear to have roughly the same heights across their extent despite having a significant twist angle (Figure 6.1-9): They should appear as a wedge with a gradually increasing height but do not.

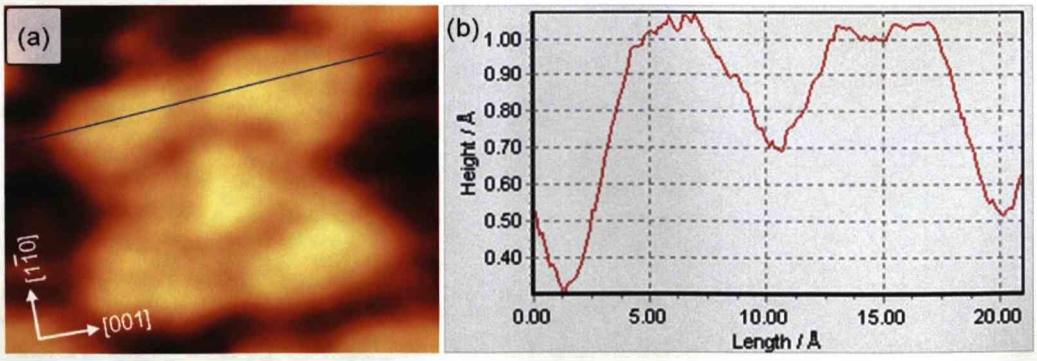

Figure 6.1-9. Phenyls of the substrate-aligned molecules exhibit roughly the same relative height across their extent as shown by the line scan, limiting the amount of topographical information that can be gained from the STM data. Image conditions: 23×18Å^2, I_T=–0.44nA, V=–773.0mV.

In addition to having constant height, the electron density in the STM data associated with the single molecule phenyl rings is also smeared over an area much greater than the area of a flat-lying Benzene ring. Importantly, this is corroborated by the calculated STM images, which also show the same large areas of density outside of those covered by the rings themselves (Figure 6.1-10). This smearing is consistent throughout the calculated images, and results in an aspect ratio for the electron density of 1.1, compared with a molecular aspect ratio of 1 (measured from the calculated images directly). The agreement between the STM images and the DFT images is arguable, however. The calculated STM images show some correlation with the experimental data for negative biases (Figure 6.1-10) but show none of the same features at positive biases.

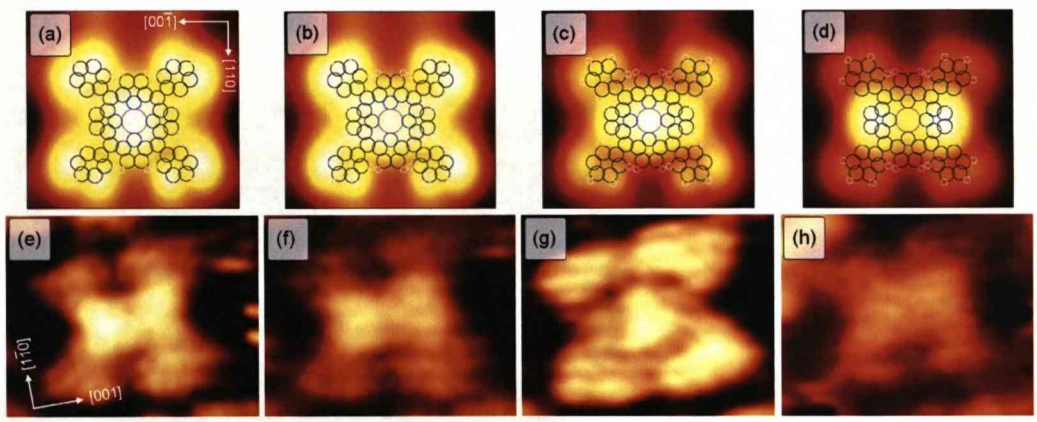

Figure 6.1-10. Comparison between DFT and experimental STM data for the single substrate-aligned molecule. DFT images are on the top row with conditions of (a) -320mV, (b) -500mV, (c) -750mV and (d) -1500mV. The corresponding STM images were taken at (e) 23×20Å^2, I_T=–0.55nA, V=–320.7mV, (f) 20×18Å^2, I_T=–0.58nA, V=–524.3mV, (g) 23×18Å^2, I_T=–0.55nA, V=–773mV and (h) 21×17Å^2, I_T=–0.59nA, V=–1546mV. In (a) to (d), the calculated asymmetry in the phenyl groups can be seen between the bottom two rings. Copper axes in (a) apply for the top row and axes in (e) apply for the bottom row.

Importantly, there are two factors that add ambiguity to the comparison between and interpretation of the data. Firstly, there is no consistency in the way the single achiral molecules have been imaged over the entire range of biases. They have been imaged identically using entirely different conditions and imaged differently using identical conditions. As previously stated, good imaging of the single molecules occurs when the STM tip is not performing particularly well for the structures, therefore, it can

never be ascertained as to whether the tip is in the same condition as in a previous experiment, given the number of variables. Secondly, the DFT calculations do not incorporate the effect of other molecules that situate on or near the object molecule's adsorption locus, shown in Figure 6.1-4. A large 8×6 unit cell was used in order to simplify the calculation and consequently minimise the computational power required. Despite the large unit cell, a little intermolecular interaction can be seen in the Cu[1-10] direction. Further disagreement can therefore be explained in terms of possible interactions between achiral molecules that affect how the phenyl groups are imaged, as exemplified in the top-most STM image in Figure 6.1-4, however, in strong support of the calculations, there are corresponding STM images of single achiral molecules for most of the calculated data (Figure 6.1-11), despite a mismatch in the bias. As a result of the uncertainty in the function of the STM and generally good STM-DFT agreement, it is proposed that the DFT-calculated single molecule configuration is an accurate representation of the real system. Of course, performing the calculations with the molecule in different adsorption sites would have been useful in solidifying this conclusion.

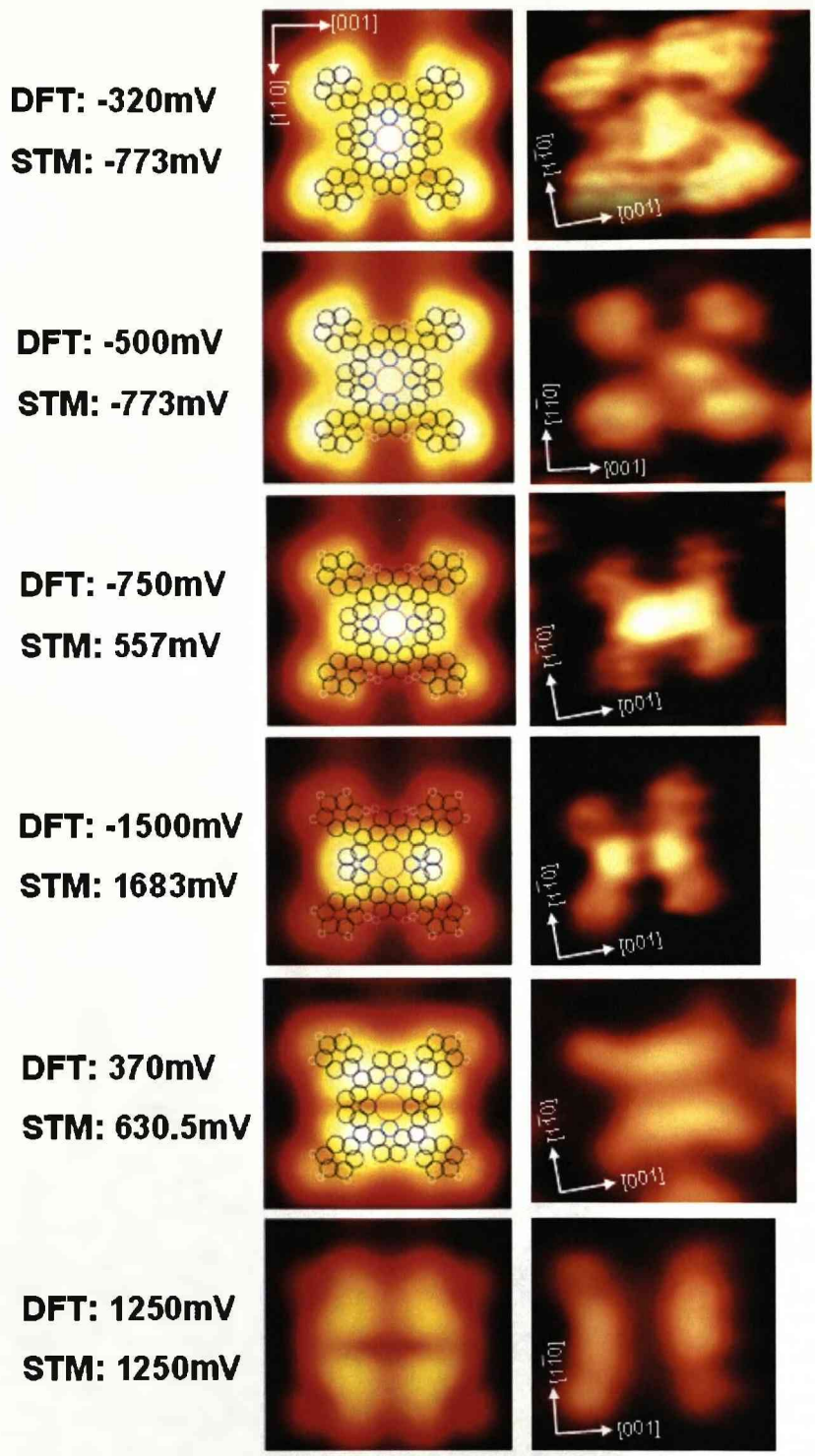

Figure 6.1-11. Image matching between calculated and experimental STM images. Bias voltages can differ dramatically but yield similar images. Shown copper axes are for the experimental STM images. The same axes are horizontal for the calculated STM images. Copper axes in the topmost calculated image apply to all calculated images. Experimental STM image conditions (from top down): 20×16Å^2 and I_T=–0.55nA, 20×17Å^2 and I_T=0.48nA, 25×21Å^2 and I_T=0.51nA, 24×26Å^2 and I_T=0.52nA, 23×19Å^2 and I_T=0.49nA, 30×28Å^2, 19×20Å^2 and I_T=0.43nA.

6.1.2. Substrate-aligned molecule net energy balance

Accompanying the cost of molecular deformations is a small substrate deformation that amounts to +19kJmol^{-1}. This leaves a total cost for the entire system of E_{COST} = +136kJmol^{-1}.

$$E_{NET} = E_{MOL-SUR} + E_{COST} \qquad \textbf{6-1}$$

Substituting an attractive molecule-surface interaction of $E_{MOL-SUR}$ = –232kJmol^{-1} into Equation 6-1, the net adsorption energy for the single substrate-aligned molecule is found to be E_{NET} = –232kJmol^{-1} + 136kJmol^{-1} = –96kJmol^{-1}. Comparing this value with that found for the Structure 1 molecule when disregarding intermolecular interactions (–95.4kJmol^{-1}), it can be seen that it is only marginally greater in magnitude.

6.2. Chirally oriented single molecule

The chiral orientation of single molecule is mostly observed alongside existing domains. Its main symmetry axis is rotated by ±40°±2° from the Cu[1-10] axis, making its alignment close to that of molecules in the organised structures (Figure 6.2-1). Its aspect ratio is similar to that observed substrate-aligned single molecule at 1.21±0.1, however the molecule itself is expected to be closer to square, as depicted in Figure 6.2-1c.

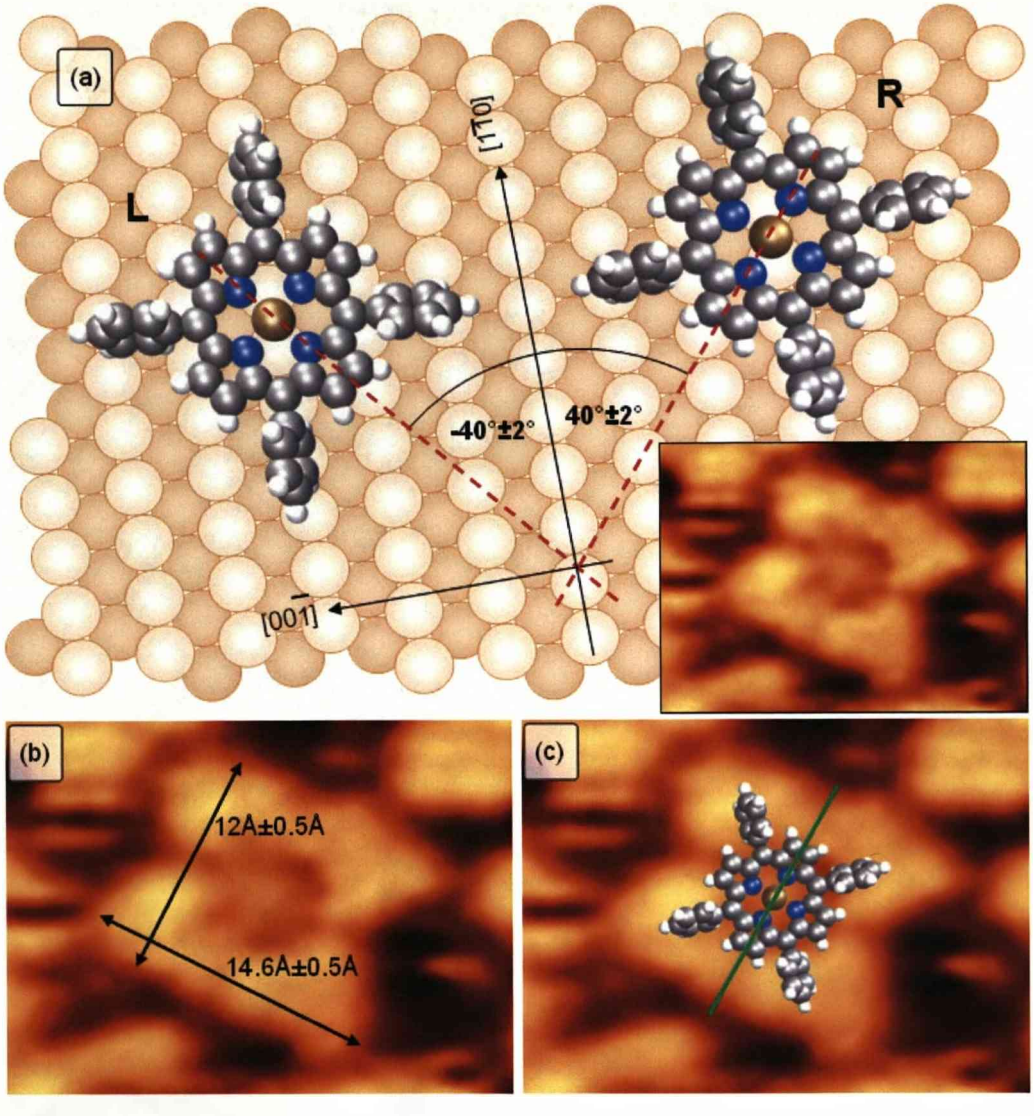

Figure 6.2-1. (a) The L and R orientations of the chirally oriented single molecule showing the alignments of ±40°±2° to the Cu[1-10] axis. Inset: an STM image of the R configuration. Image conditions: 27×20Å^2, I_T=−0.55nA, V=−773mV. The dimensions of the molecule are shown in (b), while (c) shows the expected position and orientation of the molecule relative to the STM image. The green line in (c) highlights the orientation (and symmetry axis) of the molecule. An arbitrary molecular conformation is presented. The copper axes in (a) applies to all images. Molecular conformation is assumed.

The adsorption site of the chirally oriented single molecule has been ascertained in Figure 6.2-2, which models the change in orientation of a single substrate-aligned molecule to a chiral orientation in the presence of ordered structures. The figure clearly shows a rotation of the single molecule about its bottom-right phenyl ring, thus moving the Co atom from a long-bridge site to a short-bridge site of the copper lattice. The short-bridge adsorption site and 40° rotation of the molecule allows phenyl pairs to

accommodate themselves between the copper rows, similar to the way they would in Structure 1.

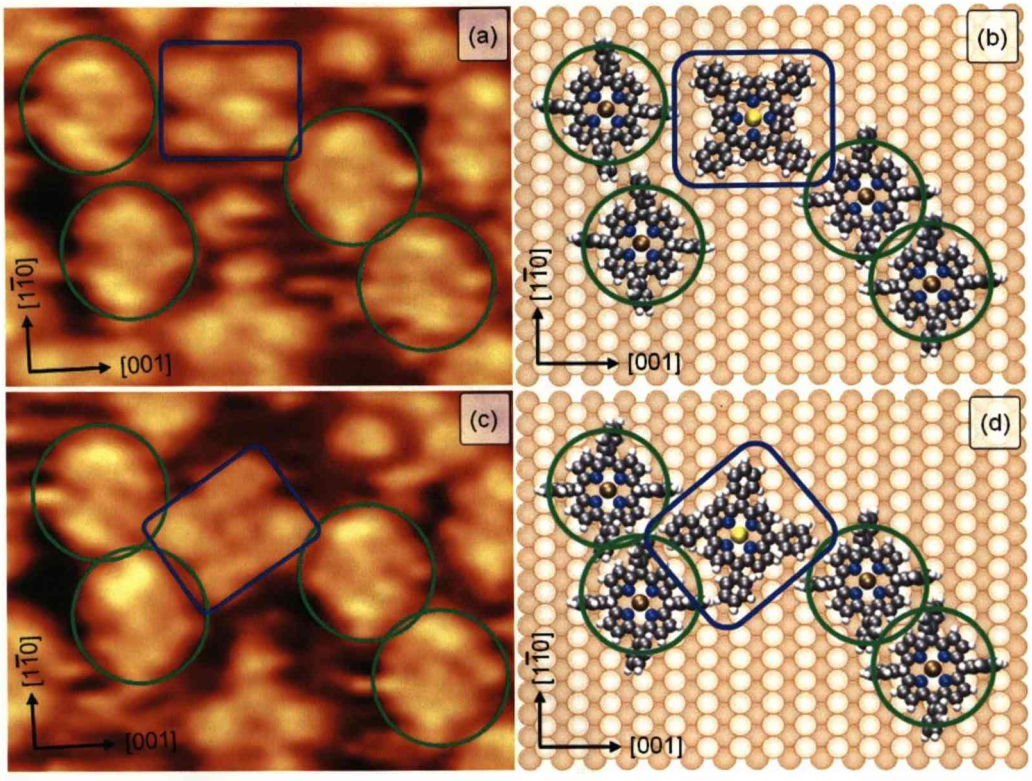

Figure 6.2-2. Changes in orientation to a chiral orientation are observed in the single molecule. The real space structures (b) and (d) relate to STM images (a) and (c) respectively. The single molecule is inhibited from joining the left hand side domain by the directionality of the only available LR interaction, which is incompatible. This possibly hinders the molecule from joining the domain on the right, despite being in the LR-1 position. The adsorption site of the single molecule goes from the long-bridge to short-bridge site from (a) to (c). Molecular conformation is assumed in both (b) and (d). Image conditions: (a) 56×43Å^2, I_T=0.4nA, V=1250mV, (c) 57×43Å^2, I_T=0.49nA, V=1250mV.

Chirally oriented single molecules are typically observed near or adjacent to assembled domains and a rare few appear to be confined by repulsive interactions to regions so small that appear not to be able to allow for a change in orientation, as shown in Figure 6.2-3.

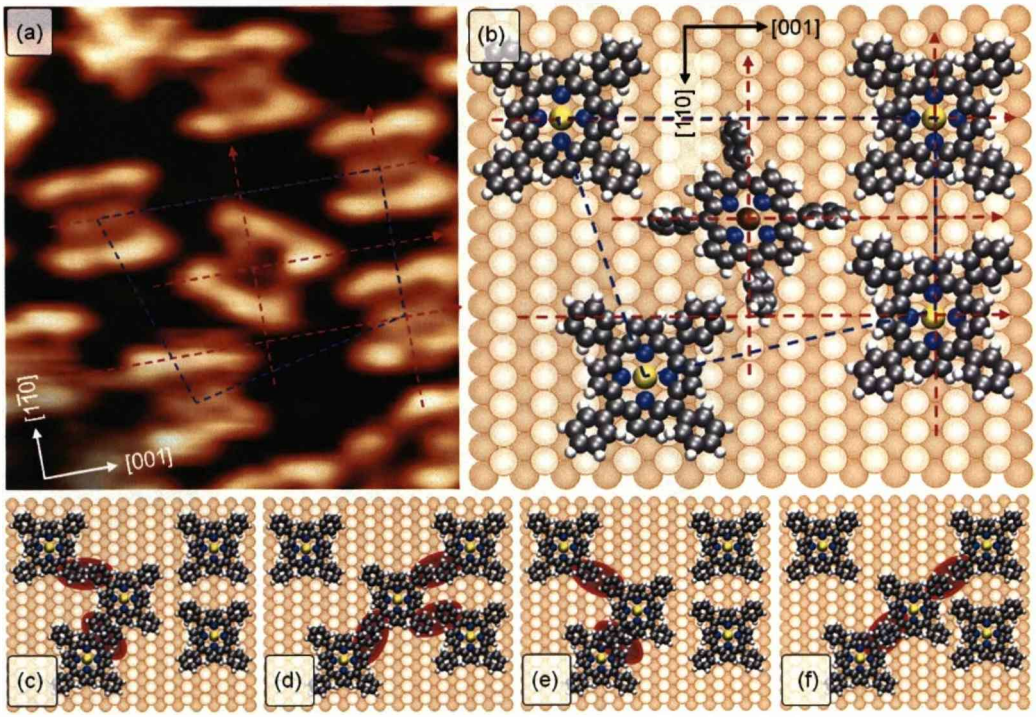

Figure 6.2-3. (a) A single chirally oriented molecule 'trapped' between several substrate-aligned molecules. (b) Model of the STM image. Red and blue dotted lines between molecular centres in (a) have been overlaid onto the model with a maintained aspect ratio. (c) – (f) show the overlapping of phenyl groups that arises from the central molecule changing to the substrate-aligned conformation and moving to any of the four long-bridge sites surrounding its original short-bridge site. Molecular conformation of the chiral molecule in (b) is assumed.

Furthermore, there are observed several possible conformations of the chirally oriented molecule that are distinguished by the configuration of phenyls. In some observations they remain in their nearly-flat configuration, having similar apparent height and a broad nature as in the substrate-aligned conformation (left image of Figure 6.2-4), while in other STM data the phenyl pair aligned with the Cu[001] axis becomes more prominent, possibly due to greater relative height (right image of Figure 6.2-4). This increased apparent height is indicative of an anisotropic change in the twist angles of the diametrically opposite phenyl pairs and suggestive of a more Structure 1-like molecular conformation for the molecule in this image.

Figure 6.2-4. 3D visualisation of the chirally oriented molecule shows two conformations. Left: The chirally oriented molecule (bottom-left) next to and interacting only very weakly with substrate-aligned molcules. A very dim core and equal phenyl heights indicate a similar conformation to the achiral molecules but with a different substrate interaction. This could be a trapped molecule, as in Figure 6.2-3. Right: The chirally oriented molecule shown in Figure 6.2-2 wedged between two ordered structures. The phenyl pair aligned with the Cu[001] axis shows greater apparent height/intensity than the other pair, suggesting that they are upright (greater twist angle).

6.3. Switching single molecule

The rarest single molecule is a switching orientation, of which only one clear observation has been made. This means only one orientation and/or chirality has been observed, however, given its rotation and the presence of two mirror forms of the first chiral form, it is unlikely that this orientation would not adopt a mirror opposite under the right conditions, unless a significant change to the symmetry of the underlying copper lattice is induced. A rotation of 76°±2° is observed for this orientation. This conformation has an aspect ratio of 1.12±0.9, i.e. its appearance in the STM images is that of a less distorted molecule than both the achiral and chiral 1 conformations. It is suspected that the alignment of the molecule in the other orientations, having similar symmetry axes to that of the copper substrate, would be preferred hence the relative rarity of this orientation compared to the other achiral and chiral conformations. The adsorption site is unattainable with the available data.

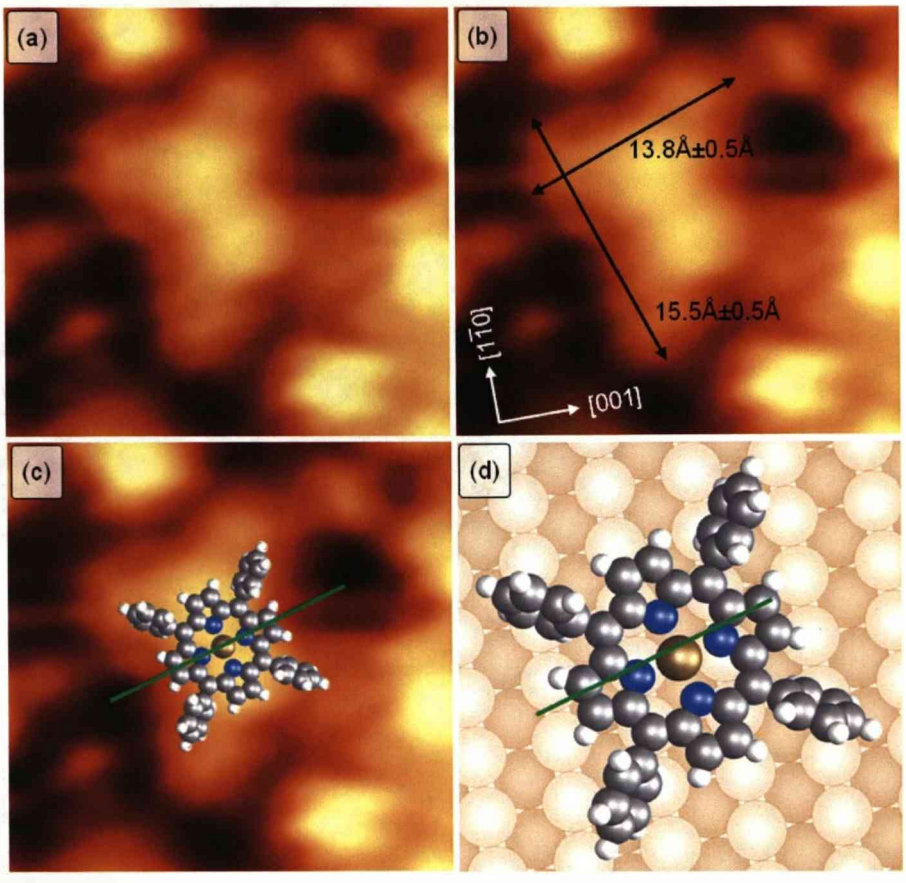

Figure 6.3-1. (a) The switching molecule. Image conditions: 25×24Å^2, I_T=0.51nA, V=758mV. (b) The aspect ratio of the molecule in this orientation is similar to other single molecule conformations. (c) The anticipated orientation and position of the molecule on the STM image. (d) The molecule relative to the copper lattice of the surface. Molecular conformation is arbitrary.

The conditions required for this conformation to occur are unknown, however, single molecules have, on several occasions, been observed switching between achiral and both chiral orientations. The sequence of STM images in Figure 6.3-2 shows the clearest instance. In the figure, the molecule is surrounded by both domain-bound and immobilised achiral molecules, therefore, it is suspected that competing forces are responsible for the changes in orientation, the nature and/or magnitude of which are impossible to detail with the available data.

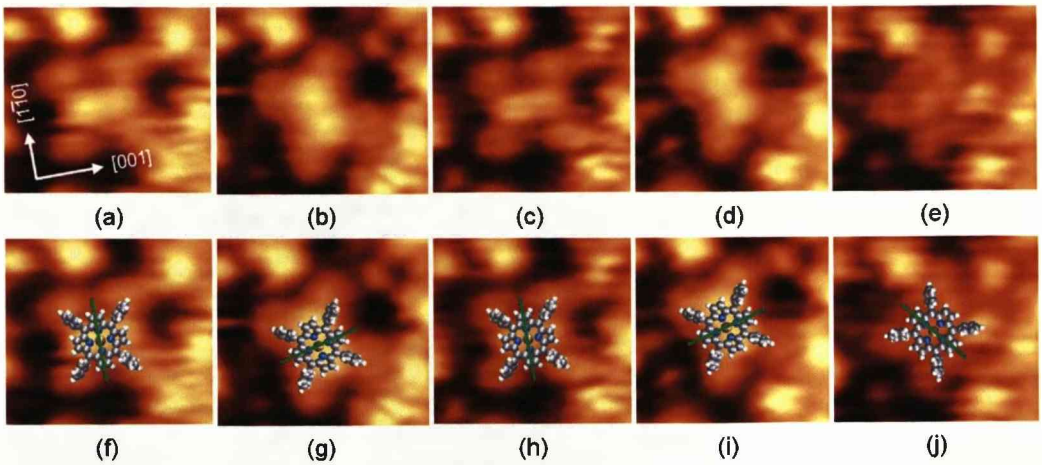

Figure 6.3-2. Orientation switching in the single molecule. The molecule switches from achiral (a), to switching (b), back to the achiral (c), back to the switching (d) then to the chiral (e) orientations respectively in this sequence of STM images. Scan time between images is 45s. The adsorption site has not been ascertained for (b) and (d). (f) to (j) show the positions of the molecule (with arbitrary conformation) on (a) to (e) respectively. Copper axes in (a) apply to all images. Image conditions: (a) 26×23Å^2, I_T=0.47nA, V=630.5mV, (b) 26×23Å^2, I_T=0.5nA, V=557.5mV, (c) 26×23Å^2, I_T=0.51nA, V=557.5mV, (d) 24×25Å^2, I_T=0.51nA, V=758mV, (e) 26× 23Å^2, I_T=0.5nA, V=901.2mV.

Single molecules adopt a saddled conformation that has been observed in previous work[21,27,31,54,87,88], however, significant changes must be made in order for them to join a domain. This is discussed in the following chapter.

CHAPTER 7

Co-TPP on Cu(110) – Discussion, Conclusion and Outlook

The adsorption and self-assembly of Co-TPP molecules on Cu(110) produces a wealth of structure and complexity. The preceding chapters have endeavoured to characterise all of the observed organised structures and the single molecule phase. This chapter links the observed phenomena by a discussion of the role of single molecules in domain formation and the relationships between the ordered structures.

7.1. Domain formation from single molecules

Single molecules generally have no significant interaction with other molecules on the surface and they are observed in three distinct orientations: one whose symmetry axes align with those of the copper and two with a chiral orientation (Table 7.1-1). The copper-aligned single molecule is observed relatively frequently and adopts a saddled geometry as it adsorbs at the long-bridge site. Other orientations are rare and are generally observed in close proximity to organised structures, or in confined regions of the surface.

Table 7.1-1. Single molecule summary table.

Copper-aligned	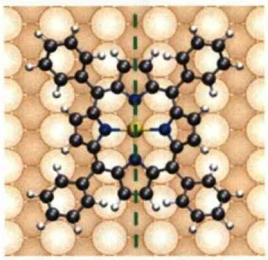	±0°
Chiral orientation	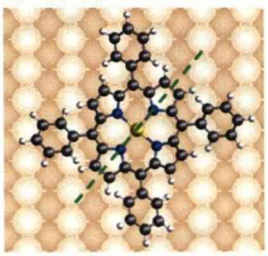	±40°
Switching molecule	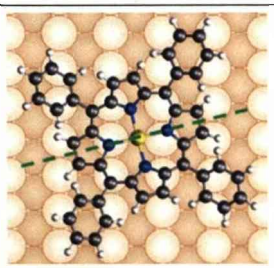	76° (only one observation)

The relative numbers of the three orientations of single molecule (Chapter 6) appear to reflect their respective involvement in domain formation and/or growth. The substrate-aligned orientation (section 6.1) is essentially inert on the surface and it does not appear to be directly involved in domain formation. Large numbers of this type are consequently observed relative to the other orientations. Conversely, there have been relatively few observations of the chirally oriented single molecule (section 6.2), suggesting that this type is accommodated within the ordered structures. The switching single molecule (section 6.3) is another such example.

The transition of the substrate-aligned to the chiral orientation appears to be a necessary step for the former to become part of a domain. This transition requires a translation from the long-bridge adsorption site to the short-bridge adsorption site of the copper substrate, which is normally accompanied by conformational changes.

Switching from the substrate-aligned to chiral configuration has been observed in close proximity to domains (Figure 6.2-2), however, a chirally oriented molecule has never been observed definitively joining a domain. This may be due to steric hindrance from adjacent structures or an orientation of the molecule that is incompatible with the potential host domain (Figure 6.2-2). This effect is observed in what is thought to be a parallel case of chiral micro-domains that are incapable of joining host domains due to their incompatible chirality, shown in Figure 7.1-1.

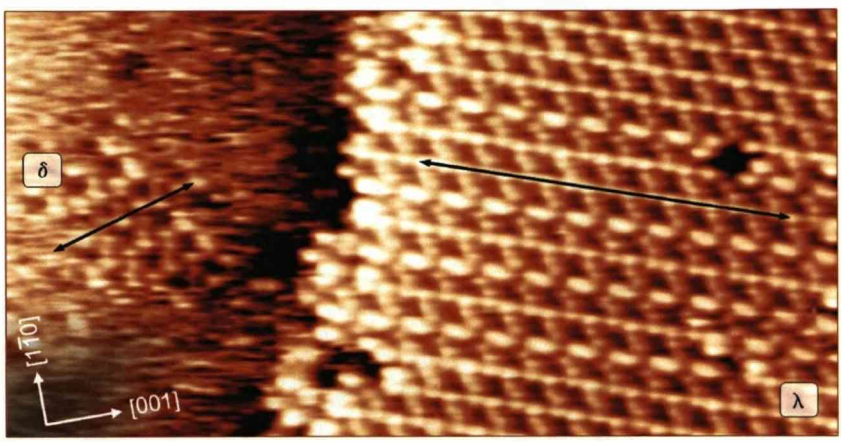

Figure 7.1-1. Chiral micro-domains form during domain growth of Structure 1. Their integration into the host domain depends on their chirality. In this case, a Structure 1 δ micro-domain (left) cannot join the host λ domain on the right. The small region of δ domain subsequently disintegrated. Image conditions: V=611.3mV, I_T=0.24nA, 300×156Å^2.

A further reason could be the presence of competing structures or incompatible intermolecular separations that hinder the molecule from being fully incorporated into a domain. Despite this uncertainty, it remains plausible to argue that the two configurations shown in Figure 6.2-4 are two stages in the transition (Figure 7.1-2), where the first is a change in adsorption site and orientation (left image in Figure 6.2-4 and Figure 7.1-2a-b). The possibility of conformational changes, especially to the macrocycle, during the first step has not been ruled out, although the darkening of the core is suspected to be mostly (if not entirely) an electronic effect as the phenyl rings do not appear to alter their orientation significantly (left in Figure 6.2-4). A subsequent change – an increase in the twist angles of the L and R phenyl rings (Right image in Figure 6.2-4 and Figure 7.1-2b-c) – might only occur as the

molecule comes into contact with other molecules within an ordered domain. This alteration is necessary for the molecule to form the intermolecular interactions necessary for domain formation. A further 5°±2° rotation of the chirally oriented molecule would have to take place that would also allow accommodation of the top and bottom phenyls in the corrugations separating the Cu[1-10] rows (Figure 7.1-2(c)-(d)). Of course, to reach the final Structure 1 conformation (Figure 7.1-2(e)), all of the intermolecular interactions would have to be present.

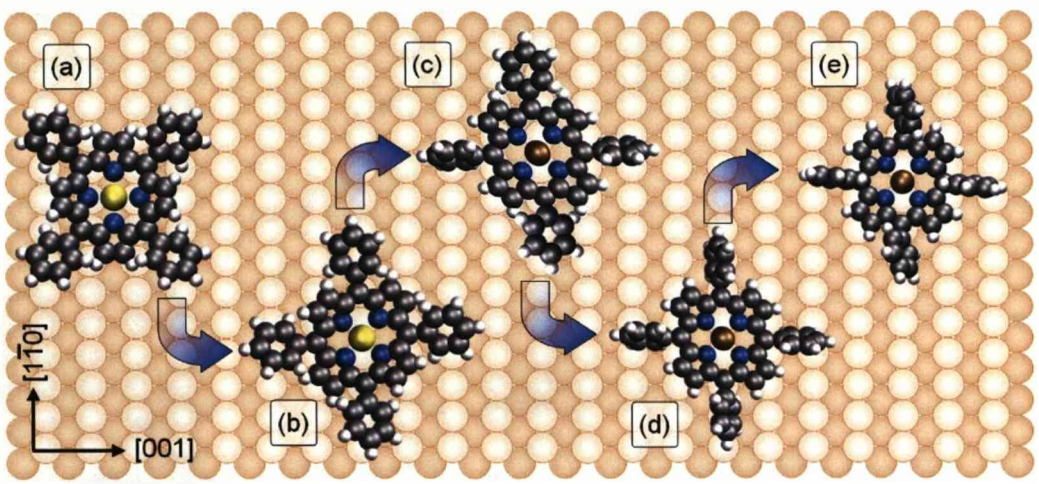

Figure 7.1-2. The proposed transition from the substrate-aligned single molecule to the adsorption in Structure 1 based on STM data. (a) The substrate-aligned molecule in the long-bridge adsorption site. (b) A change in orientation is paired with a move to the short-bridge adsorption site. (c) In the presence of domains, LR intermolecular interactions are made possible by the increase in twist angle of the L and R phenyls. (d) To join the domain, a further 5° rotation of the molecule is required. This allows the T and B phenyls to situate in the substrate corrugations with close to their minimum energy twist. (e) The final Structure 1 conformation. Molecular conformation is assumed for (b) to (d).

The energy of adsorption for the single Cu-aligned molecule (Figure 7.1-2a) and the Structure 1 molecule (Figure 7.1-2e) have been compared. This has shown that the gain in energy due to the substrate interaction and the cost in energy due to deformation of the molecule and substrate are significantly larger for the adsorption geometry adopted within Structure 1 than for a single molecule adsorbed in a long-bridge position ($+268.3 kJmol^{-1}$ compared with $+136 kJmol^{-1}$), but the net adsorption energy, ignoring intermolecular interactions, is remarkably similar for both at around $-96 kJmol^{-1}$. Given that switching is occasionally observed between different

molecular orientations (Figure 6.2-2 and Figure 6.3-2), the barrier to transformation must not be particularly large. It is shown, therefore, that the relatively small amount of energy of $-25 kJmol^{-1}$ gained from intermolecular π–π interactions between molecules assembling into Structure 1 is the crucial difference, and is sufficient to drive a change in adsorption site and conformation from a saddled geometry with highly twisted phenyl groups into a structural conformation with a nearly planar core and strong tilting deformations of the phenyl groups.

7.2. Summary of ordered structures

The Co-TPP on Cu(110) system is extremely adaptive to its local chemical and physical environment and has the ability to minimise its total adsorption energy by employing at least six distinct intermolecular π–π interactions, including two main LR and four main TB interaction types, that combine to form Structures 1, 2 and 3. A summary of the main details of the organised structures and their constituent intermolecular interactions is presented in Table 7.2-1. In the table, the structures are ordered so that they follow a roughly linear pattern of decreasing inter-centroid separation of the π–π interactions. The adsorption phase diagram in Figure 7.2-1 shows the relationship between the observed surface phase and the sublimation conditions of the doser.

Table 7.2-1. Summary of the organised structures, which are ordered in terms of the phenyl-phenyl inter-centroid separation of their constituent inter-molecular π–π interactions.

	Unit cell(s) Information				Inter-molecular Interactions Decreasing phenyl-phenyl separation						
	λ domain	δ domain	No. of Mols	Density (Atoms/Mol)	LR-1 5.4Å	LR-2 5.1Å	TB-1 7.6Å	TB-3 7.2Å	TB-4 4.4Å	TB-2 3.6Å	
Structure 1	$G^{\lambda}=\begin{bmatrix}2 & 4\\ -6 & -2\end{bmatrix}$	$G^{\delta}=\begin{bmatrix}-6 & 2\\ 2 & -4\end{bmatrix}$	1	20	2		2				
Primary Transition Line/Phase	$T_P^{\lambda}=\begin{bmatrix}2 & 4\\ -7 & -2\end{bmatrix}$	$T_P^{\delta}=\begin{bmatrix}-7 & 2\\ 2 & -4\end{bmatrix}$	1	24	2		1	1			LINE
					2			2			PHASE
Secondary Transition Line/Phase	$T_S^{\lambda}=\begin{bmatrix}2 & 4\\ -6 & -1\end{bmatrix}$	$T_S^{\delta}=\begin{bmatrix}-6 & 1\\ 2 & -4\end{bmatrix}$	1	22	2		1		1		LINE
					2				2		PHASE
Structure 3	$G=\begin{bmatrix}12 & 0\\ 0 & 8\end{bmatrix}$		4	24	2				2		
Structure 2	$G^{\lambda}=\begin{bmatrix}4 & 7\\ -7 & -2\end{bmatrix}$	$G^{\delta}=\begin{bmatrix}-7 & 2\\ 4 & -7\end{bmatrix}$	2	20.5	1	1		1		1	

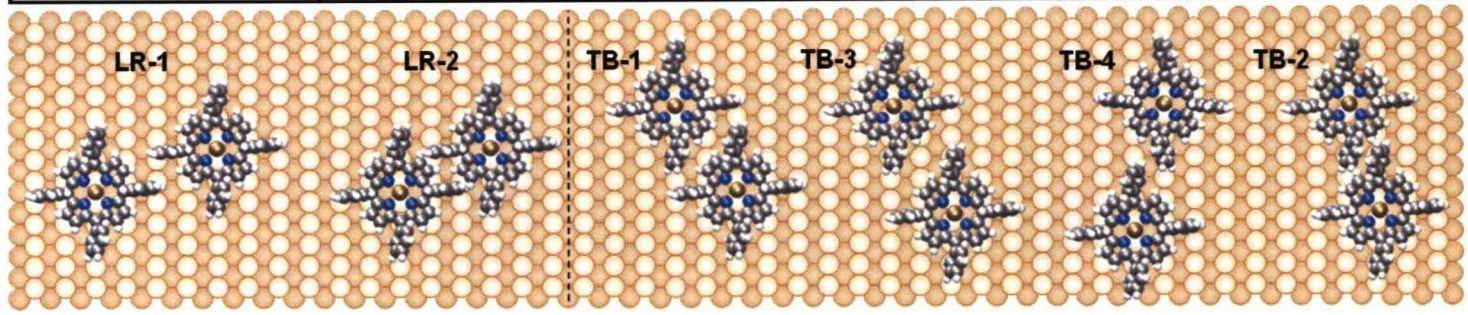

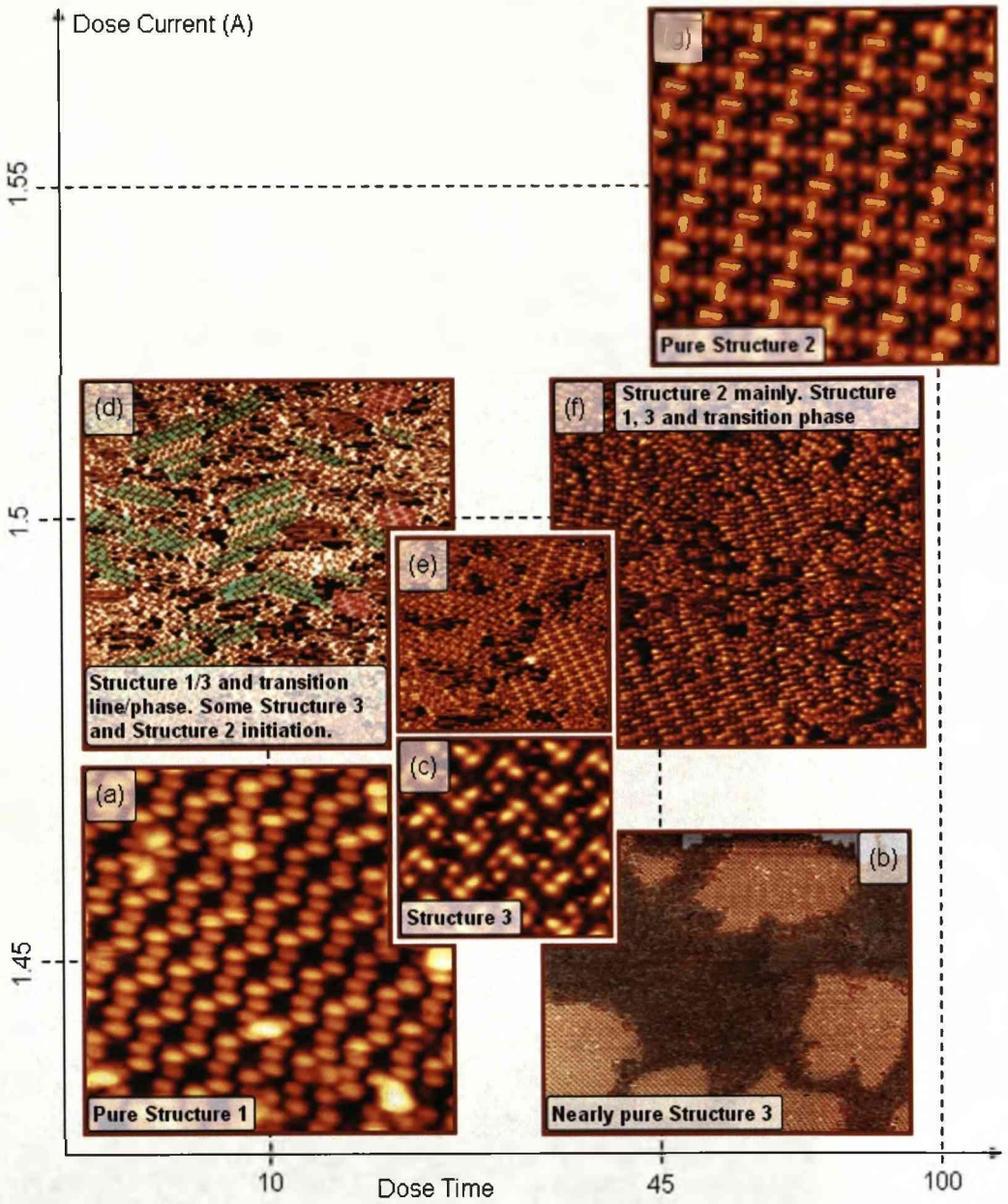

Figure 7.2-1. Adsorption phase diagram for Co-TPP on Cu(110). (a) The pure Structure 1, created under the low flux condition. (b) Structure 3 (bright) has been observed in a nearly pure state under the low flux condition also, but exists over a large sublimation regime, hence its position in the centre of the diagram (c). No pure phase has been observed for Structure 3, however, and precise sublimation conditions are not assigned. Invasion of Structure 1 by transition lines occurs with greater Structure 3 growth and Structure 2 initiation (d). (e) Structure 2 quickly becomes a dominant feature on the surface, leading to Structures 1 and 3 almost disappearing (f). (g) The highest dose current achieves a pure Structure 2 surface phase. A dose current of 1.4A resulted in almost no adsorption and dosing at 1.6A destroyed the molecule in the doser.

Figure 7.2-1(a) shows conditions that have been used to create a high density surface phase consisting only of coexisting λ ($G^{\lambda} = \begin{bmatrix} 2 & 4 \\ -6 & -2 \end{bmatrix}$) and δ ($G^{\delta} = \begin{bmatrix} -6 & 2 \\ 2 & -4 \end{bmatrix}$) domains of Structure 1. In actuality, any clean dose at a very low dose current will create this pure Structure 1 phase. The primary requirement for a pure Structure 1 phase appears to be that molecules have enough time and space to reach equilibrium, therefore, the likelihood of formation of this phase at room temperature is inversely related to the overall flux of molecules arriving at the surface. A low flux dose condition is, therefore, required. Indeed, much of the experimental data on the pure Structure 1 phase shows that only a small proportion of the substrate – around 10% – is covered by domains that are the result of molecular diffusion.

When Co-TPP is dosed onto the clean Cu(110) surface at a dose current beyond that required to create the pure Structure 1 phase primary and secondary transition lines begin to appear within Structure 1 domains. Transition structures are differentiated from boundary structures by the cause of their formation. The greater molecular flux and resultant high local molecular density is expected to force the formation of close range boundaries between tightly packed and small domains. The overall density of the transition lines is lower than that of Structure 1 as their constituent TB-3 and TB-4 interactions possess an increased Co-Co separation between the molecules. Primary transition lines are the less common of the two. The slight distortion of the Structure 1 unit cells to $T_P^{\lambda} = \begin{bmatrix} 2 & 4 \\ -7 & -2 \end{bmatrix}$ and $T_P^{\delta} = \begin{bmatrix} -7 & 2 \\ 2 & -4 \end{bmatrix}$, brought about by the presence of the TB-3 interaction (Figure 5.1-6 and Figure 5.3-2) decreases the overall density of the structure from 20 atoms per molecule for Structure 1 to 24. It isn't known what induces this distortion. Their strongest appearance, shown in Figure 5.3-3, occurred after heating the sample for a short period of time. Secondary transition lines appear more readily than primary transition lines and are described by the more distorted

unit cells, $T_S^{\lambda} = \begin{bmatrix} 2 & 4 \\ -6 & -1 \end{bmatrix}$ and $T_S^{\delta} = \begin{bmatrix} -6 & 1 \\ 2 & -4 \end{bmatrix}$. Their characteristic shorter range TB-4 interactions (Figure 5.2-7 and Figure 5.3-5) decrease the density from 20 in Structure 1 to 22 atoms per molecule. Secondary transition lines are observed to develop and propagate in a dynamic fashion; forming and disintegrating, normally between the outer two rows of a growing domain, in much the same way as the domain itself grows and rearranges itself by the addition of individual molecules and micro-domains. Their ability to hold their position in a domain as the domain grows around it, as in Figure 5.3-6, remains unexplained. The number of primary and secondary lines observed in Structure 1 domains increases with dose current, culminating in domains that predominantly consist of the secondary 2D transition phase, with its two TB-4 interactions per molecule, and other random formations of coexisting primary and secondary transition lines and phases (Figure 5.3-4 and Figure 5.3-7). An example of this is shown in Figure 7.2-1(d), in which the Structure 1 domains are greatly distorted, as highlighted in green.

Coinciding with the formation and increasing presence of transition structures is the nucleation of both Structure 2 and Structure 3, the latter of which, like the secondary transition phase, is made up by two of the shorter range TB-4 interactions. Structure 3 is an unusual phase in its incorporation of alternating intermolecular interaction directions, which create a copper-aligned (12×8) heterochiral unit cell that appears in two mirror forms within the same assembly. Each unit cell contains two pairs of chirally oriented molecules, resulting in an overall racemic assembly. Most prominently, Structure 3 is defined by the crucial incorporation of adatoms in the assembly that occupy empty regions between the molecules, which reduce the overall density of the structure to 24 atoms per molecule. The exact position on the adsorption phase diagram has been impossible to establish due to the lack of success in achieving a pure structure. The observation of a nearly pure phase after a 45s dose at 1.45A would place it directly to the right of Structure 1 on the adsorption phase diagram (Figure 7.2-1), however, its strong similarity to the secondary transition phase (Figure 5.3-10) suggests it should occur on the second row of the adsorption phase diagram, i.e. at an

elevated dose current to Structure 1. It remains unknown what precise effect the adatoms in the structure have on the assembly and, therefore, Structure 3 persists as an anomaly.

There is a concomitant decrease in the average domain size of all structures as the different organisations compete for space but, as the dose current increases further through the Structure 1/2 transition (Figure 7.2-1e and f), Structures 1 and 3 are gradually phased out and replaced by disordered regions that consist of single molecules and micro-domains that cluster near the remaining ordered assembly. Structure 2 combines both longer and shorter range intermolecular interactions in the organisation and result in large and stable chiral domains that have a density of 20.5 atoms per molecule and consist of commensurate $G^{\lambda} = \begin{bmatrix} 4 & 7 \\ -7 & -2 \end{bmatrix}$ and $G^{\delta} = \begin{bmatrix} -7 & 2 \\ 4 & -7 \end{bmatrix}$ chiral unit cells that contain two molecules. The two shortest range interactions in the entire system, LR-2 and TB-2 (Figure 5.1-6), are exclusively involved in Structure 2.

7.3. Conclusion

The room temperature adsorption and organisation of Co-TPP on Cu(110) by high resolution STM and LEED experiments and periodic DFT calculations has been investigated. The experimental data shows adsorption into three orientations of isolated Co-TPP molecule and self-organisation into three highly ordered structures: Structures 1, 2 and 3. Structure 1 assembles into two co-existing, highly ordered and stable mirror-image chiral domains that are formed from a single-molecule unit mesh that is commensurate with the surface. Periodic DFT calculations were carried out for the experimentally observed unit mesh of Structure 1, including both the molecular adlayer and, importantly, a deformable copper surface.

Co-TPP molecules within the self-assembled Structure 1 adsorb at the short-bridge site of the Cu(110) surface. A considerable chemisorption interaction between the top layer of copper atoms and the entire Co-TPP

macrocycle causes the molecule's core to be situated close to the substrate. This has two important effects: it maintains planarity of the core macrocycle and consequently induces significant tilt and twist deformations in two distinct pairs of diametrically opposite phenyls. The almost upright twisted phenyl groups, in turn, facilitate significant inter-molecular $\pi - \pi$ interactions, estimated to contribute about $-25 kJmol^{-1}$ to the total domain energy. Within the 2D domains, the interplay between attractive intermolecular interactions and steric repulsions forces each molecule to adopt a well defined chiral propeller-like conformation, with clockwise propellers generating the λ domains, while the anticlockwise propellers generate the energetically equal but mirrored δ domain. Simulated STM images obtained from these structural models show very good agreement with experimental data. The lack of porphyrin core structure in the STM images is attributed primarily to topographical effects due to strong phenyl tilting away from the surface and, secondarily, to electron donation into the Co d_{z^2} orbital.

Structures 2 and 3 strongly resemble Structure 1 when imaged by STM and are, therefore, assumed to have similar electronic and conformational characteristics i.e. planar core close to the surface, phenyls strongly tilted and short-bridge adsorption site.

Like Structure 1, the directionality of intermolecular interactions in Structure 2 results in assembly into two highly ordered chiral mirror domains, denoted λ and δ, that are formed under the high flux dose condition. Structure 2 differs to Structure 1, however, in that each molecule is involved in four different inter-molecular interactions, resulting in a distinct and larger two-molecule unit cell. The exact molecular geometry of molecules in Structure 2 has not been attained, although molecular chirality is expected to be manifest. Structure 3 is unique and its assembly into a single racemic structure is due to the alternating directions of the intermolecular π–π interactions between mirror-oriented molecules, resulting in a heterochiral four-molecule unit cell. Structure 3 incorporates what are thought to be copper adatoms into its assembly and appears unpredictably throughout the STM data.

A comprehensive picture of the quantitative costs and gains of the relevant interactions that drive the substantial porphyrin deformation and the subsequent chiral organisation into Structure 1 has been presented. Although the cost of the surface-induced deformations is very high at 237.2kJmol^{-1}, a favourable net interaction energy of about –120kJmol^{-1} is calculated, with the strong molecule-substrate interaction of $E_{MOL\text{-}SUR}$ = –334.6kJmol^{-1} more than compensating for the high costs of inducing molecular and substrate deformations.

In contrast to the organised structures, singly adsorbed copper-aligned Co-TPP molecules on Cu(110) adsorb at the long-bridge site and adopt the familiar saddle-shaped conformation. Surprisingly, when ignoring inter-molecular interactions, the calculated adsorption energies of the saddle shaped conformer and the highly distorted Structure 1 conformer are found to be almost equal. However, the phenyl tilting deformations of the latter generate favourable π–π interactions producing an additional energy gain of –25kJmol^{-1} that drives supramolecular assembly and tilts the system preference towards the distorted conformer.

In summary, this work highlights the need to capture the full molecule-metal interaction adequately in order to obtain an in-depth understanding of porphyrin behaviour at surfaces. In particular, strong molecule-metal interactions are found to stabilise unexpected distortions in adsorbed porphyrin molecules. Additionally, such surface-induced deformations can be conducive for supramolecular assembly. Finally, this analysis of Co-TPP on Cu(110) may provide a more general framework for approaching the adsorption and assembly of large molecules on strongly-interacting metal surfaces.

7.4. Outlook and Future Work

The characterisation of the Co-TPP on Cu(110) system is by no means complete. Questions still remain about the effects of temperature and, specifically, the reordering of domains after heat treating a low coverage surface phase. Domains are known to break up at around 390K but the high

density of molecules on the surface after disintegration has entirely blocked the reformation of any organised structure (Figure 7.4-1).

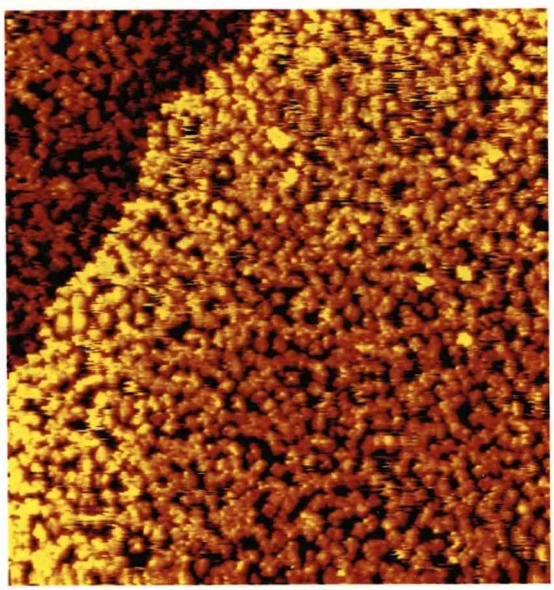

Figure 7.4-1. Heating a high coverage surface phase results in disorder and no possibility of reassembly. Image conditions: 625×670Å^2, I_T=0.5nA, V=1250mV.

It is envisaged that maintaining specific elevated temperatures after the initial heating of the low coverage phase may endow the experimentalist with control over domain selectivity. It may be necessary to dose directly onto a surface whose temperature is elevated so that the molecules can overcome any energy barriers required for shorter range bond formation and conformational alterations as they adsorb and assemble. A description of Co-TPP on Cu(110) at low temperatures also opens up further work, and may give some insight into the kinetics of domain formation.

Perhaps the most important outcome of this work is the successful use of periodic DFT in support of experimental methods. This has provided the means to approach this system in its entirety. Consequently, a truly detailed and deep understanding has been achieved, including a description of the interaction between the metal surface and the molecule, which this work clearly highlights is necessary to understand porphyrin behaviour at surfaces.

Such an approach should provide a more general framework for understanding the adsorption and assembly of other large molecules on strongly-interacting metal substrates. This system provides scope for more analysis by DFT, however. Further calculations on the single molecule adsorbed in all high symmetry sites of the underlying copper would strengthen the single molecule findings and, despite the current computational limitations, the author believes DFT can still offer something to the assembled structures of this system. However, as the unit cells for Structures 2 and 3 are too big, information on these must be gained gradually. For Structure 3 specifically, a calculated model of the 2D secondary transition phase would provide insight into the TB-4 interaction, which, it is expected, could then be directly transferred into a model of Structure 3. This would not be so easy with Structure 2 due to the four distinct interactions per molecule. At the moment, the key is in maintaining a single molecule unit cell so that the calculation is sufficiently simple.

Finally, it is known that the Structure 1 described in this work forms on other surfaces, including the Cu(110) surface that has 10ML cobalt and a 3×1 missing row oxygen surfactant layer (Figure 7.4-2). Both λ and δ domains and distortions to the structure in the form of the secondary transition phase are also observed. This means that the interpretation of the self-assembly and intermolecular interaction within this work is directly transferable to other systems. It must be noted that both systems contain Co-TPP and highly corrugated surfaces but, for the first time, this presents researchers with some predictive or, at the very least, expectative ability for such systems.

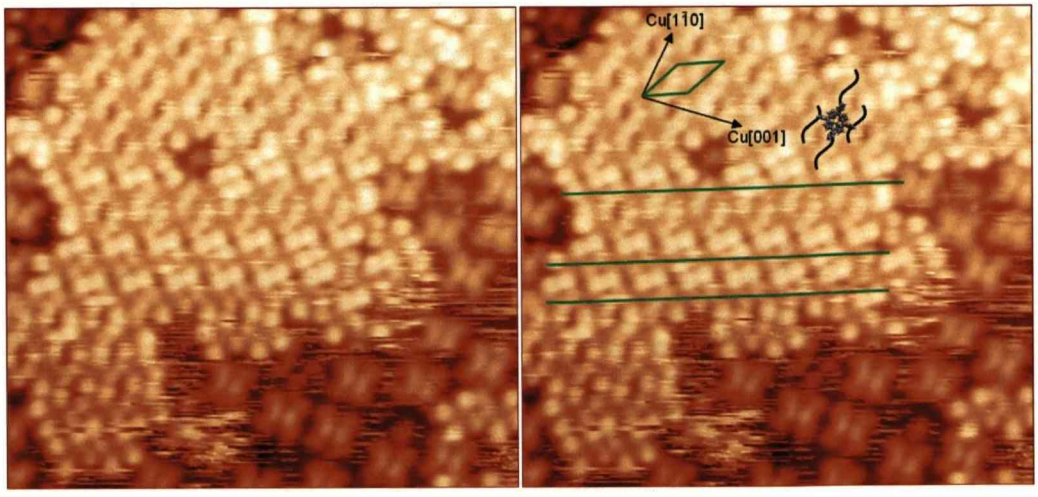

Figure 7.4-2. Uncalibrated image showing a distorted Structure 1 on the Co+O-covered Cu(110) surface. Original is on the right. Secondary transition lines are shown (underlined green). Single molecules in a saddled conformation are present and are seen to be aligned with the copper axes, which are shown by the 10×10 copper-aligned unit cell of Structure 1. The molecule position is shown also and the incorporation of each phenyl into four different lines of high interaction is indicated. The actual Structure 1 unit cell is shown in green.

Appendices and Bibliography

Appendices

Summary of chirality at solid surfaces

The following is an excerpt from Barlow and Raval[14] detailing the manifestation of chirality at solid surfaces.

'Of the various attributes that an organic molecule can bring to a metal surface, there is one that stands out for special attention. This is the ultimate selectivity function of chirality. Chirality is simply a geometric property which dictates that the mirror transformation of an object is a non-identity operation, i.e. the object and its mirror image are non-superimposable by any translation or rotation. Clearly for this to hold, the object must not possess any inverse symmetry elements (i.e. centre of inversion or reflection planes). As a result, a chiral object can exist in two distinguishable mirror, or enantiomeric, forms. The property of chirality has profound effects in physics, chemistry and biology, ranging from parity violations for weak forces, to the exclusive use of one mirror form of amino acids by all life forms on earth. In the organic system, chirality generally emerges at the tetrahedral carbon, provided sufficient complexity is present, e.g. that all the four attached substituent groups are different. The absolute configuration of such chiral centres can be labelled R (for rectus) or S (for sinister) as determined by the Cahn–Ingold–Prelog rules[130,131].

Chiral expression at surfaces has only attracted increasing attention in recent years, despite the fact that it is actually easier to create chirality in a 2D system since a surface cannot possess a centre of inversion and can only

maintain reflection mirror symmetry planes normal to the surface. Although intrinsically chiral metal surfaces can be created by cutting to expose step and kink sites that are chiral, the interesting point for the organic/inorganic interface is how the adsorption of organic molecules bestows chirality to a previously non-chiral surface. In fact, surface chirality can be manifested in a number of ways and a hierarchy of surface chirality can be identified[90]. We suggest the following classification of surface chiral systems that includes both the creation of local chiral motifs by single adsorption events (i.e. point chirality) and the creation of chiral domains arising from the chiral arrangements of the individual motifs (i.e. organisational chirality). We also differentiate between molecule-induced chirality and adsorption-induced chirality and between expressions of local and global chirality. A summary of the classification is shown in Figure A-1 and a description of how chirality can be manifested at non-chiral surfaces is given below.

Surface chirality from the adsorption of non-chiral molecules

The adsorption of non-chiral molecules at non-chiral metal surfaces has been shown to lead under certain conditions to expressions of chirality at a metal surface. The chirality is essentially adsorption-induced and two major classes of chirality are expressed, described below. In both cases, the chirality is strictly only expressed at a local level, and disappears at the global level.

Point chirality: adsorption-induced chiral motifs

This is the most basic form of chirality, arising because the adsorption site symmetry of the molecule locally destroys all surface mirror planes. For example, this can arise simply by adsorption of the molecule so that the molecular reflection planes do not align with the surface mirror planes. Therefore, any system with adsorption site (or point group) symmetry C1, C2, C3, C4 or C6 qualifies for this class of chirality, e.g. even a CO molecule tilted along a non-symmetry direction. What is very important to realise is that in such cases, energetically equivalent reflectional configurations will always

exist so that random adsorption will yield equal populations of image and mirror image adsorption motifs. This means that the surface is a 50:50 racemic mixture and possesses no overall chirality.

Organisational chirality: adsorption-induced chirally ordered domains

This type of chirality arises when ordered adsorption structures are formed where the 2D organisation of molecules destroys the reflection symmetry planes of the underlying surface. Such ordered domains belong to one of the five possible chiral space groups (P1, P2, P3, P4 or P6) that can exist at a surface. The organisational chirality generally arises because local adsorption-induced chiral motifs of the type described above can lead to asymmetries in lateral interactions, culminating in growth directions that lie along non-symmetry axes. However, again, due to the inherent non-chirality of the initial molecule, there is equal probability of nucleating reflectional chiral domains. As a result, these systems always consist of coexisting mirror chiral domains, leading to an overall non-chiral, racemic surface.

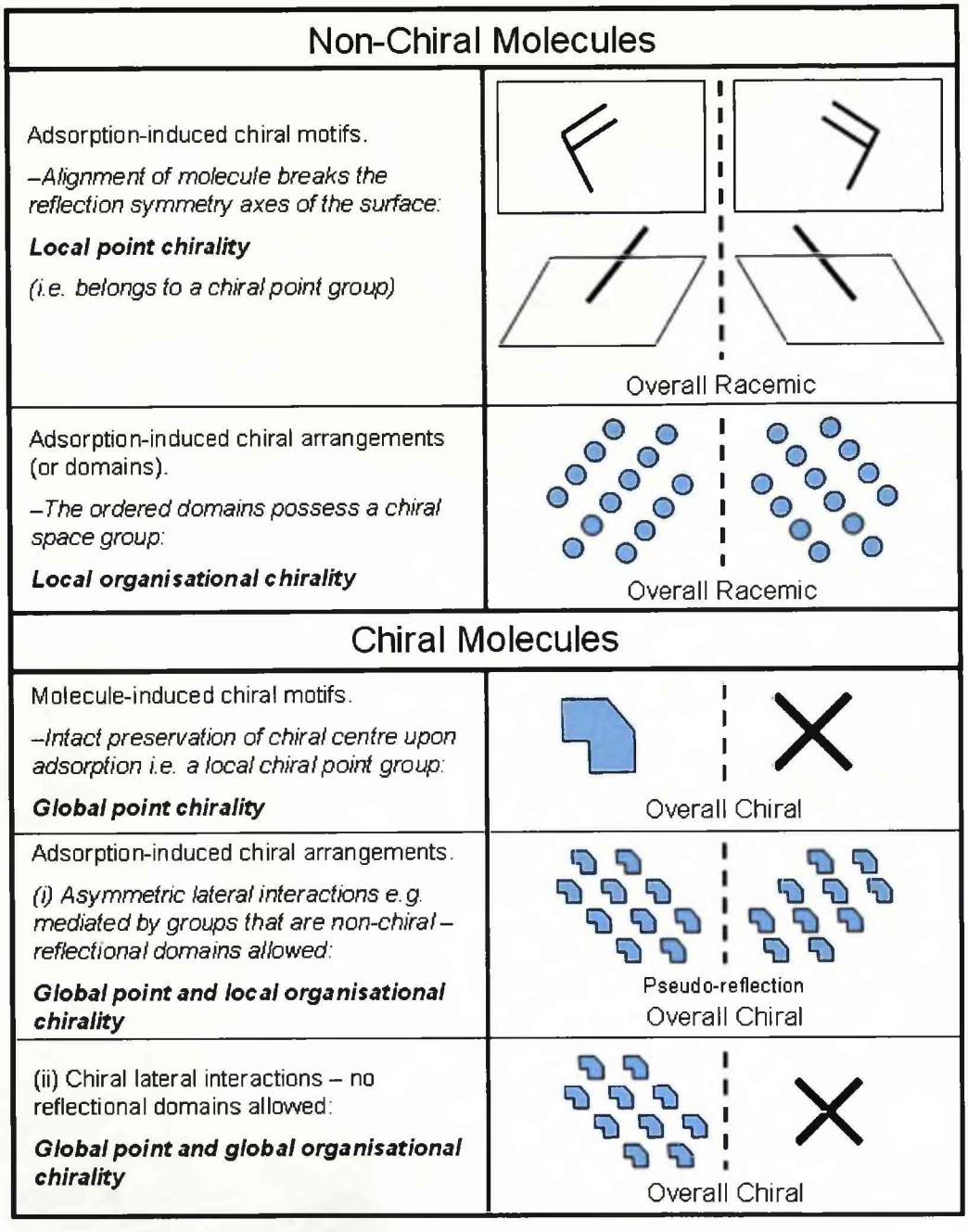

Figure A-1. Classification of chirality at a surface. Adapted from Barlow and Raval[14].

Surface chirality from the adsorption of chiral molecules

When a chiral molecule is adsorbed at a non-chiral surface, its very presence inevitably introduces chirality at the surface. However, there are different levels of chiral expressions, ranging from point chirality (molecule-

induced) to highly organised, extended forms of chirality (molecule- and adsorption-induced). Crucially, the chirality of the adsorbed molecule enables chiral expression at the surface to progress from a local to a global level.

Point chirality: molecule-induced chiral motifs

The adsorption of any chiral molecule at a surface which leaves the molecular chiral centre intact will inevitably lead to a local chiral motif. Since the inherent chirality of the molecule forbids the creation of its mirror image with all random adsorption events, no mirror chiral motifs can be conceived. Therefore, an overall chiral system is always produced.

Organisational chirality

The adsorption of chiral molecules on non-chiral surfaces can also lead to a range of ordered structures. If one ignores the local chirality possessed by the molecule and, instead, observes the organisation of the adsorbates with respect to the surface, it is found that both nonchiral and chiral arrangements can exist. Of the latter, two classes of chiral arrangements can exist, one in which reflectional domains coexist, and the other in which they cannot.

Adsorption-induced chiral organisation (at the local level). In this class, the local chiral adsorption motifs organise into a 2D chiral arrangement. However, we predict that in systems where lateral interactions are mediated by groups that are non-chiral and sufficiently remote from the chiral centres, reflectional domain arrangements may also be nucleated and will coexist at the surface. Therefore, organisationally both the image and mirror image chiral domains can exist. Overall, however, the system is still chiral, because if the inherent chirality of the molecule is taken into account, then the two domains are only pseudo-reflections of each other. At present, no published work on such systems exists and this remains a hypothetical classification.

Adsorption-induced chiral organisation (at the global level). This is the highest expression of chirality at a surface, involving both the creation of a molecule-induced chiral motif and an adsorption induced chiral organisation,

with each present in only one of its two possible mirror arrangements. As a result, only one unique chiral domain is nucleated and sustained over the entire interface so that a chiral surface is created possessing both global point and global organisational chirality. The expression of such global organisational chirality is difficult to attain and the first few examples have only been recently recorded.

Clearly, chirality can be manifested at a surface in a number of ways. However, we note that only those systems possessing global chirality can be considered to be truly chiral surfaces. To aid the reader, Table A-1 shows the various combinations of chiral manifestations that can occur at surfaces and their various outcomes in terms of exhibiting local or global chirality.'

Table A-1. Origins of both local and global surface chirality. Adapted from Barlow and Raval[14].

Manifestations of chirality						Chirality of surface	
Molecular Chirality	**Point chirality** *(chiral motif forms on adsorption)*		**Organisational chirality** *(domains form with molecules in chiral arrangements)*			**Local chirality** *(Surface is locally chiral and globally racemic)*	**Global chirality** *(Surface is locally chiral and globally chiral)*
	Chiral image created	Mirror image also created	Chiral image created	Mirror image also created			
×	×	×	×	×	→	×	×
			√	√		√	
	√	√	×	×			
			√	√			
√	√	×	√	√			√
			×	×			
			√	×			

Computational Details

The periodic DFT calculations in this study were performed by Matthew Dyer of the group of Mats Persson in the University of Liverpool's Surface Science Research Centre.

Using VASP code[132], plane waves were used as a basis set with an energy cut-off of 400eV. Valence electron-core interactions were included

using the projector augmented wave method[133] and the generalised gradient approximation was used for the exchange-correlation functional[134].

The calculations of Co-TPP in the periodic Structure 1 were based on a unit cell that was evaluated directly from the STM data and carried out on a 3×3×1 *k*-point grid. The copper surface was modelled using a four layer slab, with the bottom two layers fixed in their calculated bulk positions and the top two layers allowed to relax. Adsorption geometries were calculated by placing a Co-TPP molecule above the surface and allowing all molecular atoms and the top two layers of the copper slab to relax until all the forces on the atoms were less than $0.01 eV Å^{-1}$. STM images were calculated using the Tersoff-Hamann approximation[135].

Calculations were also performed for an isolated Co-TPP molecule on Cu(110), using a 6×8 surface unit cell leading to a minimum distance of 7.6 Å between the periodically repeated molecules. In this larger super-cell a 2×2×1 *k*-point grid was sufficient to obtain converged results, all other parameters were the same. Following experimental evidence the molecule was placed with the central cobalt atom above a long-bridge site on the surface and then a full geometry relaxation of the molecule and the top two layers was carried out.

To study the adsorption process, calculations were not only performed for the full adsorbate-surface system, but also on the isolated molecular overlayer and the isolated copper substrate in the same calculation cell. Further calculations were performed on isolated Co-TPP molecules in vacuum. It was necessary to carry out spin-polarised calculations on the isolated monolayer and isolated molecules, but not on the adsorbed system since in this case the previously partially occupied Co d_{z^2} orbital becomes fully occupied. Calculations on isolated molecules were carried out in a larger $25 Å^3$ super-cell to minimise interactions with molecules in neighbouring cells.

Alternative adsorption geometries

More than one stable conformation was calculated when relaxing the Co-TPP molecule at the short-bridge site. For comparison, data from three other conformations are presented here (Figure A-2). It can be seen that although there is variation in the exact angles at which the phenyl groups are tilted and twisted, the essential character of the deformation is conserved throughout all the conformations, with high tilt angles leading to a large energy cost due to deformation of the molecule and surface. In each case, this is regained by an even larger energy gain due to the interaction energy between the molecule and the surface, resulting in similar net adsorption energies for all conformers (Table A-2).

Table A-2. Comparison of geometric and energetic information for alternative stable adsorption conformations of CoTPP adsorbed with the cobalt atom above a short-bridge site on Cu(110).

Molecular Conformation	Conformer 1	Conformer 2	Conformer 3	Conformer (main text)
Tilt angles, Φ	149°, 144°, 149°, 144°	151°, 145°, 152°, 145°	154°, 144°, 152°, 145°	144°, 148.5°
Twist Angles, Θ	65°, 88°, 66°, 87°	60°, 82°, 60°, 83°	60°, 88°, 63°, 79°	64.5°, 86°
Height of Co atom above surface (Å)	2.1	2.1	2.2	2.1
$E_{MOL-SUR}$ ($kJmol^{-1}$)	−364.7	−352.2	−334.6	−363.7
E_{COST} ($kJmol^{-1}$)	+268.9	+263.0	+237.2	+268.3
E_{GAIN} ($kJmol^{-1}$)	−95.8	−89.2	−97.4	−95.4

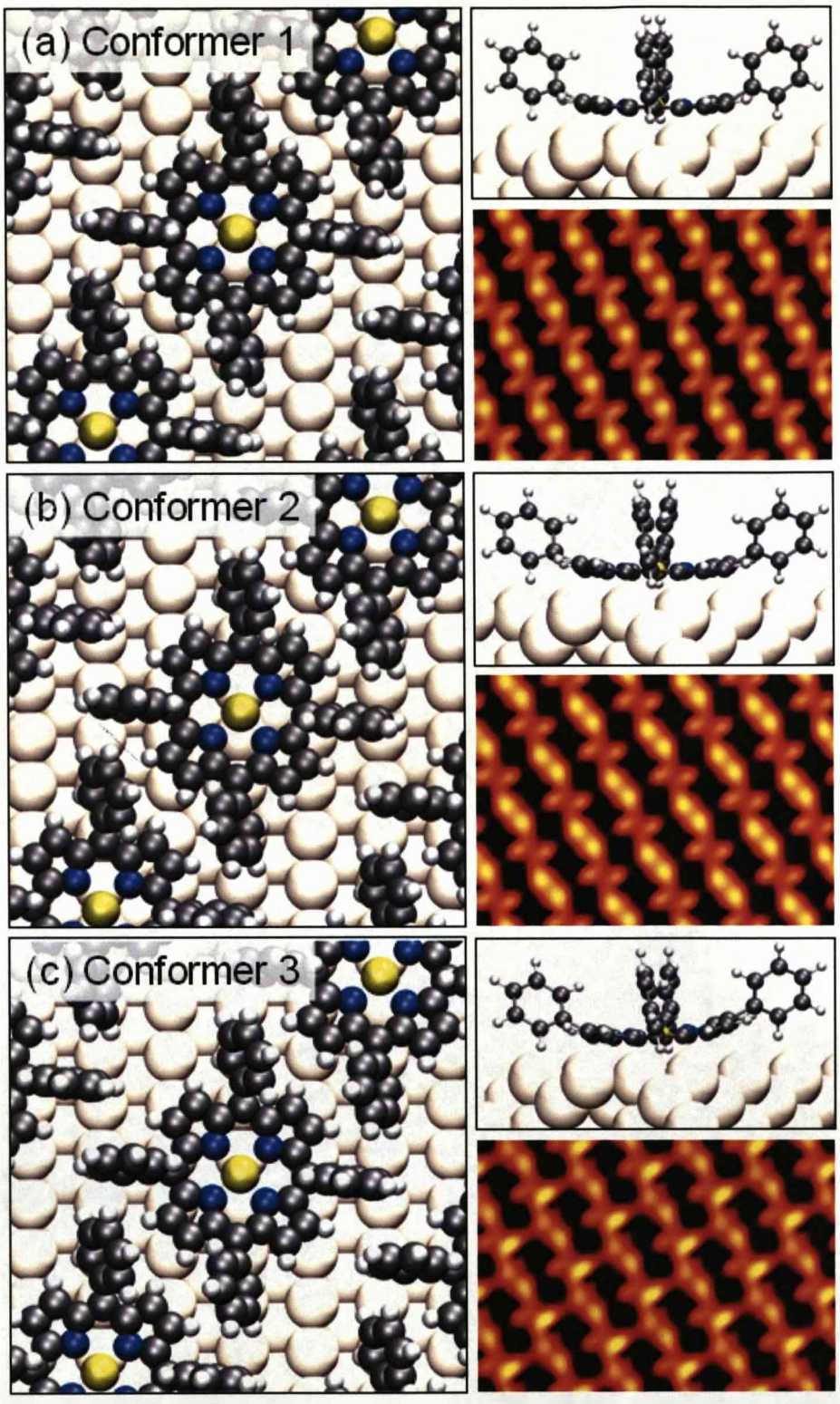

Figure A-2. Alternative stable adsorption conformations with the cobalt atom above a short-bridge site. Conformers 1-3 correspond to those in Table A-2. The geometry of each conformer is shown from above and the side. Calculated STM images are at 0.45eV.

Bibliography

(1) Beebe, R. A. *Journal of Physical Chemistry* **1926**, *30*, 1538-1544.

(2) Garner, W. E.; Kingman, F. E. T. *Nature* **1930**, *126*, 352-352.

(3) Henning, H. J. *Annalen Der Physik* **1932**, *13*, 599-620.

(4) Klein, R. *Journal of Chemical Physics* **1959**, *31*, 1306-1313.

(5) Taylor, H. S.; McKinney, P. V. *Journal of the American Chemical Society* **1931**, *53*, 3604-3624.

(6) Love, J. G.; Haq, S.; King, D. A. *Journal of Chemical Physics* **1992**, *97*, 8789-8797.

(7) Winkler, C.; Carew, A. J.; Haq, S.; Raval, R. *Langmuir* **2003**, *19*, 717-721.

(8) Erikat, I. A.; Hamad, B. A.; Khalifeh, J. M. *European Physical Journal B* **2009**, *67*, 35-41.

(9) Chehab, F.; Kirstein, W.; Nickel, B.; Peters, H.; Thieme, F. *Vakuum-Technik* **1983**, *32*, 109-115.

(10) Erley, W.; Wagner, H. *Journal of Chemical Physics* **1980**, *72*, 2207-2208.

(11) Hsu, Y. P.; Jacobi, K.; Rotermund, H. H. *Surface Science* **1982**, *117*, 581-589.

(12) Pavao, A. C.; Braga, M.; Taft, C. A.; Hammond, B. L.; Lester, W. A. *Physical Review B* **1991**, *43*, 6962-6967.

(13) Mehmood, F.; Kara, A.; Rahman, T. S.; Henry, C. R. *Physical Review B* **2009**, *79*.

(14) Barlow, S. M.; Raval, R. *Surface Science Reports* **2003**, *50*, 201-341.

(15) Ishida, T.; Terada, K.; Hasegawa, K.; Kuwahata, H.; Kusama, K.; Sato, R.; Nakano, M.; Naitoh, Y.; Haga, M. *Applied Surface Science* **2009**, *255*, 8824-8830.

(16) Shang, Z. G.; Gao, Y.; Jia, T. J.; Mo, Y. J. *Journal of Molecular Structure* **2009**, *930*, 60-64.

(17) Xu, Y. M.; Zhang, B. L.; Wu, S. H.; Xia, Y. *Analytica Chimica Acta* **2009**, *649*, 117-122.

(18) Baro, A. M.; Binnig, G.; Rohrer, H.; Gerber, C.; Stoll, E.; Baratoff, A.; Salvan, F. *Physical Review Letters* **1984**, *52*, 1304-1307.

(19) Humbert, C.; Dreesen, L.; Sartenaer, Y.; Peremans, A.; Thiry, P. A.; Volcke, C. *Chemphyschem* **2006**, *7*, 569-571.

(20) Besenbacher, F.; Lauritsen, J. V.; Linderoth, T. R.; Laegsgaard, E.; Vang, R. T.; Wendt, S. *Surface Science* **2009**, *603*, 1315-1327.

(21) Auwarter, W.; Klappenberger, F.; Weber-Bargioni, A.; Schiffrin, A.; Strunskus, T.; Woll, C.; Pennec, Y.; Riemann, A.; Barth, J. V. *Journal of the American Chemical Society* **2007**, *129*, 11279-11285.

(22) Auwarter, W.; Weber-Bargioni, A.; Riemann, A.; Schiffrin, A.; Groning, O.; Fasel, R.; Barth, J. V. *Journal of Chemical Physics* **2006**, *124*, -.

(23) Buchner, F.; Comanici, K.; Jux, N.; Steinrueck, H. P.; Marbach, H. *Journal of Physical Chemistry C* **2007**, *111*, 13531-13538.

(24) Buchner, F.; Flechtner, K.; Bai, Y.; Zillner, E.; Kellner, I.; Steinruck, H. P.; Marbach, H.; Gottfried, J. M. *Journal of Physical Chemistry C* **2008**, *112*, 15458-15465.

(25) Buchner, F.; Schwald, V.; Comanici, K.; Steinruck, H. P.; Marbach, H. *Chemphyschem* **2007**, *8*, 241-243.

(26) Gottfried, J. M.; Flechtner, K.; Kretschmann, A.; Lukasczyk, T.; Steinruck, H. P. *Journal of the American Chemical Society* **2006**, *128*, 5644-5645.

(27) Gottfried, J. M.; Marbach, H. *Zeitschrift Für Physikalische Chemie-International Journal of Research in Physical Chemistry & Chemical Physics* **2009**, *223*, 53-74.

(28) Humbert, C.; Volcke, C.; Sartenaer, Y.; Peremans, A.; Thiry, P. A.; Dreesen, L. *Surface Science* **2006**, *600*, 3702-3709.

(29) Lukasczyk, T.; Flechtner, K.; Merte, L. R.; Jux, N.; Maier, F.; Gottfried, J. M.; Steinruck, H. P. *Journal of Physical Chemistry C* **2007**, *111*, 3090-3098.

(30) Ogunrinde, A.; Hipps, K. W.; Scudiero, L. *Langmuir* **2006**, *22*, 5697-5701.

(31) Weber-Bargioni, A.; Auwarter, W.; Klappenberger, F.; Reichert, J.; Lefrancois, S.; Strunskus, T.; Woll, C.; Schiffrin, A.; Pennec, Y.; Barth, J. V. *Chemphyschem* **2008**, *9*, 89-94.

(32) Wölfle, T.; Görling, A.; Hieringer, W. *Physical Chemistry Chemical Physics* **2008**, *10*, 5739-5742.

(33) Gundlach, K.; Werwie, M.; Wiegand, S.; Paulsen, H. *Biochim Biophys Acta* **2009**, *1787*, 1499-504.

(34) Ariga, K.; Hill, J. P.; Wakayama, Y.; Akada, M.; Barrena, E.; de Oteyza, D. G. *Journal of Porphyrins and Phthalocyanines* **2009**, *13*, 22-34.

(35) Buchner, F.; Warnick, K. G.; Wolfle, T.; Gorling, A.; Steinruck, H. P.; Hieringer, W.; Marbach, H. *Journal of Physical Chemistry C* **2009**, *113*, 16450-16457.

(36) Auwärter, W.; Klappenberger, F.; Weber-Bargioni, A.; Schiffrin, A.; Strunskus, T.; Woll, C.; Pennec, Y.; Riemann, A.; Barth, J. V. *Journal of the American Chemical Society* **2007**, *129*, 11279-11285.

(37) Yoshimoto, S.; Tada, A. K.; Suto, K.; Yau, S. L.; Itaya, K. *Langmuir* **2004**, *20*, 3159-3165.

(38) de Oteyza, D. G.; Silanes, I.; Ruiz-Oses, M.; Barrena, E.; Doyle, B. P.; Arnau, A.; Dosch, H.; Wakayama, Y.; Ortega, J. E. *Advanced Functional Materials* **2009**, *19*, 259-264.

(39) Hill, J. P.; Wakayama, Y.; Ariga, K. *Physical Chemistry Chemical Physics* **2006**, *8*, 5034-5037.

(40) Rakow, N. A.; Suslick, K. S. *Nature* **2000**, *406*, 710-713.

(41) Choi, M. S.; Yamazaki, T.; Yamazaki, I.; Aida, T. *Angewandte Chemie-International Edition* **2004**, *43*, 150-158.

(42) Moresco, F.; Meyer, G.; Rieder, K. H.; Tang, H.; Gourdon, A.; Joachim, C. *Physical Review Letters* **2001**, *86*, 672-675.

(43) Moresco, F.; Meyer, G.; Tang, H.; Joachim, C.; Rieder, K. H. *Journal of Electron Spectroscopy and Related Phenomena* **2003**, *129*, 149-155.

(44) Li, C.; Ly, J.; Lei, B.; Fan, W.; Zhang, D. H.; Han, J.; Meyyappan, M.; Thompson, M.; Zhou, C. W. *Journal of Physical Chemistry B* **2004**, *108*, 9646-9649.

(45) Wearing, L. H.; Smerdon, J. A.; Leung, L.; Lograsso, T. A.; Ross, A. R.; McGrath, R. *Surface Science* **2007**, *601*, 3450-3455.

(46) Wearing, L. H.; Smerdon, J. A.; Leung, L.; Dhesi, S. S.; Ledieu, J.; Bencok, P.; Fisher, I.; Jenks, C. J.; McGrath, R. *Journal of Physics-Condensed Matter* **2008**, *20*.

(47) Shechtman, D.; Blech, I.; Gratias, D.; Cahn, J. W. *Physical Review Letters* **1984**, *53*, 1951-1953.

(48) Addou, R.; Gaudry, E.; Deniozou, T.; Heggen, M.; Feuerbacher, M.; Gille, P.; Grin, Y.; Widmer, R.; Groning, O.; Fournee, V.; Dubois, J. M.; Ledieu, J. *Physical Review B* **2009**, *80*.

(49) Cheng, W. T.; Cheng, H. W. *Aiche Journal* **2009**, *55*, 1383-1389.

(50) Uhm, Y. R.; Lee, H. M.; Rhee, C. K. *Ieee Transactions on Magnetics* **2009**, *45*, 2453-2455.

(51) Bonnell, D. A. *Scanning Tunnelling Microscopy and Spectroscopy: Theory, Techniques and Applications*; VCH Publishers, Inc.: New York, 1993.

(52) Forster, M.; Dyer, M. S.; Persson, M.; Raval, R. *Journal of the American Chemical Society* **2009**, *131*, 10173-10181.

(53) Robin, A.; Marnell, L.; Bjork, J.; Dyer, M. S.; Bermudez, P. S.; Haq, S.; Barrett, S. D.; Persson, M.; Minoia, A.; Lazzaroni, R.; Raval, R. *Journal of Physical Chemistry C* **2009**, *113*, 13223-13230.

(54) Brede, J.; Linares, M.; Kuck, S.; Schwobel, J.; Scarfato, A.; Chang, S.-H.; Hoffmann, G.; Wiesendanger, R.; Lensen, R.; Kouwer, P. H. J.; Hoogboom, J.; Rowan, A. E.; Broring, M.; Funk, M.; Stafstrom, S.; Zerbetto, F.; Lazzaroni, R. *Nanotechnology* **2009**, *20*, 275602.

(55) Leung, K.; Rempe, S. B.; Schultz, P. A.; Sproviero, E. M.; Batista, V. S.; Chandross, M. E.; Medforth, C. J. *Journal of the American Chemical Society* **2006**, *128*, 3659-3668.

(56) Kretschmann, A.; Walz, M. M.; Flechtner, K.; Steinruck, H. P.; Gottfried, J. M. *Chemical Communications* **2007**, 568-570.

(57) Bai, Y.; Buchner, F.; Wendahl, M. T.; Kellner, I.; Bayer, A.; Steinruck, H. P.; Marbach, H.; Gottfried, J. M. *Journal of Physical Chemistry C* **2008**, *112*, 6087-6092.

(58) Shubina, T. E.; Marbach, H.; Flechtner, K.; Kretschmann, A.; Jux, N.; Buchner, F.; Steinruck, H. P.; Clark, T.; Gottfried, J. M. *Journal of the American Chemical Society* **2007**, *129*, 9476-9483.

(59) Hausschild, R.; Reidel, G.; Zeller, J.; Kalt, H. *VDI Berichte (1839)* **2004**, 119-122.

(60) Jensen, K. P.; Ryde, U. *Chembiochem* **2003**, *4*, 413-424.

(61) Smith, V. PhD thesis, University of Liverpool, 2006.

(62) Gruden-Pavlovic, M.; Grubisic, S.; Niketic, S. R. *Journal of Inorganic Biochemistry* **2004**, *98*, 1293-1302.

(63) Alexander, A. E. *Journal of the Chemical Society* **1937**, 1813-1816.

(64) Tarasevich, M. R.; Khanova, L. A.; Borover, G. Y. *Journal of Electroanalytical Chemistry* **1980**, *7*, 309-316.

(65) Durand, R. R.; Anson, F. C. *Journal of Electroanalytical Chemistry* **1982**, *134*, 273-289.

(66) Mochida, I.; Suetsugu, K.; Fujitsu, H.; Takeshita, K.; Tsuji, K.; Sagara, Y.; Ohyoshi, A. *Journal of Catalysis* **1982**, *77*, 519-526.

(67) Nishiyama, F.; Yokoyama, T.; Kamikado, T.; Yokoyama, S.; Mashiko, S. *Applied Physics Letters* **2006**, *88*, -.

(68) Veld, M. I.; Iavicoli, P.; Haq, S.; Amabilino, D. B.; Raval, R. *Chemical Communications* **2008**, 1536-1538.

(69) Zotti, L. A.; Teobaldi, G.; Hofer, W. A.; Auwarter, W.; Weber-Bargioni, A.; Barth, J. V. *Surface Science* **2007**, *601*, 2409-2414.

(70) Kamikado, T.; Sekiguchi, T.; Yokoyama, S.; Wakayama, Y.; Mashiko, S. *Thin Solid Films* **2006**, *499*, 329-332.

(71) He, Y.; Ye, T.; Borguet, E. *Journal of the American Chemical Society* **2002**, *124*, 11964-11970.

(72) Auwärter, W.; Weber-Bargioni, A.; Riemann, A.; Schiffrin, A.; Groning, O.; Fasel, R.; Barth, J. V. *Journal of Chemical Physics* **2006**, *124*, 194708.

(73) Sekiguchi, T.; Wakayama, Y.; Yokoyama, S.; Kamikado, T.; Mashiko, S. *Thin Solid Films* **2004**, *464-65*, 393-397.

(74) Weber-Bargioni, A.; Auwärter, W.; Klappenberger, F.; Reichert, J.; Lefrancois, S.; Strunskus, T.; Woll, C.; Schiffrin, A.; Pennec, Y.; Barth, J. V. *Chemphyschem* **2008**, *9*, 89-94.

(75) Yokoyama, T.; Yokoyama, S.; Kamikado, T.; Mashiko, S. *Journal of Chemical Physics* **2001**, *115*, 3814-3818.

(76) Yokoyama, T.; Yokoyama, S.; Kamikado, T.; Okuno, Y.; Mashiko, S. *Nature* **2001**, *413*, 619-621.

(77) Hipps, K. W.; Lu, X.; Wang, X. D.; Mazur, U. *Journal of Physical Chemistry* **1996**, *100*, 11207-11210.

(78) Lu, X.; Hipps, K. W.; Wang, X. D.; Mazur, U. *Journal of the American Chemical Society* **1996**, *118*, 7197-7202.

(79) Moresco, F.; Meyer, G.; Rieder, K. H.; Tang, H.; Gourdon, A.; Joachim, C. *Phys Rev Lett* **2001**, *87*, 088302.

(80) Loppacher, C.; Guggisberg, M.; Pfeiffer, O.; Meyer, E.; Bammerlin, M.; Luthi, R.; Schlittler, R.; Gimzewski, J. K.; Tang, H.; Joachim, C. *Physical Review Letters* **2003**, *90*.

(81) Gimzewski, J. K.; Jung, T. A.; Cuberes, M. T.; Schlittler, R. R. *Surface Science* **1997**, *386*, 101-114.

(82) Jung, T. A.; Schlittler, R. R.; Gimzewski, J. K. *Nature* **1997**, *386*, 696-698.

(83) Kunitake, M.; Akiba, U.; Batina, N.; Itaya, K. *Langmuir* **1997**, *13*, 1607-1615.

(84) Kunitake, M.; Batina, N.; Itaya, K. *Langmuir* **1995**, *11*, 2337-2340.

(85) Ogaki, K.; Batina, N.; Kunitake, M.; Itaya, K. *Journal of Physical Chemistry* **1996**, *100*, 7185-7190.

(86) Hill, J. P.; Wakayama, Y.; Schmitt, W.; Tsuruoka, T.; Nakanishi, T.; Zandler, M. L.; McCarty, A. L.; D'Souza, F.; Milgrom, L. R.; Ariga, K. *Chemical Communications* **2006**, 2320-2006.

(87) Eichberger, M.; Marschall, M.; Reichert, J.; Weber-Bargioni, A.; Auwarter, W.; Wang, R. L. C.; Kreuzer, H. J.; Pennec, Y.; Schiffrin, A.; Barth, J. V. *Nano Letters* **2008**, *8*, 4608-4613.

(88) Auwarter, W.; Weber-Bargioni, A.; Brink, S.; Riemann, A.; Schiffrin, A.; Ruben, M.; Barth, J. V. *Chemphyschem* **2007**, *8*, 250-254.

(89) Ecija, D.; Trelka, M.; Urban, C.; de Mendoza, P.; Mateo-Marti, E.; Rogero, C.; Martin-Gago, J. A.; Echavarren, A. M.; Otero, R.; Gallego, J. M.; Mirandat, R. *Journal of Physical Chemistry C* **2008**, *112*, 8988-8994.

(90) Raval, R. *Current Opinion in Solid State & Materials Science* **2003**, *7*, 67-74.

(91) Raval, R. *Chemical Society Reviews* **2009**, *38*, 707-721.

(92) Terui, T.; Yokoyama, S.; Suzuki, H.; Mashiko, S.; Sakurai, M.; Moriwaki, T. *Thin Solid Films* **2006**, *499*, 157-160.

(93) Yokoyama, T.; Kamikado, T.; Yokoyama, S.; Mashiko, S. *Journal of Chemical Physics* **2004**, *121*, 11993-11997.

(94) Terui, T.; Sekiguchi, T.; Wakayama, Y.; Kamikado, T.; Mashiko, S. *Thin Solid Films* **2004**, *464*, 384-387.

(95) Yokoyama, T.; Tomita, Y. *Journal of Chemical Physics* **2008**, *129*.

(96) Klappenberger, F.; Weber-Bargioni, A.; Auwarter, W.; Marschall, M.; Schiffrin, A.; Barth, J. V. *Journal of Chemical Physics* **2008**, *129*.

(97) Barlow, D. E.; Scudiero, L.; Hipps, K. W. *Langmuir* **2004**, *20*, 4413-4421.

(98) Scudiero, L.; Barlow, D. E.; Hipps, K. W. *Journal of Physical Chemistry B* **2002**, *106*, 996-1003.

(99) Scudiero, L.; Barlow, D. E.; Mazur, U.; Hipps, K. W. *Journal of the American Chemical Society* **2001**, *123*, 4073-4080.

(100) Scudiero, L.; Barlow, D. E.; Hipps, K. W. *Journal of Physical Chemistry B* **2000**, *104*, 11899-11905.

(101) Comanici, K.; Buchner, F.; Flechtner, K.; Lukasczyk, T.; Gottfried, J. M.; Steinruck, H. P.; Marbach, H. *Langmuir* **2008**, *24*, 1897-1901.

(102) Inada, M.; Scifo, L.; Tanaka, S.; Grevin, B.; Suzuki, H.; Mashiko, S. *Japanese Journal of Applied Physics Part 1-Regular Papers Brief Communications & Review Papers* **2006**, *45*, 2103-2105.

(103) Grimme, S.; Muck-Lichtenfeld, C.; Antony, J. *Physical Chemistry Chemical Physics* **2008**, *10*, 3327-3334.

(104) Sinnokrot, M. O.; Sherrill, C. D. *Journal of Physical Chemistry A* **2004**, *108*, 10200-10207.

(105) Sinnokrot, M. O.; Sherrill, C. D. *Journal of Physical Chemistry A* **2006**, *110*, 10656-10668.

(106) Ye, X. Y.; Li, Z. H.; Wang, W. N.; Fan, K. N.; Xu, W.; Hua, Z. Y. *Chemical Physics Letters* **2004**, *397*, 56-61.

(107) Tsuzuki, S.; Honda, K.; Uchimaru, T.; Mikami, M.; Tanabe, K. *Journal of the American Chemical Society* **2002**, *124*, 104-112.

(108) Mück-Lichtenfeld, C.; Grimme, S. *Molecular Physics* **2007**, *105*, 2793-2798.

(109) Binnig, G.; Rohrer, H. *Helvetica Physica Acta* **1982**, *55*, 128-128.

(110) Binnig, G.; Rohrer, H. *Helvetica Physica Acta* **1982**, *55*, 726-735.

(111) Binnig, G.; Rohrer, H. *Surface Science* **1985**, *152*, 17-26.

(112) Binnig, G.; Rohrer, H.; Gerber, C.; Weibel, E. *Physica B & C* **1982**, *109*, 2075-2077.

(113) Binnig, G.; Rohrer, H.; Gerber, C.; Weibel, E. *Applied Physics Letters* **1982**, *40*, 178-180.

(114) Binnig, G.; Rohrer, H.; Gerber, C.; Weibel, E. *Physical Review Letters* **1982**, *49*, 57-61.

(115) Chen, C. J. *Introduction to Scanning Tunneling Microscopy*; Oxford University Press, INc.: New York, 1993.

(116) Baratoff, A.; Binnig, G.; Rohrer, H. *Journal of Vacuum Science & Technology B* **1983**, *1*, 703-704.

(117) Binnig, G.; Rohrer, H. *Ibm Journal of Research and Development* **2000**, *44*, 279-293.

(118) Farnsworth, H. E. *Phys. Rev.* **1929**, *34*, 679-696.

(119) Farnsworth, H. E. *Phys. Rev.* **1932**, *40*, 684-712.

(120) Farnsworth, H. E. *Phys. Rev.* **1933**, *43*, 900-906.

(121) Farnsworth, H. E. *Phys. Rev.* **1936**, *49*, 598-605.

(122) E. J. Scheibner, L. H. G., C. D. Hartman *The Review of Scientific Instruments* **1960**, *31*, 112-114.

(123) J. J. Lander, J. M., F. Unterwald *The Review of Scientific Instruments* **1962**, *33*, 782-783.

(124) Attard, G.; Barnes, C. *Surfaces*; Oxford University Press: New York, 1998; Vol. 59.

(125) R. L. Park, H. H. M. J. *Surface Science* **1968**, *11*, 188-202.

(126) D. P. Woodruff, T. A. D. *Modern Techniques of Surface Science - Second Edition*; Second ed.; The Press Syndicat eof the University of Cambridge: Cambridge, 2003.

(127) Horcas, I.; Fernandez, R.; Gomez-Rodriguez, J. M.; Colchero, J.; Gomez-Herrero, J.; Baro, A. M. *Review of Scientific Instruments* **2007**, *78*, -.

(128) Yildirim, H.; Kara, A.; Durukanoglu, S.; Rahman, T. S. *Surface Science* **2006**, *600*, 484-492.

(129) Dyer, M. S.; A., R.; Raval, R.; Persson, M. *In Preparation*.

(130) Cahn, R. S.; Ingold, C. K.; Prelog, V. *Angew. Chem* **1966**, *78*.

(131) Cahn, R. S.; Ingold, C. K.; Prelog, V. *Angew. Chem. Int. Ed.* **1966**, *5*.

(132) Kresse, G.; Furthmüller, J. *Physical Review B* **1996**, *54*, 11169-11186.

(133) Kresse, G.; Joubert, D. *Physical Review B* **1999**, *59*, 1758-1775.

(134) Perdew, J. P.; Chevary, J. A.; Vosko, S. H.; Jackson, K. A.; Pederson, M. R.; Singh, D. J.; Fiolhais, C. *Physical Review B* **1992**, *46*, 6671-6687.

(135) Tersoff, J.; Hamann, D. R. *Physical Review Letters* **1983**, *50*, 1998-2001.